# Simulation dans le domaine temporel de la propagation acoustique en conduit traité en présence d'un écoulement : caractérisation et suppression des instabilités hydrodynamiques

Yuanyuan Deng


*N° d'ordre NNT: 2020LYSEC35*

***THÈSE de DOCTORAT DE L'UNIVERSITÉ DE LYON***
***opérée au sein de l'École Centrale de Lyon***

***École Doctorale N° 162***
***Mécanique Énergétique Génie Civil Acoustique***

***Spécialité de doctorat : Acoustique***

*Soutenue publiquement le 3/12/2020, par*
***Yuanyuan Deng***

---

# *Time-domain simulation of sound propagation in a lined flow duct: characterization and suppression of hydrodynamic instabilities*

---

*Devant le jury composé de:*

| | | | |
|---|---|---|---|
| *Dragna, Didier* | *Maître de conférences* | *École Centrale de Lyon* | *Directeur de thèse* |
| *Gabard, Gwénaël* | *Senior researcher* | *Le Mans Université* | *Rapporteur* |
| *Galland, Marie-Annick* | *Professeur* | *École Centrale de Lyon* | *Directeur de thèse* |
| *Ichchou, Mohamed* | *Professeur* | *École Centrale de Lyon* | *Examinateur* |
| *Lombard, Bruno* | *Directeur de recherche* | *LMA* | *Examinateur* |
| *Marx, David* | *Chargé de recherche* | *Université de Poitiers* | *Examinateur* |
| *Piot, Estelle* | *Ingénieure de recherche* | *ONERA Toulouse* | *Rapporteur* |
| *Roger, Michel* | *Professeur* | *École Centrale de Lyon* | *Examinateur* |

Deuxieme de couverture

# Résumé

Il a été clairement établi expérimentalement que des instabilités hydrodynamiques peuvent être générées dans un conduit en présence d'écoulement quand un absorbant acoustique est placé sur une des parois. Ces instabilités apparaissent également dans les simulations numériques issues des équations d'Euler linéarisées, et empêchent une prédiction correcte des champs acoustiques. Les objectifs de la thèse sont de caractériser finement les instabilités qui apparaissent dans les simulations temporelles pour un conduit traité avec écoulement, de proposer des méthodes pour éviter leur génération et finalement d'évaluer leur efficacité.

Les méthodes numériques utilisées sont présentées dans un premier temps. Les équations d'Euler linéarisées sont résolues dans le domaine temporel avec des schémas aux différences finies d'ordre élevé, faiblement dissipatifs et dispersifs. Une condition aux limites d'impédance a été développée dans le domaine temporel spécifiquement pour ces schémas d'ordre élevé. Les études ont porté sur une série de cas test développée pour étendre le cas de référence, le conduit « NASA GIT », au cas de la propagation de modes supérieurs. Les résultats obtenus avec ces simulations dans le domaine temporel sont comparés avec ceux issus d'une méthode modale et ceux provenant d'un logiciel commercial résolvant les équations d'Euler dans le domaine fréquentiel par éléments finis. Un bon accord est observé entre ces trois méthodes et également avec les données issues des mesures. Il apparaît que des instabilités sont générées en simulation numérique, aussi bien dans le domaine temporel que fréquentiel.

Une analyse fine des instabilités générées dans les simulations temporelles est ensuite réalisée, par une analyse modale développée à partir de la méthode des caractéristiques. L'influence des paramètres numériques est précisée, notamment en termes de nombre d'ondes et de formes modales. Une convergence est observée quand la taille des éléments diminue. Par ailleurs, un réglage optimal du filtre sélectif spatial utilisé dans la résolution numérique doit être opéré, afin de retrouver les caractéristiques attendues pour l'instabilité. L'impact d'autres facteurs est également présenté : fréquence d'excitation, profil de la vitesse moyenne, impédance du traitement, ...

Finalement, la méthode GTS (pour Gradient Term Suppression), qui a été proposée initialement pour éviter la génération d'instabilités dans des écoulements cisaillés, est mise en œuvre et évaluée dans les configurations précédemment étudiées. Elle consiste à réduire le terme lié au gradient de l'écoulement moyen dans les équations d'Euler linéarisées. L'étude montre qu'il existe un impact sur les champs acoustiques obtenus, notamment sur les modes se propageant dans le sens de l'écoulement. Ainsi la pression peut, selon les cas, être sous- ou sur- estimée de quelques dBs. Cette étude suggère ainsi que d'autres méthodes développées pour réduire les instabilités de Kelvin Helmholtz pourraient être efficaces dans le cas d'un conduit traité sous écoulement.

**Mots clés**: propagation acoustique en conduit; absorbant acoustique sous écoulement; simulation temporelle; instabilité hydrodynamique; suppression des instabilités.

# Abstract

Hydrodynamic instabilities in a lined flow duct have been reported in several experiments. Such instabilities also appear in the numerical solutions of the linearized Euler equations and preclude the accurate prediction of the acoustic field. The objectives of the thesis are to finely characterize instabilities appearing in time-domain simulations of a lined flow duct, to propose methods to remove these instabilities and finally to evaluate their efficiency.

Firstly, the numerical methods are presented. The linearized Euler equations are solved in the time domain using high-order and low dissipative and dispersive finite-difference schemes. A time-domain impedance boundary condition developed for high-order methods is implemented. A series of test cases is proposed with the aim of extending the NASA GIT benchmark data for higher-order mode propagation. Results obtained with the time-domain simulations are compared to those obtained with a mode matching method and a commercial software that solves the linearized Euler equations in the frequency domain with a finite element method. A good agreement is found between the results for the three methods and the experimental data. The presence of an instability is shown in the solutions of the linearized Euler equations both in the frequency and time domain.

An analysis of instabilities generated in time-domain simulations is then conducted, using a modal analysis based on the method of characteristics. The impact of the numerical parameters on the properties of instabilities, namely wavenumber and mode shape, is investigated. A convergence is obtained as the mesh size decreases. In addition, a fine tuning of the spatial selective filter used in the numerical algorithm is necessary to retrieve the predicted characteristics of the instabilities. A parametric study is then performed to examine the effects of the source frequency, the mean flow profile and the impedance on the instability.

Finally, the gradient term suppression (GTS) method, originally proposed for avoiding the generation of instabilities in shear flows, is implemented and evaluated on the configurations previously studied. It corresponds to the reduction of the mean flow gradient term in the linearized Euler equations. The effectiveness of the method for a lined flow duct is illustrated. It is shown however that the acoustic field is impacted, especially for the downstream propagating modes. The sound pressure level can then be overestimated or underestimated by a few dBs. As a future work, this study indicates that other methods targeting Kelvin Helmholtz instabilities could also be adopted for the suppression of instabilities in a lined flow duct.

**Key words**: duct acoustics; lined flow duct; time-domain simulation; hydrodynamic instabilities; suppression of instabilities.

# Acknowledgements

This study is performed in the acoustic center of Laboratoire de Mécanique des Fluides et d'Acoustique in École Centrale de Lyon from 2017 to 2020. It is supported by the China Scholarship Council (CSC) under the China Scholarship Council and Ecoles Centrale Group (CSC-GEC) program.

Firstly, I want to express my gratitude to my supervisors, Marie-Annick Galland and Didier Dragna for their support during the three years. They guide me in the research of acoustics, and they are always willing to discuss with me. I'm deeply impressed not only by their profound knowledge in acoustics but also their concentrated and cautious attitudes in scientific research. I want to express my great thanks to their continuous encouragement during the three years, especially in the third when the Covid-19 spreads. I also want to thank them for their great patience to correct my scientific writings.

I appreciate that Michel Roger accepted to be the president of the jury and held the defense. I want to thank Estelle Piot and Gwénaël Gabard, who cautiously reviewed the thesis and gave detailed suggestion and corrections which improved the quality of the manuscript. I want to thank Mohamed Ichchou, Bruno Lombard and David Marx for accepting to be my jury members, and for all those interesting discussions about this study. I also want to thank professor Ichchou for interviewing me three years ago in Beijing. My adventure started then.

Then I would like to thank all the people in the acoustic team of LMFA for their company in last three years. It's a great pleasure to work with them. I can not forget to thank my colleagues. I want to thank Étienne and Georgois, who give me a lot of laughter during the three years. I want to thank Thomas for his kind help on coding. I would like to thank Antoni for those discussions about hydrodynamic instabilities. I want to thank Patricia for discovering Lyon with me. I also want to thank Courtey, Elina, Ariane, Marion, Yann, Simon, Igor, Gabriele, Danny, Léo, Jean, Mathieu, Daher, Hugo, Alexis, Mochene, Arthur, Rafaël, Paul, Pierre, Vianney.

I also want to thank my friends, Nour, Ying Zhu, Jianzhao Wu, Zecong Qing, Haining Luo, Peng Wang, Mingfa Zhang, Shiwei Li and Dong Han, who help me in different aspects and share great moments in Lyon with me.

I want to give my great thanks to my parents, who provide me consistent encouragement and comfort. At last, I want to thank my husband for his patience and faith in me.

# Contents

# 1 Introduction

## 1.1 Context of the study

Since the 1970s, certifications and requirements have become more stringent after the first international aircraft noise standard was promulgated by the International Civil Aviation Organization (ICAO). The Advisory Council for Aviation Research and Innovation in Europe (ACARE) also set some targets for noise reduction in 2050, which mentioned the noise need to be reduced to 65 % relative to the year 2000 [1]. Although the noise of a single aircraft has been reduced by approximately 75 % in the past 30 years, the growing of air traffic leads to that many EU citizens still face high noise levels, especially for residents near airports. Regarding the noise around airports, four suggestions have been put forward by ICAO: reduction at source, land-use management and planning, noise abatement operational procedures and operating restrictions. Among them, operating restrictions limit access to an airport, which have an obvious side effect on local economies. Besides, in terms of long-range and low-carbon travel, there is no other choice than aviation. Therefore, technological innovation in the aviation manufacturing industry is still the priority to solve this problem.

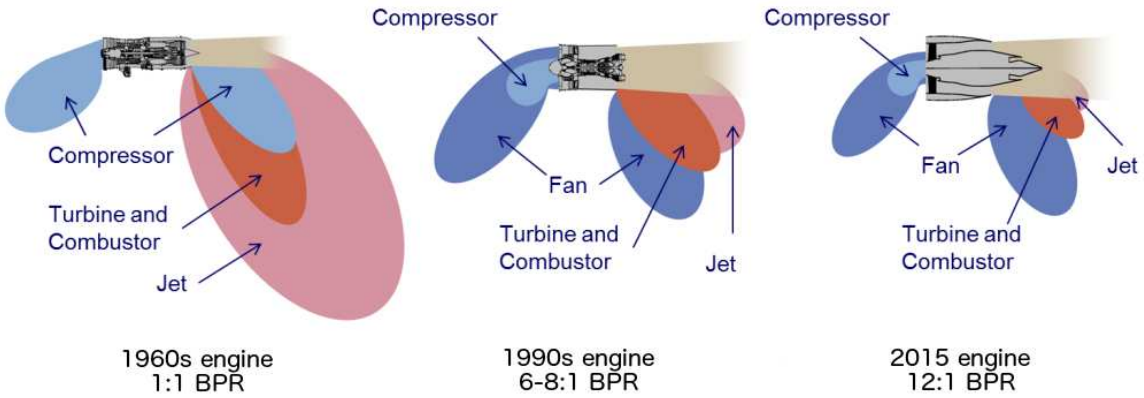


Figure 1.1: Evolution of propulsion-noise sources over time; original figure courtesy of Pratt & Whitney [2].

To improve fuel efficiency and reduce the jet mixing noise, the bypass ratio of aircraft engines has been progressively increased. Since the 1960s, a decrease of 20 EPNdB has been achieved

for the noise of an individual aircraft [3]. With a sharp reduction of the jet noise, the fan noise becomes a significant loud noise source as shown in figure 1.1.

Aircraft manufacturers generally install acoustic liners in the intake and bypass duct of a turbo engine aiming at eliminating the fan noise. Thanks to these treatments, the overall aircraft perceived noise level can be reduced by 4∼5 dB at take-off stage and 2 dB at landing. To ensure high efficiency of acoustic liners and guide process improvement at the design stage, the sound field along a lined duct with the presence of a mean flow should be predicted accurately at first.

Indeed, many techniques, such as the finite element method (FEM), the mode matching method, solutions of linearized Euler equations (LEE), the boundary element method (BEM) etc., have been proposed. A general review of techniques used in Computational Aeroacoustics (CAA) can be found in [3, 4]. The wide availability of the finite element method (FEM) makes it popular since the 1980s. It has been broadly applied for implementing heterogeneous materials, considering complex geometries and dealing with nonlinearities [5]. Nevertheless, when a three-dimensional problem is considered, the computation can be costly. The BEM discretizes a surface rather than a volume, and as a result presents a low computation cost. However, it can not fully present a mean flow profile because of a uniform flow. The mode matching method describes the sound field with the solution of a mode basis. It is widely adopted for its efficiency and its accuracy when higher-order modes propagation is included.

Regarding that a new design of aircraft demands multi-objective optimizations accounting for aircraft performances, operational costs, environmental impacts, etc., a fast approach is desirable. The time-domain approach is beneficial to solve broadband problems. In the meanwhile, it also suits to deal with nonlinear problems. Therefore, the time-domain approach is chosen as one of the main tools to study the sound field in a lined flow duct in this study.

Actually, the sound field in a lined duct has not been fully understood yet. The studies or experimental data on higher-order modes propagation in a lined flow duct are insufficient. Besides, other difficulties still exist in the numerical simulation of the sound field in a lined flow duct.

Firstly, the impedance of acoustic liners is originally described in the frequency domain. In the early stage of the study, the use of Ingard-Myers boundary condition with the assumption of a uniform flow has been widely adopted. However numerous studies have questioned the use of a uniform flow and have highlighted the importance of considering the effect of the boundary layer. Consequently, the problems arose—what is the appropriate boundary condition used to describe the interaction between the acoustic propagation and acoustic liners. Moreover, to include the effect of acoustic liners in the time-domain calculation, it is imperative to find an equivalent alternative of the frequency-domain impedance boundary condition. Indeed, the direct computation of the convolution from the frequency domain to the time domain is costly. Hence, the second difficulty lies in the implementation of a time-domain impedance boundary condition. In this study, a model which approximates well liner impedance characteristics is established. The impedance boundary condition is implemented with the consideration of a mean flow profile

instead of applying the Ingard-Myers boundary condition with the a uniform flow.

Furthermore, the existences of instabilities, which result from complex interactions between the acoustic waves, the mean flow and acoustic liners, have been observed over recent decades in several experimental results [6, 7, 8, 9]. These phenomena reveal the existence of hydrodynamic instabilities in certain circumstances, for example, a high mean flow velocity, a liner with small resistance and for plane waves [10]. These instabilities are observed more often in numerical simulations than in engineering applications, especially in time-domain simulations, and they hinder the application of time-domain methods in engineering practice. It is worthwhile to explore the answers to these questions: what is the nature of these instabilities? Can these instabilities be predicted when solving the acoustic field? Is it possible to remove instabilities without greatly impacting the acoustic field? What is the cost of a stable simulation when the instabilities are removed? These issues are discussed through the thesis.

## 1.2 Outline of the thesis

The outline of this study is arranged as follows: chapter 2 presents three numerical tools, namely the mode matching method, solving LEE in the frequency domain by using a finite element method (based on the commercial software COMSOL) which is commonly applied in the study of duct acoustics and a high-order time-domain LEE solver. The objective of this chapter is to validate the use of the time-domain approach in studying the sound field in a lined flow duct. Among these three methods, the high-order time-domain solver is a homemade approach first developed by the acoustic team of LMFA [11]. The impedance model, as well as the implementation of the impedance boundary condition in the time domain, is introduced. A comparison of the results is then conducted among the three approaches against the experimental data provided by the NASA GIT benchmark experiment below the cut-off frequency ($f \leq 3$ kHz). The higher-order modes propagation is also studied. The effect of the boundary layer thickness on the acoustic propagation is finally discussed.

Chapter 3 presents the modal analysis approach which solves the LEE in the frequency domain by seeking the solution as a sum of modes. This chapter aims at presenting the viability of the modal analysis approach in interpreting the sound field with mode solutions. The modal analysis approach is essentially an eigenvalue problem (EVP). In the first part, the EVP is established and solved by the Chebyshev spectral method. In the second part, the validation of the modal analysis approach is conducted by comparing the results with an analytical/semi-analytical approach. Specifically, modes and mode shapes of acoustic propagation for a rigid duct and a lined duct with a uniform flow are presented. Finally, the impact of a shear flow on the acoustic propagation is investigated. The modal analysis approach will be continuously utilized in the analysis of hydrodynamic instabilities in the next chapter.

Chapter 4 is dedicated to investigating hydrodynamic instabilities generated during the propagation of acoustic waves in a lined flow duct. There are two primary aims of this study: 1. To

characterise the hydrodynamic instabilities by using the time-domain LEE solver and the modal analysis approach. 2. To analysis how the source frequency, a mean flow and a liner impedance impact instabilities. The first part covers four cases according to the existence and the type of instabilities. These four cases are: case 0, without mean flow and with a ceramic tubular liner (CT57); case 1, with a weak shear flow and a mass-spring-damper (MSD) liner; case 2, with a strong shear flow and a MSD liner; case 3, with a strong shear flow and a CT57 liner. In the second part, the Briggs-Bers criterion is applied to specify the type of instabilities for case 2 and case 3. The characterization of the instabilities, namely the spatial growth rate, the wavelength and the mode shapes of the instabilities for case 2, are compared between the modal analysis approach and the LEE time-domain method. As the impact of numerical parameters has been indicated in many researches, the third part presents a study for the influence of the selective filtering and the mesh size on instabilities in time-domain simulations. Finally, a parametric study on the source frequency, the mean flow profile and the liner impedance is carried out.

The strategies to suppress instabilities in a lined duct are presented in chapter 5. The chapter sets out to show the effect of the partial Gradient Term Suppressing (GTS) method on removing instabilities and its impact on the acoustic field. In the first part, the commonly used methods for suppressing the instabilities in a lined flow duct are reviewed as well as the techniques to remove the Kelvin-Helmholtz instabilities in shear flows. In the second part, one of the techniques targeted for suppressing Kelvin-Helmholtz instabilities, namely the partial GTS method, is adopted to diminish the instabilities related to acoustic liners. In the third part, the partial GTS method is evaluated according to its viability to suppress instabilities and the ability to predict an accurate sound field. Three cases, which are a rigid duct, a duct lined with a MSD liner and a duct lined with a CT57 liner, are tested in the frequency domain and in the time domain. The responses of acoustic waves, convective instabilities and absolute instabilities to the partial GTS method are investigated.

# 2 Acoustic propagation in a lined flow duct

To achieve maximum performance of acoustic liners, it is necessary to accurately predict the acoustic propagation in the design stage of acoustic liners. While sound propagation along an acoustically lined duct with the presence of a mean flow has been largely studied in the literature, there are still open questions. Recently, researchers have conducted numerous studies on this topic regarding the issues, i.e., suitable boundary conditions[12, 13, 11], the interface boundary condition between lined and unlined part [14, 15, 16], and instabilities [17, 8, 18] along the lined surface. For developing a deep understanding of this topic, three methods, namely, a mode matching method, the commercial software COMSOL Multiphysics solving linearized Euler equations (LEE) in the frequency domain and a high-order finite difference time-domain solver of LEE [19] proposed by the acoustic team of LMFA, are presented in this chapter.

The objective of this chapter is to present these methods aiming at dealing with acoustic propagation in a lined flow duct. Firstly, the configuration used through the thesis is described. A brief overview of acoustic liners is given. Accordingly, the three approaches are introduced in details. Another objective of this chapter is to validate the use of the high-order low dissipative and dispersive finite difference time-domain solver by comparing the results obtained from the three methods. For this, a well known benchmark problem proposed by Jones *et al.* [20] is considered. The results obtained by three methods are compared with the experimental results considering the plane wave propagation. An extension is also proposed considering higher-order modes propagation. Two cases, corresponding to wave propagation without and with a mean flow, are investigated below and above the duct cutoff frequency.

## 2.1 Set-up modeling

The set-up used to model the acoustic propagation in a duct with the presence of a mean flow is introduced. An acoustic liner is partially installed on the wall of a duct to absorb acoustic waves. A brief overview of acoustic liner models, namely Mass-Spring-Damper (MSD) liners, ceramic tubular liners and Single Degree Of Freedom (SDOF) liners, is provided.

### 2.1.1 Set-up configuration

A partially lined duct, with dimensions of $L_x \times L_y \times L_z$, is considered. The duct is split into three sections, a first rigid part, a lined part and a second rigid part. The mean flow $\boldsymbol{u_0}$ is from left to right with a bulk Mach number $M$. An acoustic liner is located in the middle of the upper wall with a length $L_t$ as shown in figure 2.1. An acoustic source $Q$, which can be impulsive or harmonic, is installed in the source plane. The exit plane is supposed to be anechoic which means that no sound is intended to be reflected. $\rho_0$ is the density of the air and $c_0$ is the speed of sound. Note that convention $e^{i\omega t}$ is adopted throughout the study.

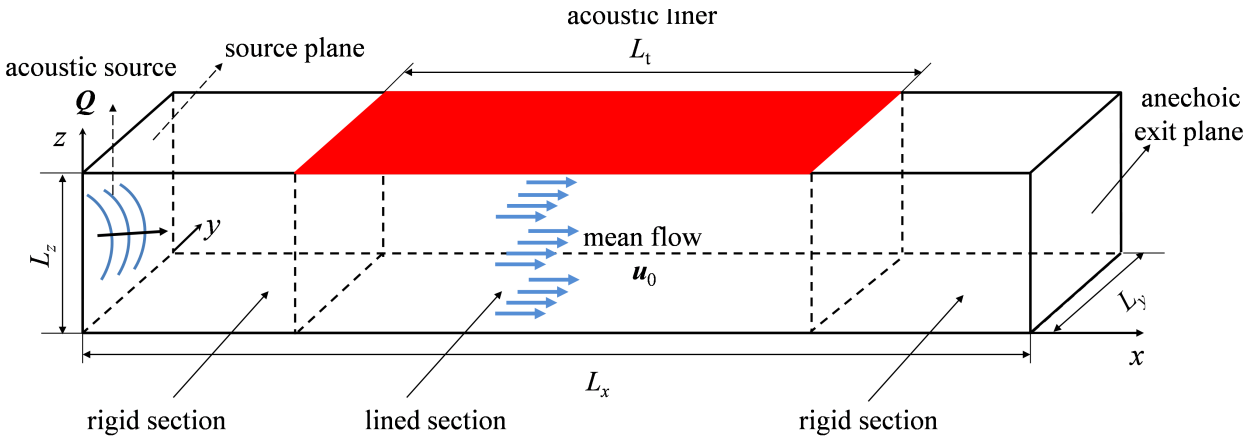


Figure 2.1: The schematic view of numerical set-up.

### 2.1.2 Acoustic liner models

Aircraft noise has several sources. Among them, engine noise, generated by the exhausting jets and moving turbomachinery blades, is one of the main contributors in the take-off and approach stage. The engine noise has a broadband spectrum, with a frequency content in the range of 50 Hz to 10 kHz. The corresponding Sound Pressure Level (SPL) can even reach 160 dB. Noise attenuation can be realized by installing acoustic liners in the intake and bypass of nacelles; this technique has been proved to be one of the efficient strategies to attenuate the engine noise. However, acoustic liners are not effective for the whole frequency range in the takeoff and landing phase. Noise reduction by acoustic liners is just effective in a certain narrow frequency band around the fan blade-passing frequency. Active control of noise [21, 22, 23], which does not convert the acoustical energy to heat as passive techniques, aims at reducing noise by means of electronic transducing systems. They are adapted to any frequencies and usually used for low frequencies, where passive techniques are not efficient. Noise reduction through active control can be achieved through breaking the vortices, constructing an anti-phase sound field or increasing the acoustic damping. Another approach, namely hybrid techniques [24, 25, 26], which consist in a combination of the two techniques mentioned above to cover the entire frequency range. High frequency noise is reduced by passive techniques and the low frequency components by active

control.

However, active control is rare in realistic applications, and therefore only passive acoustic liners are hence considered to reduce noise in this study. Acoustic liners can be divided into locally reacting liners and non-locally reacting liners. Locally reacting liners, for example, Single Degree OF Freedom (SDOF) and Double Degree OF Freedom (DDOF) liners, are commonly used in nacelles. Interactions between acoustic liners and sound waves are supposed to be local. Generally, these liners include a perforated or micro-perforated plate and backing cavities. The structure of these liners, for example, the length of the cavities, are designed to attenuate the tonal noise. For non-locally reacting liners, such as porous materials and metallic foams, acoustic waves can propagate in all directions inside the materials. The noise reduction is completed by the energy dissipation arising from the friction between the wave transmission and liners.

For a locally reacting liner, the surface impedance is the unique parameter to describe its acoustic properties. It models the interactions between acoustic waves and acoustic liners. The surface impedance $Z(\omega)$ is defined by

$$Z(\omega) = \frac{\hat{p}(\omega)}{\hat{v}_n(\omega)}, \tag{2.1}$$

where $\omega$ is the frequency of the source, $\hat{p}(\omega)$ is the acoustic pressure and $\hat{v}_n(\omega)$ is the normal acoustic velocity on the lined surface. The surface impedance is originally described in the frequency domain.

In this study, locally reacting liners described by an impedance boundary condition are considered. For time-domain simulations, the impedance should be translated into an equivalent function in the time domain. Several time-domain impedance models have been proposed [27, 28, 13]. Among them, a three-parameters model, the Mass-Spring-Damper (MSD) has been widely adopted in many studies [29, 30, 31]. Another commonly chosen models is the extended Helmholtz resonator model, proposed by Rienstra [28]. It provides a guaranteed physical time-domain representation. Detailed introduction about the implementation of a time-domain impedance boundary condition is given in Section 2.3. The examples given below contain impedance models used in calculations, namely MSD models and two kinds of realistic locally reacting liners, respectively, ceramic tubular liners and SDOF liners.

#### Mass-Spring-Damper liners

The first kind of liners introduced here is the MSD liner. Tam and Auriault [27] proposed this 3-parameter model aiming at implementing the time-domain impedance boundary condition. Later, MSD liners are widely chosen in the analytical and numerical studies for their simplicity.

Assuming that the acoustic displacement in the normal direction is $\xi$, the motion of the MSD system is governed by

$$m\frac{\partial^2 \xi}{\partial t^2} + R\frac{\partial \xi}{\partial t} + K\xi = p, \tag{2.2}$$

where $R$, $m$ and $K$ are respectively the damping, mass and spring stiffness. The impedance of the MSD liner is thus

$$Z(\omega) = R + \mathrm{i}\omega m + \frac{K}{\mathrm{i}\omega}. \tag{2.3}$$

The normalized impedance and admittance of the MSD liner used are shown in figure 2.2, with $R = 0.2$, $m = 5.4 \times 10^{-3}$ and $K = 0$.

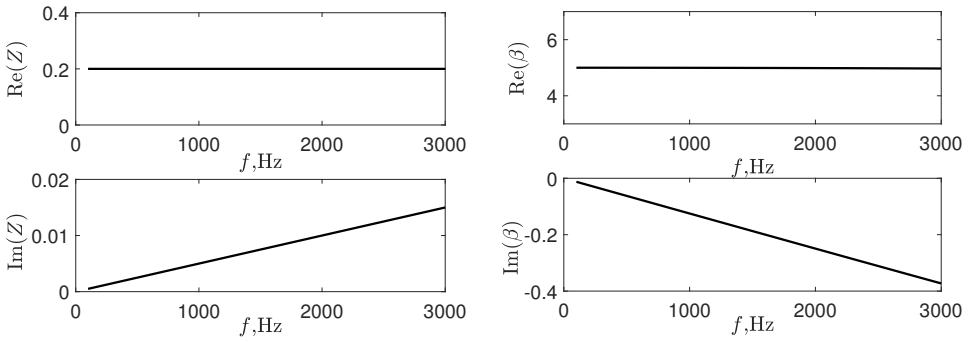


Figure 2.2: Real and imaginary parts of the normalized impedance (left) and admittance (right) of the MSD liner.

### Ceramic tubular liners

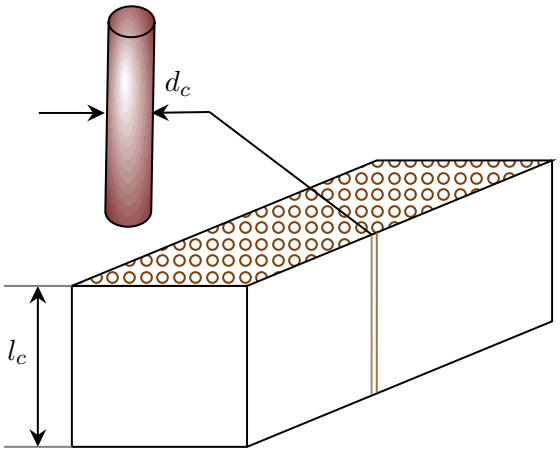


Figure 2.3: A schematic view of ceramic tubular liner.

Ceramic tubular liners have been investigated extensively for the past 25 years [32, 20, 33, 34, 35, 36, 37]. It is well chosen for their linear reaction to the grazing flow and the incident acoustic level. Another advantage of ceramic tubular liners is its wide frequency range corresponding to the engine noise in nacelles.

The ceramic tubular liners consist of a tight pack of ceramic tubes and a rigid backplate. The tubes are parallelly installed, and perpendicular to the opening of the tubes as shown in figure 2.3. The tube has a length $l_c$ and its diameter is $d_c$. The porosity of the surface of the material is $\sigma_p$. Following Monteghetti *et al.* [13], the normalized acoustic surface impedance $Z$

can be modelled as

$$Z = \frac{1}{\sigma_p} \coth\left(\mathrm{i}k_c l_c\right), \tag{2.4}$$

where $k_c$ is the acoustic wavenumber inside the tube. Bruneau [38] derived an expression for the wavenumber $k_c$ in an air-filled isothermal cylindrical cavity of diameter $d_c$:

$$k_c = k_0 \sqrt{\left[\frac{1 + (\gamma - 1) K_h}{1 - K_v}\right]}, \tag{2.5}$$

where $k_0 = \omega / c_0$ is the acoustic wavenumber and $\gamma = 1.4$ is the ratio of specific heats. $K_h$ and $K_v$ are given by:

$$K_h = \frac{4}{k_h d_c} \frac{J_1\left(k_h d_c/2\right)}{J_0\left(k_h d_c/2\right)}, \qquad K_v = \frac{4}{k_v d_c} \frac{J_1\left(k_v d_c/2\right)}{J_0\left(k_v d_c/2\right)}. \tag{2.6}$$

In the above equations, $J_0$ and $J_1$ are respectively the $0^{\text{th}}$- and $1^{\text{st}}$-order Bessel functions of the first kind. The parameters $k_h$ and $k_v$, obtained with:

$$k_h = \sqrt{\frac{-\mathrm{i}k_0}{l_h}}, \qquad k_v = \sqrt{\frac{-\mathrm{i}k_0}{l'_v}}, \tag{2.7}$$

are related to the thermal characteristic length $l_h = \nu/(c_0 \mathrm{Pr})$ and to the viscous characteristic length $l'_v = \nu / c_0$, where $\nu = 1.84 \times 10^{-5}$ m$^2$/s is the kinematic viscosity and Pr $= 0.71$ is the Prandtl number.

The geometrical properties of the ceramic tubular liner, referring to CT57 liner used in the NASA GIT experiment [20], are reported in Table 2.1. The NASA GIT experiment, which has been widely used as a benchmark for studying acoustic propagation in a lined duct, will be also investigated in section 2.4. Nevertheless, with these parameters, the agreement with the impedance data given by Jones *et al.* [20] was not sufficient. The parameters $d_c$ and $l_c$ have been modified to enable a better fit between the impedance data and the broadband model. The effective parameters thus obtained are given in Table 2.2. Finally, the normalized impedance and admittance (inverse of the impedance) of the broadband CT57 liner for $M = 0$ and $M = 0.335$ are shown in figure 2.4. The educed impedance of NASA GIT experiment is also attached for comparison.

Table 2.1: Properties of the CT57 liner

| surface porosity $\sigma_p$ | tube diameter $d_c$ | tube length $l_c$ |
|---|---|---|
| 57% | 0.6 mm | 85.6 mm |

Table 2.2: Parameters used in the CT57 liner impedance model

| $M$ | effective tube diameter $d'_c$ | effective tube length $l'_c$ |
|---|---|---|
| 0 | 0.72 mm | 75.3 mm |
| 0.335 | 0.75 mm | 77.5 mm |

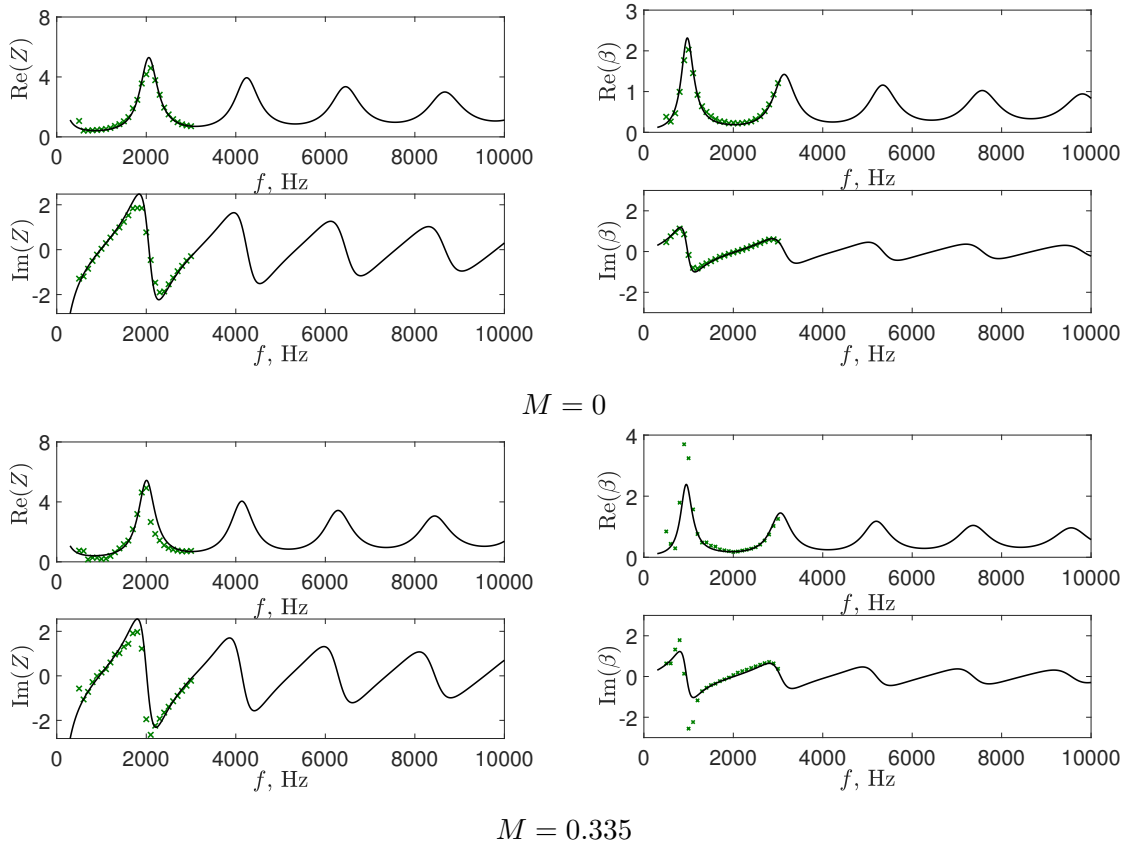


Figure 2.4: Real and imaginary parts of the normalized impedance and admittance of the CT57 liner for $M = 0$ and $M = 0.335$: $\times$ educed values by NASA , ——— broadband impedance and admittance.

### Single degree of freedom liners

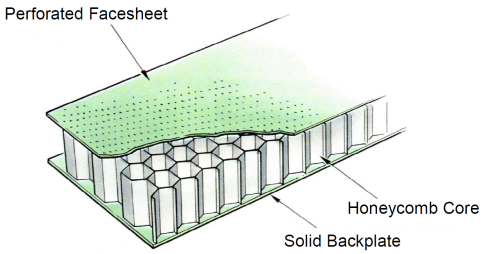


Figure 2.5: A schematic view of SDOF liner [28].

SDOF liners are composed of a resistive layer, air cavities and a rigid backing as shown in figure 2.5. The resistive layer can be a perforated plate or a wire mesh sheet. The liner may have

different responses according to the choice of the resistive layer. The liner is not sensitive to a mean flow and has a wide bandwidth when the covering is a wire mesh sheet. The liner shows nonlinear responses to a mean flow, and its acoustic attenuation has a narrow bandwidth when a perforated plate is used. The thickness of the resistive layer compared to the wavelength is small. The air cavities can be seen as a layer of honeycomb cores. The backing is supposed to be rigid. The SDOF is also supposed to be a locally reacting liner, and the acoustic waves can only propagate parallel to the cavity axis. The acoustic performance of SDOF liners is quite similar to Heltmoltz-type resonator. It is usually applied to give an optimal attenuation according to the designed frequency. However, a major problem with SDOF liner is that higher-order modes are propagative along the transverse direction [39]. Several semi-empirical models [40, 41, 42, 43] have been proposed for predicting the impedance of SDOF liners. Among them, the model of Guess [40] is introduced.

The impedance model of Guess takes account of the effects of viscosity, radiation, backing and also of high sound amplitude and steady tangential airflow. The full expression of the impedance associates all the effects together, and it is given in the non-dimensional form as

$$Z = Z_V + Z_R + \theta_{NL} + \mathrm{i}\chi_B, \tag{2.8}$$

where $Z_V$ is the viscous and mass impedance, $Z_R$ is the radiation impedance, $\theta_{NL}$ is the non-linear resistance, and $\chi_B$ is the specific reactance. The viscous and mass impedance $Z_v$ is given as

$$Z_v = \frac{\sqrt{8\nu\omega}t'_p}{\sigma_0 c_0 d} + \mathrm{i}\left(\frac{\omega t_p}{\sigma_0 c_0} + \frac{\sqrt{8\nu\omega}t'_p}{\sigma_0 c_0 d}\right), \tag{2.9}$$

where $\omega$ is the angular frequency, $t_p$ is the plate thickness, $t'_p = t_p + d$ is the corrected length, $\sigma_0$ is the open area ratio, $d$ is the hole diameter and $L$ is the backing depth.

By assuming $\dfrac{\omega d}{c_0} < \dfrac{1}{2}$, the expression for radiation impedance is

$$Z_R = \frac{\pi^2}{2\sigma_0}\left(\frac{d}{\lambda}\right)^2 + \mathrm{i}\left(\frac{\omega\delta}{\sigma_0 c_0}\right), \tag{2.10}$$

with end correction

$$\delta = \frac{8}{3\pi}\frac{d\left(1 - 0.7\sqrt{\sigma_0}\right)}{1 + 305M^3}. \tag{2.11}$$

The non-linear resistance, which is due to the high sound amplitude and steady flow tangential to the plate, is developed by Ingard [44] as

$$\theta_{NL} = \frac{1 - \sigma_0^2}{\sigma_0}\left[\frac{|u_{or}| + |v_{tr}|}{c_0}\right], \tag{2.12}$$

where $|u_{or}|$ is the amplitude of the orifice velocity, and $|v_{tr}|$ is the magnitude of the turbulent velocity fluctuation through a turbulent boundary layer.

Backing impedance is determined by the nature of the backing to perforated plates. Since the

cell walls are perpendicular to the perforated face sheet, the backing impedance is purely reactive and the specific backing reactance is given as

$$\chi_B = \coth\left(\frac{\mathrm{i}\omega L}{c_0}\right) \tag{2.13}$$

As non-linear effects are not considered, the final expression of the normalized impedance $Z$ is

$$Z = \left[\frac{\sqrt{16\nu\mathrm{i}\omega}}{\sigma_0 c_0}\left(1+\frac{t_p}{d}\right) - \frac{(d\mathrm{i}\omega)^2}{\sigma_0 c_0^2} + \mathrm{i}\omega\frac{\left(t_p+\delta\right)}{\sigma_0 c_0} + \coth\left(\frac{\mathrm{i}\omega L}{c_0}\right)\right]. \tag{2.14}$$

One example of SDOF referring to the sample of Busse-Gerstengarbe [45] is considered. The corresponding parameters are shown in the Table. 2.3. The normalized impedance and admittance of the SDOF liner are shown in figure 2.6.

Table 2.3: Parameters used in the SDOF liner impedance model

| cell depth $L$ | hole diameter $d$ | plate thickness $t_p$ | open area ratio $\sigma_0$ |
|---|---|---|---|
| 12.7 mm | 1.45 mm | 1 mm | 4.4% |

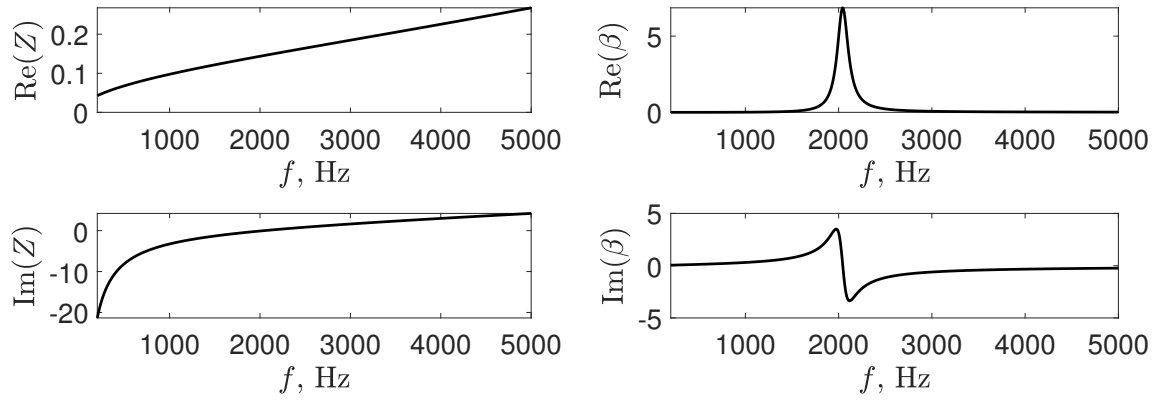


Figure 2.6: Real and imaginary parts of the normalized impedance (left) and admittance (right) of the SDOF liner.

## 2.2 Frequency-domain approaches

Frequency-domain approaches, whether they are analytical or numerical, are particularly well-suited for predicting tonal noise. Two kinds of frequency-domain approaches are adopted in the study. The first one is the mode matching method, a semi-analytical approach, which offers an efficient way for predicting acoustic propagation. However, it is based on the assumption that the mean flow profile is uniform. The second method is based on a finite element model. It solves LEE in the frequency domain by using the commercial software COMSOL Multiphysics. The second method is more costly but it can handle more realistic flows. Both methods are well spread, and a detailed description is given in this section.

### 2.2.1 Mode matching method

The acoustic field can be described as an infinite sum over the eigenmodes in each homogeneous section along the duct. Eigenmodes are defined by the boundary condition. And the mode matching method is the way to ensure the continuity between the rigid and the lined sections. Many studies have been conducted on the derivation of numerical and analytical mode matching methods. An overview is given to show the development of this method.

#### Review of mode matching methods

The analytical mode matching method [46, 47] has the advantage of being efficient. By assuming that only the fundamental mode propagates, the analytical solution is easy to be drawn. This method is quick since the roots of the governing eigen equation do not need to be found. However, for higher frequency and larger size problem, it is reported to be inaccurate. By including higher-order modes, the accuracy of the prediction can be improved at the expense of calculation efficiency. This requires iterative methods as the Newton-Raphson method [48, 49] or the Secant method [50, 51]. Without a mean flow, the governing equations can be simply solved by enforcing continuity of pressure and axial velocity at the interface between the input and exit planes. However, with the presence of a mean flow, the analytical solution becomes less straightforward.

Another challenge of the analytical mode matching method lies in the choice of appropriate boundary conditions when a mean flow exists. Aurégan *et al.* [14] performed an experiment with a reactive silencer under a grazing flow. They pointed out that the realistic condition was between the continuity of displacement and velocity rather than energy conservation and axial momentum conservation. This modified condition considers the effect of viscosity in the acoustic and hydrodynamic boundary layer. For circular dissipative silencers with a mean flow, Kirby and Denia [15] argued that the transverse continuity condition rather than the axial continuity condition should be used to match between the mean flow region and absorbing materials. It is due to the assumption of the infinitely thin depth made for a perforated screen of dissipative silencers in the analytical derivation. Indeed, the depth of a perforated screen can not be neglected in the experimental study. Furthermore, the viscous boundary layer adjacent to one side of the perforated screen affects the measurement of the impedance, while the analytical model assumes an infinitely thin boundary layer. Compared with the experiment and the analytical method, the use of continuity of pressure and displacement gives a more accurate prediction for the transmission loss than the use of continuity of pressure and velocity. Gabard [52] proposed a modified mode matching scheme. He utilized the conservation of mass and momentum and considered the contribution of the boundary terms. The acoustic power at the interface between the rigid and lined part was analysed. He indicated that the edge conditions, which enforce that the streamline along the lined wall is smooth and continuous, can also achieve conservation of energy.

Improvements have also been made for developing numerical mode matching methods to

avoid the iterative procedures to find roots of the eigen equation. Astley *et al.* [53] used a finite element method to solve the governing equations. A point collocation technique is applied to match the acoustic pressure and the normal particle velocity across the interface between rigid and lined section. Pagneux and his co-works proposed a series of multimodal method[54, 55, 56] to consider the sound propagation along the non-uniform lined ducts. Glav [57, 58] adopted a point matching technique to study uniform silencers with irregular cross-section. However, the convergence of this method was sensitive to the silencer geometry and collection grids. For a long time in the literature, the numerical mode matching methods were supposed to be less efficient than analytical ones. Kirby [59] questioned the general assumption and performed comparisons between analytical methods [47, 15], numerical methods [60, 15] and a hybrid finite element method [61]. The results showed that the numerical methods and a hybrid finite element method were not slower than the general analytical method for calculating the transmission loss with the accuracy converging to the one decimal place. He indicated that the numerical methods can be applied in an iterative design environment and it was the most efficient technique. Pagneux and his co-works proposed a series of multimodal method[54, 55, 56] to consider the sound propagation along the nonuniform lined ducts.

**Calculation of the wavenumbers**

The mode matching method used in [62] is utilized in the present study. Assuming a uniform mean flow, the governing equations can be simplified to the convected Helmholtz equation:

$$\left(\mathrm{i}k_0 + M\frac{\partial}{\partial x}\right)^2 \hat{p} - \nabla^2 \hat{p} = 0. \tag{2.15}$$

In each section of the lined duct, the solution of Eq. (2.15) can be sought as a modal expansion:

$$\hat{p}(x,y,z,\omega) = \sum_{m,n} \cos\left(\sigma_m y\right)\left[A_{m,n}\cos\left(\gamma_n^+ z\right)\mathrm{e}^{-\mathrm{i}k_{mn}^+ x} + B_{m,n}\cos\left(\gamma_n^- z\right)\mathrm{e}^{-\mathrm{i}k_{mn}^- x}\right], \tag{2.16}$$

where $m$ and $n$ are the number of modes along $y$- and $z$- directions. On the lined surface of the duct, the Ingard-Myers boundary condition:

$$\left.\frac{\partial \hat{p}}{\partial z}\right|_{z=L_z} + \frac{\beta}{\mathrm{i}k_0}\left(\mathrm{i}k_0 + M\frac{\partial}{\partial x}\right)^2 \hat{p}(z=L_z) = 0 \tag{2.17}$$

is imposed. The wavenumbers along the $y$-direction are given by $\sigma = m\pi/L_y$. In the unlined sections, the wavenumbers along the $z$-direction are similarly equal to $\gamma^{\pm} = n\pi/L_z$. The wavenumbers $k$ can then be obtained from the dispersion relation

$$k^2 + \sigma^2 + \gamma^2 = \left(k_0 - Mk\right)^2, \tag{2.18}$$

leading to:

$$k^{\pm} = \frac{-Mk_0 \pm \sqrt{k_0^2 - (1-M^2)(\gamma^2+\sigma^2)}}{1-M^2} \tag{2.19}$$

In the lined section, the wavenumbers $\gamma$ and $k$ can not be obtained analytically. Each mode however satisfies the boundary condition in Eq. (2.17) leading to the equation:

$$\mathrm{i}k_0\gamma \sin(\gamma L_z) + \beta(k_0 - Mk)^2 \cos(\gamma L_z) = 0. \tag{2.20}$$

Combining Eqs. (2.18) and (2.20) leads to an equation in the form $f(k) = 0$ that can be solved numerically to obtain the values of $k^{\pm}$. For this, we employ the *MATLAB* function `fsolve`, using as an initial guess the values of $k^{\pm}$ for the unlined sections. The wavenumbers $\gamma^{\pm}$ are then obtained from Eq. (2.18). Note that, in our study the solutions of the dispersion relation in Eq. (2.20) only consist of acoustic waves, since the wavenumbe in the rigid part is used as initial guess to obtain the wavenumber in the lined section. For more general cases as pointed out in [63, 4], acoustic modes, vorticity modes as well as entropy modes can exist. Specifically, when flow is not uniform but a shear flow, vorticity modes are presented and convect with the mean flow.

To simplify the notation, Eq. (2.16) can be rewritten as

$$\hat{p}(x,y,z,\omega) = \sum_{m,n} \left[ A_{m,n}\psi^{+}_{m,n}(y,z)\mathrm{e}^{-\mathrm{i}k^{+}_{mn}x} + B_{m,n}\psi^{-}_{m,n}\mathrm{e}^{-\mathrm{i}k^{-}_{mn}x} \right]. \tag{2.21}$$

In the rigid and lined section, $\psi^{\pm}$ are respectively

$$\psi^{\pm}_r = \Lambda_{m,n}\cos(\frac{m\pi}{L_y}y)\cos(\frac{n\pi}{L_z}z),\ \psi^{\pm}_t = \Lambda_{m,n}\cos(\frac{m\pi}{L_y}y)\cos(\gamma^{\pm}_n z), \tag{2.22}$$

where indices $r$ and $t$ notify the coefficient in the rigid and lined section. The coefficient $\Lambda_{m,n}$ which depends on the combination of $m$ and $n$ are given in Appendix A.

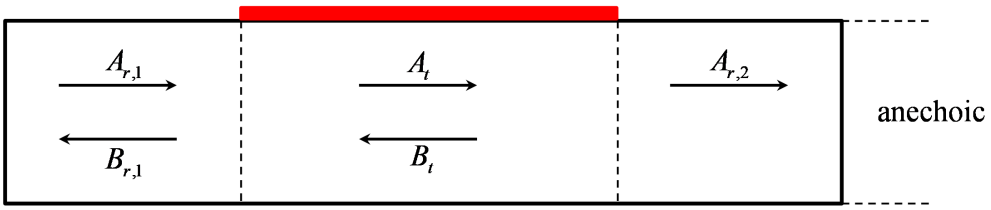


Figure 2.7: The configuration considered in the calculation of acoustic propagation in a lined duct.

### Calculation of the amplitudes

Figure 2.7 shows the configuration used in the calculation of acoustic propagation in a partially lined duct. Specifically, $A_{r,1}$ and $A_{r,2}$ are the amplitudes of outgoing waves in the first and

second rigid section. Reflected waves are generated at the interface between the rigid and lined section. $B_{r,1}$ and $B_t$ denote the amplitude of reflected waves in the first rigid and lined section. No reflected waves exit in the second rigid section, since the exit plane of the duct is supposed to be anechoic. The modal contents of the source are imposed by setting the values of $A_{r,1}$ in the first rigid duct section. The interfaces conditions, i.e., continuity of pressure and normal velocity, are then imposed to obtain the unknown values of $A_{r,2}$, $B_{r,1}$, $A_t$ and $B_t$ in the duct.

Applying $\frac{\partial p}{\partial x} = -\mathrm{i}k\hat{p}$ and $\frac{\partial v_x}{\partial x} = -\mathrm{i}k\hat{v}_x$ with the Euler equation

$$\frac{\partial v_x}{\partial t} + u_{0x}\frac{\partial v_x}{\partial x} = -\frac{\partial p}{\partial x}, \tag{2.23}$$

the velocity along the $x$-axis $\hat{v}_x$ can be expressed as

$$\hat{v}_x = \frac{k}{\omega - Mk}\hat{p}. \tag{2.24}$$

The continuity of pressure at the interfaces can be written as

$$A_{r,1}\psi_r^+ + B_{r,1}\psi_r^- = A_t\psi_t^+ + B_t\mathrm{e}^{\mathrm{i}k_t^- L_t}\psi_t^- \tag{2.25}$$

and

$$A_t\mathrm{e}^{-\mathrm{i}k_t^+ L_x}\psi_t^+ + B_t\psi_t^- = A_{r,2}\psi_r^+. \tag{2.26}$$

The continuity of velocity is derived as

$$A_{r,1}\frac{k_r^+}{\omega - Mk_r^+}\psi_r^+ + B_{r,1}\frac{k_r^-}{\omega - Mk_r^-}\psi_r^- = A_t\frac{k_t^+}{\omega - Mk_t^+}\psi_t^+ + B_t\mathrm{e}^{\mathrm{i}k_t^- L_x}\frac{k_t^+}{\omega - Mk_t^-}\psi_t^- \tag{2.27}$$

and

$$A_t\mathrm{e}^{-\mathrm{i}k_t^+ L_x}\frac{k_t^+}{\omega - Mk_t^+}\psi_t^+ + B_t\frac{k_t^-}{\omega - Mk_t^-}\psi_t^- = A_{r,2}\frac{k_r^+}{\omega - Mk_r^+}\psi_r^+. \tag{2.28}$$

Eq. (2.25) is given as an example to show the process of implementing the continuity equations. We project on the modal basis of the rigid duct, that is to say we multiply a mode $\psi_r'$ of a fixed order ($m$, $n$) in the rigid section and integrate the product:

$$\int_0^{L_z}\int_0^{L_y}(A_{r,1}\psi_r^+ + B_{r,1}\psi_r^-)\psi_r'\mathrm{d}y\mathrm{d}z = \int_0^{L_z}\int_0^{L_y}(A_t\psi_t^+ + B_tE^-\psi_t^-)\psi_r'\mathrm{d}y\mathrm{d}z \tag{2.29}$$

where $E^- = \mathrm{e}^{\mathrm{i}k_t^- L_x}$, $E^+ = \mathrm{e}^{-\mathrm{i}k_t^+ L_x}$.

As $\int_0^{L_y}\int_0^{L_z}\psi_r\psi_r\mathrm{d}y\mathrm{d}z = 1$, the left side of Eq. (2.29) leads to $A_{r,1} + B_{r,1}$. Hence Eq. (2.29) is rewritten as:

$$A_{r,1} + B_{r,1} = A_t \underbrace{\int_0^{L_z}\int_0^{L_y} \psi_t^+ \psi_r' \mathrm{d}y\mathrm{d}z}_{X^+} + B_t E^- \underbrace{\int_0^{L_z}\int_0^{L_y} \psi_t^- \psi_r' \mathrm{d}y\mathrm{d}z}_{X^-} \tag{2.30}$$

with

$$X^{\pm} = \int_0^{L_y}\int_0^{L_z} \Lambda_{m,n}\cos(\frac{m\pi}{L_y}y)\cos(\gamma_n^{\pm}z)\Lambda_{m,n}\cos(\frac{m'\pi}{L_y}y)\cos(\frac{n'\pi}{L_z}z)\mathrm{d}y\mathrm{d}z. \tag{2.31}$$

The value of $X^{\pm}$ is:

$$X^{\pm} = \begin{cases} 0, & m \neq m' \\ \Lambda_{m,n}^2 \dfrac{Ly}{2}\displaystyle\int_0^{L_z} \cos(\gamma_n^{\pm}z)\cos(\frac{m'\pi}{L_z}z)\mathrm{d}z, & m = m' \end{cases} \tag{2.32}$$

and should be calculated numerically according to the number of modes $m$ and the impedance boundary condition. The modes, which are propagative in the rigid section, can be supposed to be the incident modes for the lined section. Similarly, the same derivation can also be applied to Eq. (2.26), (2.27) and (2.28), leading to

$$\begin{aligned} A_{r,1} + B_{r,1} &= X^+ A_t + E^- X^- B_t \\ A_{r,2} &= E^+ X^+ A_t + X^- B_t \\ K_r^+ A_{r,1} + K_r^- B_{r,1} &= K_t^+ X^+ A_t + K_t^- E^- X^- B_t \\ K_r^+ A_{r,2} &= K_t^+ E^+ X^+ A_t + K_t^- X^- B_t \end{aligned} \tag{2.33}$$

$$K_r^+ = \frac{k_r^+}{\omega - Mk_r^+},\ K_r^- = \frac{k_r^-}{\omega - Mk_r^-},\ K_t^+ = \frac{k_t^+}{\omega - Mk_t^+},\ K_t^- = \frac{k_t^-}{\omega - Mk_t^-}. \tag{2.34}$$

Eq. (2.33) can be finally written as a matrix system:

$$\begin{bmatrix} \mathbf{0} & \mathbf{I} & -\mathbf{X}^+ & -\mathbf{X}^-\mathbf{E}^- \\ \mathbf{I} & \mathbf{0} & -\mathbf{X}^+\mathbf{E}^+ & -\mathbf{X}^- \\ \mathbf{0} & \mathbf{K_r^-} & -\mathbf{X}^+\mathbf{K_t^+} & -\mathbf{X}^-\mathbf{K_t^-}\mathbf{E}^- \\ \mathbf{K_r^+} & \mathbf{0} & -\mathbf{X}^+\mathbf{K_t^+}\mathbf{E}^+ & -\mathbf{X}^-\mathbf{K_t^-} \end{bmatrix} \begin{bmatrix} \mathbf{A_{r,2}} \\ \mathbf{B_{r,1}} \\ \mathbf{A_t} \\ \mathbf{B_t} \end{bmatrix} = \begin{bmatrix} -\mathbf{A_{r,1}} \\ \mathbf{0} \\ -\mathbf{K_r}\mathbf{A_{r,1}} \\ \mathbf{0} \end{bmatrix}. \tag{2.35}$$

$N$ modes are excited in the first section, and each mode is corresponding to a certain ($m$, $n$). $\mathbf{A_{r,1}}$, $\mathbf{A_{r,2}}$, $\mathbf{B_{r,1}}$, $\mathbf{A_t}$ and $\mathbf{B_t}$ are column vectors with a length of $N$. $\mathbf{I}$ and $\mathbf{0}$ are respectively identity matrix and zero matrix. $\mathbf{E}^{\pm}$, $\mathbf{K_r^{\pm}}$ and $\mathbf{K_t^{\pm}}$ are the diagonal matrices with a size of $N \times N$. $\mathbf{X}^{\pm}$ are matrices with a size of $N \times N$, but they are not diagonal. The amplitudes in each section are obtained by solving the system matrix in *MATLAB*.

### 2.2.2 Solving LEE in the frequency domain

The mode matching method can provide efficient predictions for acoustic propagation in a lined duct. However, the mathematically convenient assumption of a uniform flow is questionable in realistic conditions. The Ingard-Myers boundary condition is also not accurate under some situation as shown by Gabard [16]. He showed that the use of Ingard-Myers boundary condition may overestimate sound attenuation.

To consider a more realistic mean flow, the second method, solving LEE in the frequency domain with the commercial software COMSOL Multiphysics version 5.4 is introduced. The model is constructed in the "aeroacoustics branch" using the "Linearized Euler, Frequency Domain" module and is shown in figure 2.8. The acoustics perturbations of density, velocity, and pressure with a mean flow, which can be assumed as ideal gas flow, can be calculated in this module. The governing equations are:

$$\mathrm{j}\omega\hat{\rho} + \hat{\rho}\left(\nabla \cdot \boldsymbol{u_0}\right) + \boldsymbol{u_0} \cdot \nabla\hat{\rho} + \hat{\boldsymbol{v}} \cdot \nabla\rho_0 + \rho_0\left(\nabla \cdot \hat{\boldsymbol{v}}\right) = S_c \tag{2.36}$$

$$\mathrm{j}\omega\hat{\boldsymbol{v}} + \left[\left(\hat{\boldsymbol{v}} + \frac{\hat{\rho}}{\rho_0}\boldsymbol{u_0}\right) \cdot \nabla\right]\boldsymbol{u_0} + \left(\boldsymbol{u_0} \cdot \nabla\right)\hat{\boldsymbol{v}} + \frac{1}{\rho_0}\nabla\hat{p} = S_m \tag{2.37}$$

$$\mathrm{j}\omega\hat{p} + \hat{\boldsymbol{v}} \cdot \nabla p_0 + \gamma\hat{p}\left(\nabla \cdot \boldsymbol{u_0}\right) + \boldsymbol{u_0} \cdot \nabla\hat{p} + \gamma p_0\left(\nabla \cdot \hat{\boldsymbol{v}}\right) = S_e \tag{2.38}$$

where $\hat{\boldsymbol{v}}$ and $\hat{\rho}$ refer to acoustic velocity and acoustic density in the frequency domain respectively. The properties of the background mean flow, such as pressure $p_0$, velocity $u_0$, temperature $T_0$ and density $\rho_0$ need to be specified in the "model input" and "fluid properties". A plug flow will not be used since a flow profile can be directly implemented.

The initial values of $\hat{\rho}$, $\hat{\boldsymbol{v}}$ and $\hat{p}$ can be imposed in "initial value" (with the default value set to 0). The source terms $S_c$, $S_m$ and $S_e$ in Eqs. (2.36)-(2.38) are defined by "domain sources" in the module. Specifically, the domain source can be set according to:

$$\begin{gathered} S_c = M_s \\ S_m = \boldsymbol{A} - \frac{\boldsymbol{u_0}M_s}{\rho_0} \text{ or } S_m = \frac{1}{\rho_0}(\boldsymbol{F} - \boldsymbol{u_0}M_s) \\ S_e = p_{rc} + \frac{\gamma p_0 M_S}{\rho_0} \text{ or } S_c = (\gamma - 1)Q_s + \frac{\gamma p_0 M_s}{\rho_0} \end{gathered} \tag{2.39}$$

where $M_s$ is a mass source, $\boldsymbol{A}$ is an acceleration source, $\boldsymbol{F}$ is a volume source, $p_{rc}$ is a pressure rate of change source and $Q_s$ is a volumetric heat source.

Concerning the boundary conditions, the rigid and lined wall boundary condition can be defined respectively in the "rigid wall" and "impedance". Specifically, the Ingard-Myers boundary condition is applied to the upper wall of the lined section. One should notice that the classic impedance boundary condition can be obtained from the Ingard-Myers boundary condition with a mean flow velocity diminishing to zero on the walls. The value of impedance can be an analytical function or interpolated data. To model anechoic terminations, perfectly matched layer

(PML) domains are added at the input and the output of the duct. PML aims at absorbing the propagating waves without introducing reflections.

The COMSOL solution of the frequency-domain LEE is based on the finite element approach. There are several types of discretization available, such as linear, quadratic Lagrange and quadratic serendipity. To obtain higher accuracy, quadratic Lagrange elements are selected for simulations performed in the study. Many types of mesh are available in COMSOL, such as triangular, quad and tetrahedral mesh. An unstructured tetrahedral mesh is used for its simplicity. The choice of "boundary layers" can also be selected to generate fine meshes in the normal direction along the chosen layers. It is applied for all the surface walls of the duct region in our study.

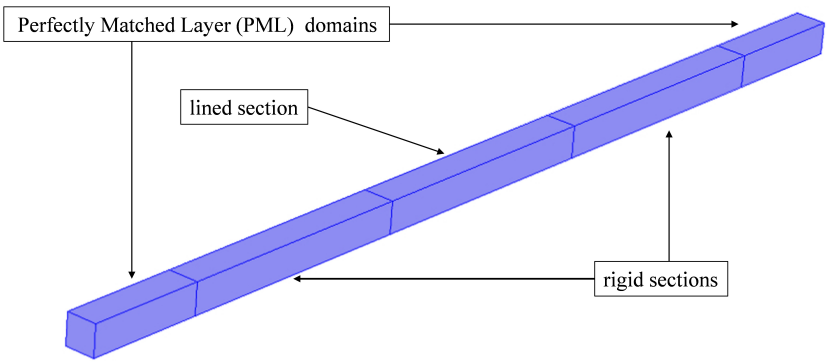


Figure 2.8: Finite element model built in COMSOL Multiphysics

A parallel sparse direct solver `PARDISO` is chosen and "parallel sparse direct solver for cluster" is selected, which allows COMSOL running in a distributed mode. During the calculation, all matrix factorization is stored as blocks and written in the disk if the estimated memory is exhausting the physically available memory.

## 2.3 Time-domain approach

Time-domain methods are well suited for solving broadband and multi-dimensional problems, and also have advantages for dealing with nonlinear and transient problems. With the enhanced computation capabilities, time-domain approaches have been developed [64, 12, 65] in recent decades. Compared to frequency-domain methods, they allow one to obtain results over a large band of frequencies in a single simulation. This is of particular interest for broadband eduction methods [65, 66, 19, 67].

The time-domain analysis is based on the previous study of Troian *et al.* [19]. Assuming a homentropic flow and neglecting the mean pressure gradient, the governing equations are given

by:

$$\frac{\partial p}{\partial t} + (\boldsymbol{u_0} \cdot \nabla)\, p + \rho_0 c_0^2 \nabla \cdot \boldsymbol{v} = \rho_0 c_0^2 Q \tag{2.40}$$

$$\frac{\partial \boldsymbol{v}}{\partial t} + (\boldsymbol{u_0} \cdot \nabla)\, \boldsymbol{v} + (\boldsymbol{v} \cdot \nabla)\, \boldsymbol{u_0} + \frac{1}{\rho_0} \nabla p = 0 \tag{2.41}$$

where $p$ and $\boldsymbol{v}$ are the acoustic pressure and velocity in the time domain, respectively. The mean flow is $\boldsymbol{u_0} = u_0 \boldsymbol{e_x}$, and $Q$ is a source term.

The numerical scheme to solve the linearized Euler equations in Eqs. (2.40) and (2.41) can be written as

$$\frac{\partial \mathbf{U}}{\partial t} + \frac{\partial \mathbf{E}}{\partial x} + \frac{\partial \mathbf{F}}{\partial y} + \frac{\partial \mathbf{G}}{\partial z} + \mathbf{H} = \mathbf{S}, \tag{2.42}$$

where the vector of unknown variables $\mathbf{U} = [p, \rho_0 v_x, \rho_0 v_y, \rho_0 v_z]^T$ and the vectors $\mathbf{E}$, $\mathbf{F}$, $\mathbf{G}$, $\mathbf{H}$ and $\mathbf{S}$ are given respectively by

$$\begin{gathered} E = \begin{pmatrix} u_{0x} p + \rho_0 c_0^2 v_x \\ u_{0x} \rho_0 v_x + p \\ u_{0x} \rho_0 v_y \\ u_{0x} \rho_0 v_z \end{pmatrix}, F = \begin{pmatrix} u_{0y} p + \rho_0 c_0^2 v_y \\ u_{0y} \rho_0 v_x \\ u_{0y} \rho_0 v_y + p \\ u_{0y} \rho_0 v_z \end{pmatrix}, G = \begin{pmatrix} u_{0z} p + \rho_0 c_0^2 v_z \\ u_{0z} \rho_0 v_x \\ u_{0z} \rho_0 v_y \\ u_{0z} \rho_0 v_z + p \end{pmatrix}, \\ H = \begin{pmatrix} 0 \\ \rho_0 \boldsymbol{v} \cdot \nabla u_{0x} \\ \rho_0 \boldsymbol{v} \cdot \nabla u_{0y} \\ \rho_0 \boldsymbol{v} \cdot \nabla u_{0z} \end{pmatrix}, S = \begin{pmatrix} \rho_0 c_0^2 Q \\ 0 \\ 0 \\ 0 \end{pmatrix}. \end{gathered} \tag{2.43}$$

### 2.3.1 Finite difference scheme

Finite difference schemes are used to calculate the spatial derivatives of the variables, namely the pressure and velocity, at each node of the grid. The general form of a finite difference scheme is given as:

$$\frac{\partial u}{\partial x}(x_0) = \frac{1}{\Delta x} \sum_{j=-M}^{N} a_j u(x_0 + j\Delta x), \tag{2.44}$$

where $\Delta x$ is the grid spacing and $a_j$ are the coefficients of the chosen numerical scheme. The derivative of $u(x_0)$ is obtained from the $N$ grid points located forwards and the $M$ grid points located backwards. The finite difference schemes are called centered if $M = N$ and non-centered otherwise. The coefficients of the finite difference schemes can be determined classically from the Taylor expansion. We use here optimized schemes developed in the computational aeroacoustics community, which aim at reducing the dispersion error. The general idea behind these optimized schemes is explained thereafter. The schemes are designed in consideration of dispersion properties [68].

Applying Fourier transform:

$$\hat{u}(k) = \mathcal{F}\left[u(x)\right] = \int_{-\infty}^{+\infty} u(x)\, \mathrm{e}^{-\mathrm{i}kx} dx. \tag{2.45}$$

on Eq. (2.44), the effective wavenumber is obtained as

$$\mathrm{i}k^* = \frac{-\mathrm{i}}{\Delta x} \sum_{j=-M}^{N} a_j \mathrm{e}^{\mathrm{i}k\Delta x j}. \tag{2.46}$$

For the centered scheme, Eq. (2.46) can be simplified as

$$\mathrm{i}k^* = \frac{2}{\Delta x} \sum_{j=1}^{N} a_j \sin(k\Delta x j). \tag{2.47}$$

The difference between the effective wavenumber $k^*$ and the exact wavenumber $k$ is denoted by the dispersion error. The schemes are developed to obtain a small value of dispersion error for a larger range of wavenumbers up to $k\Delta x = \pi/2$ corresponding to four points per wavelength. Figure 2.9 shows the relation of the effective wavenumber and the real wavenumber when a series of finite difference schemes are used, namely the fourth order 5 points standard finite difference scheme, fourth order 11 points optimized finite difference scheme and tenth order 11 points standard finite difference scheme. The coefficients are given in Appendix A of [69]. Compared with fourth order scheme, the 11 points optimized scheme has an obviously less dispersion error compared with the five points standard scheme. Its performance is even better than the tenth order standard 11 points finite difference scheme for $\pi/4 \leq k\Delta x \leq \pi/2$.

Through the whole study, the fourth order 11 points optimized finite difference scheme is chosen to calculate the spatial derivation for the interior points. For the boundary points, the non-centered fourth-order finite difference schemes over 11 points of Berland *et al.* [70] are chosen.

### 2.3.2 Time integration method

The LEE can be rewritten in the general form:

$$\frac{\partial u}{\partial t} = F(u). \tag{2.48}$$

There are a lot of time-integration algorithms to advance this type of equation in time. Among them, Runge-Kutta algorithms [69, 71, 72, 73] are largely used. Optimized Runge-Kutta algorithms have been proposed in order to improve stability and accuracy. Low-storage optimized Runge-Kutta algorithms are more desirable for its low storage requirements and relatively high performance of accuracy and stability. The process to obtain the variable $u$ from $n$-th to the

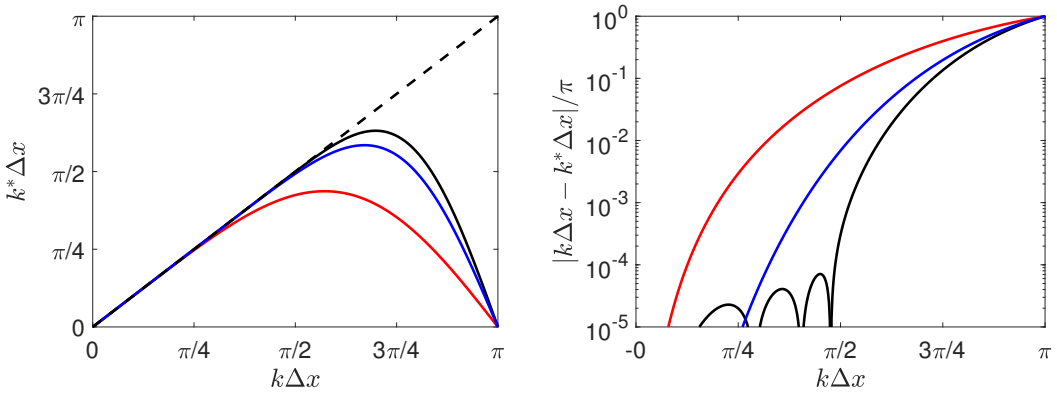


Figure 2.9: Effective wavenumber obtained with several finite difference schemes. Left, effective wavenumber as a function of exact wavenumber and right, dispersion error in logarithmic scales. fourth order 5 points finite difference scheme: ——; fourth order 11 points optimized finite difference scheme: ——; tenth order 11 points optimized finite difference scheme: ——.

$(n+1)$-th iteration for the explicit $p$-stage Runge-Kutta algorithm is shown as

$$\begin{aligned} u^0 &= u^n, \\ u^l &= u^n + \alpha_l \Delta t F(u)^{l-1} \text{ for } l = 1, ..., p, \\ u^{n+1} &= u^p, \end{aligned} \tag{2.49}$$

where $\alpha_l$ is the coefficient of the algorithm and $\Delta t$ is the time-step. The equation

$$u^{n+1} = u^n + \sum_{j=1}^{p} \prod_{l=p-j+1}^{p} \alpha_l \Delta t^j \frac{\partial^j u^n}{\partial t^j} \tag{2.50}$$

can be written for linear $F(u)$, where $\gamma_j = \prod_{l=p-j+1}^{p} \alpha_l$. Then applying temporal Fourier transform to Eq. (2.50), the amplification factor of this time marching scheme can be evaluated as

$$G_{RK}(\omega\Delta t) = \frac{\hat{u}^{n+1}(\omega)}{\hat{u}^n(\omega)} = 1 + \sum_{j=1}^{p} \gamma_j (\mathrm{i}\omega\Delta t)^j, \tag{2.51}$$

and can also be expressed as $|G_{RK}(\omega\Delta t)|\mathrm{e}^{\mathrm{i}\omega^*\Delta t}$. For the angular frequency $\omega$, the exact angular amplification factor is given as $\mathrm{e}^{\mathrm{i}\omega\Delta t}$. The difference in phase is written as $\omega^*\Delta t - \omega\Delta t$.

Figure 2.10 shows the amplification rate and the differences in phase for several Runge-Kutta algorithms, namely the standard fourth order four-stage, optimized fourth order six-stage and optimized second order six-stage Runge-Kutta algorithm. The coefficients are given in Appendix. C of Bogey & Bailly [69] and Table 1 of Berland *et al.* [74]. It is seen that the stability properties of optimized schemes are better than the standard Runge-Kutta scheme as the amplification factor remains below 1 for higher values of $\omega\Delta t$. For the phase difference, the optimized Runge-Kutta six-stage algorithm has a broader range of frequency, where the phase difference is close to 0. The optimized fourth order six-stage Runge-Kutta algorithm of Berland *et al.* [74] is employed

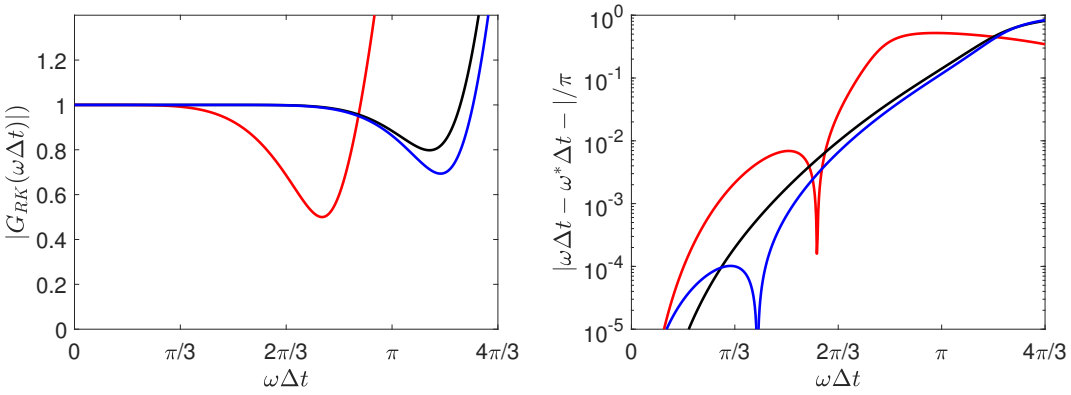


Figure 2.10: The amplification rate (left) and differences (right) in phase for several Runge-Kutta algorithms. Standard fourth order four-stage Runge-Kutta algorithm: ——; optimized fourth order six-stage Runge-Kutta algorithm: ——; optimized second order six-stage Runge-Kutta algorithm: ——.

for time integration in the present study.

### 2.3.3 Selective filter

The acoustic waves with large wavenumber ($k\Delta x \geq \pi/2$) are not resolved with the finite difference scheme. In addition, these short waves can lead to numerical instabilities. It is thus imperative to remove them from the calculations. To do that, selective filtering [75, 70, 76] is applied at every point and after every time step in the time-domain simulation. The selective filtering acts as an artificial dissipation for short waves without affecting the physical long waves. For a central $2N+1$ point stencil filter, which is employed on $u(x)$, it is in the form of

$$u^f(x_0) = u(x_0) - \sigma_d D_u(x_0), \text{ with } D_u(x_0) = \sum_{j=-N}^{N} d_j u(x_0 + j\Delta x), \tag{2.52}$$

where $d_j = d_{-j}$ and $\sigma_d$ is a constant between 0 and 1. The spatial Fourier transform of Eq. (2.52) is applied

$$D_k(k\Delta x) = d_0 + \sum_{j=1}^{N} 2d_j \cos(jk\Delta x), \tag{2.53}$$

where $D_k$ is the damping function holding $D_k(k\Delta x = 0) = 0$ and $D_k(k\Delta x = 1) = 1$. The dissipation is small for the long waves and quite effective for the short waves. The parameter $d_j$ are developed to minimize the integral dissipation

$$\int_{\ln \pi/16}^{\ln \pi/2} D_k(k\Delta x) \mathrm{d}(\ln(k\Delta x)). \tag{2.54}$$

Figure 2.11 illustrates damping functions of the standard tenth-order and optimized sixth-order centered 11-point selective filtering. Corresponding coefficients can be found in [69, 76]. It is shown that the optimized selective filtering provides appreciable dissipation over $\pi/2 \leq k\Delta x \leq \pi$.

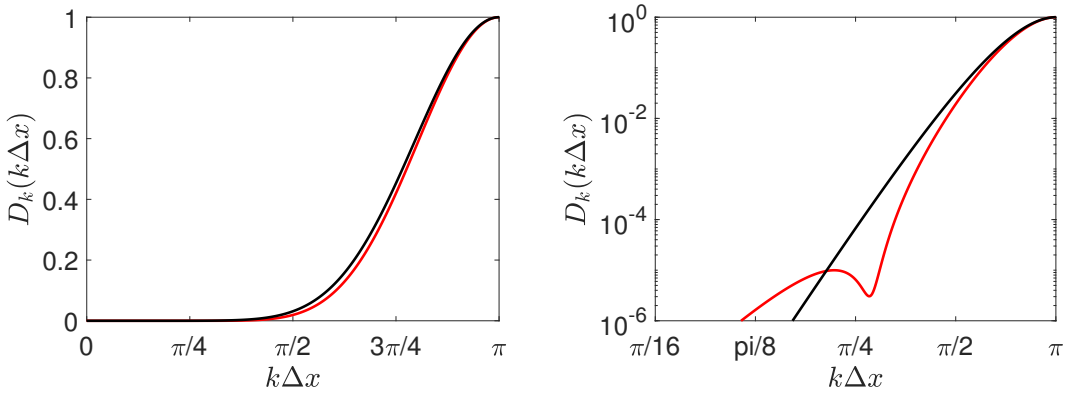


Figure 2.11: Damping functions of the optimized selective filters: optimized 11-points sixth-order centered selective filter ——; standard 11-points centered tenth-order selective filter: ——. Left, linear scale; right, logarithm scale.

Moreover, its impact is weaker than the standard method for the waves with small wavenumbers, for example, $\pi/16 \leq k\Delta x \leq \pi/2$. In the present work, two types of selective filters, namely the centered 11-points sixth-order selective filter of Bogey *et al.* [76] and the optimized non-centered selective filter of Berland [70] are utilized.

### 2.3.4 Boundary conditions

In this part, the impedance boundary condition and non-reflective boundary condition are respectively introduced. The implementation of boundary conditions is a key point in the time-domain simulation to describe the complex interactions of acoustic waves, mean flow and acoustic liners. In practice, the impedance boundary condition can be imposed by utilizing either the impedance, admittance or reflection coefficient. When the acoustic and aerodynamic perturbations (vorticity and entropy waves) leave the computation domain, spurious waves may arise. Since spurious waves could contaminate the acoustic solution, implementation of a non-reflective boundary condition is necessary.

#### Admittance boundary condition

The surface impedance describes the macroscopic properties of locally acoustic liners in the frequency domain. To perform time-domain calculations, the representation of the frequency-domain impedance boundary condition involves the convolution

$$p(t) = \int_{-\infty}^{t} Z(t-t')v_n(t')\mathrm{d}t', \tag{2.55}$$

where $Z(t)$ is the inverse Fourier transform of the impedance function $Z(\omega)$. To derive physically admissible time-domain impedance functions, several requirements need to be satisfied according to Rienstra [28]:

• Reality condition: For $Z(\omega) = Z^*(-\omega^*)$, and therefore $Z(t) \in \mathbb{R}$.

- Passive condition: The impedance wall is a passive wall for $\omega \in \mathbb{R}$, $\mathrm{Re}(Z(\omega)) \geq 0$.
- Causality condition: $Z(\omega)$ should be analytic and non zero for $\mathrm{Im}(\omega) < 0$.

Indeed, the direct calculation of convolution integral is non-desirable due to its large computational cost. In the recent three decades, many efforts have been undertaken to develop formulation for the impedance boundary condition in the time domain. Nearly in the same period, the teams of Özyörük and Long [77] and Tam and Auriault [27] presented their researches on implementing the Myers boundary conditions in the time domain. Tam and Auriault [27] used a MSD model mentioned previously. An implementation of the time domain impedance boundary condition was presented with a mean flow. Tam and Auriault [27] noticed the existence of instabilities generated on the liner. They assumed the instabilities are of Kelvin-Helmholtz type. They supposed that the instabilities could be avoided by using an effective impedance of acoustic liners including the effect of a mean flow instead of assuming the existence of a vortex sheet in the Myers boundary condition. Thereafter, the implementation of the three-parameter model was conducted by Fung *et al.* [78] by using reflection coefficients. They argued that the implementation on the reflection coefficient would get rid of instabilities that may be due to the direct translation of impedance into time domain of Tam and Auriault [27]. Later, Li *et al.* [79] proposed an effective impedance model including the mean flow convection effect. Rienstra [28] proposed the extended Helmholtz resonator (EHR) model which can easily satisfy the requirements referring to the implementation of impedance boundary condition in the time domain. Based on this impedance model, several implementations of impedance boundary condition[80, 65, 81] into the time domain have been carried out. Chevaugeon *et al.* [80] and Pascal *et al.* [81] applied a discontinous Galerkin CAA method to implement the EHR model. While a finite difference scheme was utilized by Richter *et al.* [65]

Formulations of the time-domain impedance boundary condition have been also developed for more general impedance functions. In particular, the use of a rational function to approximate impedance functions has been the subject of several studies. Özyörük & Long [77] proposed the $z$-transform, which was originally used in the computational electromagnetics. The impedance model was built in the $z$-domain by a rational function. The time-domain impedance corresponded to an infinite impulse and a digital recursive filter. Later, recursive convolution methods were proposed by Reymen *et al.* [36]. The convolution was calculated through simple algebraic recursive relation with the assumption that the pressure was piecewise constant or piecewise linear within a time step. Subsequently, Li *et al.* [82] proposed an improved multipole broadband impedance model through splitting the rational polynomial function into residues and poles. Then Dragna *et al.* [83] proved that the recursive convolution methods were at the best in the second-order accurate in time. The numerical accuracy was limited when using high-order time-integration methods. Bin *et al.* [84] represented the frequency domain impedance boundary condition as a linear sum of second-order frequency responses. Zhong *et al.* [85] used a controllable canonical form transferred the rational polynomials into an equivalent state space

mode. This state space model involved several first-order ordinary differential equations, which can be implemented straightforwardly. Monteghetti *et al.* [13] relied on a diffusive technique and recast the time-domain impedance boundary condition as first order differential equations. Troian *et al.* [19] applied the auxiliary differential equations (ADE) method, which not only guaranteed the accuracy but also kept low memory requirements compared with $z$-transform and recursive methods.

One can choose to use impedance, admittance or reflection coefficients to implement the lined wall boundary conditions in solving the LEE in the time domain. The approach of Troian *et al.* [19], corresponding to a broadband time-domain admittance boundary condition,

$$\begin{aligned} \hat{v}_n(\omega) &= \beta(\omega)\hat{p}(\omega) \\ v_n(t) &= \int_{-\infty}^{t} \beta(t')p(t-t') \end{aligned} \tag{2.56}$$

is applied in the present study. A detailed introduction is given below.

The broadband admittance model $\beta(\omega)$ can be written as a rational function by using a partial fraction decomposition,

$$\beta(\omega) = Y_\infty + \sum_{k=1}^{P} \frac{A_k}{\lambda_k + \mathrm{j}\omega} + \sum_{k=1}^{S} \left( \frac{B_k - \mathrm{j}C_\mathrm{k}}{\alpha_k - \mathrm{j}\beta_\mathrm{k} + \mathrm{j}\omega} + \frac{B_k + \mathrm{j}C_\mathrm{k}}{\alpha_k + \mathrm{j}\beta_\mathrm{k} + \mathrm{j}\omega} \right) \tag{2.57}$$

where $\lambda_k$ and $\alpha_k \pm \mathrm{j}\beta_\mathrm{k}$ are respectively the real poles and complex conjugate pole pairs of $\beta(\omega)$, $P$ and $S$ denote their number and $Y_\infty$, $A_k$, $B_k$ and $C_k$ are numerical coefficients determined from the vector fitting algorithm [86]. These coefficients are determined to fit measured admittance data or calculated admittance values from a model over a given frequency range. Thus according to a certain practical problem, different impedance models can be considered.

The use of a rational function enables us to calculate the convolution by advancing in time first-order differential equation, which is solved at the same time as LEE with a small additional computational cost. This method, originated from electromagnetism [87], is referred to as the auxiliary differential equation method.

First of all, the inverse Fourier transform of the admittance model $\beta(\omega)$ can be expressed as

$$\beta(t) = Y_\infty \delta(t) + \sum_{k=1}^{P} A_k \mathrm{e}^{-\lambda_k t} H(t) + \sum_{k=1}^{S} 2[B_k \cos(\beta_k t) + C_k \sin(\beta_k t)]\mathrm{e}^{\alpha_k t} H(t), \tag{2.58}$$

where $\delta$ is the Dirac generalized function. Combining Eq. (2.58) with Eq. (2.56), $v_n$ can be expressed as

$$v_n(t) = Y_\infty p(t) + \sum_{k=1}^{P} A_k \phi(t) + \sum_{k=1}^{S} 2[B_k \psi_k^{(1)}(t) + C_k \psi_k^{(2)}(t)], \tag{2.59}$$

where $\phi_k$ and $\psi_k$, which are called accumulators in Reymen *et al.* [36], are respectively

$$\begin{aligned}
\phi(t) &= \int_{-\infty}^{t} p(t')\mathrm{e}^{-\lambda_k(t-t')}\mathrm{d}t' \\
\psi_k^{(1)}(t) &= \int_{-\infty}^{t} p(t')\mathrm{e}^{-\alpha_k(t-t')}\cos(\beta_k(t-t'))\mathrm{d}t' \\
\psi_k^{(2)}(t) &= \int_{-\infty}^{t} p(t')\mathrm{e}^{-\alpha_k(t-t')}\sin(\beta_k(t-t'))\mathrm{d}t'.
\end{aligned} \tag{2.60}$$

Taking time derivative of the above equation, leads to:

$$\begin{cases}
\dfrac{\mathrm{d}\phi_k}{\mathrm{d}t} + \lambda_k\phi_k(t) = p(t) \\
\dfrac{\mathrm{d}\psi_k^{(1)}}{\mathrm{d}t} + \alpha_k\psi_k^{(1)}(t) + \beta_k\psi_k^{(2)}(t) = p(t) \\
\dfrac{\mathrm{d}\psi_k^{(2)}}{\mathrm{d}t} + \alpha_k\psi_k^{(2)}(t) - \beta_k\psi_k^{(1)}(t) = 0
\end{cases} \tag{2.61}$$

Finally, the time-domain admittance boundary condition is obtained through combining Eq. (2.61) with Eq. (2.59).

#### Non-reflective boundary condition

To allow acoustic waves to leave the computation domain without significant reflections, non-reflective boundary conditions are required. Specifically, additional zones are added to surround the computational domain to attenuate the outgoing disturbances. Various approaches [88, 89, 90, 91] to construct the absorbing zones have been proposed. Among them, the perfectly matched layer method [91], developed for electromagnetic wave propagation [92], is one of the most popular. The original formulation was shown to lead to numerical instabilities in the presence of a mean flow and an extension has been proposed by Hu [91].

In the present study, non-reflecting boundary conditions proposed by Tam & Dong [89] and extended to three dimensions in Bogey & Bailly [90] are chosen. These boundary conditions are based on the far-field asymptotic solutions of the linearized Euler equations. Sponge zones, combining additional damping and grid stretching, are also implemented to decrease the reflected waves.

## 2.4 Test case

In order to compare the three methods and ascertain the viability of the high order finite difference time-domain solver to deal with wave propagation problems, the benchmark problem of NASA GIT experiment [20] is considered as a test case. It is widely used for the validation for aeroacoustic solvers to solve wave propagation along a lined duct. The plane wave ($f \leq 3000$ Hz) and high-order modes propagation ($f = 5000$ Hz and $f = 7000$ Hz) have been studied by applying

three methods with a mean flow $M = 0$ and $M = 0.335$.

The partially lined duct, which consists of 3 sections with dimensions of $L_x = 0.812$ m, $L_y = L_z = 0.0508$ m is considered. The liner is located in the middle of the upper wall with a length $L_t = 0.406$ m as shown in figure 2.1. The ceramic tubular liner mentioned in section 2.1.2 is used. The acoustic pressure is measured by 31 microphones placed along the lower wall. The source is harmonic, with frequencies from 500 Hz to 3 kHz, in steps of 100 Hz. It is located at the input section of the duct. Experiments were conducted for 5 flow speeds, with average Mach numbers $M$ equal to 0, 0.079, 0.172, 0.255, 0.335 and 0.4. At the duct exit, although the exit impedance has been measured by NASA, it will be further assumed that the termination is anechoic. The air density $\rho_0$ is 1.29 kg/m$^3$. The speed of sound in air $c_0$ is 344.283 m/s.

The coefficients of the interpolation using a rational function, obtained by fitting the curve of the normalized broadband admittance model in figure 2.12 are given in Table 2.4. Note that for the CT57 liner, there are no real poles and six complex conjugate pole pairs are sufficient to accurately interpolate the admittance model from 500 Hz to 10 kHz. The impedance and admittance models for the CT57 liner and their interpolations by the rational function are shown as a function of frequencies in figure 2.12. The normalized impedance and admittance for $M = 0$ and $M = 0.335$ educed by NASA are also attached for comparison. It is seen that the two curves are superimposed. The admittance provided by the rational function will be used through the paper for the three methods.

Table 2.4: Coefficients of the rational function for the normalized broadband admittance model

$M = 0$

| | $i=1$ | $i=2$ | $i=3$ | $i=4$ | $i=5$ | $i=6$ |
|---|---|---|---|---|---|---|
| $\alpha_i$ | 18854 | 3096 | 2868 | 2423 | 1872 | 1056 |
| $\beta_i$ | 81463 | 61748 | −47536 | 33516 | −19660 | −6047 |
| $B_i$ | 10908 | 2500 | 2659 | 2595 | 2525 | 2399 |
| $C_i$ | −15119 | 291 | 4 | −104 | 148 | 261 |
| $Y_\infty$ | 0.29 | | | | | |

$M = 0.335$

| | $i=1$ | $i=2$ | $i=3$ | $i=4$ | $i=5$ | $i=6$ |
|---|---|---|---|---|---|---|
| $\alpha_i$ | 15066 | 3119 | 2785 | 2319 | 1776 | 991 |
| $\beta_i$ | −76133 | 60206 | −46238 | −32593 | −19127 | 5904 |
| $B_i$ | 7884 | 2720 | 2669 | 2538 | 2447 | 2316 |
| $C_i$ | 12946 | 367 | 58 | 144 | 165 | −250 |
| $Y_\infty$ | 0.29 | | | | | |

The mean flow velocity profile $\boldsymbol{u_0} = u_0 \boldsymbol{e_x}$ is defined as:

$$u_0(y,z) = Mc_0 \frac{n_y+1}{n_y}\left(1-\left|1-\frac{2y}{L_y}\right|^{n_y}\right)\frac{n_z+1}{n_z}\left(1-\left|1-\frac{2z}{L_z}\right|^{n_z}\right) \tag{2.62}$$

where $n_y$ and $n_z$ are two parameters describing the flow profile, which can be related to the

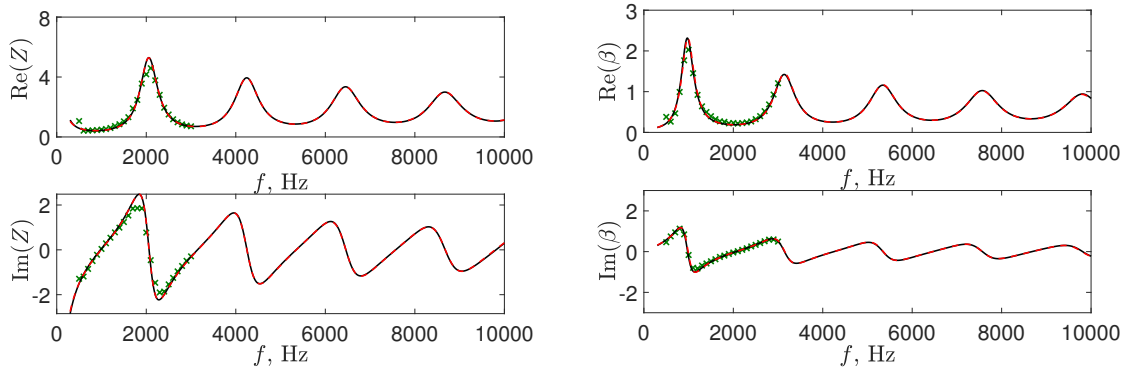


(a) $M = 0$

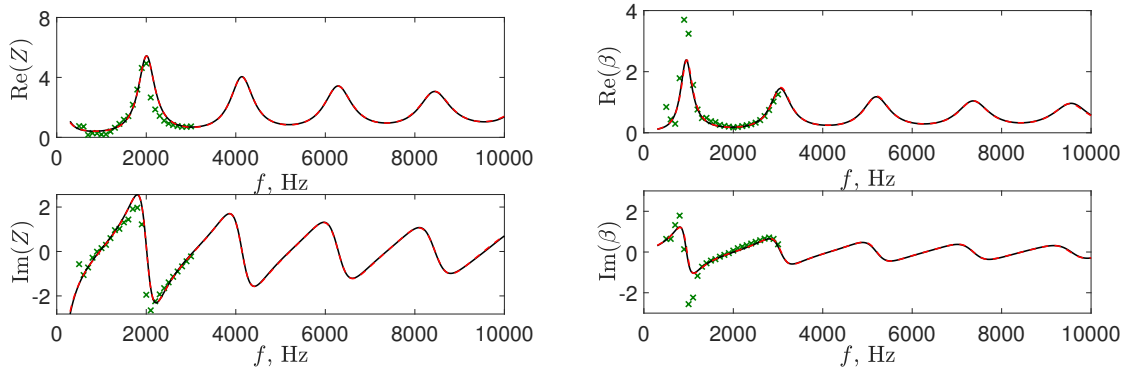


(b) $M = 0.335$

Figure 2.12: Real and imaginary parts of the normalized impedance and admittance of the CT57 liner for $M = 0$ (a) and $M = 0.335$ (b): $\times$ educed values by NASA , ——— broadband impedance and admittance, and - - - - their interpolation using a rational function.

boundary layer thickness. Thus, the displacement thickness, defined by:

$$\delta^* = \int_0^{Lz/2} \left(1 - \frac{u_0(L_y/2, z)}{u_0(L_y/2, L_z/2)}\right) \mathrm{d}z, \tag{2.63}$$

is given by $\delta^* = L_z/[2(n_z + 1)]$. The parameters of the flow profile are set to $n_y = n_z = 24$, corresponding to $\delta^*/L_y = \delta^*/L_z = 2$ %.

To generate acoustic waves, the source terms $S_c$, $S_m$ and $S_e$ in Eqs. (2.36)-(2.38) in the module "domain sources" in COMSOL are used. $S_c$ is given by:

$$S_c\,(x, y, z) = \exp\left[-\ln 2 \frac{(x - x_s)^2}{B_s^2}\right] \sum_{m=0}^{r} \sum_{n=0}^{s} A_{m,n} \cos\left(\frac{m\pi y}{L_y}\right) \cos\left(\frac{n\pi z}{L_z}\right). \tag{2.64}$$

where $r$ and $s$ are integers. The Gaussian half-width of the source $B_s$ is set to $5.3 \times 10^{-3}$ m. The source is centered at $x_s = 5 \times 10^{-2}$ m. In order to generate only acoustic fluctuations, $S_m$ is set to zero and $S_e = \gamma p_0 S_c/\rho_0$.

For the LEE in the time domain, the source $Q$ in Eqs. (2.40) is defined as

$$Q = S_c \lambda(t). \tag{2.65}$$

The source signal $\lambda(t)$ is defined as

$$\lambda(t) = \frac{t - t_s}{t_c} \left[ -\ln 2 \frac{(t - t_s)^2}{t_c^2} \right] H(t), \tag{2.66}$$

where the source signal $t_s = 8 \times 10^{-4}$ s and $t_c = 1.4 \times 10^{-4}$ s respectively stand for a time shift and a parameter determining the frequency content. $H(t)$ is the unit step function.

Because the simulations performed with COMSOL are based on finite element approach, the computation is quite demanding in terms of memory space. We have therefore chosen to perform simulations in a 2D geometry for frequencies below 3 kHz, for which only the plane wave mode is propagative and for which 3D effects are expected to be negligible. In this case, a very fine mesh is employed. For frequencies above 3 kHz, higher-order modes are propagative and a 3D simulation is mandatory. The mesh size is set to 8 points and 9 points per wavelength for the maximum and minimum size. The use of "boundary layer" also allows one to have a refined mesh near the boundaries. The mesh in the cross-section of the duct used for $f = 7$ kHz is shown in figure 2.13. All the simulations were performed on standard desktop computers with similar specifications (CPU clockspeed around 3GHz and 32GB of RAM). For the last simulation containing approximately 3 million elements of mesh grids, the physical memory was overwhelmed leading COMSOL to use swap spaces on the hard-drive. Computation was largely slowed down and it took nearly 56 hours to obtain the numerical solution. A finer mesh grid would even lead to the sudden stop of the simulation, as the available memory space on the hard-drive was not sufficient.

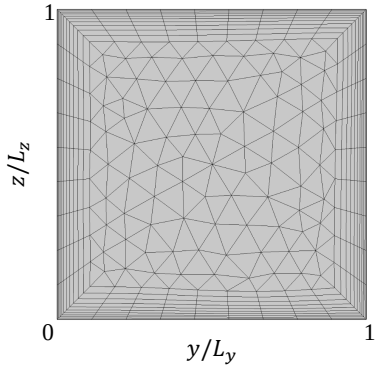


Figure 2.13: Mesh grids of the duct cross-section in COMSOL.

For the high order finite difference time-domain solver, the time step is $2 \times 10^{-6}$ s and the whole simulation lasts for $2 \times 10^{-2}$ s. The grid is uniform along the $x$-direction with a mesh spacing $\Delta x = 1.1 \times 10^{-3}$ m. At each side of the duct, damping zones are implemented. In these zones, the mesh spacing is gradually increased with a stretching factor of 3 %. Along the $y$- and $z$-directions, the grid is similar with 55 points. In the middle of the duct, the mesh spacing is $\Delta y = \Delta z = \Delta x$. Near the walls, it is gradually reduced with a shrinking factor of 1 %. The mesh size along the duct for $x$- and $z$-direction is shown in figure 2.14. The simulations performed

with an in-house solver of the time-domain LEE, written in Fortran 90, run for approximately 6 hours, for a grid with 4 million points.

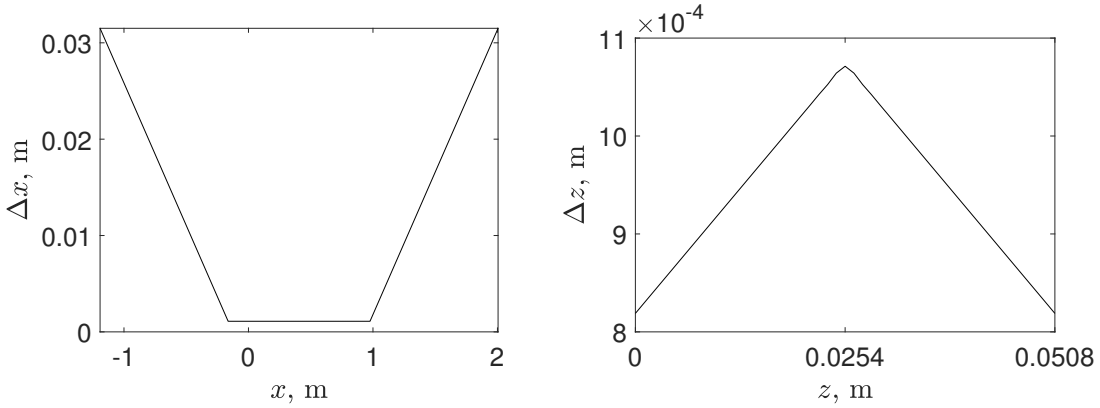


Figure 2.14: Mesh size along the $x$- (left) and $z$-direction (right) for time domain approach.

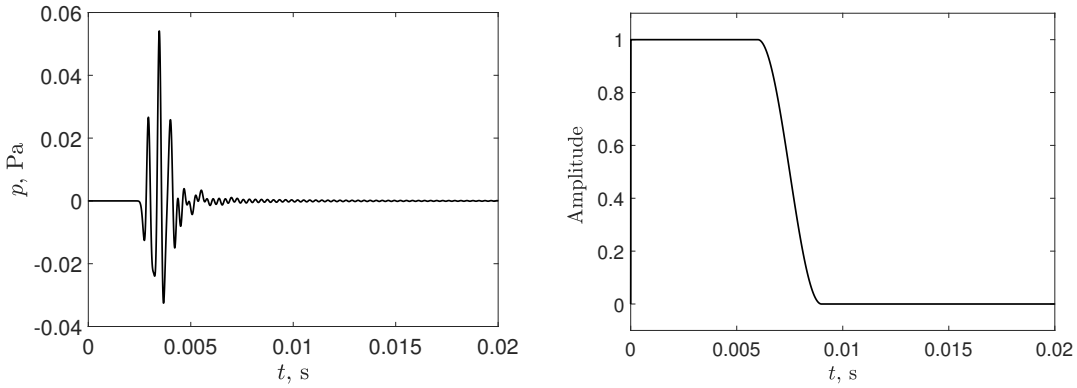


Figure 2.15: Left, pressure signal for $M = 0$ and for solving the LEE in the time domain obtained by the receiver located at $x = 0.86\ L_x$, $y = 0.5\ L_y$, $z = 0$. Right, the window function used for signal processing.

The pressure signals are collected at every time step through the receivers located at every grid node on the lower wall. In order to obtain the frequency spectrum of the pressure field, a tapered cosine window is applied to the pressure signals to discard the instability component. The Fourier transform of the filtered signals is then computed. Example of the pressure signal obtained by a receiver located at $x = 0.86\ L_x$, $y = 0.5\ L_y$, $z = 0$ with the window function used for signal processing is shown in figure 2.15.

### 2.4.1 Plane wave

We now consider results for frequencies below 3 kHz, for which NASA experimental results are available. For these frequencies and the Mach numbers $M = 0$ and $M = 0.335$, only the plane wave mode is propagative in the rigid sections. For the three methods, the modal amplitudes are then set to $A_{0,0} = 1$ and $A_{m,n} = 0$ for $m \geq 1$ or $n \geq 1$. For comparison, the sound pressure level (SPL) and phase at the source plane are set as 130 dB and 0°.

The results obtained by the three numerical methods are shown in figure 2.16. The measured data from the NASA GIT experiment [20] are also provided. The SPL presents the classical pattern for plane wave propagation in a duct. It is almost constant in the unlined sections and decreases continuously along the lined section. For 1 kHz, discrepancies are observed between all the three methods and the NASA experiment with and without flow. This frequency is related to the resonance frequency of the liner and the predictions are strongly sensitive to the liner admittance. Also, it can be noted that the result obtained by solving LEE in the frequency domain for $M = 0.335$ exhibits an increase of the pressure in the lined region. Additional simulations for this particular case have been conducted to investigate the effect of the mesh grid on the results. It was not possible to obtain a converged solution even for a finer mesh. Such kind of pressure increase is an evidence for the existence of instabilities with a shear flow.

Although some differences exist at some specific frequencies, results of the three numerical methods are all in close correspondence and agree with the experimental results. The difference between the numerical methods and the experimental results can be mainly attributed to the discrepancy between the real behaviour of the liner used in the NASA experiment and the admittance model.

### 2.4.2 Higher-order modes

Table 2.5: Mode amplitudes for the higher-order modes case.

| | $A_{0,0}$ | $A_{1,0}$ | $A_{0,1}$ | $A_{1,1}$ | $A_{2,0}$ | $A_{0,2}$ |
|---|---|---|---|---|---|---|
| 5 kHz | 1 | -1 | -1 | 1 | - | - |
| 7 kHz | | | | | 1 | 1 |

Simulations are now performed for higher-order modes propagation. Two cases corresponding to without and with a mean flow are investigated. In the first one, the first 4 modes, corresponding to the mode indices ($m$, $n$) equal to (0,0), (0,1), (1,0) and (1,1), are excited and results for a frequency of 5 kHz are analyzed. In the second one, the first 6 modes are considered with the additional modes (2,0) and (0,2). The comparison is performed at a frequency of 7 kHz. The mode amplitudes for each case are indicated in Table 2.5.

Results for the three different methods, with the same normalization as used in Sec. 2.4.1, are shown in figure 2.17. A good agreement among the three different methods is obtained. At 5 kHz, the three numerical solutions are almost superimposed. For a frequency of 7 kHz, a discrepancy between the frequency-domain solution of the LEE and other methods can be observed in the SPL. Although the difference exists in the SPL, the phase graph has an excellent match with the others.

### 2.4.3 Existence of an instability

It has been indicated in section 2.4.1 that an instability has been observed in the results obtained with COMSOL at 1 kHz with Mach number $M = 0.335$. In fact, this instability has also

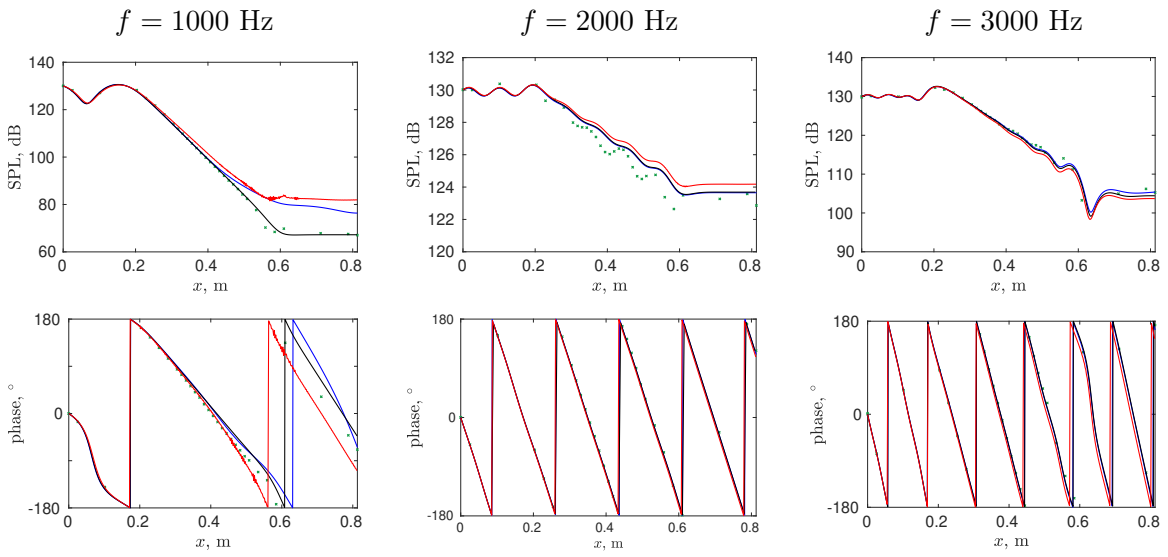


(a) $M = 0$

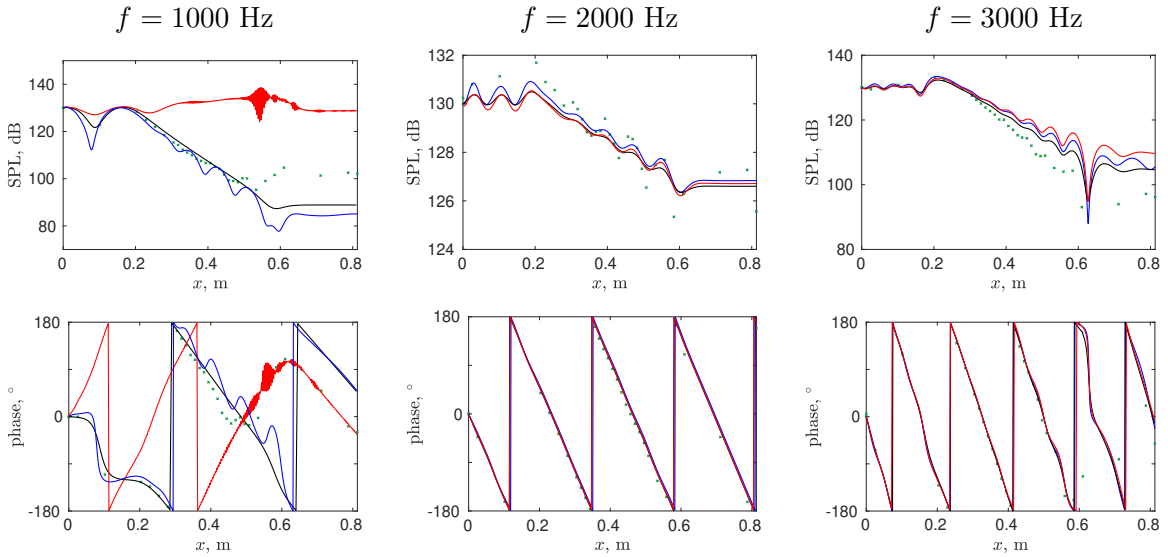


(b) $M = 0.335$

Figure 2.16: SPL and phase of the acoustic pressure along the duct when only the plane wave mode propagates for (a) $M = 0$ and (b) $M = 0.335$. ——— mode matching method, ——— solving LEE in the frequency domain, ——— solving LEE in the time domain and × NASA experiments.

been observed in the numerical solution of LEE in the time domain. Figure 2.18 presents the pressure signal at the receiver ($x = 0.86\ L_x$, $y = 0.5\ L_y$ and $z = 0$) for $M = 0.335$ obtained by solving LEE in the time domain. The signal is composed of two wave packets. The first wave packet ($t < 0.006$ s) corresponds to the acoustic pulse generated by the source. A second wave packet, with an arrival time at $t = 0.01$ s can be distinguished. Its amplitude is growing with time, indicating an instability. Its period is approximately of $10^{-3}$ s, which corresponds to a frequency of 1 kHz. As the signal is windowed for signal processing, only the first wave packet is accounted for when computing the SPL as in figure 3.4 (b). This instability encountered in the solutions of LEE with a shear flow has been analysed theoretically and experimentally in previous

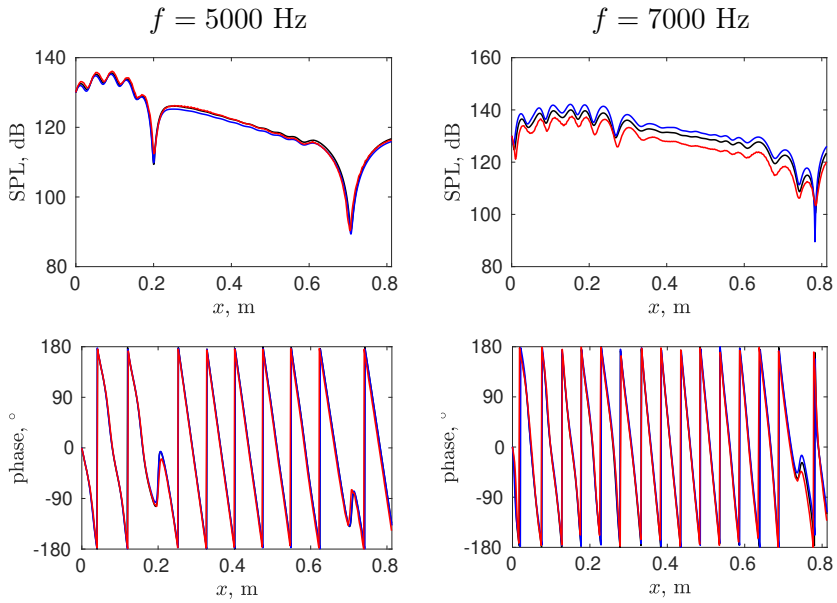


(a) $M = 0$

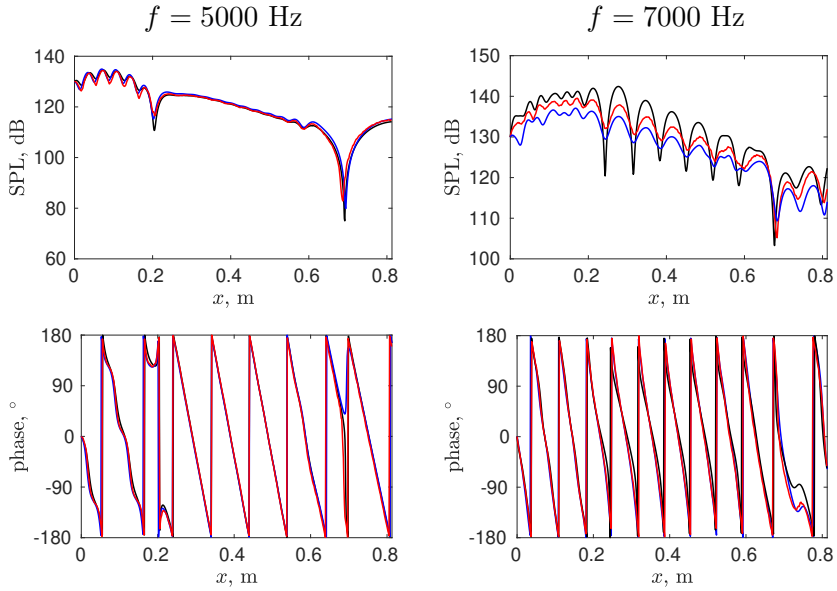


(b) $M = 0.335$

Figure 2.17: SPL and phase of the acoustic pressure along the duct when higher-order modes propagate for (a) $M = 0$ and (b) $M = 0.335$. ——— mode matching method, ——— solving LEE in the frequency domain and ——— solving LEE in the time domain.

studies [93, 94, 33, 95]. Specifically, for the same geometry, a similar instability was observed at 1 kHz by Burak [33] both in the time and frequency domains. The instability generated in the acoustic propagation in a lined flow duct will be investigated in chapter 4.

Snapshots of the acoustic pressure along the duct up to $t = 18$ ms are shown for two Mach numbers in figure 2.19. At $t = 1.3$ ms, the acoustic signal arrives at the leading edge of the liner. A diffracted wave of small amplitude is generated and travels in the opposite direction to that of the direct wave. The direct pulse continues its propagation along the duct, being gradually attenuated by the liner. Without a mean flow, after $t = 6$ ms, the main acoustic pulse has left

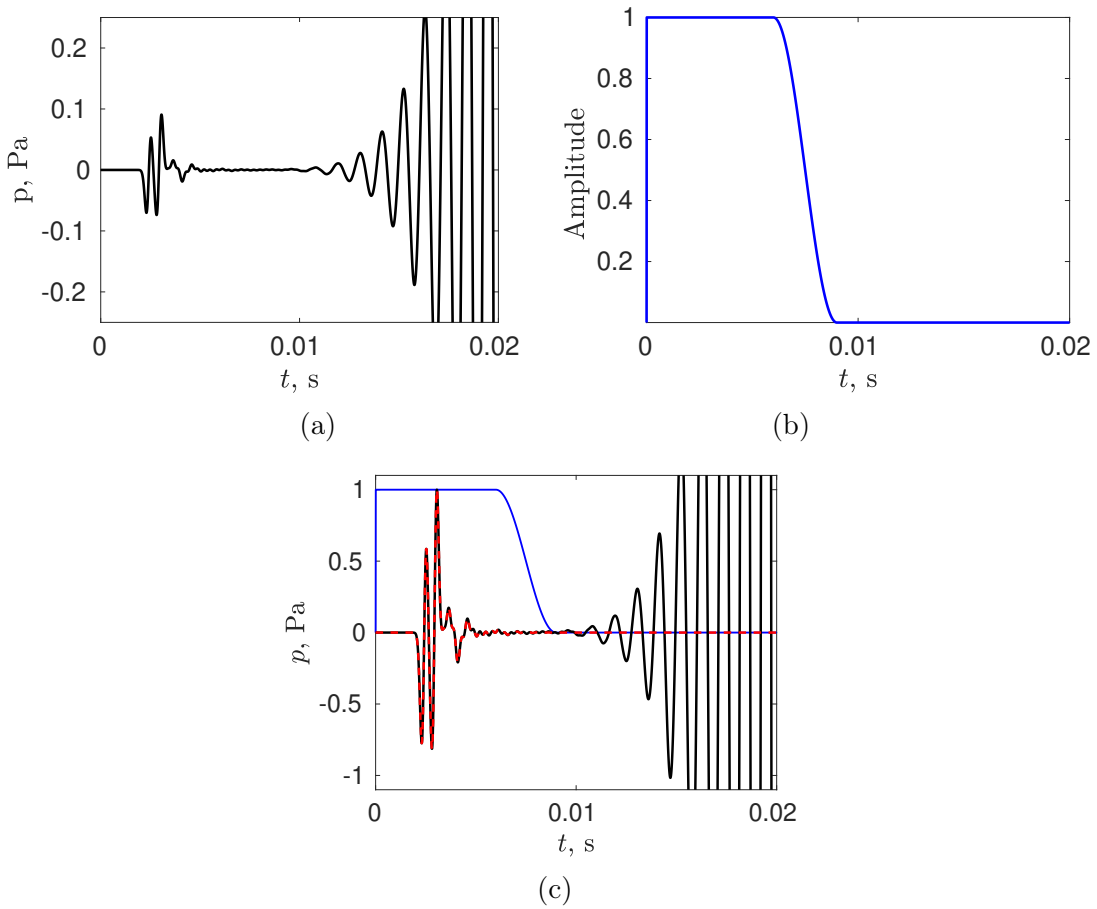


Figure 2.18: Pressure signal for $M = 0.335$ and for solving LEE in the time domain obatined by a receiver located at $x = 0.86\ L_x$, $y = 0.5\ L_y$, $z = 0$. (a), pressure signal; (b), the window function used for signal processing and (c), comparison the normalized pressure before(——) and after the window ( - - - - ).

the duct. The remaining pressure fluctuations are then small and the acoustic pressure signal is almost null, as observed in figure 2.15 and figure 2.19 (a). However, for $M = 0.335$, an instability is generated at the leading edge of the liner and grows continuously along the lined section during the acoustic signal propagation. As $t$ increases, the instabilities almost spread the whole calculation domain. The efficiency and accuracy of the time-domain solutions will finally be hindered.

### 2.4.4 Effect of flow profile

In this section, the effect of flow profiles on sound propagation is investigated. For this, the 2D LEE are solved in the time domain. Several mean flow profiles are considered with boundary layer thickness $\delta^*$ corresponding to 0.5 $\%L_z$, 2 $\%L_z$ and 8 $\%L_z$. The 2D mean flow profile $\boldsymbol{u_0} = u_0 \boldsymbol{e_x}$ already used in section 2.4, is given by

$$u_0(z) = Mc_0 \frac{n_z + 1}{n_z} \left( 1 - \left| 1 - \frac{2z}{L_z} \right|^{n_z} \right), \tag{2.67}$$

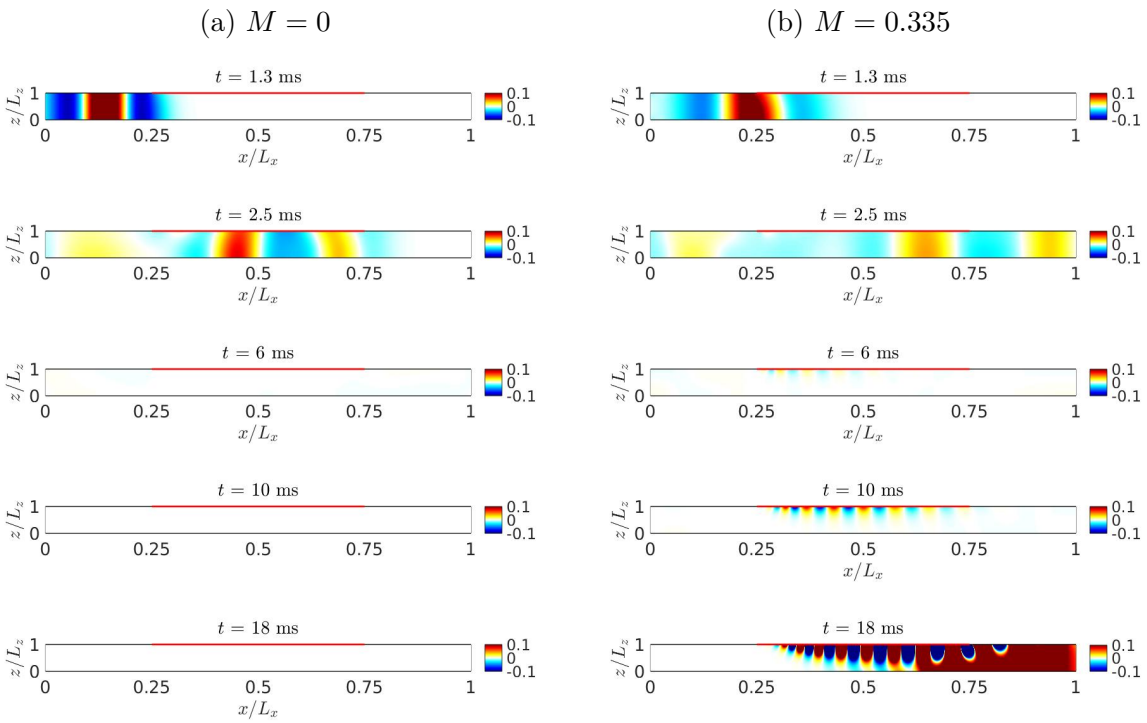


Figure 2.19: Pressure map (Pa) along the duct for $M = 0$ and $M = 0.335$ at $y = L_y/2$ at different times.

where $n_z$ is respectively 99, 24 and 5.5. These profiles are displayed in figure 2.20. Instead of the plane source used previously, the source imposed is a point source. Indeed, for a thick boundary layer, it has been observed that using a plane source generates some trapped waves near the duct boundaries. This leads to some oscillations on the SPL, which makes it difficult to compare. For a point source, these trapped waves were not distinguishable.

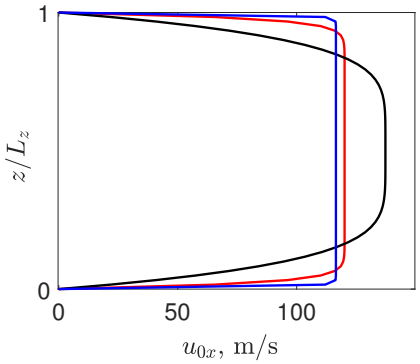


Figure 2.20: A sketch of flow profiles. —— $\delta^* = 0.5\ \%L_z$ , —— $\delta^* = 2\ \%L_z$, —— $\delta^* = 8\ \%L_z$.

Figure 2.21 shows the pressure signals obtained by the receiver located at the same position as in figure 2.15 for the three profiles. As discussed previously, these signals are composed of two wave packets. The first, containing the acoustic information, is approximately the same for the three profiles. The second one, corresponding to the hydrodynamic instability, is dramatically different depending on the boundary layer thickness. Note also that, as indicated in the literature [65], this

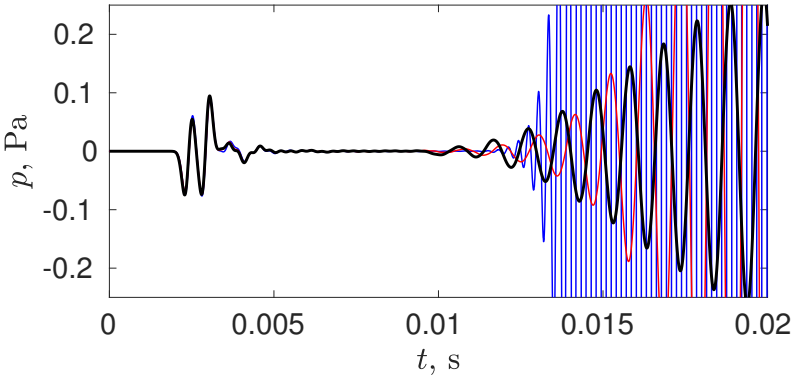


Figure 2.21: Time series of pressure obtained at $x = 0.84L_x$, $y = 0.5L_y$, $z = 0$ for different flow profiles. —— $\delta^* = 0.5\ \%L_z$, —— $\delta^* = 2\ \%L_z$, —— $\delta^* = 8\ \%L_z$.

instability is very sensitive to the numerical parameters, and in particular to the filter applied at each iteration to remove short waves.

The SPL and phase along the duct for different frequencies and for the three flow profiles are shown in figure 2.22. It can be seen that the flow profile has an affect mostly for the low frequency range. At higher frequencies, the results are all similar for the three flow profiles.

To assess the effect of flow profile, another quantity of interest, namely the power difference $\Delta W$, is considered. It is defined in this case as the difference in acoustic power at the sections $x = 0$ and $x = L$ of the duct following Troian *et al.* [19].

$$\Delta W = \log_{10}(W_R/W_L), \tag{2.68}$$

where $W_R$ and $W_L$ are respectively the sound power computed at exit plane of the first rigid section and the lined section. The power $W$ is obtained by the integration of the sound intensity $I$ over the cross-section of the duct

$$W(x) = \iint I(x, y, z)dy\,dz. \tag{2.69}$$

The acoustic intensity $I$ with the presence of a mean flow [96] can be approximated as

$$I(x, y, z) = \frac{1}{2}\left[(1 + M^2)\mathrm{Re}(\hat{p}\hat{v}_x^*) + \frac{M}{\rho_0 c_0}\mathrm{Re}(\hat{p}\hat{p}^*) + M\rho_0 c_0 \mathrm{Re}(\hat{v}_x\hat{v}_x^*)\right]. \tag{2.70}$$

Figure 2.23 shows the frequency variations of $\Delta W$ calculated for different flow profiles $\delta^*$, as well as estimated from the NASA measurements. The impact of $\delta^*$ on $\Delta W$ is weak except near the resonance and also for $f > 2.5$ kHz. A peak is observed at around 1 kHz close to the liner resonance. For $\delta^* = 2\ \%L_z$ and $8\ \%L_z$, a good agreement between the time-domain approach and NASA experiment is retrieved. The power difference $\Delta W$ is underestimated for $\delta^* = 0.5\ \%L_z$ especially around 1 kHz, which is supposed to relate with the observed instabilities.

Since the Fourier transform is utilized to convert time-domain signals into the frequency

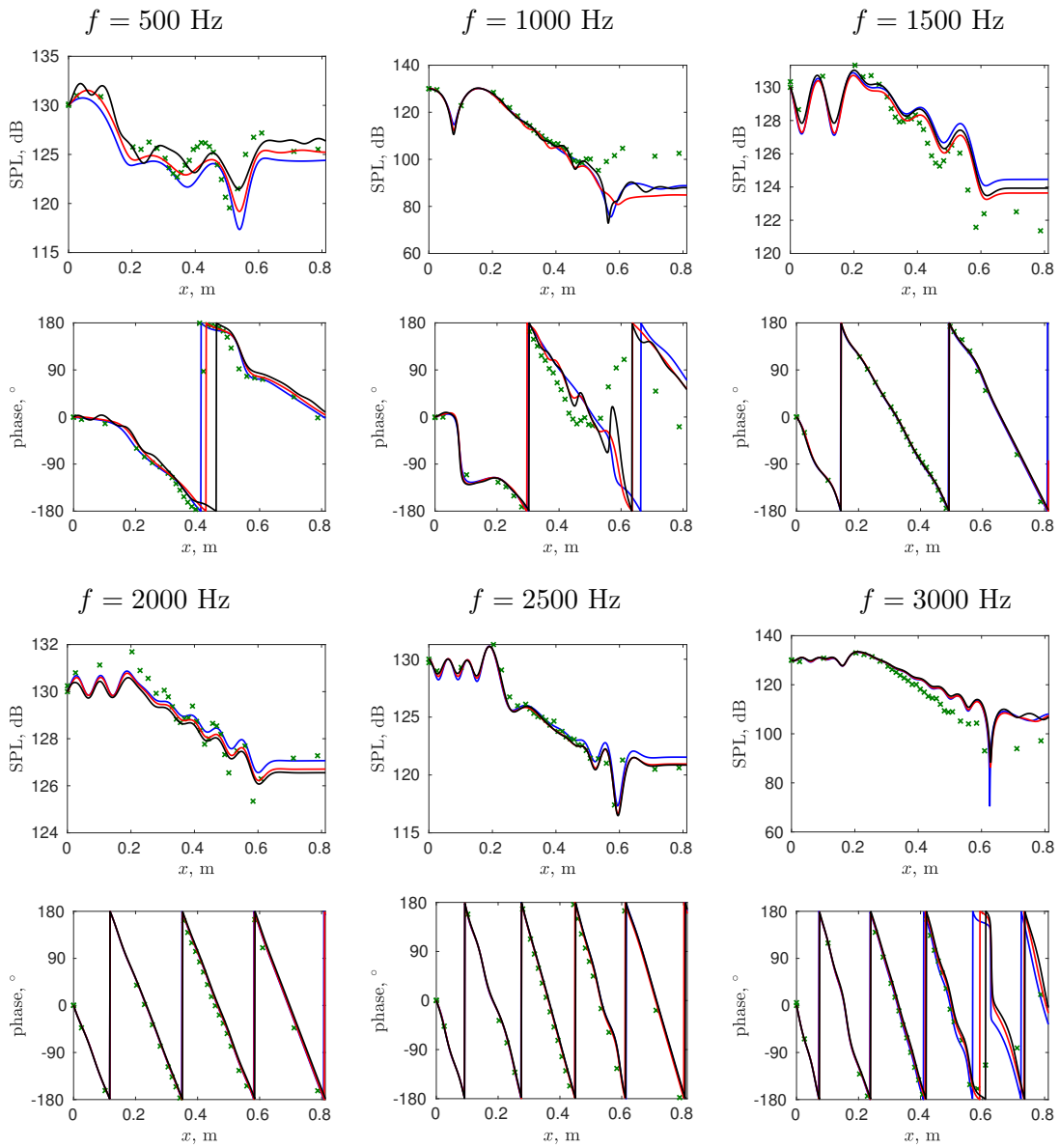


Figure 2.22: SPL and phase of the acoustic pressure along the duct for $M = 0.335$ and for different boundary layer thickness: $\delta^* = 0.5\ \%L_z$ ——, $\delta^* = 2\ \%L_z$ ——, $\delta^* = 8\ \%L_z$ —— and $\times$ NASA experiments.

domain, the effect of the window function on thepower difference $\Delta W$ is also studied. Three different windows, shown in figure 2.24, are considered. Other parameters are maintained the same as in section 2.4.1. It should be mentioned that the window function $b$ is used in the whole study. The power difference $\Delta W$ is overestimated with the use of a narrow window, while it is underestimated by using a broad window. It is seen that the effect of the window function is not obvious except near 1 kHz, because that instabilities around 1 kHz are eliminated. Therefore the effort of the window function is pronouncing around the frequency range where instabilities exist. It should be also noticed that if the window is relatively narrow, the acoustic signal could be truncated when instabilities are filtered.

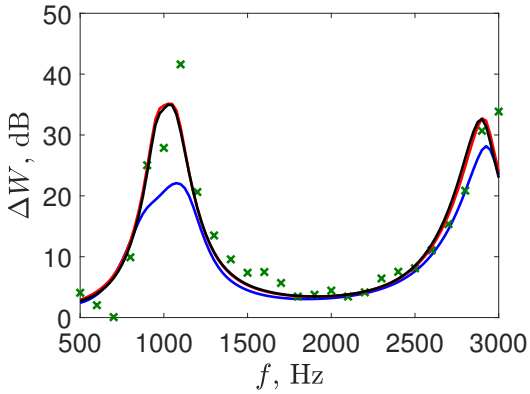


Figure 2.23: Power difference $\Delta W$ for $M = 0.335$ with different boundary layer thickness: $\delta^* = 0.5\ \%L_z$ ——, $\delta^* = 2\ \%L_z$ ——, $\delta^* = 8\ \%L_z$ —— and $\times$ NASA experiments.

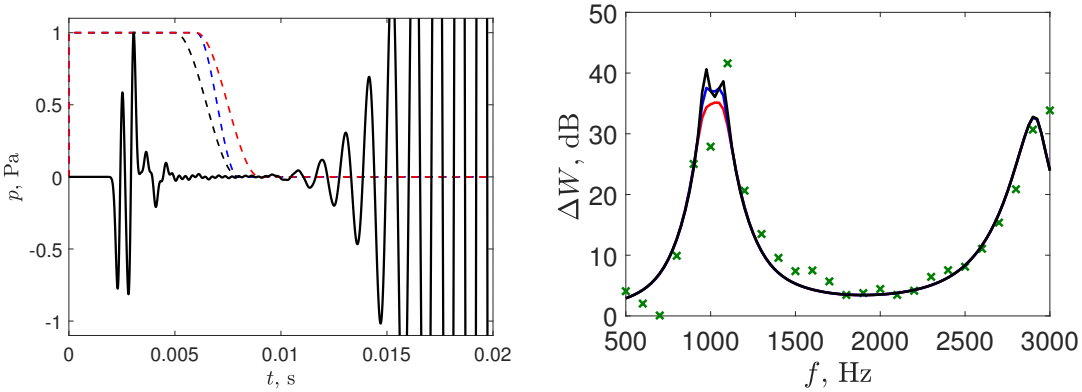


Figure 2.24: Three windows (left) considered and power difference $\Delta W$ (right): window function $a$ ——, window function $b$ ——, window function $c$ —— and $\times$ NASA experiments.

## 2.5 Conclusion

Three approaches, aiming at predicting acoustic propagation in a partially lined flow duct, have been introduced. They are respectively mode matching method, solving LEE in the frequency domain and solving LEE in the time domain.

A benchmark problem proposed by Jones *et al.* [20] was tested and extended. Plane wave and higher-order modes propagation without and with a mean flow were analysed by using the three methods. When only the plane wave mode propagates, the three methods showed excellent agreement with the reference NASA experimental data. When the source frequency was above the cutoff frequency($f \approx 3$ kHz) with higher-order propagative modes, the numerical results were also in good agreement. The viability of the time-domain method to predict the acoustic propagation in a lined flow duct was ascertained.

The effect of flow profile on the sound propagation was studied. The results showed that SPL and phase of acoustic propagation in the low frequency range were sensitive to the flow profile. Instabilities were found in the solutions of LEE when acoustic waves propagate with a shear flow along the lined duct.

# 3 Modal analysis for duct acoustic propagation with a shear flow

Describing the sound field by its modal behaviour is quite interesting to have a further interpretation of the complex sound field. To include a more realistic flow profile and benefit the advantage of modal techniques, the modal analysis approach is utilized and the modes are determined numerically. It is essentially an EigenValue Problem (EVP) aiming at relating the acoustic propagation with modes behaviour.

Indeed, the modal analysis approach is quite a common strategy when the interest focuses on instabilities generated in numerical simulations. The governing equations solved in the EVP can be LEE [97, 29], Pridmore-Brown equations [95] and linearized Navier-Stokes equations [98, 10]. Mode solutions, especially for the ones related to instabilities, can then be obtained.

In this chapter, the implementation of EVP is presented for an infinite lined duct. The modal analysis approach is validated by using an analytical/semi-analytical solution with a uniform flow. Finally, the impact of a mean flow on the modes is investigated.

## 3.1 Governing equations

The configuration considered in the modal analysis approach is shown in figure 3.1. Monochromatic waves propagate in a two-dimensional infinite and homogeneous duct. The duct height is denoted by $H$. The walls can be rigid or lined. A parallel mean flow goes from left to right. The physical quantities with dimensions of length, time, velocity, and pressure are nondimensionalized using $H$, $H/c_0$, $c_0$ and $\rho_0 c_0^2$, respectively. The flow is supposed to be isentropic. The acoustic propagation is governed by LEE. The nondimensionalized LEE are given by:

$$\frac{\partial p}{\partial t} + u_0 \frac{\partial p}{\partial x} + \frac{\partial u}{\partial x} + \frac{\partial v}{\partial z} = 0 \tag{3.1a}$$

$$\frac{\partial u}{\partial t} + u_0 \frac{\partial u}{\partial x} + v \frac{\mathrm{d}u_0}{\mathrm{d}z} + \frac{\partial p}{\partial x} = 0 \tag{3.1b}$$

$$\frac{\partial v}{\partial t} + u_0 \frac{\partial v}{\partial x} + \frac{\partial p}{\partial z} = 0 \tag{3.1c}$$

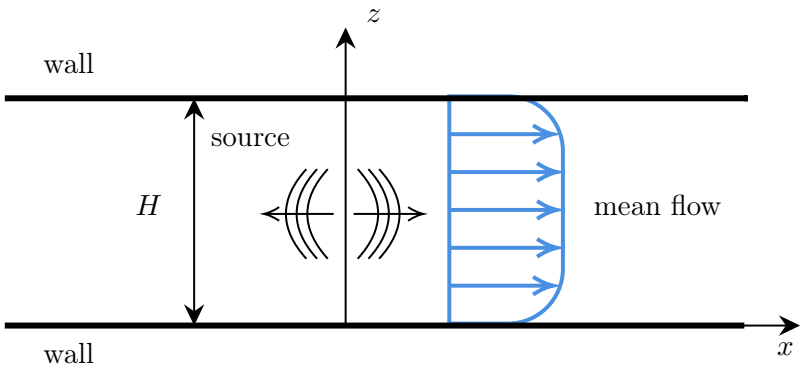


Figure 3.1: The configuration considered in the modal analysis approach.

The modal analysis approach is based on the use of a mode expansion. Then the acoustic perturbations are sought as

$$\begin{aligned} u &= U(z)\,\mathrm{e}^{\mathrm{i}(\omega t - kx)}, \\ v &= V(z)\,\mathrm{e}^{\mathrm{i}(\omega t - kx)}, \\ p &= P(z)\,\mathrm{e}^{\mathrm{i}(\omega t - kx)}, \end{aligned} \tag{3.2}$$

where $U$, $V$ and $P$ are the mode shapes, which depend only on $z$, and $k$ is the mode wavenumber. Note that $\omega$ and $k$ can be complex-valued.

Substituting Eqs. (3.2) into the nondimensionalized LEE, leads to:

$$\begin{aligned} &\mathrm{i}(\omega - u_0 k)P - \mathrm{i}kU + \frac{\mathrm{d}V}{\mathrm{d}z} = 0 \\ &\mathrm{i}(\omega - u_0 k)U + \frac{\mathrm{d}u_0}{\mathrm{d}z}V - \mathrm{i}kP = 0 \\ &\mathrm{i}(\omega - u_0 k)V + \frac{\mathrm{d}P}{\mathrm{d}z} = 0 \end{aligned} \tag{3.3}$$

## 3.2 Implementation of the EVP

### 3.2.1 Boundary condition

To implement boundary conditions, the EVP is not directly formulated using the physical variables; instead, **characteristic variables**, i.e. $U$, $P-V$ and $P+V$, are used. The idea of using characteristics variables is quite common, for instance, Fung & Ju [99] utilized characteristics variables for implementation of the time-domain impedance boundary condition.

Specifically, $P-V$ and $P+V$ are the characteristic waves travelling along the $-z$ and $+z$-direction, respectively. Thus, at $z=0$, the incident wave on the boundary is $P-V$ and the reflected wave is $P+V$. Therefore, $P+V$ is determined with the boundary condition and not from LEE. Similarly, at $z=1$, the incident and reflected wave are $P+V$ and $P-V$, respectively

and, hence, $P-V$ is determined with the boundary condition. Eq. (3.3) can be rewritten as:

$$\begin{pmatrix} 1 & \frac{-1}{2\mathrm{i}\omega}\frac{\mathrm{d}u_0}{\mathrm{d}z} & \frac{1}{2\mathrm{i}\omega}\frac{\mathrm{d}u_0}{\mathrm{d}z} \\ 0 & 1-\frac{1}{\mathrm{i}\omega}\frac{\mathrm{d}}{\mathrm{d}z} & 0 \\ 0 & 0 & 1+\frac{1}{\mathrm{i}\omega}\frac{\mathrm{d}}{\mathrm{d}z} \end{pmatrix} \begin{pmatrix} U \\ P-V \\ P+V \end{pmatrix} = \frac{k}{\omega} \begin{pmatrix} u_0 & \frac{1}{2} & \frac{1}{2} \\ 1 & u_0 & 0 \\ 1 & 0 & u_0 \end{pmatrix} \begin{pmatrix} U \\ P-V \\ P+V \end{pmatrix}. \tag{3.4}$$

This matrix of the system has to be completed with appropriate boundary conditions. We will consider two cases, namely a rigid duct and a lined duct. These two cases are illustrated in figure 3.2.


Figure 3.2: Sketches of a rigid duct case (left) and a lined duct case (right).

For the rigid duct case, the boundary conditions on the walls are

$$[P+V]\Big|_{z=0} = [P-V]\Big|_{z=0} \quad \text{and} \quad [P+V]\Big|_{z=1} = [P-V]\Big|_{z=1}. \tag{3.5}$$

For the lined duct case, the rigid wall boundary condition is imposed on the lower wall as previously and the Ingard-Myers boundary condition is imposed on the lined upper wall as

$$[P+V]-[P-V]\Big|_{z=1} = (\mathrm{i}\omega + u_0\frac{\mathrm{d}}{\mathrm{d}x})\frac{[P+V]+[P-V]}{\mathrm{i}\omega}\beta\Big|_{z=1}. \tag{3.6}$$

For a shear flow whose velocity vanishes on the walls, the classic impedance boundary condition

$$[P-V]\Big|_{z=1} = \frac{1-\beta}{1+\beta}[P+V]\Big|_{z=1} \tag{3.7}$$

is retrieved from the Ingard-Myers boundary condition in Eq. (3.6).

### 3.2.2 Chebyshev spectral method

The EVP in Eq. (3.4) requires the calculation of spatial derivatives. They can be determined by finite difference methods or Chebyshev spectral methods. Chebyshev spectral methods are generally preferred as they generate smaller numerical errors for a given number of grid points than finite difference schemes. A comparison between the Chebyshev spectral method and the finite difference scheme was conducted by Marx [29]. It shows that the Chebyshev spectral method can attain more accurate results with a relatively small computation cost. Therefore, the Chebyshev spectral method [100] is selected in the modal analysis approach.

To discretize the computation domain, a differentiation matrix is defined based on a set of points

$$z_j = \cos\left(\frac{j\pi}{N}\right), j = 0, 1, \cdots, N, \tag{3.8}$$

which hold $1 = z_0 > z_1 > \cdots z_N = -1$. These points are known as Chebyshev points or Chebyshev-Gauss-Lobatto points. This matrix is the Chebyshev differentiation matrix $\mathbf{D}$. For $N \geq 1$, the Chebyshev differentiation matrix $\mathbf{D}$ has a size of $(N+1) \times (N+1)$. The entries of the matrix are given as

$$\begin{aligned} D_{00} &= \frac{2N^2+1}{6} \\ D_{jj} &= \frac{-z_j}{2(1-z_j^2)}, j = 1, \cdots, N-1, \\ D_{ij} &= \frac{c_i}{c_j}\frac{(-1)^{i+j}}{z_i - z_j}, i \neq j, i, j = 0, \cdots N, \\ D_{NN} &= -\frac{2N^2+1}{6}, \end{aligned} \tag{3.9}$$

where

$$c_i = \begin{cases} 2, & i = 0 \text{ or } N, \\ 1, & \text{otherwise.} \end{cases} \tag{3.10}$$

The corresponding differentiation matrix is given in figure 3.3. Following Trefethen [100], $D_{ii} = -\sum_{j=0, j\neq i}^{N} D_{ij}$ is applied to reduce the rounding errors.

The Chebyshev points are scaled so as to $(z_i)_{1\leq i\leq N+1}$, with $z_1 = 0$ and $z_{N+1} = 1$. To be noticed, the indices of $z$ is from 1 to $N+1$ after scaled. The number of Chebyshev points is $N+1$. Eq. (3.4) could be rewritten as a generalized eigenvalue problem $\mathbf{AX} = \frac{k}{\omega}\mathbf{BX}$. The size of matrix $\mathbf{A}$ and $\mathbf{B}$ is $(3N+3) \times (3N+3)$. $\mathbf{X}$ is a $(3N+3) \times 1$ column vector. The spatial differentiation of a vector is acquired by multiplying this vector with the differentiation matrix $\mathbf{D}$.

The next step is to implement the boundary condition in the discretized LEE. The variables at the boundaries should satisfy both the LEE and the boundary conditions. To avoid having an over-constrained system, some information must be discarded. The wavenumbers and mode shapes are obtained by solving the EVP with `eig` function of *MATLAB*. The matrices $\mathbf{A}$ and $\mathbf{B}$ of the discretized problem including boundary conditions are given in Appendix B.

$$
\mathbf{D} \;=\;
\begin{array}{|c|c|c|}
\hline
\dfrac{2N^2+1}{6} & 2\dfrac{(-1)^j}{1-z_j} & \dfrac{1}{2}(-1)^N \\
\hline
-\dfrac{1}{2}\dfrac{(-1)^i}{1-z_i} & \dfrac{(-1)^{i+j}}{z_i+z_j} \;\; \dfrac{-z_j}{2\left(1-z_j^2\right)} \;\; \dfrac{(-1)^{i+j}}{z_i-z_j} & \dfrac{1}{2}\dfrac{(-1)^{N+i}}{1+z_j} \\
\hline
-\dfrac{1}{2}(-1)^N & -2\dfrac{(-1)^{N+j}}{1+z_j} & -\dfrac{2N^2+1}{6} \\
\hline
\end{array}
$$

Figure 3.3: A sketch of Chebyshev differentiation matrix.

## 3.3 Test cases with a uniform flow

The aim of this section is to validate the use of the modal analysis approach to obtain mode solutions. For this, an analytical and a semi-analytical method for two cases—without a mean flow and with a uniform flow, are available. Acoustic propagation is investigated for two different scenarios, i.e., a rigid duct and a lined duct. The wavenumbers and mode shapes are compared between the two approaches. One should notice that a flow profile can be imposed in the modal analysis approach.

### 3.3.1 Rigid duct

When acoustic waves propagate along a rigid duct with a uniform mean flow, the wavenumbers and mode shapes can be obtained analytically from the convected Helmholtz equation

$$\left(\mathrm{i}\omega + M\frac{\partial}{\partial x}\right)^2 p - \frac{\partial^2 p}{\partial x^2} - \frac{\partial^2 p}{\partial z^2} = 0. \tag{3.11}$$

The wavenumber along the $x$-direction is

$$k = \frac{-M\omega \pm \sqrt{M^2\omega^2 - \left(1-M^2\right)\left[(n\pi)^2 - \omega^2\right]}}{1-M^2}, \tag{3.12}$$

where $n$ is a non-negative integer. The acoustic propagation without a mean flow and with a uniform mean flow $M = 0.3$ at $\omega = 0.9271$ along a rigid duct is analyzed. The parameter $N$ in Chebyshev matrix is set to $N = 150$ through the study if no declaration is made. Actually, $N = 150$ is far more enough to ensure converged results. A detailed study of the effect of Chebyshev points on the obtained wavenumbers and mode shapes is shown in section 3.4.2. The wavenumbers along the $x$-direction obtained through both methods are compared in figure 3.4. It shows a good agreement between the results obtained through both methods with or without a uniform mean flow. The wavenumbers near $k = 3.09 + 0\mathrm{i}$ in the complex $k$-plane only obtained with the modal analysis approach are a series of solutions corresponding to the dispersion relation $\omega - u_0 k = 0$.

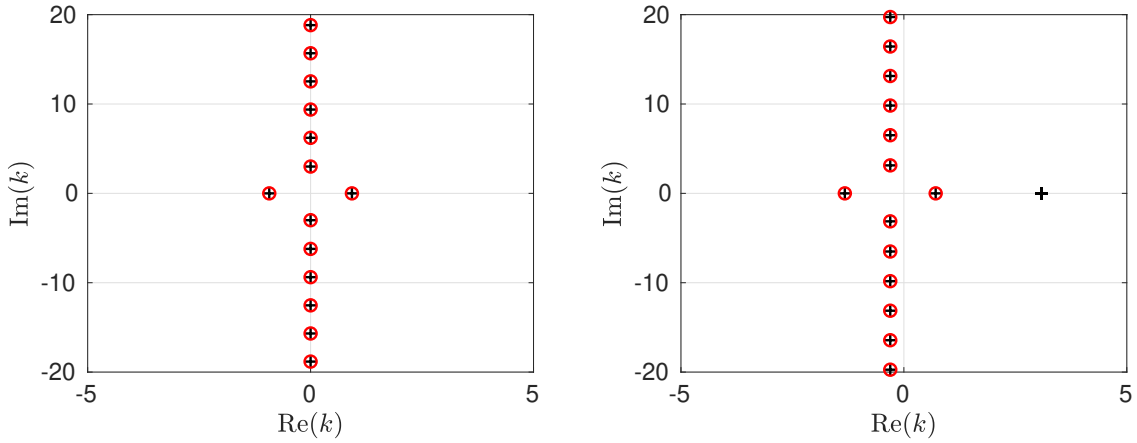


Figure 3.4: Mode wavenumbers of acoustic propagation along the rigid duct for $M = 0$ (left) and $M = 0.3$ (right). ○ analytical solution and + modal analysis approach.

### 3.3.2 Lined duct

In this part, the modal analysis approach for calculating the modes along a lined duct without and with a uniform mean flow is validated by comparing with a semi-analytical solution.

The semi-analytical method, which is used to obtain the axial wavenumbers in the lined section, as introduced in section 2.2.1 is applied. The source and mean flow are similar as the rigid duct case. The MSD liner introduced in section 2.1.2 is installed on the upper wall. Its impedance at $\omega = 0.9271$ is $Z = 0.2 + 0.005\mathrm{i}$.

The wavenumbers obtained by using these two approaches are shown in figure 3.5. Good matches between the two methods can also be noticed without and with a uniform mean flow. For the uniform flow, a mode with wavenumber around $k = 4.704 + 2.958\mathrm{i}$ is only obtained through the modal analysis approach. This mode corresponds to Ingard-Myers instabilities. As discussed in chapter 2, it is not calculated using the semi-analytical method for determining modes from the dispersion relation. The modes with wavenumber around $k = 3.098 + 0\mathrm{i}$ are also due to solutions of $\omega - u_0 k = 0$. Even if the acoustic propagation is not plane any more because of acoustic liners, we still name the first downstream propagative mode as the "plane wave" mode.

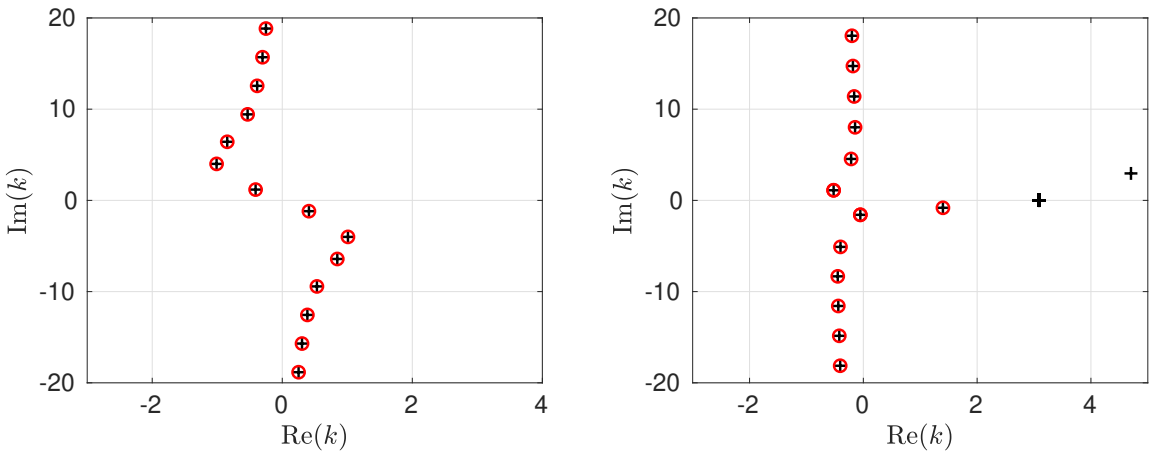


Figure 3.5: Mode wavenumebrs of acoustic propagation along the lined duct for $M = 0$ (left) and $M = 0.3$ (right). ○ semi-analytical solution and + modal analysis approach.

The mode shapes $|U|$, $|V|$ and $|P|$ of the "plane wave" mode for the two scenarios are displayed in figure 3.6. $|U|$, $|V|$ and $|P|$ are normalized by the maximum of $|P|$. The mode shapes do not resemble a "plane" anymore due to the lined wall. The maximum of $|P|$ and $|U|$ are obtained on the rigid wall for $M = 0$ and on the lined wall for $M = 0.3$. However the maximum of $|V|$ for the "plane wave" mode is found on the lined wall no matter whether the mean flow is imposed. The agreement for the two scenarios between the two approaches is excellent. The mode shapes referring to Ingard-Myers instability, are also displayed in figure 3.7. The amplitude of the mode shapes grows rapidly from the rigid wall to the lined wall.

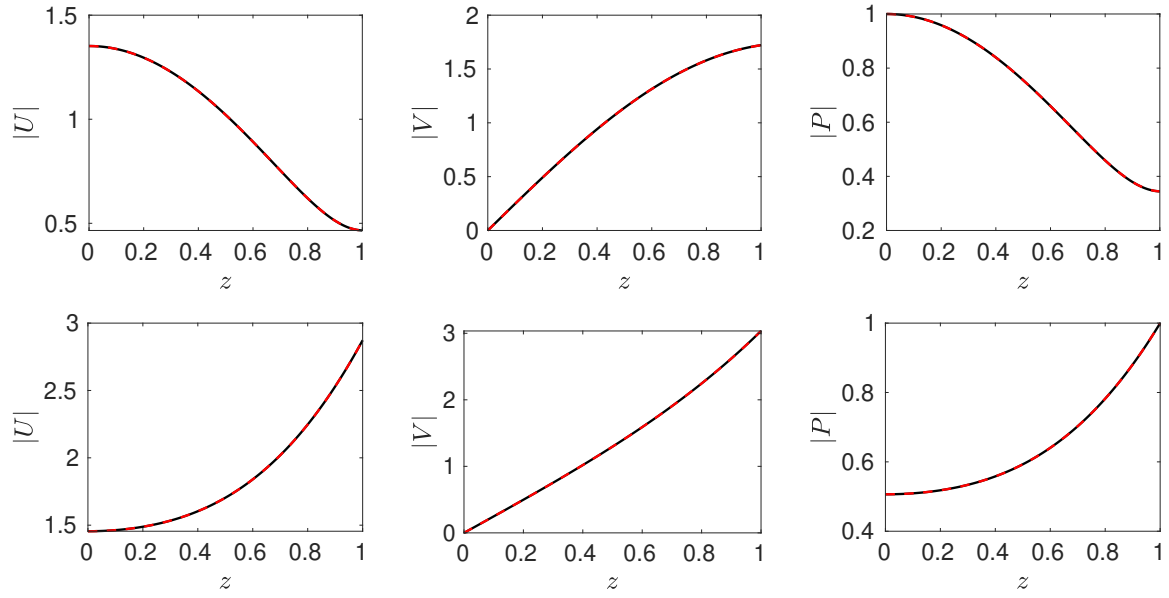


Figure 3.6: The shapes of the "plane wave" mode for the lined duct case without mean flow (upper) and with a uniform mean flow $M = 0.3$ (lower). Left, $|U|$; middle, $|V|$; right, $|P|$. - - - semi-analytical solution and ——— modal analysis approach.

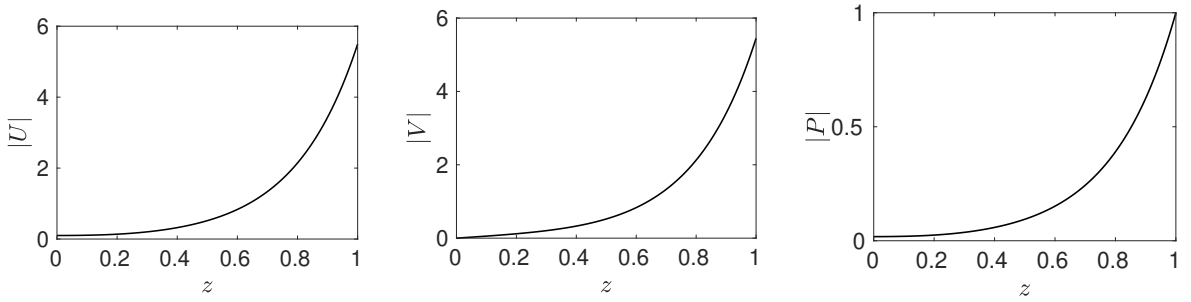


Figure 3.7: The shapes of the mode referring to Ingard-Myers instability. Left, $|U|$; middle, $|V|$; right, $|P|$.

## 3.4 Modal analysis with a shear flow

Since the modal analysis approach is validated sound propagation with a shear flow can thus be considered. The source and the liner used in this part are the same as used in section 3.3.2. The profile of the shear mean flow is illustrated in section 2.4.4. The default value of the boundary layer thickness is $\delta^* = 5$ % corresponding to $n_z = 9$.

### 3.4.1 Rigid duct case

Acoustic propagation in the rigid duct with the presence of a shear mean flow is analysed. The wavenumbers are given in figure 3.8 and the shapes of the "plane wave" mode are shown in figure 3.9. Changes are observed for higher-order modes compared to the case of a uniform flow (figure 3.4). The "plane wave" mode for the uniform and the shear flow is respectively situated at $k = 0.7132$ and $k = 0.71$. Figure 3.9 shows the significant effect of the shear mean flow on the shapes of the "plane wave" mode, especially, on $|V|$.

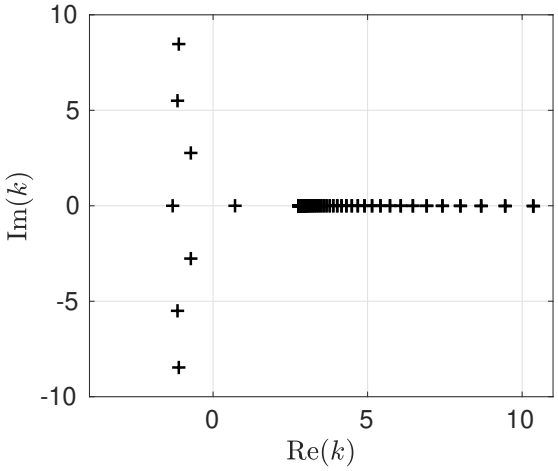


Figure 3.8: Mode wavenumbers of acoustic propagation with a shear mean flow.

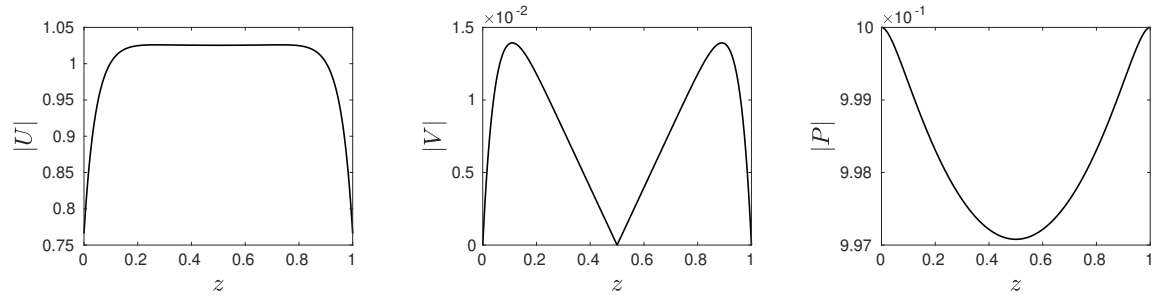


Figure 3.9: The shapes of the "plane wave" mode for a shear mean flow $M = 0.3$. Left, $|U|$; middle, $|V|$; right, $|P|$.

### 3.4.2 Lined duct case

Finally, acoustic propagation along a lined duct with a shear mean flow is considered. The wavenumbers obtained with $N = 150$ are shown in figure 3.10. The mode situated at $k = 1.336 - 0.850\text{i}$ is referring to the "plane wave" mode. It is slightly damped because of the acoustic liner. A branch of continuous modes is observed close to the real axis for $\text{Re}(k) > 2.78$. As mentioned before, the modes with wavenumber $k_0^*$ are such that $\omega - k_0^* u_0(z^*) = 0$. The number of these modes is $N + 1$. These modes only appear with a mean flow. The phase velocity of this mode equals to its mean flow velocity on the position $z = z^*$. The mode ($k = 6.783 + 1.97\text{i}$) in the right upper quarter with a positive imaginary part is a possible unstable mode if it propagates downstream. A detailed analysis on the unstable mode and the instability will be given in the next chapter.

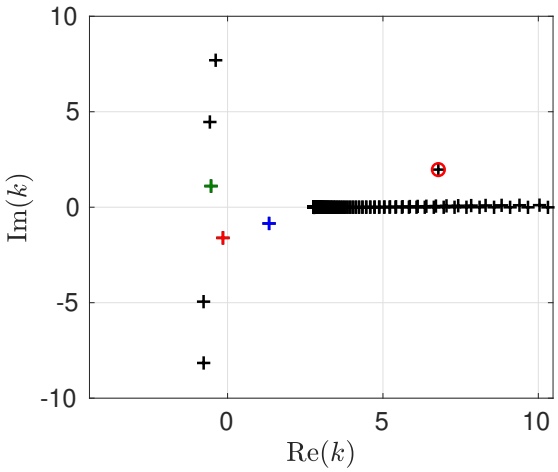


Figure 3.10: Mode wavenumbers of acoustic propagation with a shear mean flow. 1st evanescent downstream mode, +; 1st evanescent upstream mode, +; "plane wave" mode, +; unstable mode, ○.

A convergence study is performed to analyze the effect of the discretization on the mode wavenumbers and mode shapes. As shown in Table 3.1, the wavenumbers of the first evanescent downstream mode (1st down), the first evanescent upstream mode (1st up), the "plane wave" mode

(plane) and the possible unstable mode (unstable) are presented for an average Mach number $M = 0.3$ and for $N = 20,\ 60,\ 100$, and 150. It shows that acoustic modes can be obtained with less computation cost compared with the unstable mode. The convergence for both acoustic modes and unstable mode is obtained for $N = 150$.

Table 3.1: Wavenumbers obtained by using different values of $N$ in the Chebyshev matrix.

| | $N = 20$ | $N = 60$ | $N = 100$ | $N = 150$ |
|---|---|---|---|---|
| $1^{\text{st}}$ down | $-0.147 - 1.607\text{i}$ | $-0.147 - 1.607\text{i}$ | $-0.147 - 1.607\text{i}$ | $-0.147 - 1.607\text{i}$ |
| $1^{\text{st}}$ up | $-0.532 + 1.108\text{i}$ | $-0.532 + 1.108\text{i}$ | $-0.532 + 1.108\text{i}$ | $-0.532 + 1.108\text{i}$ |
| plane | $1.336 - 0.850\text{i}$ | $1.336 - 0.850\text{i}$ | $1.336 - 0.850\text{i}$ | $1.336 - 0.850\text{i}$ |
| unstable | $6.544 + 2.049\text{i}$ | $6.781 + 1.973\text{i}$ | $6.783 + 1.970\text{i}$ | $6.783 + 1.970\text{i}$ |

The corresponding mode shapes for different values of Chebyshev points $N$ are shown in figure 3.11. The results are converged for $N = 150$. It also shows the characteristics of the unstable mode may be predicted inaccurately with a relatively small $N$. For all modes, the magnitudes of $|U|$ are relatively larger than those of $|V|$ and $|P|$. The maximum of $|U|$ and $|V|$ are obtained in the vicinity of the lined wall. For $|P|$, its maximum value is located on the rigid wall for the first evanescent modes. For the "plane wave" mode and unstable mode, the peak of $|P|$ is located on the lined wall. It is noted that the mode shapes of the possible unstable mode has a sharp increase from the rigid wall to the lined wall, which indicates the existence of instabilities.

### 3.4.3 Effect of the boundary layer thickness

The effect of mean flow profiles on the wavenumbers and mode shapes are examined for the rigid duct case and the lined duct case. The boundary layer thickness $\delta^*$ is respectively 0.5 %, 2 % and 5 % with average Mach number $M = 0.3$. The results for a uniform flow are also attached for comparison.

#### Rigid duct case

Table 3.2 shows that the effect of boundary layer thickness on the cut-off frequency $\omega_n$ for the $n$-th mode on the $x$-direction. With the increase of the boundary layer thickness $\delta^*$, the cut-off frequency for the $n$-th mode $(n \geq 2)$ gradually decreases. The ratios between the cut-off frequency for the shear mean flow and the uniform flow are also indicated. For the same boundary layer thickness $\delta^*$, the ratio becomes close to 1 when higher-order modes are considered. It indicates that the cut-off frequency is less affected by the mean flow profile for higher order modes.

The effect of mean flow profiles on the wavenumbers and mode shapes are respectively shown in figures 3.12 and 3.13. Concerning the wavenumbers, the downstream and upstream "plane wave" modes are not sensitive to flow profiles, while higher order evanescent modes are more affected by flow profiles. The higher evanescent modes tend to be left-shifted and their damping rates ($\text{Im}(k)$) is decreasing with the increase of the boundary layer thickness $\delta^*$.

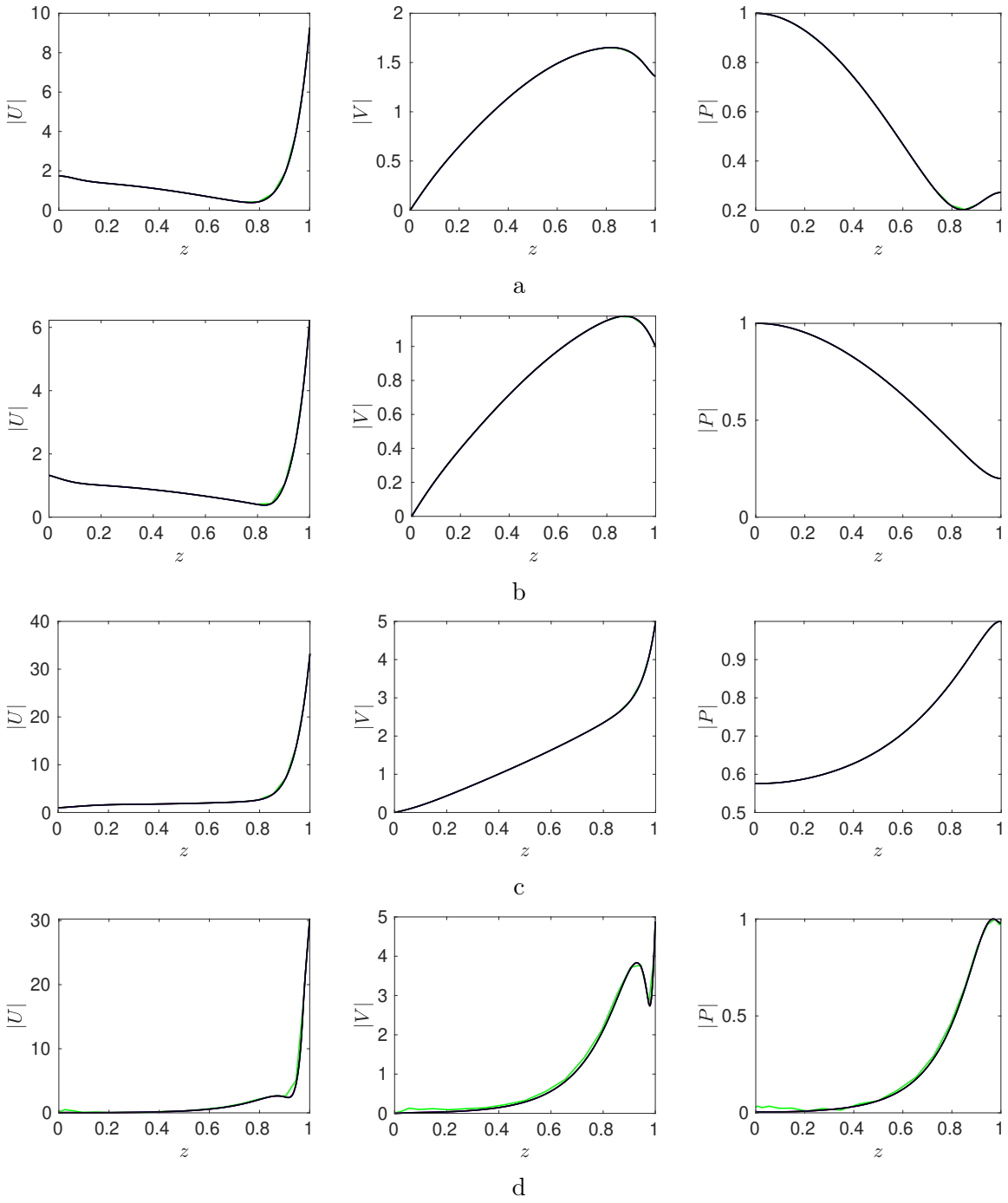


Figure 3.11: The mode shapes obtained for different values of $N$ in Chebyshev matrix for a, the 1st evanescent downstream mode; b, the 1st evanescent upstream mode; c, "plane wave" mode and d, the unstable mode. Left, $|U|$; middle, $|V|$; right, $|P|$. : $N = 20$; : $N = 60$; : $N = 100$; : $N = 150$.

The mode shapes $|U|$, $|V|$ and $|P|$ are studied for the first downstream evanescent mode, the upstream and downstream "plane wave" mode. The mode shapes of the upstream and downstream "plane wave" mode are strongly affected comparing with the evanescent mode, even if their mode wavenumbers have hardly changed. For $\delta^* = 0.5$ %, the results are close to the uniform flow case.

Table 3.2: Cut-off frequency $\omega_n$ for the $n$-th mode on the $x$-direction for several value of $\delta^*$.

The percentage in blue shows the ratio between the cut-off frequency $\omega_n$ for a shear flow and a uniform flow.

| | $n = 2$ | $n = 3$ | $n = 4$ |
|---|---|---|---|
| the uniform flow | 2.9992 | 5.9946 | 8.9910 |
| $\delta^* = 0.5$ % | 2.9945 (99.84 %) | 5.9891 (99.91 %) | 8.9836 (99.92 %) |
| $\delta^* = 2$ % | 2.9871 (99.60 %) | 5.9752 (99.68 %) | 8.9642 (99.70 %) |
| $\delta^* = 8$ % | 2.9556 (98.55 %) | 5.9427 (99.13 %) | 8.9456 (99.51 %) |

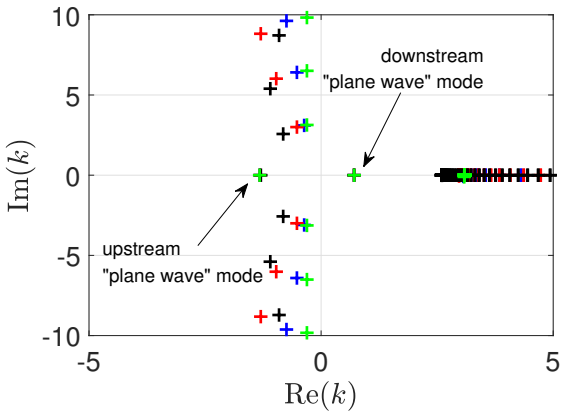


Figure 3.12: Mode wavenumbers of acoustic propagation along a rigid duct and for several values of the boundary layer thickness. +: uniform flow; +: $\delta^* = 0.5$ %; +: $\delta^* = 2$ %; +: $\delta^* = 5$ %.

### Lined duct case

The effect of flow profiles on the wavenumbers for the lined duct case is presented in figure 3.14. For the "plane wave" mode, the first evanescent downstream and upstream mode, they do not have obvious variation when the boundary layer thickness changes. The unstable mode is more sensitive to flow profiles. With the increase of the boundary layer thickness, the wavelength of the unstable mode decreases gradually. The imaginary part of this mode, which represents the spatial growth rate of this mode if it propagates downstream, shows a decreasing trend when the boundary layer thickness of the mean flow becomes thicker..

Figure 3.15 shows the corresponding mode shapes for the 1$^{st}$ evanescent downstream mode, the 1$^{st}$ evanescent upstream mode, the "plane wave" mode and the unstable mode for different values of boundary layer thickness. $|U|$ and $|V|$ near the lined wall are affected greatly by the boundary layer thickness. Especially for $|U|$, a thin boundary layer will lead to a rapid increase of amplitude $|U|$ close to the lined wall. The effect of boundary layer thickness $\delta^*$ on $|P|$ is noticeable only for the"plane wave" mode and the unstable mode. The results obtained with a uniform flow and with a shear flow $\delta^* = 0.5$ % are quite close, except on the lined wall, where great discrepancies are observed. It can be explained by the different boundary conditions applied on the lined wall.

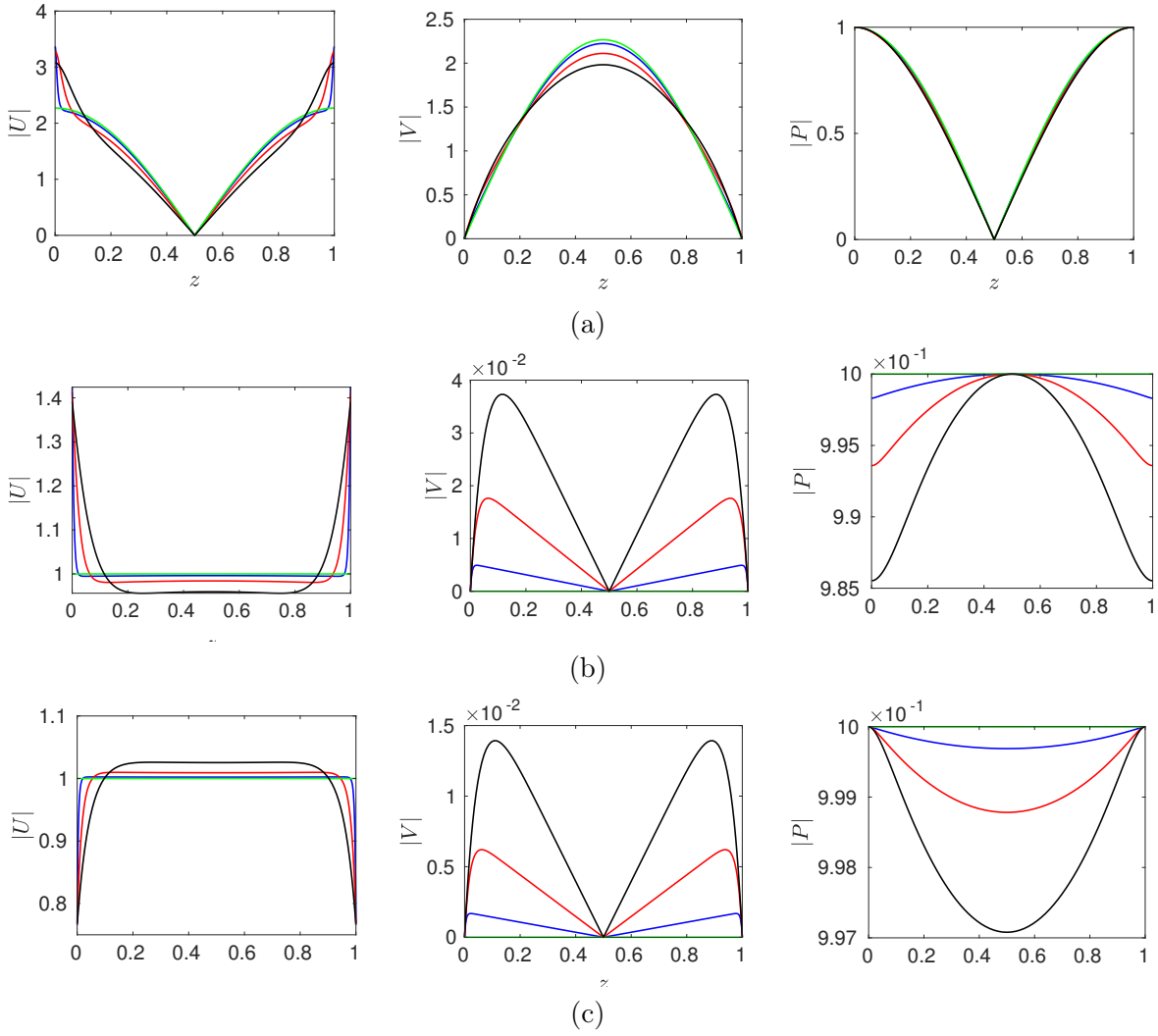


Figure 3.13: Mode shapes for acoustic propagation along a rigid duct for several values of $\delta^*$. (a), 1st evanescent downstream mode; (b), upstream "plane wave" mode; (c), downstream "plane wave" mode. Left, $|U|$; middle, $|V|$; right, $|P|$. — : uniform flow; — : $\delta^* = 0.5$ %; — : $\delta^* = 2$ %; — : $\delta^* = 5$ %.

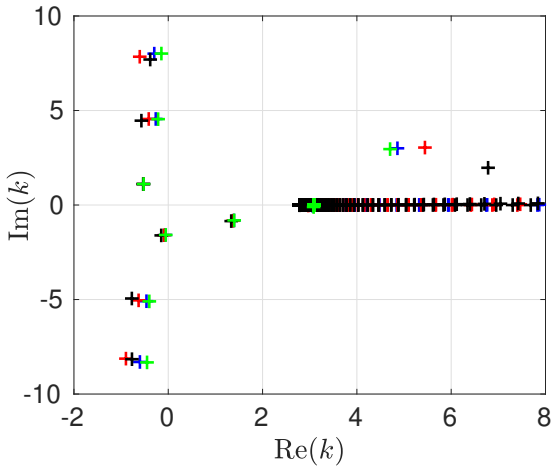


Figure 3.14: Mode wavenumbers of acoustic propagation along a lined duct and for several values of boundary layer thickness. +: the uniform flow; +: $\delta^* = 0.5$ %; +: $\delta^* = 2$ %; +: $\delta^* = 5$ %.

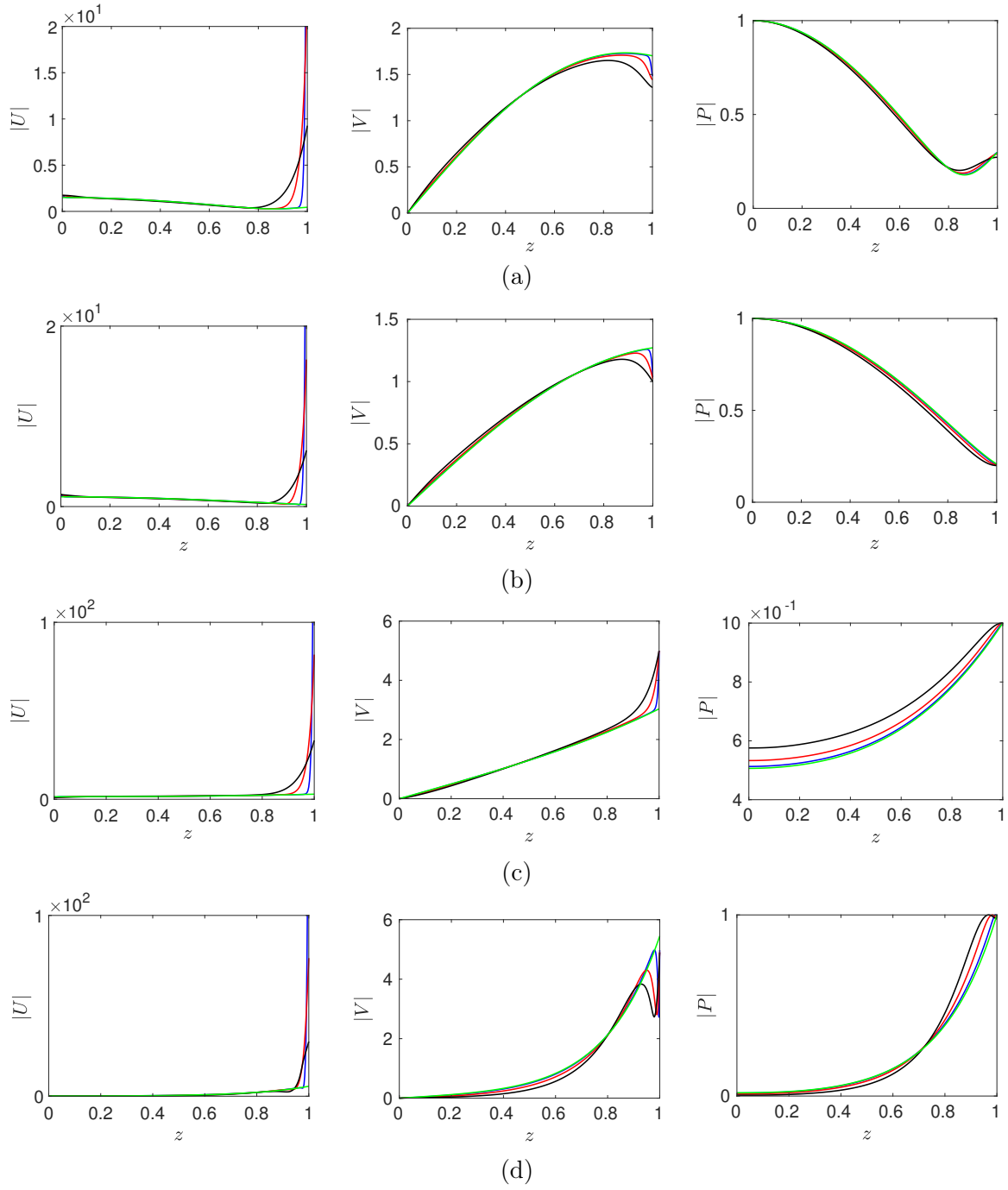


Figure 3.15: Mode shapes for acoustic propagation along a lined duct for several values of $\delta^*$. (a), 1st evanescent downstream mode; (b),1st evanescent upstream mode; (c), "plane wave" mode and (d), unstable mode. Left, $|U|$; middle, $|V|$; right, $|P|$. — : uniform mean flow; — :$\delta^* = 0.5\%$; — : $\delta^* = 2\%$; — : $\delta^* = 5\%$.

## 3.5 Conclusion

A modal analysis approach has been introduced to interpret the acoustic propagation with the behaviour of modes with the presence of a mean flow. Firstly, the method was presented. A generalized EVP problem was formulated and was solved by using the Chebyshev spectral method. To validate the modal analysis method, the acoustic propagation was compared between the modal analysis approach and the analytical/semi-analytical method for the rigid duct and the lined duct with or without a uniform mean flow. The results of wavenumbers and mode shapes showed a good agreement between these two approaches.

Then acoustic propagation with a shear flow has been investigated for a rigid duct and a lined duct. The wavenumbers and mode shapes were illustrated. The effect of boundary layer thickness on the cut-off frequencies for the rigid duct was examined. The results showed that for the same average Mach number, the cut-off frequencies were decreasing with the increase of the boundary layer thickness. The effect of the boundary layer thickness on the wavenumbers and mode shapes were also investigated.

As discussed in chapter 2, instabilities can be seen in numerical simulations of acoustic propagation in a lined duct with a mean flow. In this chapter, the modal analysis approach is provided to describe the acoustic propagation with mode solutions. A detailed study of the instabilities will be carried out in chapter 4 by using the modal analysis approach and the time-domain method.

# 4 Characterization of the instability

As shown in the previous chapter, instabilities are observed during the acoustic propagation along a lined flow duct, and are caused by the complex interactions of acoustic waves with mean flow and liners. These instabilities have attracted many interests in recent decades.

The presence of instabilities over acoustic liners was first revealed experimentally through the transmission coefficient [6, 7, 8, 9]. The transmission coefficient became larger than 1 around the liner resonance at sufficiently high Mach numbers, implying an increase of acoustic energy.

Meyer *et al.* [6] experimentally investigated the influence of turbulent flows with different bulk velocities on sound attenuation along a rectangular duct lined with porous materials, a damped Helmholtz resonator and an undamped Helmholtz resonator. A decrease in sound absorption was observed with the increase of flow velocity. A negative attenuation with an exponentially increasing amplitude was found in the experiment for an undamped Helmholtz resonator. Brandes *et al.* [7] investigated reflection and transmission coefficients of a radial $\lambda/4$-resonators. They noticed that the strong amplification in the downstream direction for frequencies close to the resonance frequency of the liner was related to a strong coupling between an acoustic and a hydrodynamic mode. They found the amplified wave in the lined duct propagated at a speed in the order of the flow velocity, but the nature of the amplified wave was not clear. Aurégan *et al.* [8] performed an experimental study on acoustic propagation with a grazing flow along a rectangular duct lined with a ceramic liner. They showed that the transmission coefficient could be larger than 1 at Mach number 0.3. Moreover, the static pressure drop was greatly affected by the acoustic waves. They attributed all these phenomena to the existence of hydrodynamic instabilities.

By applying optical flow measurements[94, 101, 18], full spatial characterization of hydrodynamic instabilities was obtained, with its convective nature reveal. The study of Marx *et al.* [101] is the first to characterize the instability over a locally reacting liner. The wavelength, convection speed and growth rate of the instability were given. Alomar *et al.* [18] performed a study on a porous liner. They found the hydrodynamic instability wave travelled at half the mean flow velocity. It was also indicated that the inhomogeneities of the wall-normal velocity field and the detachment of the vorticity core were not observed in the case of a locally reacting liner [101]. They suggested the existence of flow inside porous materials.

Motivated by the experimental observation of instabilities, analytical and numerical researches

have been performed. The use of the Ingard-Myers boundary condition [102, 103], which describes how acoustic perturbations interact with an impedance wall for a vanishingly-thin inviscid boundary layer, was an usual approach in the early stage on this subject. By doing so, instabilities were reported in many studies [104, 27, 34, 63, 105, 79].

Tester [104] theoretically studied the acoustic propagation in a lined duct with a uniform mean flow. A spatially amplified mode was found, which could be attributed to convective instabilities. Tam and Auriault [27] also noticed instabilities in their study. They pointed out that the instabilities were of Kelvin-Helmholtz kind. They thought the instabilities are caused by the postulate of a vortex sheet discontinuities next to the impedance in the Ingard-Myers boundary condition. They argued that this instabilities would not be present if an impedance boundary condition could include the effect of mean flow instead of considering kinetic effect of a vortex sheet in Ingard-Myers boundary condition.

Özyörük *et al.* [34] found that when applying Myers boundary condition with a plug flow, simulations suffered from instability issues. Rienstra [63] investigated the ducts modes in a cylindrical duct and found the existence of the acoustic surface modes and hydrodynamic surface modes, which propagated close to the surface of the duct wall. He found that one of the modes corresponding to an instability by applying the Crighton-Leppington criterion. However the Crighton-Leppington criterion was proved to be flawed by Brambley, as shown in the example 1 in [31]. Instead, the Briggs-Bers criterion [106, 107] was suggested to be applied.

However, some studies have even questioned the validity of the Ingard-Myers boundary condition, since the assumption of a uniform flow is not realistic. Aurégan *et al.* [108] analysed sound propagation in a 2D duct lined with a ceramic liner and a SDOF liner by using a multimodal method. They first assumed the flow was uniform. Then the transmission and reflection coefficients were compared between from the experiments and numerical simulations. The hypothesis of a uniform flow used in the numerical simulation was questioned due to the large discrepancies observed.

Brambley [31] showed that part of the instabilities lay in the ill-posedness of the mathematical model since the system supported an arbitrarily quick exponential growth at arbitrarily short wavelength. Later Myers boundary condition was modified to consider the effect of a thin boundary layer to regularize the problem [109].

Besides applying modified Myers boundary condition in the time domain simulation, considering a finite boundary layer thickness has been explored to improve the modelling of instabilities [28, 110, 97, 111, 29, 112]. A detailed numerical analysis with a MSD liner showed that the unstable mode transformed from an absolute one to a convective one [113] by using a impedance boundary condition with a mean velocity profile instead of the Ingard-Myers condition. However, even if with a full velocity profile, absolute instabilities seem to be present in time-domain simulations for liners with a more realistic broadband impedance [114].

The purposes of this chapter are to answer the questions if the instability in the time domain is physical or numerical and whether we can have a precise prediction of the instability or not.

Actually it is an extension of the study of Marx [29]. Attention should be paid that neither the Myers boundary condition nor the modified Myers boundary condition is used. Since the modal analysis is a general approach to conduct stability analysis, it is used as a reference for comparison. The results concerning the characterization of the instability are compared between modal analysis and time-domain results. The effects of selective filtering and mesh size on instabilities are studied. Finally, a parametric study is conducted to investigate the effect of source frequency, mean flow and acoustic liners on instabilities.

## 4.1 Existence of an instability in the time-domain simulation

When acoustic waves propagate with the presence of a shear flow along a lined duct, time-domain simulations are sensitive to instabilities. To exemplify the instability generated in the time domain simulation, two examples based on the test case in section 2.4 are illustrated. A SDOF liner and a CT57 liner are considered. The impedances of the SDOF liner and the CT57 liner are shown in figure 2.6 and 2.12. The mean flow Mach number is $M = 0.335$. In figure 4.1, acoustic responses to an impulsive source are shown for the SDOF liner and the CT57 liner. The pressures are recorded by a microphone installed at $x = 0.28$ m on the lined wall. Figure 4.1 presents the received pressure for these two cases. The pressure consists of two wave packets. One is the response to the acoustic impulse and the other is related to the instability. After the acoustic impulse propagates away, the instability generates and increases rapidly. The amplitude of the instability is larger than the acoustic part. The frequency of the instability for the SDOF liner is close to the resonance of the SDOF liner, 2 kHz. When the liner is replaced by the CT57 liner, the same phenomenon is also observed as mentioned before. The ceramic liner has several resonance frequencies. However, the frequency of the instability is around 1 kHz.

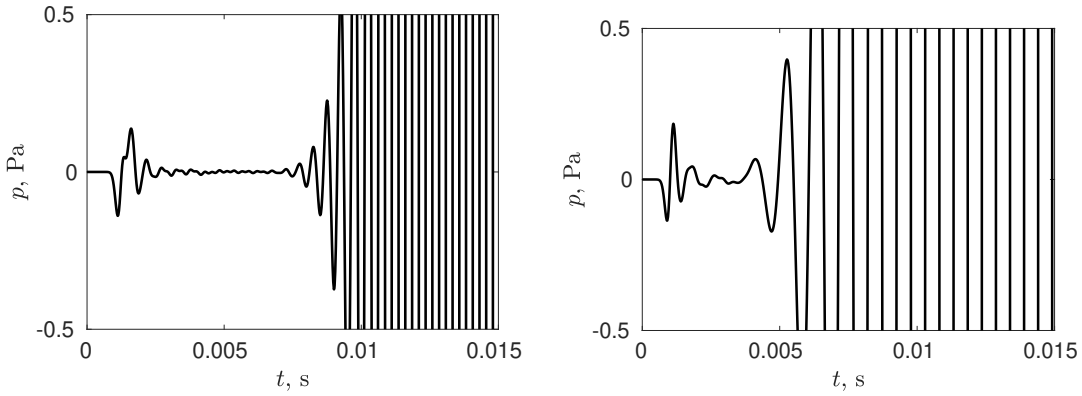


Figure 4.1: Acoustic propagation along a lined duct with a shear flow for a SDOF liner (left) and a CT57 liner (right).

To study the hydrodynamic instabilities in the flow duct, a two-dimensional lined duct, of size $H \times L$, is considered, as shown in figure 4.2. The acoustic liner is installed on the upper wall, while the lower wall is rigid. A point source is fixed in the center of the duct. The source is impulsive,

unless stated otherwise. A parallel shear flow of velocity profile $u_0$ goes from left to right, and vanishes on the walls. Nondimensional parameters are used and the nondimensionalization refers to section 3.1.

Since the occurrence of hydrodynamic instabilities depends on the characteristics of the liner, the mean flow profile and the source frequency, four cases corresponding to the existence of the hydrodynamic instabilities are proposed. Their pressure responses to the impulsive source are analysed.

For the time-domain approach, the source term $Q$ is chosen as

$$Q\left(x,z,t\right)=\lambda(t)\exp\left(-\frac{x^2+\left(z-0.5\right)^2}{B_s^2}\ln 2\right), \tag{4.1}$$

where $B_s$ is the Gaussian half-width of the source, with a value of 0.104. Both impulsive and harmonic sources are used in this study. For impulsive sources, $\lambda(t)$ is defined as:

$$\lambda(t)=\frac{t-t_s}{t_c}\exp\left(-\frac{\left(t-t_s\right)^2}{t_c^2}\ln 2\right)H(t) \tag{4.2}$$

where $t_s = 5.42$ is a time shift, $t_c$ specifies the frequency content of the source signal and has been set to $t_c = 0.95$ in order to excite only frequencies below the duct cut-off frequency. Finally, $H(t)$ is the Heaviside function. In the case of a harmonic source $\lambda(t)$ is defined as:

$$\lambda(t)=\exp\left(\mathrm{i}\omega t\right)H(t) \tag{4.3}$$

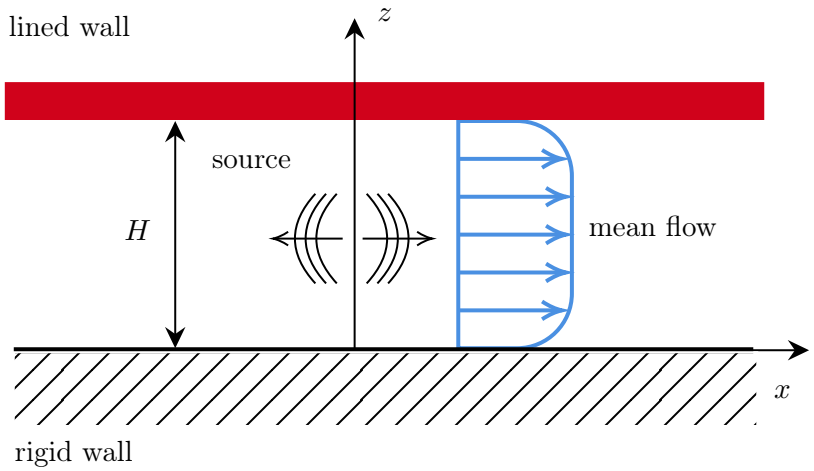


Figure 4.2: Time-domain simulation model

### 4.1.1 Case 0

In case 0, the ceramic tubular liner CT57 used in the NASA GIT experiment[20], is installed on the lined wall. The impedance of the CT57 liner varying with $\omega$ is shown in figure 4.3. Acoustic

propagation with no mean flow is studied.

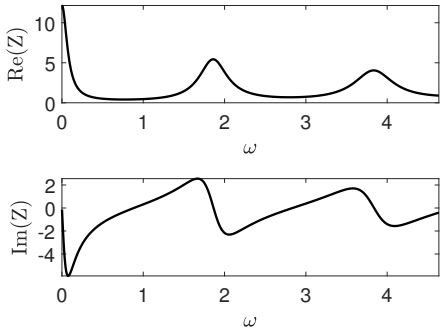


Figure 4.3: The impedance of the CT57 varying with $\omega$.

Figure 4.4 shows the snapshots of acoustic propagation along the duct for case 0. The sound is generated by an impulsive source. Acoustic waves attenuate along the lined wall during their propagation. It is shown that when the CT57 liner is applied without a mean flow, no instability is observed along the lined wall.

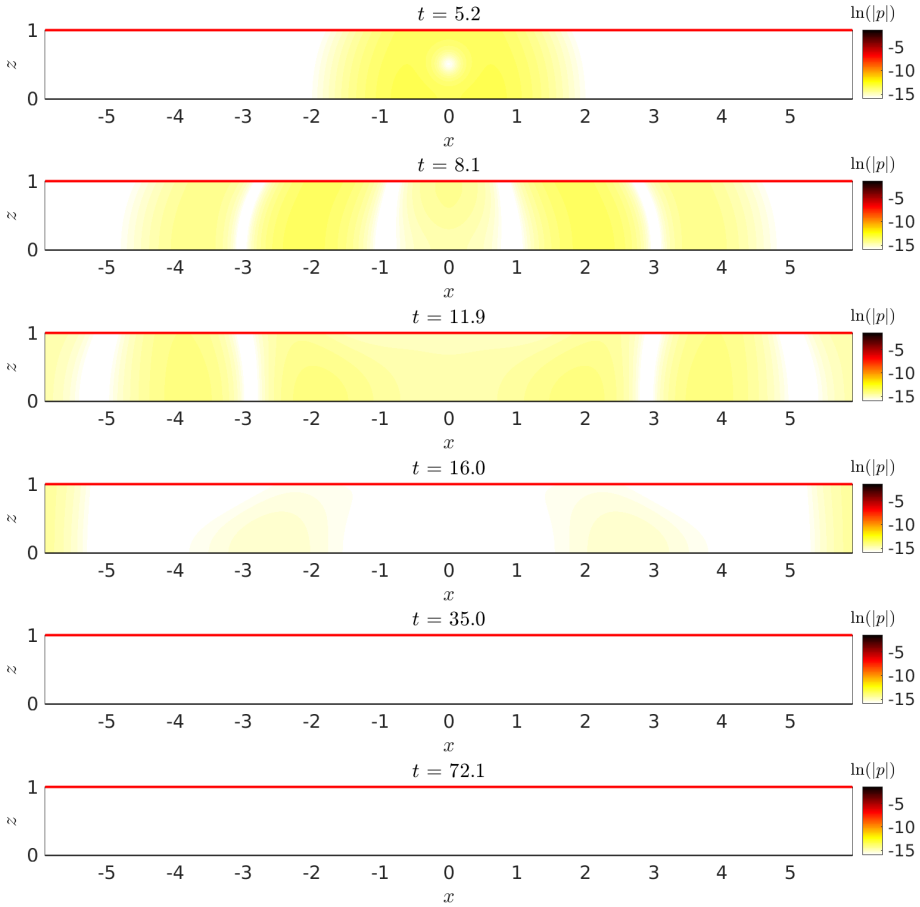


Figure 4.4: Snapshots of pressure response $\ln|p(x,t)|$ to an impulsive source for case 0.

In order to better show the phenomenon of sound propagation on the lined surface, figure 4.5 shows that the pressure response along the $x$-direction on the lined wall varying with time for

case 0. The position of the source on the $x$-axis is marked by the red dash line. Two branches originating from $t = t_s$ are observed, corresponding to upstream and downstream propagating waves. Without a mean flow, the two branches are symmetric. These acoustic waves are attenuated along the lined wall. After $t \approx 25$, they have left the computational domain and the remaining fluctuating pressure is almost null. It indicates that no instability is generated during the propagation of acoustic waves.

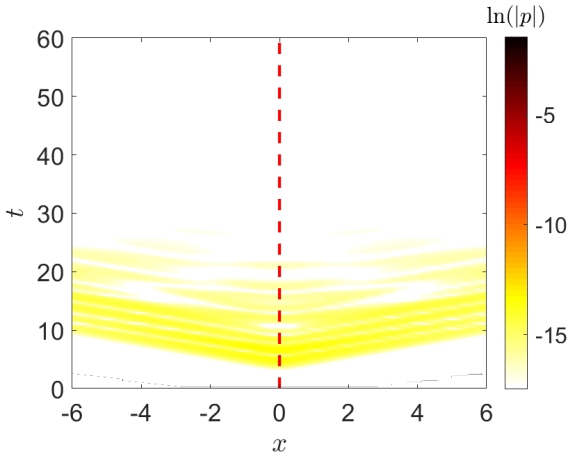


Figure 4.5: Pressure response $\ln |p\,(x, z = 1, t)\,|$ to an impulsive source on the lined wall for case 0. The source position is indicated by the vertical dashed line.

### 4.1.2 Case 1

In case 1, a mass-spring-damper liner is used. The corresponding parameter of the MSD liner is $R = 0.2$, $m = 5.4 \times 10^{-3}$ and $K = 0$. The left figure of figure 4.6 shows the impedance varying with $\omega$. The Mach number of the mean flow is $M = 0.1$, and the thickness of the boundary layer is $\delta^* = 5\%$. The profile of the mean flow is shown in the right figure.

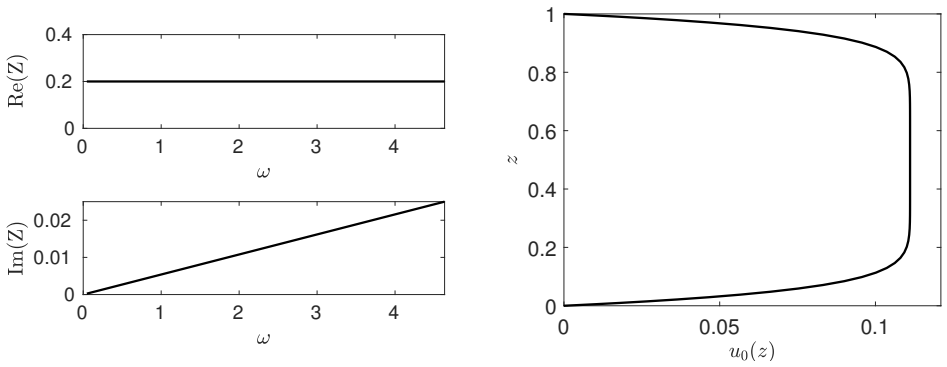


Figure 4.6: Liner and mean flow used in the case 1. Left, impedance of the MSD liner and right, the mean flow profile.

The acoustic propagation along the lined duct is shown in figure 4.7. The acoustic waves are observed to be attenuated along the lined wall. No hydrodynamic instability is generated even if a mean flow is imposed. After the acoustic waves convect away the duct, the pressure in the

domain is null. The pressure response on the lined wall for case 1 is also shown in figure 4.8. The similar branches related with acoustic propagation are also retrieved. To conclude, instabilities are not generated with the presence of a weak mean flow along a duct lined with the MSD liner.

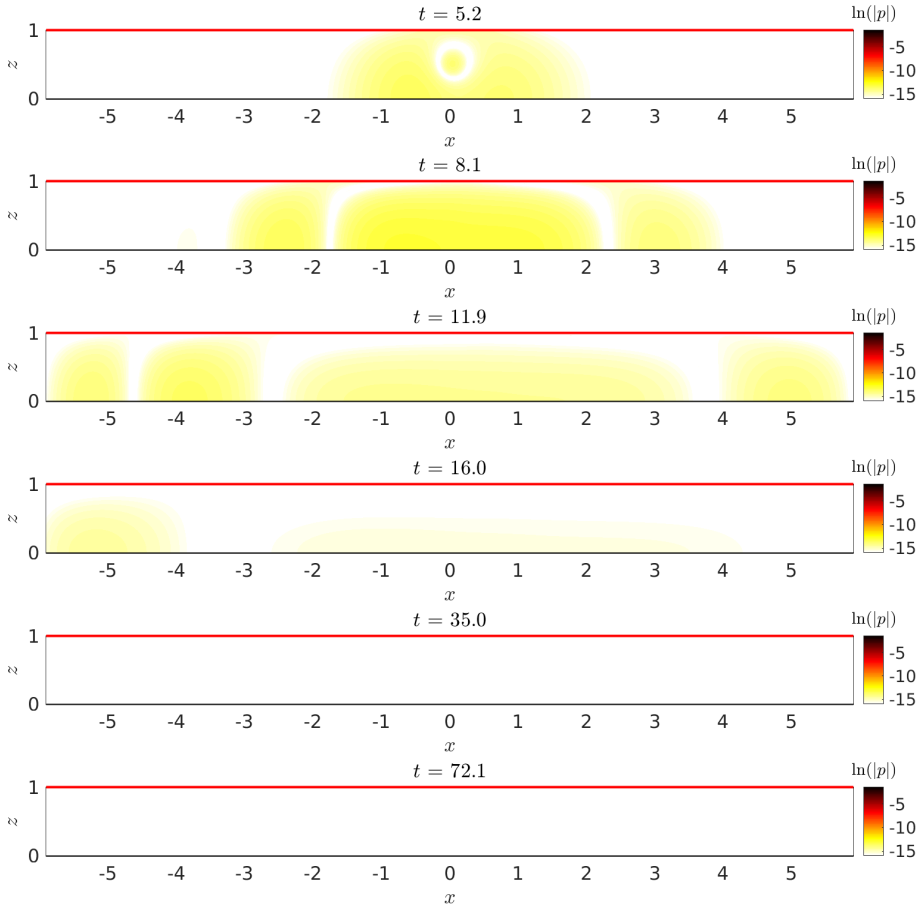


Figure 4.7: Snapshots of pressure response $\ln|p(x,\, t)|$ to an impulsive source for case 1.

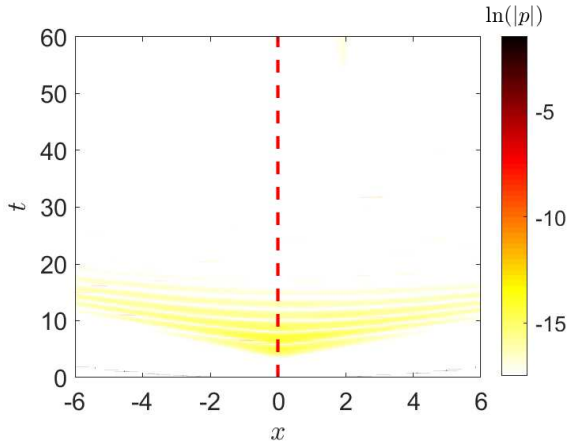


Figure 4.8: Pressure response $\ln|p(x,\, z=1,\, t)|$ to an impulsive source on the lined wall for case 1. The source position is indicated by the vertical dashed line.

### 4.1.3 Case 2

The MSD liner is still used in case 2. The mean flow Mach number for case 2 is $M = 0.3$, which is larger than case 1. The thickness of the boundary layer is $\delta^* = 5\%$. The flow profile is shown in figure 4.9.

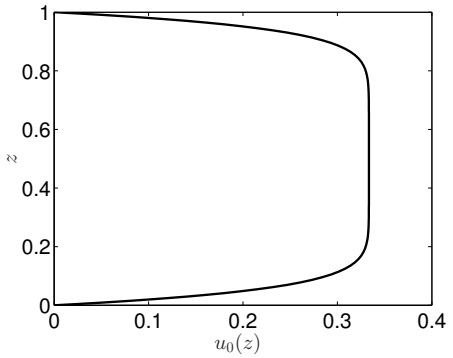


Figure 4.9: The mean flow profile in case 2.

Figure 4.10 shows that instabilities are generated along the lined wall during acoustic propagation. The velocity of instabilities is smaller than the acoustic waves. For example, instabilities start to generate after sound waves already leave the duct at $t = 16$. After acoustic waves propagate away, the amplitude of instabilities amplifies during its movement, as illustrated at $20 \leq t \leq 60$. At $t = 90$, spurious waves with small wavelengths start to be generated in the entire computational domain.

Figure 4.11 shows pressure response $\ln |p\,(x,\, t)\,|$ on the lined wall for case 2. There are two kinds of components in the figure. The first one is acoustic waves, which exist for $t \leq 20$. Another kind of pattern is however observed in the downstream direction for $10 \leq t \leq 60$. Its magnitude and its spatial content increase as it propagates away from the source, indicating it is an instability. Moreover, since the pressure response is given as a function of the distance and time variation, the velocity of acoustic waves and instabilities can be deduced from the slopes of the different branches. It can then be estimated that the propagation velocity of the instability is smaller than that of the acoustic waves. To conclude, acoustic waves are generated during the acoustic propagation along the duct lined with the MSD liner, when a strong mean flow is imposed.

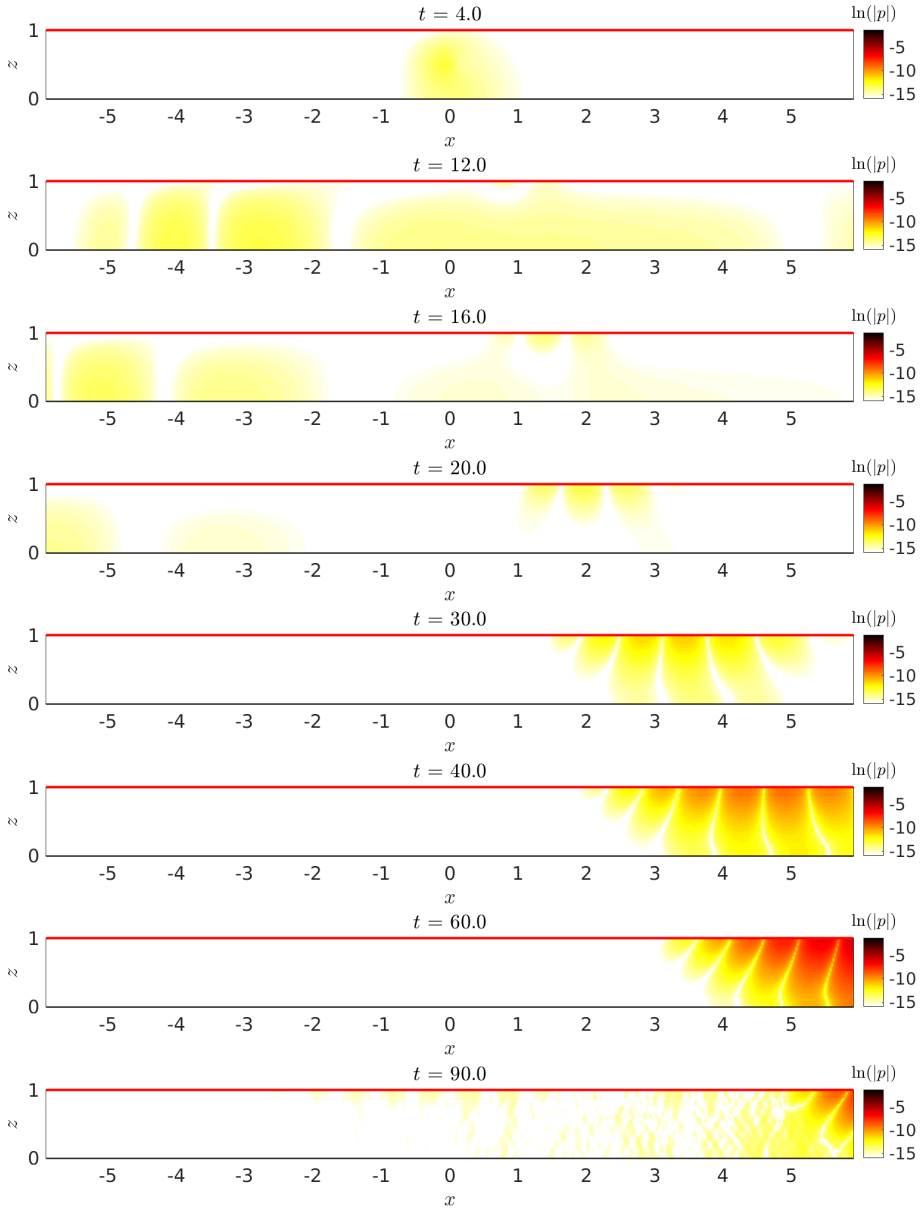


Figure 4.10: Snapshots of pressure response $\ln|p(x,\,t)|$ to an impulsive source for case 2.

### 4.1.4 Case 3

In case 3, the liner used is the same as in case 0. The Mach number is $M = 0.335$ and the boundary layer thickness of the flow profile is $\delta^* = 2\%$ as shown in figure 4.12. This case is inspired by the NASA GIT benchmark problem [20], since instabilities have been reported in a lot of numerical studies based on this test case [79, 33, 114]. Li [79] solved the linearized Euler equation in the time domain. He postulated the nature of the instability generated in solving LEE in the time domain is of Tollmien-Schlichting kind. He thought the spatial growth rate of the instability was a linear one. Burak *et al.* [33] also observed the instability at 1 kHz with adopting a large eddy simulation and a linearized Navier-Stokes solver. Therefore, case 3 is devoted to analysing the instabilities mentioned in the study of NASA GIT experiment.

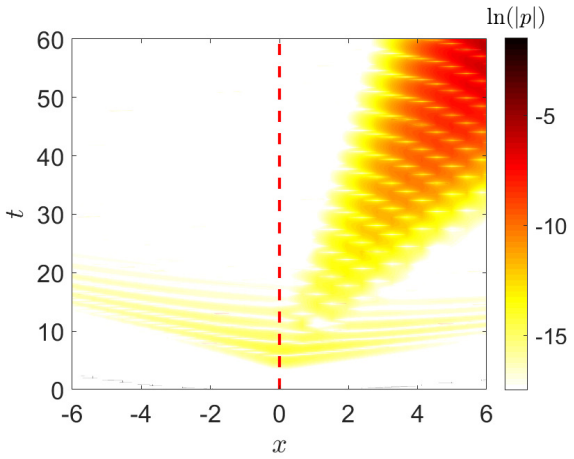


Figure 4.11: Pressure response $\ln|p(x, z = 1, t)|$ to an impulsive source on the lined wall for case 2. The source position is indicated by the vertical dashed line.

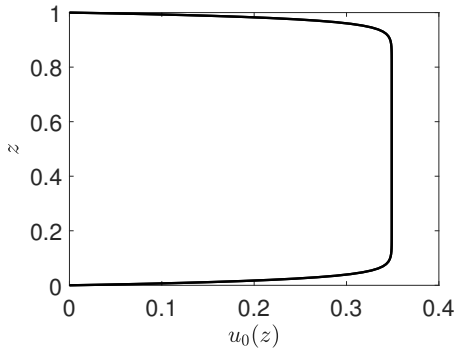


Figure 4.12: The Mean flow profile used in case 3

Figure 4.13 shows the snapshots of pressure responses along the duct for case 3. The instabilities are much more pronounced compared with figure 4.10. Once instabilities are generated, they spread all the domain and become the predominant contribution. In figure 4.14, similar branches and instability patterns, respectively related to the acoustic propagation and hydrodynamic instabilities, are observed. One obvious difference between the figure 4.11 lies in the feature of instabilities. For example, the instabilities in case 3 seem to grows temporally and spatially. However, the instabilities in case 2 convect away from the duct even if they also amplify during their movements.

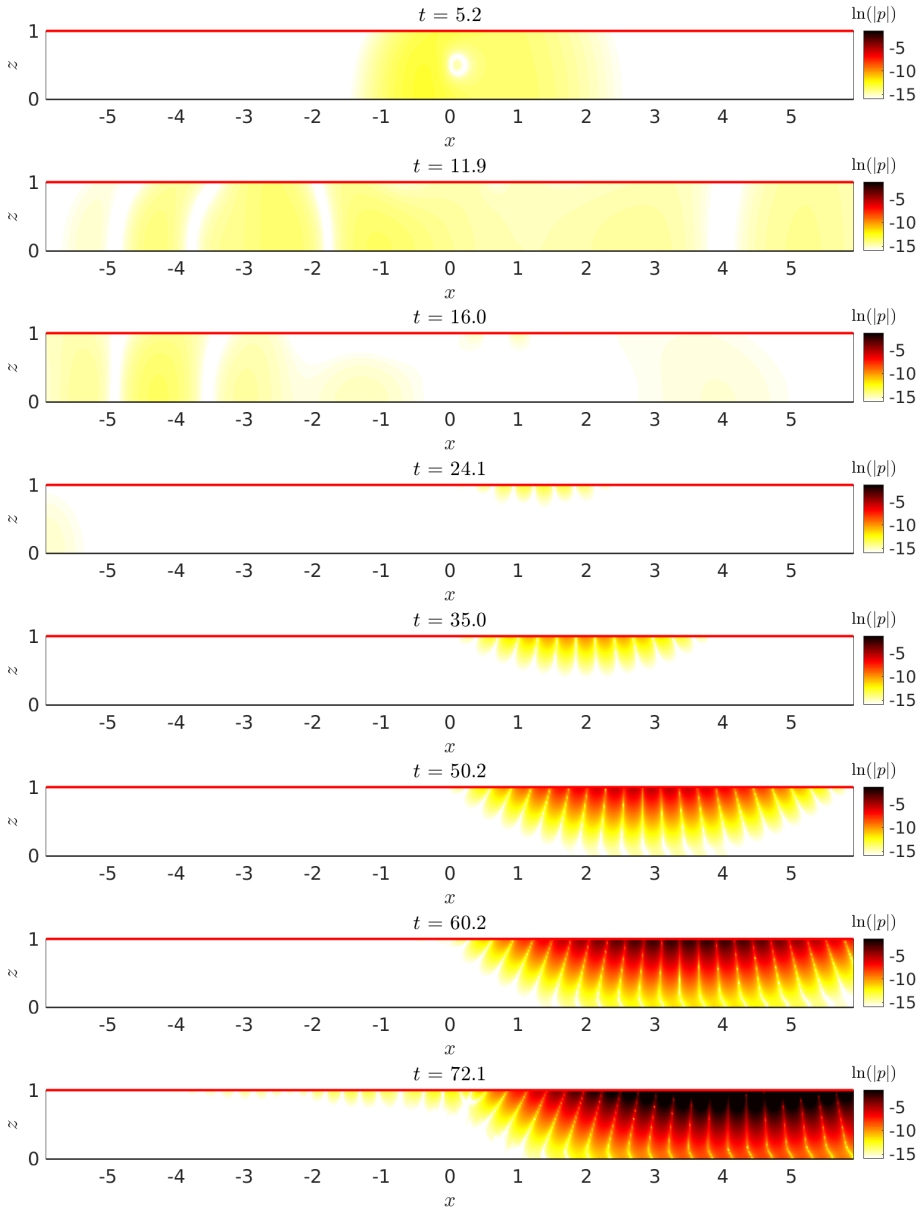


Figure 4.13: Snapshots of pressure response $\ln|p(x, t)|$ to an impulsive source for case 3.

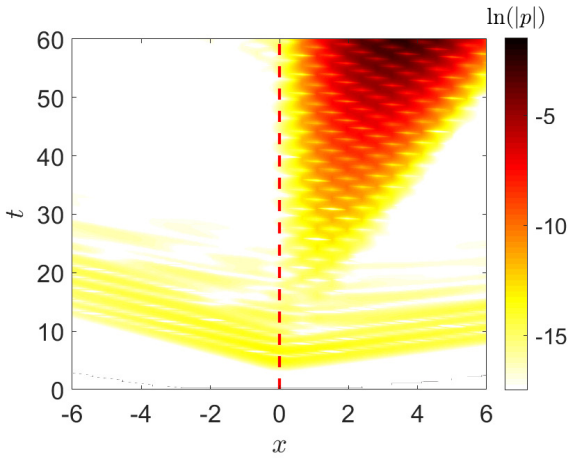


Figure 4.14: Pressure response $\ln|p(x, z = 1, t)|$ to an impulsive source on the lined wall for case 3. The source position is indicated by the vertical dashed line.

## 4.2 Analysis of stability

This section aims at correlating the instability observed in time-domain simulations with the modal representation. Therefore, a harmonic source is imposed on both approaches. Subsequently, the type, the wavenumber and mode shapes of the instability are investigated. The method for characterization of instabilities in time-domain solutions is presented. The results are compared with the prediction of the modal analysis approach.

### 4.2.1 Wavenumbers of 4 cases obtained by modal analysis

The wavenumbers of all the modes for the 4 cases at $\omega = 0.9271$ ($f = 1000$ Hz) are shown in figure 4.15. For case 0 and 1, there is no mode in the upper-right complex $k$-plane and therefore no possible instabilities. For case 2 and case 3, several modes are located in the upper right complex $k$-plane. These are possible unstable modes, and their stability depends on their propagation direction. If the mode is an upstream decaying mode, the propagation is stable. On the other hand, if it propagates in the stream wise direction, it corresponds to an instability. The propagation direction of this mode therefore needs to be determined.

In figure 4.15, noticeable modes other than the acoustic modes and the instability are convected modes which satisfy the dispersion relation $ku_0(z) = \omega$. For a sheared mean flow, they come as a continuous spectrum, located in the $k$-plane along the horizontal half-line starting at $k = \omega/\max(u_0)$. In solving the eigenvalue problem numerically, this continuous spectrum turns into individual modes, which are greatly dependent on the discretization. In particular, the wavenumbers of these modes may have small positive imaginary parts and thus be weakly unstable. Note that the use of selective filters, as employed in the time-domain simulations, tends to move the convected modes towards the lower right quadrant of the $k$-plane [29] and thus to make all these modes stable. As we are primarily interested in the instability, no specific method is employed to have an accurate prediction of these modes. Such a method has been for instance described in Vilenski and Rienstra [115].

### 4.2.2 Briggs-Bers criterion

The Briggs-Bers criterion [106, 107] was first proposed to analyse the plasma instability and then was extended to the instabilities in fluid mechanics and aeroacoustics[116, 117, 118, 119]. Later it has been applied in the stability analysis of acoustic propagation in a lined flow duct [31]. It allows one to determine the propagation direction of the modes, and, if an unstable mode is present, whether it is convective or absolute. However, before using the Briggs-Bers criterion, it should be checked whether it is applicable. For instance, as discussed by Brambley [31], the acoustic propagation in a lined duct with a plug flow and the Myers impedance boundary condition is mathematically ill-posed. The system supports the instability waves grow at an infinite large growth rate, therefore the Briggs-Bers criterion can not be used.

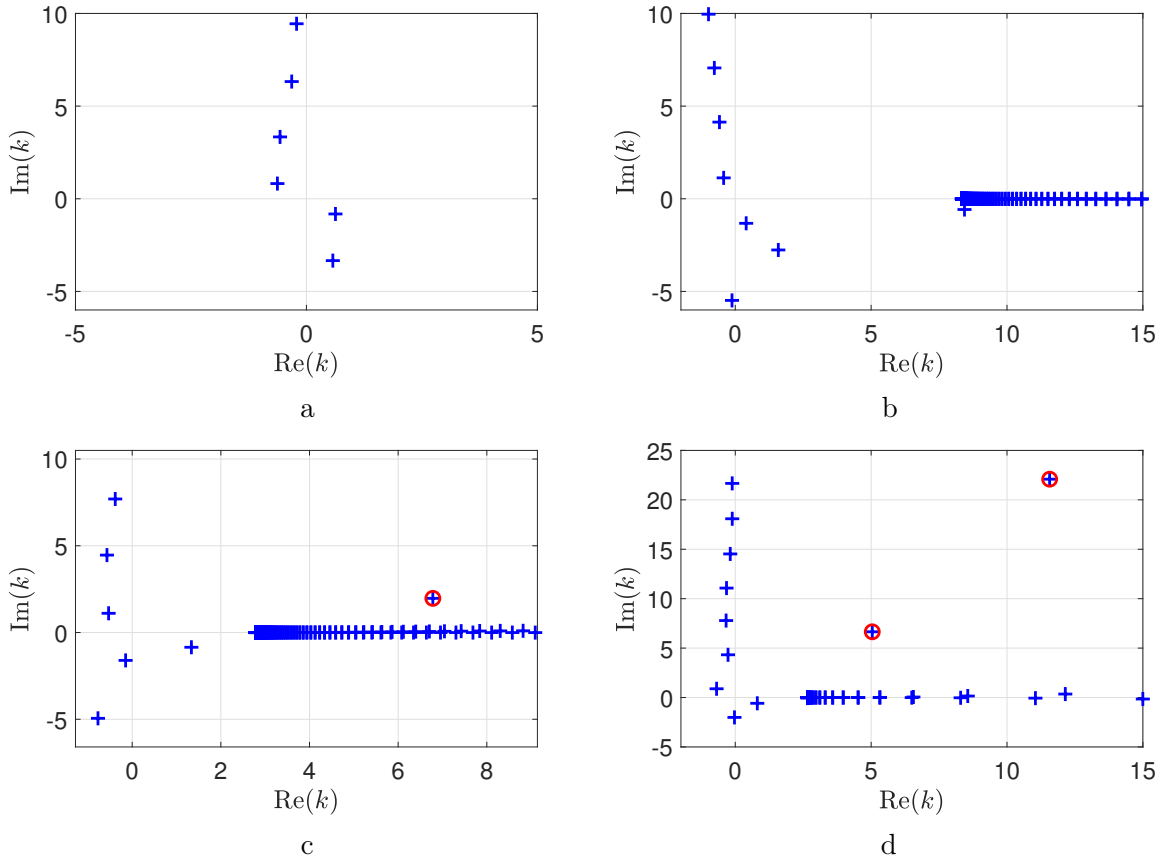


Figure 4.15: Wavenumber obtained from modal analysis at $\omega = 0.9271$. a, case 0; b, case 1; c, case 2 and d, case 3. + modes obtained from modal analysis, ∘ possible unstable hydrodynamic modes.

### Bounded temporal growth rate

Since there are possible unstable modes in cases 2 and 3, it is necessary to check whether the Briggs-Bers criterion is applicable, before applying the stability analysis. Specifically, the maximum of the amplification rate for all modes, particularly the possible unstable one, should be bounded. For this based on the dispersion relation $D(k, \omega)$, the frequency $\omega$ is given as a function of wavenumber $k$. We need to check that there is a minimum of the imaginary part of $\omega$ satisfying

$$\omega_{\min} = \min_{k \in \mathbb{R}} [\mathrm{Im}(\omega(k))]. \tag{4.4}$$

In other words, for a purely real wavenumber $k$, the temporal growth rate $\mathrm{Im}(\omega(k))$ of the possible unstable mode needs to be calculated.

The temporal growth rate $\mathrm{Im}(\omega)$ of the unstable mode in case 2 is shown in figure 4.16. An example of an ill-posed problem applied with the Ingard-Myers boundary condition, rather than the impedance boundary condition is also given in the figure. The temporal growth rate of the possible mode is studied when $\mathrm{Re}(\omega)$ gradually increases from -1.5 to 1.5. The figure shows that the temporal growth rate $-\mathrm{Im}(\omega)$ of the mode has a trend to become infinitely large for

an arbitrary $\omega$ by adopting Ingard-Myers boundary condition with a uniform flow. Therefore the Briggs-Bers criterion, in this case, is not applicable. However, with the impedance boundary condition considered, the growth rate is bounded at $\mathrm{Im}(\omega) \approx -0.23$, meaning that the instability will not amplify at an arbitrarily large growth rate for any given real frequency. The Briggs-Bers criterion can thus be applied in this case.

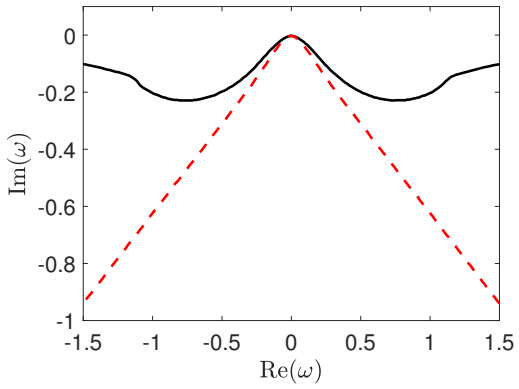


Figure 4.16: Temporal trajectory of the unstable mode. The case 2, ——— and the case adopting Ingard-Myers bounadry condition with a uniform flow $M = 0.3$, - - - - .

Similarly, the temporal growth rate $\mathrm{Im}(\omega)$ of the unstable mode for case 3 is shown in figure 4.17. $\mathrm{Im}(\omega)$ is bounded. It should be noticed that several discontinuities are observed. The reason is that the dispersion relation $D(k, \omega)$ has several roots of real $k$ at a certain $\omega$. Among all the roots, we are primarily interested in the one obtained at the largest negative value of $\mathrm{Im}(\omega)$. Table 4.1 indicates the number of purely real $k$ obtained for different ranges of $\omega$. Because of the symmetry between the positive and negative $\mathrm{Re}(\omega)$, only the positive values of $\mathrm{Re}(\omega)$ are considered. Figure 4.18 illustrates the different numbers of real $k$ obtained for different range of $\mathrm{Re}(\omega)$ during the variation of $\mathrm{Im}(\omega)$ from -0.7417 to 0.7417.

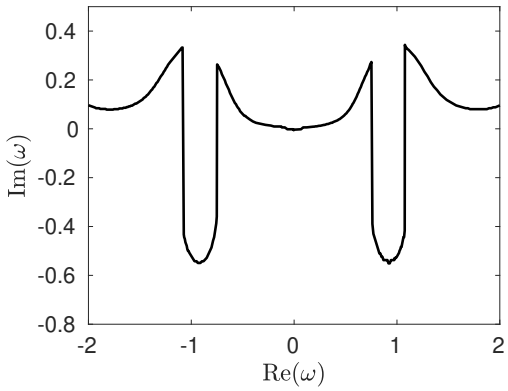


Figure 4.17: Temporal trajectory of the unstable mode for case 3.

Table 4.1: Number of real roots $k$ of $D(\omega, k)$ for $\omega$ at different ranges.

| Re($\omega$) | $0 \sim 0.7547$ | $0.7547 \sim 0.8715$ | $0.8715 \sim 0.9960$ |
|---|---|---|---|
| $N$ | 1 | 3 | 1 |
| | $0.9960 \sim 1.0384$ | $1.0384 \sim 1.0801$ | $1.0801 \sim 1.4834$ |
| | 2 | 3 | 1 |

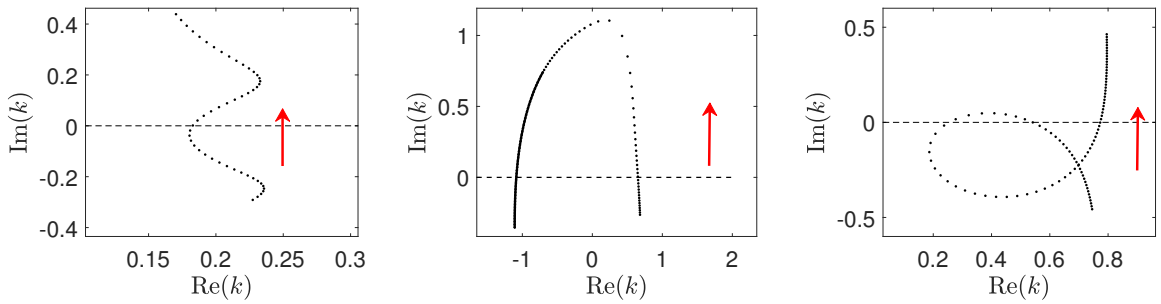


Figure 4.18: Three trajectories of the unstable mode Im $(\omega)$ varying from -0.7417 to 0.7417. Left, Re $(\omega) = 0.1854$; middle, Re $(\omega) = 0.9735$; right, Re $(\omega) = 1.0662$.

### Procedure of applying Briggs-Bers criterion

Applications of the Briggs-Bers criterion include distinguishing the unstable modes from the stable modes and indicating the type of instability existing in the system. A detailed introduction of the Briggs-Bers criterion can be found in Appendix C. Procedures[106] to conduct analysis based on the criterion are:

• When $\omega$ is real, the mode wavenumber which has a positive imaginary part Im $(k)$ is the candidate for the unstable mode. To determinate if a possible unstable mode contributes to instabilities and whether the instabilities are convective or absolute ones, the trajectories of wavenumbers in the complex $k$-plane are recorded as $\omega$ varies. More specifically, the value of Re $(\omega)$ remains unchanged while Im $(\omega)$ is varied from $-\infty$ to 0. And then repeating this process for numerous values of Re $(\omega)$. If the mode derives from the lower half plane, the mode is a downstream propagating mode, and if the mode is originating from the upper half plane, the mode is an upstream propagating one. If the trajectory of the downstream propagating mode crosses the real-$k$ axis, the mode is an unstable one.

• Once the existence of the unstable mode is ascertained, the type of instabilities can be indicated by the presence or not of a saddle point. The saddle point corresponds to merging roots of $k$ from different halves of the $k$-plane. Mathematically, it represents a second-order algebraic branch point at a certain $\omega$. If the trajectories of the wavenumbers in the $k$-plane show a saddle point, the absolute instabilities can be deduced. Attention should be paid on the merging points, one root should come from the lower-half $k$-plane, and the other should come from the upper, as shown in figure 4.19.

• During the variation of Im $(\omega)$ from $-\infty$ to 0, the trajectory of modes crosses the real $k$-axis, and no saddle point is observed, then the amplifying waves are of convective type. An illustration

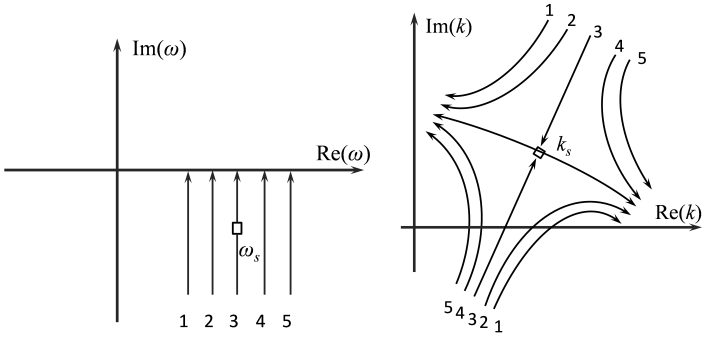


Figure 4.19: Trajectory of wavenumber $k$ with variation of $\omega$ when absolute instabilities are consisted. Left, variation of the frequency $\omega$ in the complex plane. Right, corresponding variation of the wavenumber $k$ with $\omega$. □ referring to the saddle point.

is given in figure 4.20.

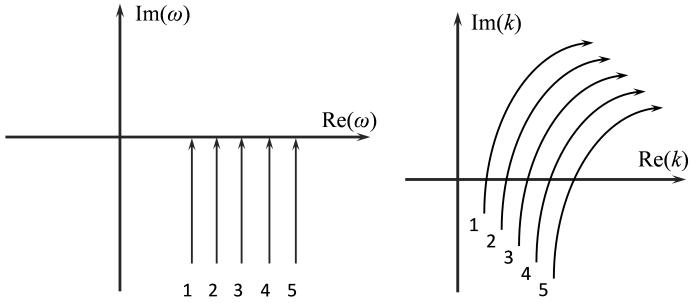


Figure 4.20: Trajectory of wavenumber $k$ with variation of $\omega$ when convective instabilities are consisted. Left, variation of the frequency $\omega$ in the complex plane. Right, corresponding variation of the wavenumber $k$ with $\omega$.

Following the procedures mentioned before, figure 4.21 shows this process for case 2. The illustration is given for $\mathrm{Re}(\omega) = 0.9271$, while the imaginary part $\mathrm{Im}\,(\omega)$ goes from $-1.4$ to 0. The wavenumber of the possible unstable mode crosses the real $k$-axis from the lower $k$-plane when $\mathrm{Im}\,(\omega)$ is approaching 0. The crossing of the real $k$-axis from the lower half $k$-plane indicates that this mode is indeed a downstream propagating mode and is thus an instability. It has been carefully checked that on a large range of values of $\mathrm{Re}\,(\omega)$ no saddle point is observed. To sum up, the instabilities in case 2 corresponds to convective instabilities.

The trajectories of the wavenumbers for case 3 are shown in figure 4.22. $\mathrm{Re}\,(\omega)$ is set respectively to $\omega = 0.9660$, 0.9670 and 0.9679, meanwhile $\mathrm{Im}\,(\omega)$ varies from $-1.4$ to 0. The trajectories for both possible unstable modes are displayed in the left and right figure. Figure 4.22 shows that both possible unstable modes cross the real $k$-axis from the lower $k$-plane when $\mathrm{Im}\,(\omega)$ is approaching 0. The crossing of the real $k$-axis from the lower half $k$-plane indicates that these modes are indeed downstream propagating modes and are thus instabilities. In the left of figure 4.22, one mode coming from the lower $k$-plane and the other from the upper $k$-plane merge at $\omega_s = 0.9670 - 0.2716\mathrm{i}$. The corresponding $k$ is around $0.5 + 1.6\mathrm{i}$. Since a saddle point is observed in case 3, the instabilities in case 3 are absolute instabilities.

In addition to the mode related to the saddle, there is another unstable mode in the system. The second unstable mode which also crosses the real-$k$ from the lower $k$-plane during the variation of Im $(\omega)$. A large inspection for different Re$(\omega)$ has been made. Except for the merging root near $k = 0.5 + 1.6$i, no other saddle points are observed. Therefore the second unstable mode will lead to a convective instability.

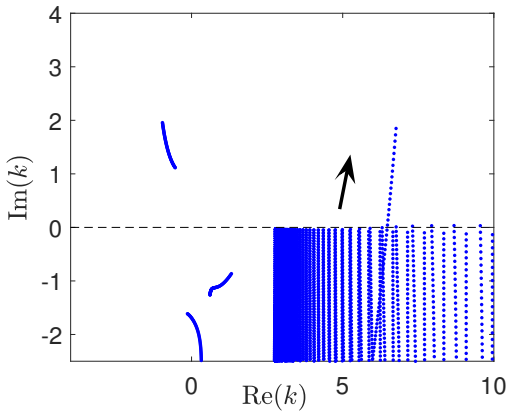


Figure 4.21: Trajectories of the wavenumber for case 2 by increasing values of Im $(\omega)$. The arrow denotes the direction of path varies from -1.4 to 0.

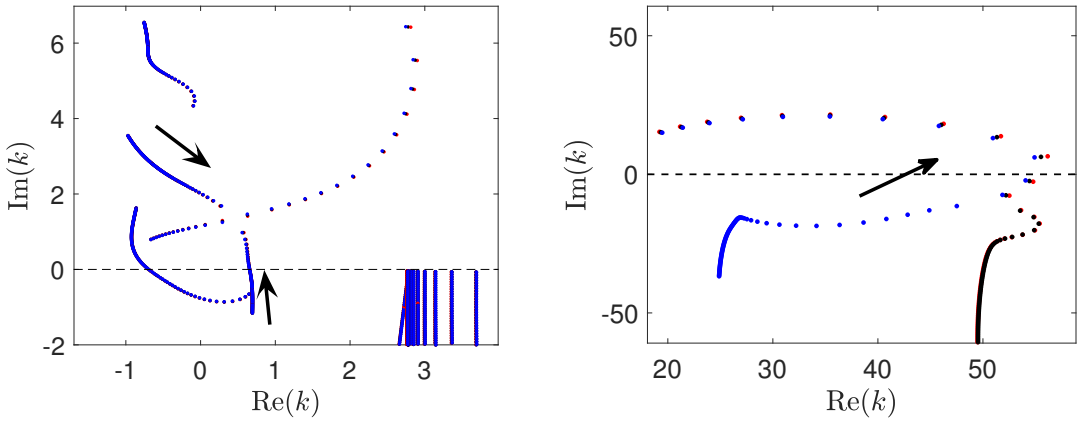


Figure 4.22: Trajectories of the wavenumber for case 3 by increasing values of Im $(\omega)$. The arrow denotes the direction of path varies from -1.4 to 0. Re $(\omega) = 0.9660$, •; Re $(\omega) = 0.9670$, •; Re $(\omega) = 0.9679$, •. Left the saddle point form by one of the possible unstable mode. Right, the second unstable mode.

### 4.2.3 Characterization of the hydrodynamic instability

The characteristics of the instability observed in the time-domain simulations can also be investigated by considering acoustic propagation driven by a harmonic source at $\omega = 0.9271$ ($f$ =1 kHz). The types of instabilities are studied for cases 2 and 3. The determination of mode wavenumbers and mode shapes of the instabilities will be conducted on case 2.

For the modal analysis approach, there are 150 points along the duct height to obtain a

converged result. For the time-domain method, the time step is $\Delta t = 0.0014$. The grid size along the $x$-direction for the calculated domain is $\Delta x = 0.02$, which is fine enough for ensuring far more than 10 points per wavelength. 175 points are used for discretization along the duct height. The selective filter is applied on all the domain apart from the first grid point to remove the grid-to-grid oscillations. The strength of the selective filter is denoted by $x_\nu$ and its default value is 0.5. Receivers are located along the lined wall to collect pressure signal $p(x, t)$ for all the time iterations.

### Instability type

The pressure responses to the harmonic source $\omega = 0.9271$ are obtained from the time-domain approach. Figure 4.23 shows the pressure response on the lined wall varying with time for case 2 and case 3. The response of pressure has a constant value at $x = 0$ since a harmonic source is used. The attenuation of the pressure can be noticed along the lined wall, and the hydrodynamic instability is observed in the downstream direction. For case 2, when a steady-state is attained, the magnitude of the instability at a given location is not increasing over time. The amplification of amplitude grows with the distance from the sound source. It thus appears that the instability observed in the time-domain simulation is also a convective one.

However, the instability in case 3 not only grows with $x$-axis but also grows with time. It shows that the instabilities in case 3 are absolute ones. As shown in figure 4.22, two unstable modes respectively lead to convective instabilities and absolute instabilities. We infer that the instabilities shown in figure 4.23 are the results of a combination of two types of instabilities. The conclusion drawn by the time-domain approach agrees with the prediction of the modal analysis approach.

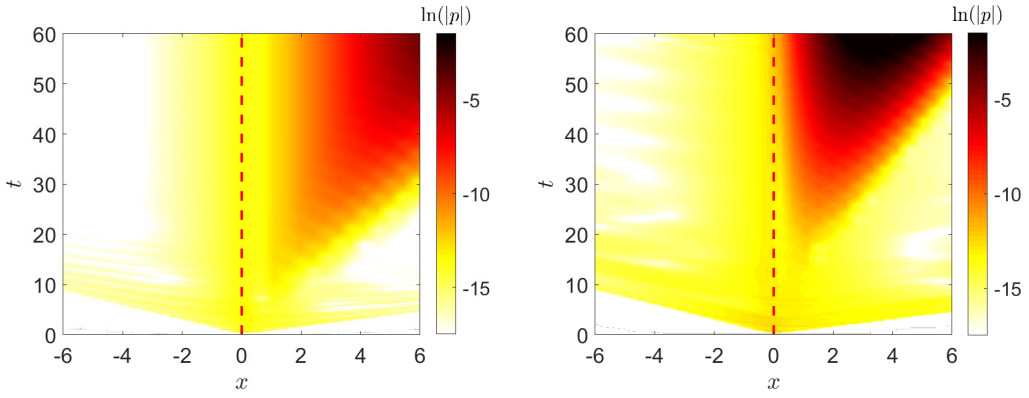


Figure 4.23: Pressure response $\ln|p(x, z = 1, t)|$ to a harmonic source at $\omega = 0.9271$ obtained from the time-domain simulation for left, case 2; right, case 3. The source position is indicated by the vertical dashed line.

### Wavenumber

The investigation of the wavenumber and mode shapes of instabilities is done on the case 2, for which the instabilities are convective ones. If the instability is convective and is the main contribution to the pressure field, the fluctuating pressure will have the form:

$$p\left(x,z,t\right) = P_{\mathrm{HI}}\left(z\right)\mathrm{e}^{\mathrm{i}\omega t}\mathrm{e}^{-\mathrm{iRe}(k_{\mathrm{HI}})x}\mathrm{e}^{\mathrm{Im}(k_{\mathrm{HI}})x}, \tag{4.5}$$

where $P_{\mathrm{HI}}$ is the mode shape of the instability and $k_{\mathrm{HI}}$ is its wavenumber. In this case, the phase of the complex pressure, denoted by arg is given by:

$$\arg[p\left(x,z,t\right)] = -\mathrm{Re}\left(k_{\mathrm{HI}}\right)x + \omega t + \arg[P_{\mathrm{HI}}\left(z\right)]. \tag{4.6}$$

The real part of the instability wavenumber can then be estimated from the time-domain solution through the axial evolution of the phase of the complex pressure. Figure 4.24 shows $\arg(p)$ along the liner ($z = 1$) at $t = 90$, for which it has been checked that the instability is well developed. The phase has been unwrapped to ensure that $\arg(p)$ is continuous. The estimated slope for $2 \leq x \leq 6$ of the phase is $-6.89$, which is very close to the prediction of modal analysis $\mathrm{Re}(k_{\mathrm{HI}}) = 6.78$.

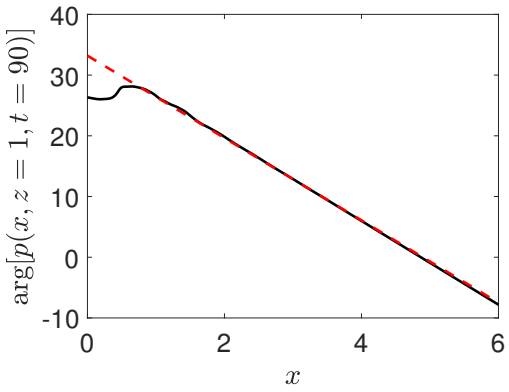


Figure 4.24: Comparison of the phase of the pressure on the lined wall from the time-domain solution at $t = 90$ ——— and from the analytical solution in Eq. (4.6) ($\arg(p) \propto -6.78x$) - - - -.

Similarly, the growth rate of the convective instability $\mathrm{Im}\left(k_{\mathrm{HI}}\right)$ in Eq. (4.5) can be calculated from the logarithm of $|p(x,z,t)|$:

$$\ln\left|p\left(x,z,t\right)\right| = \mathrm{Im}\left(k_{\mathrm{HI}}\right)x + \ln\left|P_{\mathrm{HI}}\left(z\right)\right|. \tag{4.7}$$

A snapshot of $\ln|p|$ at $t = 90$ from the time-domain simulation is depicted in figure 4.25 (a). The instability is seen growing from the source at the vicinity of the liner. Figure 4.25 (b) shows the spatial variation of $\ln|p(x, z = 1, t = 90)|$. A linear growth is observed downstream, where the instability is the dominant contribution to the pressure field. The estimated slope for $2 \leq x \leq 6$ is 1.99, which is again in close agreement with the spatial growth rate predicted by the modal analysis approach $\mathrm{Im}\left(k_{\mathrm{HI}}\right) = 1.97$.

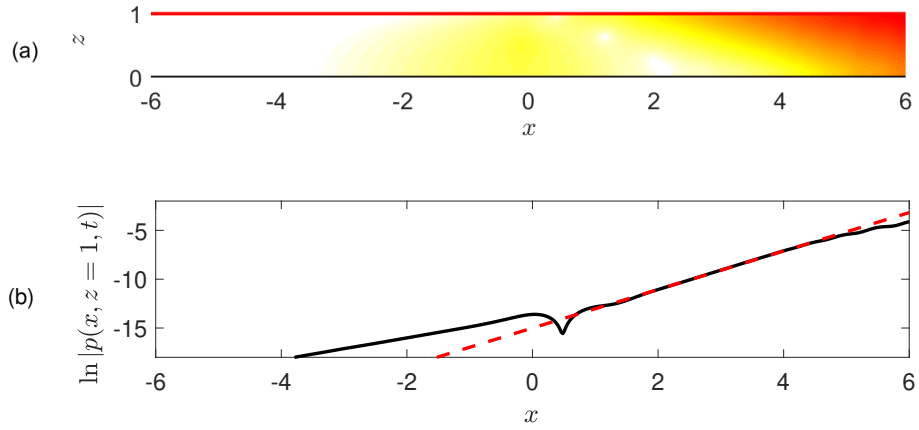


Figure 4.25: (a) Snapshot of $\ln|p|$ at $t = 90$ and (b) comparison of the amplitude of the pressure on the lined wall from the time-domain solution ——— and from the analytical solution in Eq. (4.7) ($\ln|p| \propto 1.97x$) - - - - -.

### Mode shapes

The mode shapes $|P|$, $|U|$ and $|V|$ of the instability determined from the modal analysis approach are compared with the vertical profiles of $p$, $u$ and $v$ calculated from the time-domain solution in figure 4.26. The results of the time-domain solution correspond to the section $x = 4$ at $t = 90$, for which it has been checked that the solution is not changing after additional time iteration. When the time-domain solution is in a steady-state, the vertical profiles of $p$, $u$ and $v$ should hold similar shapes regardless of $x$-position and time iteration. For comparison, the mode shapes of the instability and the vertical profiles of $p$, $u$ and $v$ are normalized by the maximum of the pressure modulus. The peak of the amplitudes are observed near the lined wall. Then they gradually decrease to a small value on the rigid wall. The match between modal analysis and the time-domain solution is remarkable.

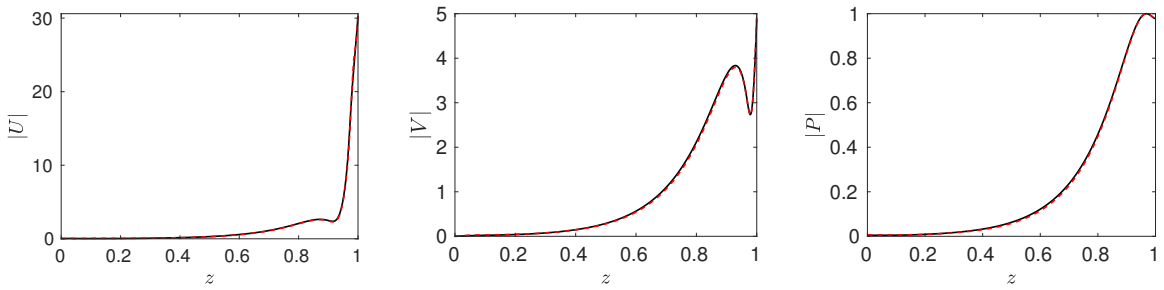


Figure 4.26: Comparisons of mode shapes of the instability. Left, $U(z)$, middle, $V(z)$ and right, $P(z)$ ——— determined from the time-domain solution at $x = 4$ and $t = 90$ and - - - - - calculated by modal analysis.

### 4.2.4 Validation at $\omega = 0.4636$

To check the viability of the time-domain method in obtaining the characteristics of instability, additional simulations by using the time-domain method are performed at $\omega = 0.4636$ ($f = 500$ Hz) and $\omega = 1.8542$ ($f = 2000$ Hz) for case 2. One should pay attention that the impedance model used in case 2 is a broadband one, therefore the impedance at different frequency is not the same as shown in Table 4.2. Except the frequency and the impedance, the other parameters are the same as in section 4.2.3.

Table 4.2: Impedance at different frequencies for the MSD liner used in case 2.

| $\omega$ | 0.4636 | 0.9271 | 1.8542 |
|---|---|---|---|
| $Z$ | $0.2 + 0.0025$ i | $0.2 + 0.005$ i | $0.2 + 0.01$ i |

Figure 4.27 shows the mode wavenumbers predicted by the modal analysis approachg at $\omega = 0.4636$. The reference result $\omega = 0.9271$ is also indicated. The wavenumbers of the "plane wave" mode ($k = 0.79 - 0.33$i) and the unstable mode ($k_{\mathrm{HI}} = 2.57 + 1.31$i) show the most evident change. Compared with $\omega = 0.9271$, the spatial growth rate of the unstable mode slightly decreases. However the wavelength becomes three times longer. Figure 4.28 shows the evolution of $\arg(p)$ and $\ln|p|$ along the lined wall for $\omega = 0.4636$ obtained from the time-domain solution at $t = 90$ and predicted with the analytical solution in Eq. (4.5), where the value of $k_{\mathrm{HI}}$ obtained from modal analysis has been used. Here again, an excellent match is observed.

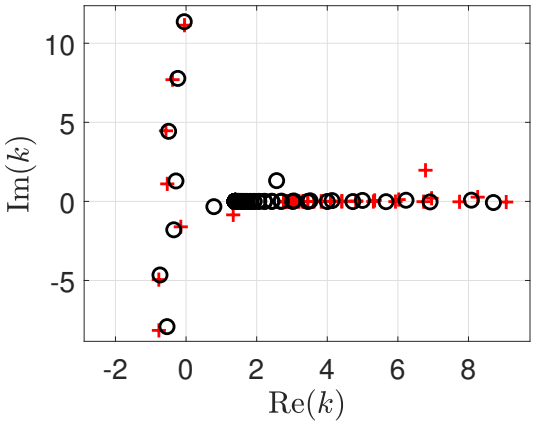


Figure 4.27: Wavenumber obtained by modal analysis for $\omega = 0.4636$. $\circ$ $\omega = 0.4636$, $+$ $\omega = 0.9271$.

Comparisons of mode shapes of the instability between the time-domain method and the modal analysis approach at $\omega = 0.4636$ are shown in figure 4.29. The vertical profiles $u$, $v$ and $p$ of the time-domain solution at $x = 5.5$ at $t = 90$, for which it has been checked that the solution is not changing after additional time iterations. Compared with figure 4.26, the predicted results obtained by the two methods are consistent in terms of trends. It also shows that the peak of the $|U|$ at $\omega = 0.4636$ is nearly twice large than the one at $\omega = 0.9271$. In conclusion, the match of mode shapes obtained through the two approaches is quite well.

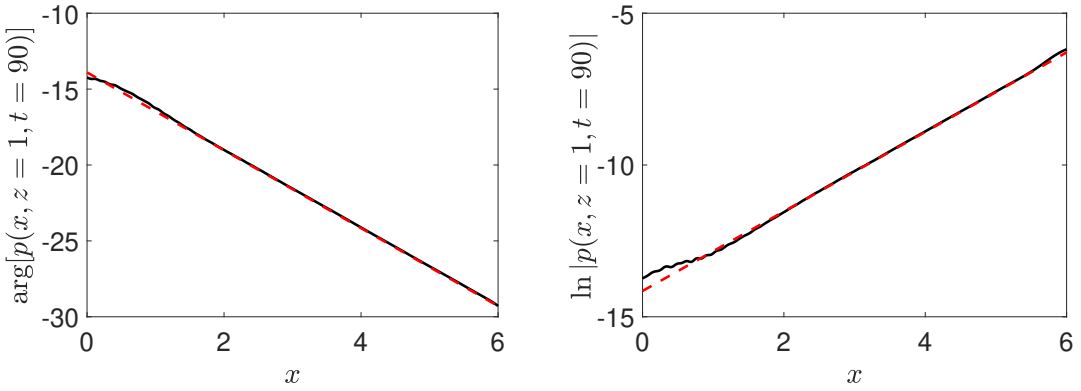


Figure 4.28: Comparisons of the phase (left) and amplitude (right) of the pressure on the lined wall for $\omega = 0.4636$ from the time-domain solution at $t = 90$ ——— and from the analytical solution - - - - .

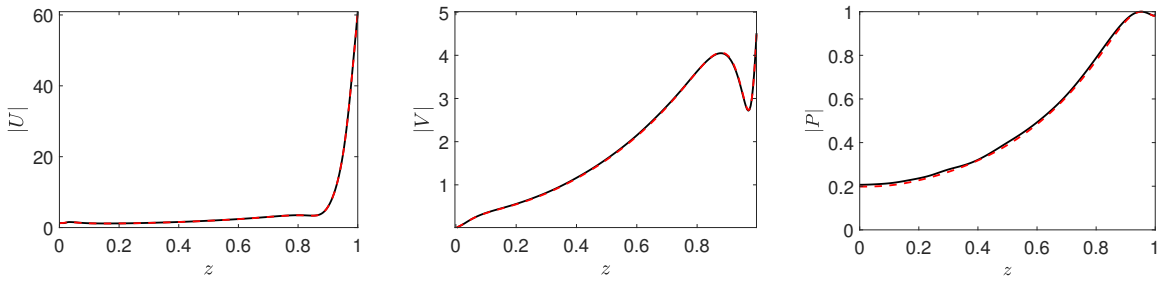


a. b. c.

Figure 4.29: Comparison of the mode shape of the instability for (a) $U(z)$, (b) $V(z)$ and (c) $P(z)$ ——— determined from the time-domain solution at $x = 5.5$ and $t = 90$ and - - - - calculated by the modal analysis approach.

The wavenumber distribution for case 2 at $\omega = 1.8542$ is displayed in figure 4.30. The wavenumbers, both the acoustic modes and hydrodynamic modes, are quite different from the reference result. The unstable mode obtained at $\omega = 0.9271$ does not exist when $\omega = 1.8542$, which indicates the system is stable at this frequency. The time-domain approach at $\omega = 1.8542$ is also performed. The instabilities are observed, even if they are not expected. It may be due to the fact that the source in the time-domain simulations is not purely harmonic, and excites, at the transient stage, a broadband frequency range. Instabilities, related to lower frequencies, are thus generated. Once the instabilities are excited by the sudden jump in the implementation of the harmonic excitation, the instabilities may convect in a small range of frequencies. The difference compared with the previous cases is that the instability will not be converged and it will convect away from the calculated domain. In the later stage of simulation, small grid to grid oscillations gradually accumulate leading to inevitable numerical instabilities. Finally, the numerical instability make the simulation crash, therefore no converged characteristics of the instability can be acquired.

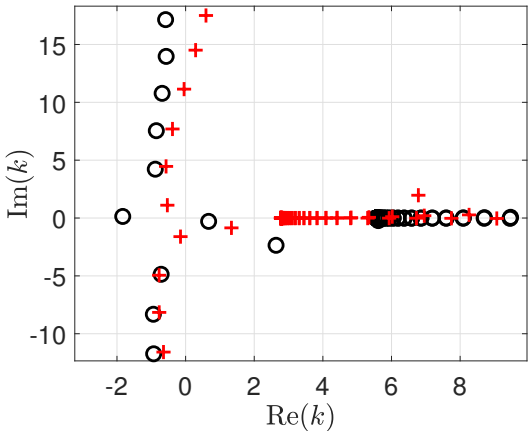


Figure 4.30: Wavenumber obtained by modal analysis at $\omega = 1.8542$. $\circ$ $\omega = 1.8542$; $+$ $\omega = 0.9271$.

## 4.3 Convergence of the LEE time-domain approach

Previous studies on the same topic, i.e., instabilities appearing during sound propagation in a lined flow duct, have mentioned the impact of spatial filters and grid resolution on the instabilities. It was concluded that selective filtering is effective to remove or partly remove the instability [120, 121] and that the use of fine grids can reinforce the instability [113, 122], in particular when using the Myers impedance boundary condition instead of resolving the boundary layer as done here. Therefore, one of the main objective is to study the effects of both factors on the hydrodynamic instabilities. A parametric study on the impacts of the source, a mean flow and acoustic liners on instabilities are also performed.

### 4.3.1 Effect of the filtering strength

In time-domain simulations, a selective filter of strength $x_\nu$ is applied on the whole domain to remove the grid-to-grid oscillations. In the previous sections, $x_\nu$ was set to 0.5. Simulations are now performed with different values of $x_\nu$ in order to study how the properties of the hydrodynamic instability are modified.

Figure 4.31 shows the real and imaginary parts of the instability wavenumber obtained with the time-domain solutions as a function of $x_\nu$. The results are compared with the reference wavenumber obtained by the modal analysis approach. When the strength of selective filter is between 0.7 and 1, the strong dissipation of the selective filter results in a noticeable deviation between the reference result and the time-domain prediction. In particular, the growth rate of the instability is overestimated. As $x_\nu$ decreases, $\mathrm{Re}(k_{\mathrm{HI}})$ and $\mathrm{Im}(k_{\mathrm{HI}})$ start to approach the reference wavenumber. The value of $x_\nu$ does not make a significant difference to $\mathrm{Re}(k_{\mathrm{HI}})$ and $\mathrm{Im}(k_{\mathrm{HI}})$, when it is in the range between 0.2 and 0.5. For $x_\nu$ below 0.2, spurious numerical waves with a short wavelength are rapidly growing near the duct walls and the calculation become unstable instantly. Therefore, for accurately predicting the physical instability, the filter strength should be chosen as small as possible while sufficiently large to stabilize the numerical calculation.

To conclude, a value of $x_\nu$ between 0.2 and 0.5 seems to be a good compromise.

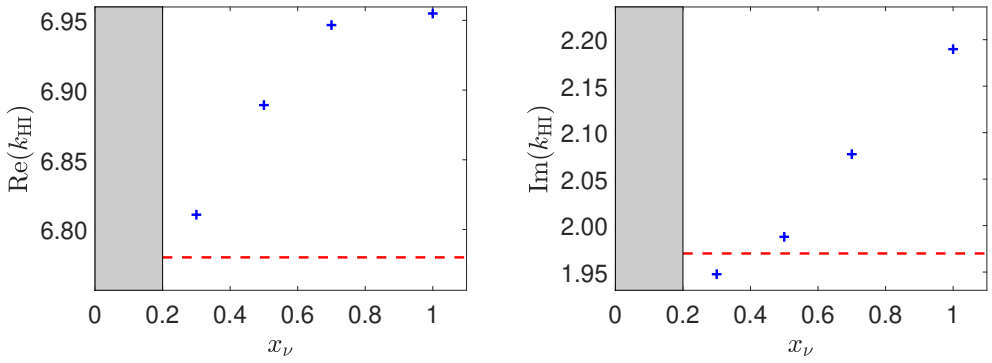


Figure 4.31: Left, real and right, imaginary parts of the instability wavenumber: + estimated from the time-domain solution as a function of the filtering strength $x_\nu$ and - - - predicted by modal analysis. The grey region indicates unstable simulations.

### 4.3.2 Effect of the mesh size along the duct height

Along the $x$-direction, centered high-order finite-difference schemes, with dispersion-relation preserving properties, are employed. It is assumed that the mesh size $\Delta x$ is small enough so that the dispersion properties of the instability are well-reproduced. In particular, it has been checked that $k^*(k_{\mathrm{HI}})$ is very close to $k_{\mathrm{HI}}$, where $k^*$ is the effective wavenumber of the centered finite-difference scheme employed here. No particular effect in reducing $\Delta x$ is thus expected. The grid along the $z$-direction is anticipated to have more impact on the instability. Indeed, non-centered schemes are used near the walls, which enhance dispersion. They can amplify or dissipate even constant-amplitude waves, contrary to centered schemes. In addition, the instability is directly related to the mean flow profile through $u_0$ and $\mathrm{d}u_0/\mathrm{d}z$. The discretization of the mean flow profile, in particular within the boundary layer, is expected to play a role in the results.

Figure 4.32 shows the impact of the number of grid points along the $z$-direction $n_z$ on the real and imaginary parts of the instability wavenumber. For $n_z \leq 155$, the deviations of $\mathrm{Re}(k_{\mathrm{HI}})$ and $\mathrm{Im}(k_{\mathrm{HI}})$ between using time-domain approach and modal analysis are noticeable. Note that the mesh is already fine enough for $n_z = 55$ to precisely calculate the acoustic propagation. The number of points per wavelength is indeed about $2\pi n_z/\omega \approx 370$, which is very large. However, that is still not sufficient to precisely calculate the hydrodynamic instability. As $n_z$ increases, the features of hydrodynamic instability can be captured and the wavenumber gradually approaches the prediction of modal analysis. With $n_z \geq 175$ the time-domain solution is deemed converged. With successive increase in the point of grid from 175 to 305, no significant modifications of wavenumbers are found compared with prediction of modal analysis. In summary, fine grids are needed to capture accurately the instability in the time-domain simulation.

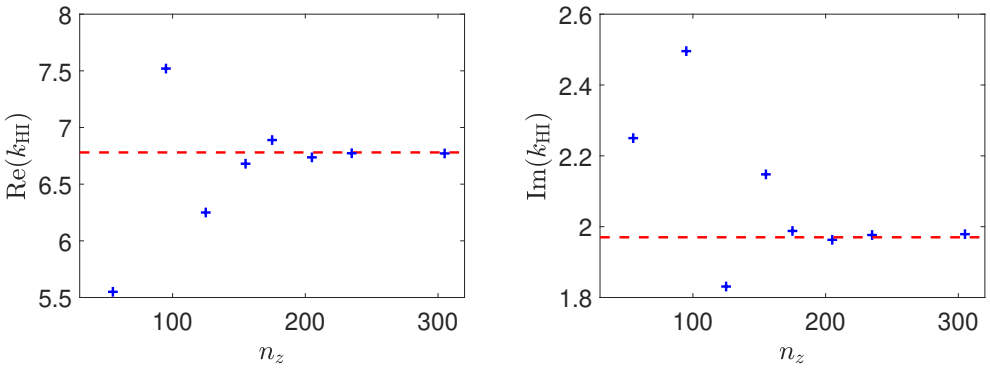


Figure 4.32: Left, real and right, imaginary parts of the instability wavenumber: + estimated from the time-domain solution as a function of the number of grid points along the duct height $n_z$ and ---- predicted by the modal analysis approach.

## 4.4 Parametric study

As shown in the four test cases, the hydrodynamic instability can be observed under certain conditions. Furthermore, the properties of the hydrodynamic instability have significant differences when various mean flow and the liners are imposed. For example, in cases 2 or 3, the hydrodynamic instabilities can be convective or absolute ones, when different mean flow and liners are imposed in the duct. Therefore, it is necessary to further understand the characteristics of hydrodynamic instability, so that the optimal solution of multi-objective optimizations for the acoustic treatment can be obtained to maximize the efficiency of acoustic liners. A parametric study by using modal analysis is conducted to investigate the effects of some parameters, i.e., the source frequency $\omega$, the boundary layer thickness $\delta^*$, the Mach number $M$ and the liner impedance $Z$ on hydrodynamic instabilities.

### 4.4.1 Effect of frequency $\omega$

The effect of frequency $\omega$ on $k_{\mathrm{HI}}$ is shown in figure 4.33. Except for the frequency and liner impedance, the other parameters are kept the same as case 2 in section 4.2.1. One should notice that the liner model is broadband one, and then the variation of the frequency will cause the instability to change. The frequency $\omega$ varies from 0.4636 to 1.2052 (corresponding to 500 Hz to 1300 Hz). The real part of wavenumber $\mathrm{Re}(k_{\mathrm{HI}})$ increases gradually with frequency $\omega$, indicating a decrease of the wavelength of the instability, as seen in the left of the figure. In the right of the figure, a maximum spatial growth rate of the instability is obtained at $\omega \approx 0.8344$. Moreover, the instability will only exist in a certain frequency range $0.4636 \leq \omega \leq 1.2052$: the unstable mode will not be present if the frequency is too low or high.

### 4.4.2 Effect of boundary layer thickness $\delta^*$

The boundary layer thickness of the mean flow $\delta^*$ varies from 2 % to 7 %, while the Mach number keeps $M = 0.3$. The other parameters are chosen as case 2 in section 4.2.1. The effect of the

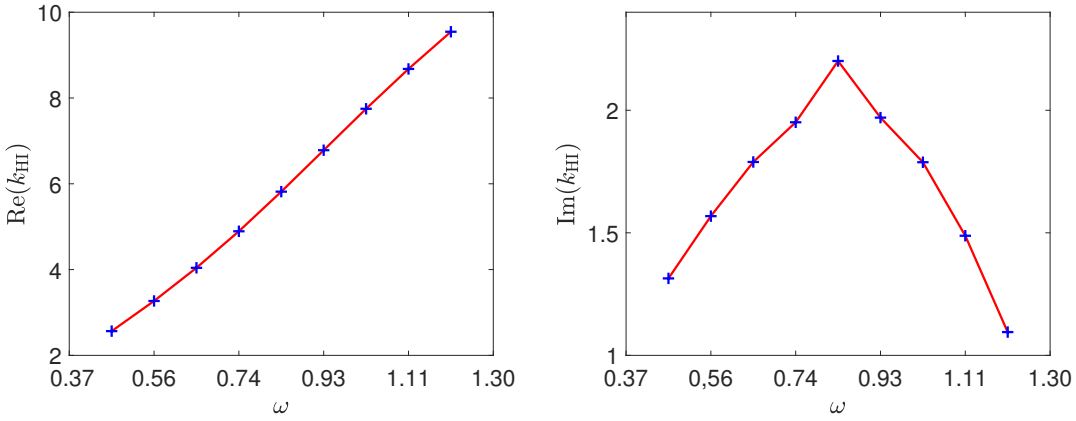


Figure 4.33: Effect of frequency $\omega$ on the wavenumber $k_{\mathrm{HI}}$. Left, Re($k_{\mathrm{HI}}$) and right, Im($k_{\mathrm{HI}}$).

boundary layer thickness on the wavenumber $k_{\mathrm{HI}}$ is displayed in figure 4.34. The wavelength of the instability tends to become longer when the boundary layer of the mean flow becomes thinner, and the spatial growth rate of instability tends to be much larger. When the boundary layer thickness approaches to 0, the instability is related to the instabilities in the application of Ingard-Myers boundary condition. Simulations have also been performed by using a relatively thick boundary layer, for example $\delta^* = 10\%$, and no instability is observed. It also has been demonstrated in previous studies [110]. The results indicate that instabilities tend to be observed for the mean flow with a thin boundary layer.

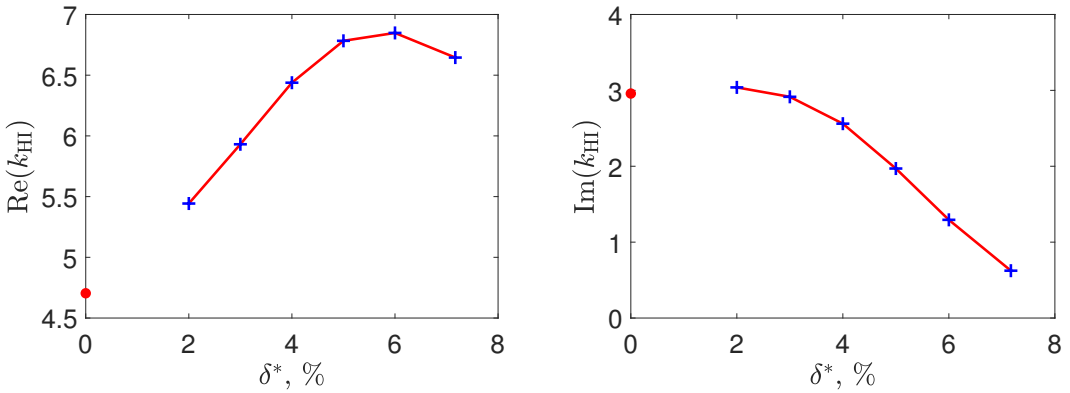


Figure 4.34: Effect of boundary layer thickness $\delta^*$ on the wavenumber $k_{\mathrm{HI}}$. Left, Re($k_{\mathrm{HI}}$) and right, Im($k_{\mathrm{HI}}$). Wavenumber calculated by using the Ingard-Myers boundary condition, ●.

### 4.4.3 Effect of Mach number $M$

The effect of Mach number $M$ on the wavenumber $k_{\mathrm{HI}}$ is presented in figure 4.36. The Mach number of the mean flow varies from $M = 0.3$ to $M = 0.55$ with the boundary layer thickness remains $\delta^* = 5\%$. The mean flow profiles are illustrated in figure 4.35. Other parameters keeps same as case 2 in section 4.2.1. With the increase of Mach number $M$, the wavelength of the instability grows continuously, while the spatial growth rate of the instability gradually decreases.

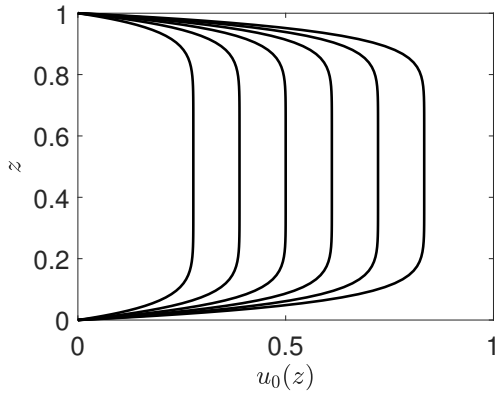


Figure 4.35: Flow profiles varying with Mach number. From left to right, Mach number is respectively $M = 0.3$, 0.35, 0.4, 0.45, 0.5 and 0.55.

To be noticed, since the ratio of the boundary layer thickness is kept the same, the real thickness of the boundary layer becomes thicker. In the situation, the instabilities turn to become weaker with the increase of Mach number $M$. Marx & Aurégan [10] also conducted the study of the effect of a mean flow Mach number on the wavenumber of instabilities. They showed that there was a threshold of mean flow Mach number for the existence of instabilities. When the mean flow Mach number $M$ was increased, the maximum of the spatial growth rate for instabilities shifted towards a higher frequency. Therefore an accurate description of the mean flow profile is necessary to precisely predict the instability.

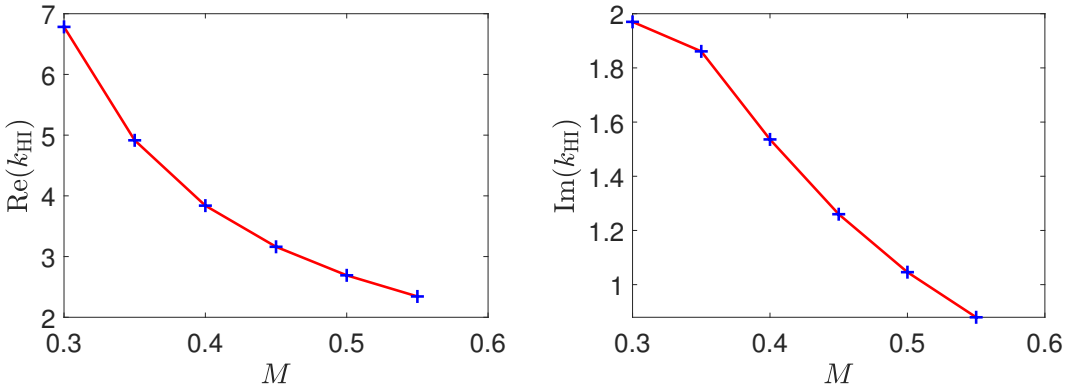


Figure 4.36: Effect of Mach number $M$ on the wavenumber of the unstable mode $k_{\mathrm{HI}}$. Left, $\mathrm{Re}(k_{\mathrm{HI}})$ and right, $\mathrm{Im}(k_{\mathrm{HI}})$.

### 4.4.4 Effect of resistance Re($Z$)

The effect of resistance on the hydrodynamic instability is investigated at $\omega = 0.9271$. The resistance of the MSD liner $\mathrm{Re}(Z)$ increases from 0.05 to 0.4 with the reactance kept constant $\mathrm{Im}(Z) = 0.005$. The other parameters are chosen as case 2 in section 4.2.1. Actually, the resistance of a acoustic liner aims at modelling dissipation effect; therefore the increasing of $\mathrm{Re}(Z)$ may help to prevent the generation of instabilities. Figure 4.37 shows that the wavelength

of the instability tends to be shorter with the increase of resistance. Meanwhile, the spatial growth rate fluctuates. The maximum of the spatial growth is obtained at $\mathrm{Re}(Z) \approx 0.2$. It is also checked that when the resistance is quite large, for example $\mathrm{Re}(Z) = 0.85$, no unstable mode is observed.

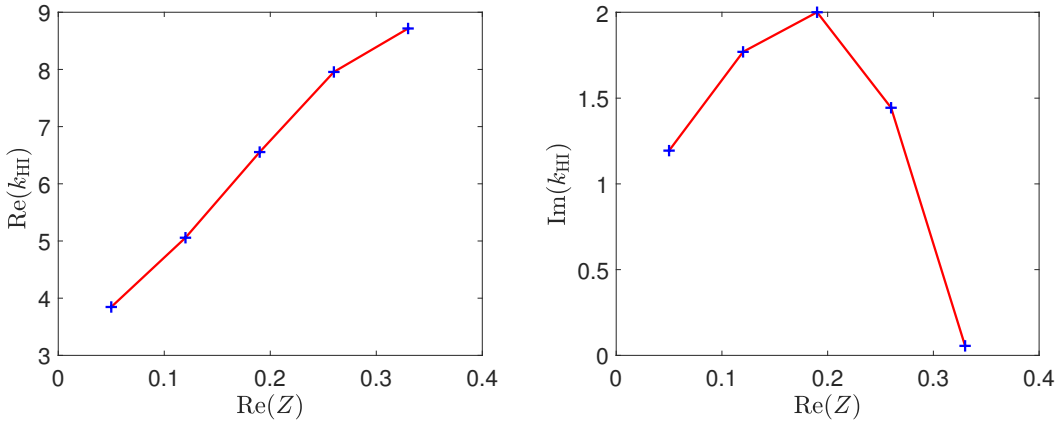


Figure 4.37: The effect of resistance $\mathrm{Re}(Z)$ on the wavenumber $k_{\mathrm{HI}}$. Left, $\mathrm{Re}(k_{\mathrm{HI}})$ and right, $\mathrm{Im}(k_{\mathrm{HI}})$.

The effect of resistance is also studied on case 3 of section 4.2.1, where absolute instabilities are observed. The resistance of the liner CT57 is increased with a value 0.4 and 0.8, while the reactance is maintained the same. The impedance of the original CT57 is denoted by $Z_{\mathrm{ct}}$, while the others are expressed as $Z_{\mathrm{ct}} + 0.4$ and $Z_{\mathrm{ct}} + 0.8$. The impedance and admittance are both given in figure 4.38. The pressure response to a harmonic source at $\omega = 0.9271$ for the modified liners on the lined wall are respectively shown in figure 4.39. The absolute instability are weakened greatly by increasing the resistance of the CT57 liner. The dissipation due to increasing the resistance of the liner is encouraging.

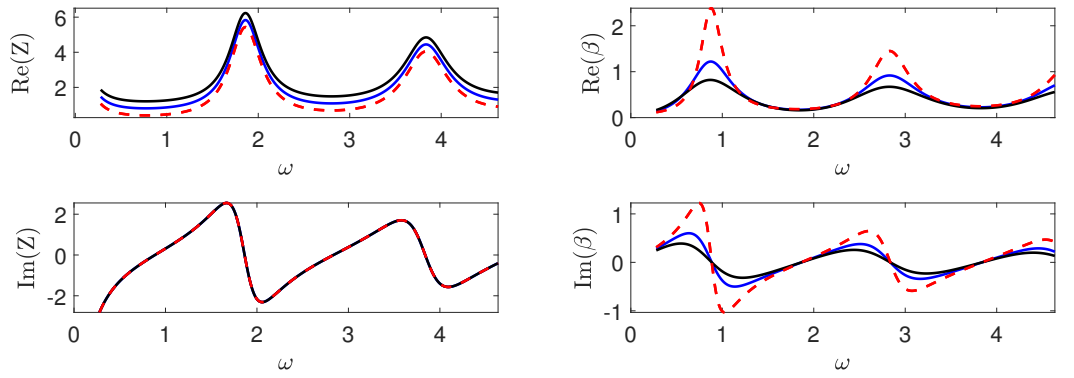


Figure 4.38: Impedance and admittance of the modified liner. $Z_{\mathrm{CT57}}$, - - -; $Z_{\mathrm{CT57}} + 0.4$, ——— and $Z_{\mathrm{CT57}} + 0.8$, ———. Left, impedance $Z$ and right, admittance $\beta$.

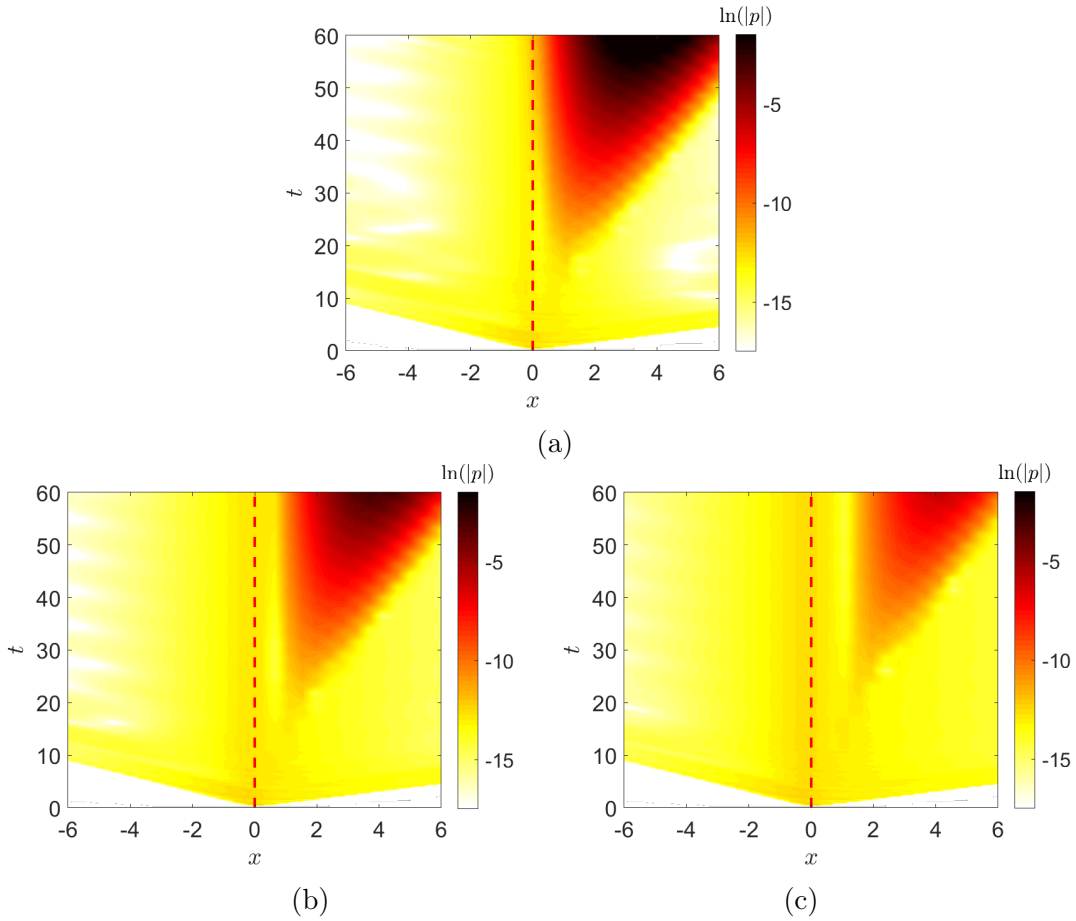


Figure 4.39: The pressure response $\ln|p(x, z = 1, t)|$ by applying liners $Z_{\mathrm{ct}}$, $Z_{\mathrm{ct}}+0.4$ and $Z_{\mathrm{ct}}+0.8$ at $\omega = 0.9271$. (a),$Z_{\mathrm{ct}}$; (b), $Z_{\mathrm{ct}} + 0.4$ and (c), $Z_{\mathrm{ct}} + 0.8$.

### 4.4.5 Effect of reactance Im($Z$)

The impact of reactance on the instability is shown in figure 4.40. The reactance Im($Z$) varies from 0.001 to 0.1 while the resistance remains Re($Z$) = 0.2. The other parameters are the same as used in case 2 of section 4.2.1. The effect of reactance on the instability is shown in figure 4.40. The wavelength becomes shorter during the variation of Im($Z$) from 0.001 to 0.1. At the same time, the spatial growth rate of the unstable mode grows successively, which implies instabilities becomes more vigorous. The transition from convective instability to absolute instabilities may be stimulated.

To validate the speculation that the increase of admittance would enhance the instability, several MSD liners are utilized. The MSD liner models are linear ones. The resistance of the MSD models remains 0.2 and the reactances of the MSD model at $\omega = 0.9271$ ($f = 1000$ Hz) are 0.005, 0.1 and 0.2. The corresponding parameters of MSD liners are given in Table 4.3 and their impedances and admittances are shown in figure 4.41.

When the MSD2 liner is applied, the temporal-spatial analysis is performed as shown in figure 4.42. The saddle point obtained at $\omega_s = 0.9243 - 0.0185\mathrm{i}$ ($f = 997 - 20\mathrm{i}$ Hz) is located at $k_s = 7.18 + 7.77\mathrm{i}$. The pressure responses $\ln|p\,(x, z = 1, t)\,|$ to a harmonic source at $\omega = 0.9271$

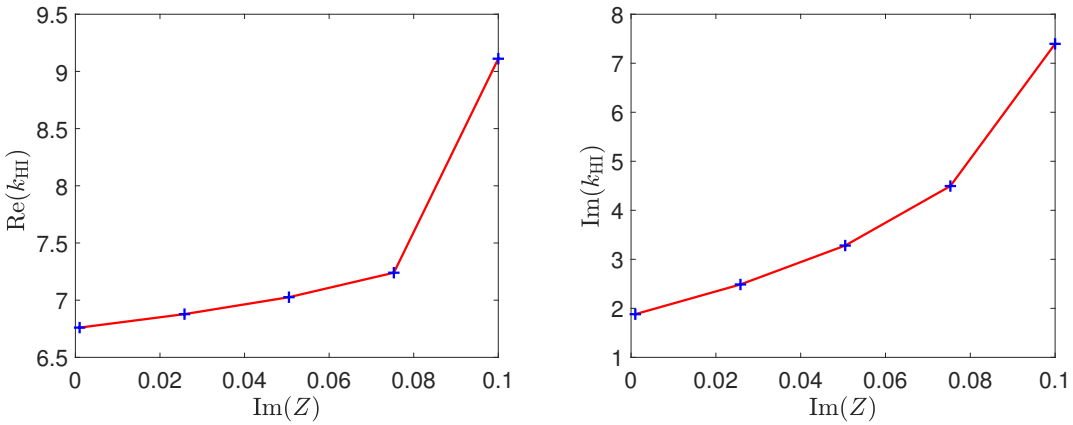


Figure 4.40: Effect of reactance $\mathrm{Im}(Z)$ on the wavenumber $k_{\mathrm{HI}}$. Left, $\mathrm{Re}(k_{\mathrm{HI}})$ and right, $\mathrm{Im}(k_{\mathrm{HI}})$.

Table 4.3: Parameters of several MSD liners

| $Z(\omega)$ | $R$ | $m$ | $K$ |
|---|---|---|---|
| MSD | 0.2 | $5.4 \times 10^{-3}$ | 0 |
| MSD2 | 0.2 | $1.08 \times 10^{-1}$ | 0 |
| MSD3 | 0.2 | $2.16 \times 10^{-1}$ | 0 |

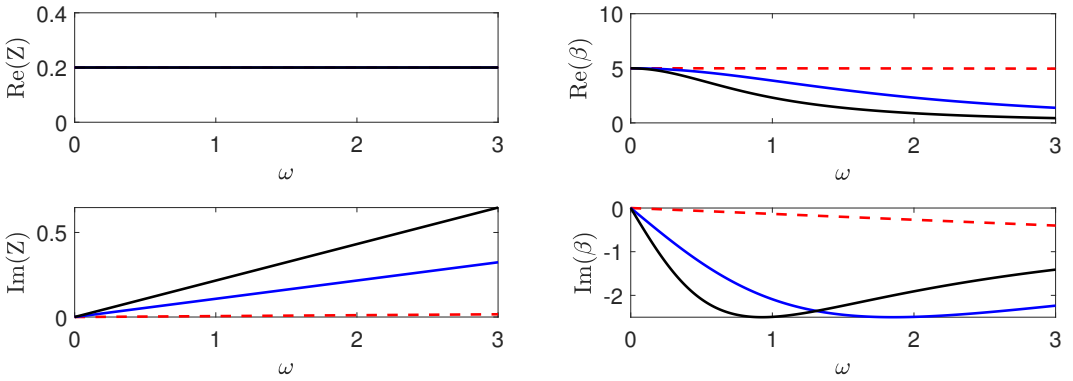


Figure 4.41: Impedance (left) and admittance (right) model for several MSD liners. $Z_{\mathrm{MSD}}$, ----; $Z_{\mathrm{MSD2}}$, ——— and $Z_{\mathrm{MSD3}}$, ———.

for MSD2 liner and MSD3 liner are shown in figure 4.43. The type of instabilities is clearly the absolute one for both case. Furthermore, the instabilities for the MSD3 liner is much severe than the MSD2 liner. The results indicates that the increase of $\mathrm{Im}(Z)$ can lead to stronger instabilities.

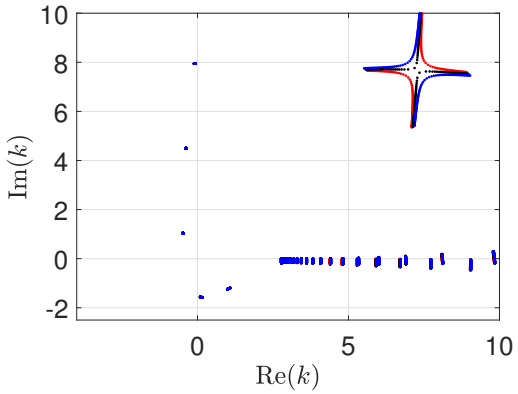


Figure 4.42: Trajectories of wavenumbers $k$ with the $\mathrm{Im}\,(\omega)$ increasing from large negative to 0 for different reactance $\mathrm{Im}\,(Z)$. $\mathrm{Im}\,(Z) = 0.1$, $\mathrm{Re}\,(\omega) = 0.9234$, •; $\mathrm{Re}\,(\omega) = 0.9243$, •; $\mathrm{Re}\,(\omega) = 0.9252$, •.

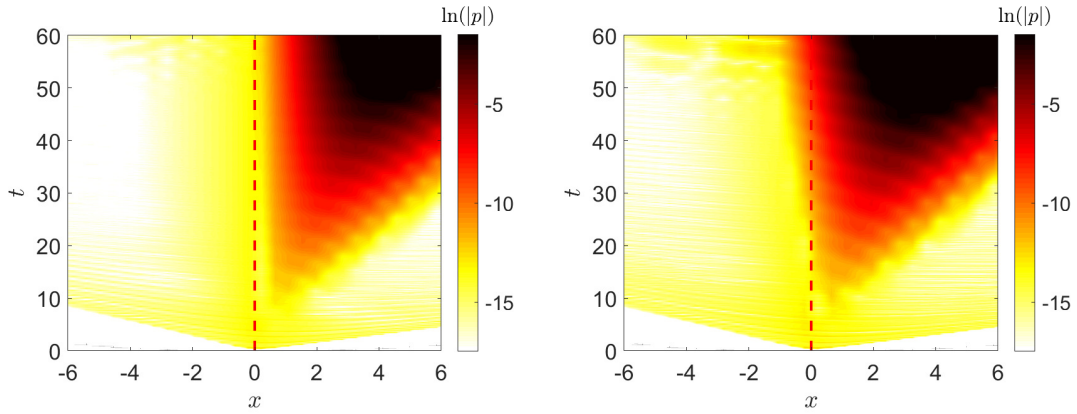


Figure 4.43: Pressure response to the source at $\omega = 0.9271$ on the lined wall $z = 1$ for left, $\mathrm{Im}(Z) = 0.1$ and right, $\mathrm{Im}(Z) = 0.2$. ---- source position on the $x$-axis.

## 4.5 Conclusion

In the present chapter, four cases: without instability, with convective instabilities and with absolute instabilities, were studied in the frequency domain and time domain. These four cases were proposed according to the existence of the hydrodynamic instabilities during the acoustic propagation along a lined flow duct.

The modal analysis approach developed in the previous chapter was used to determine the distribution of modes and mode shapes. The Briggs-Bers criterion was then applied to determine the propagation direction of modes and to separate unstable downstream propagating modes from stable upstream propagating modes. It was also used to specify the type of instabilities for each case considered. It was shown that no instability, convective instability and absolute instability were involved in the four cases.

The characterization of instabilities was focused on case 2. The method to obtain the wavenumber of instabilities from the time-domain approach was presented. The results of the characterization of the hydrodynamic instability from the time-domain simulations were also

compared with the modal analysis approach. A good agreement for the wavenumber and mode shape of the instability between the time-domain solutions and the modal analysis approach was obtained. The impact of the grid resolution and selective filter on instabilities, which have been reported to have a significant influence on instabilities in the literature, was investigated. It turns out that very fine grids, compared to what is required for acoustic waves, are necessary to precisely calculate the instability.

A parametric study was conducted to study the effect of the source frequency, the mean flow profile and the impedance of the liner on the hydrodynamic instability. The instabilities existed in a certain range of frequency and had a maximum growth rate in this range. The mean flow profile, containing the boundary layer thickness and Mach number, had a complex effect on the instability. The importance of a precise determination of flow profile was therefore addressed. The instabilities tended to become more severe when a small resistance and a relatively large reactance were adopted.

# 5 Removing instabilities in the lined flow duct

The previous chapter has examined the hydrodynamic instabilities generated during the acoustic propagation in a lined flow duct. Although the nature of the instabilities is proved to be physical, these instabilities are found very rarely experimentally and only under special conditions [110]. When a time-domain LEE solver is employed to study the problem as presented in the previous chapter, the instabilities often develop during the acoustic propagation. The acoustic field is contaminated by the instabilities, and the prediction of the acoustic field is not reliable anymore. Occasionally, they can even lead to diverged results and hinder the time-domain simulation.

The objective of the chapter is to present the partial Gradient Term Suppressing (GTS) method for removing the instabilities generated during the acoustic propagation in a lined flow duct. The impact of the partial GTS method on the acoustic propagation is hence imperative to address. It is imperative to notice the compensate for a stable computation.

The outline of this chapter is as follows: the techniques commonly applied to suppress instabilities are reviewed in the first part. The partial Gradient Term Suppressing (GTS) method is then presented. Finally, three cases are tested to investigate the effect of the partial GTS method on acoustic propagation, convective instabilities and absolute instabilities in the frequency domain and in the time domain.

## 5.1 Techniques of removing instabilities

Various numerical techniques to remove or at least attenuate the instability on the liner have been explored in the past. The strategies to remove instabilities can be classified into three classes, which are using coarse meshes and selective filtering, taking account of viscous effects and substituting the LEE by related and stable equations.

### 5.1.1 Selective filtering and coarse meshes

Since the instability often appears in fine grids, the use of coarse grids and an artificial damping has been recommended to attain a stable simulation [123]. In computational aeroacoustic calculation, selective filters are applied to remove spurious short waves. They work as a low-pass spatial filter and are regarded as artificial dissipation terms. Previous researches [123, 29, 120] examined

the role played by selective filtering and mesh size on suppressing the instabilities related with a lined flow duct.

Richter & Thiele [123] reported that resolving a shear flow with boundary layer without using Myers boundary condition was capable of accounting for the diffraction effects. Nevertheless, instabilities still existed in the system. In the case of a "plug flow" with the use of Myers boundary condition, it was shown that an additional dissipative low order filtering stabilized the hydrodynamic instabilities. Even if a 3-point selective filter can stabilize the Myers boundary condition and the impact of filtering on the acoustic propagation is small for a generic intake case, the suppression of instabilities by adjusting selective filters is however a process of trial and error. It depends strongly on the numerical schemes and the instabilities themselves. As a result, it may not be a reliable strategy to remove instabilities. On the other hand, the selective filters are designed to remove grid-to grid oscillations. It is demanded to have relatively small modifications on the acoustic part. If the instabilities do exist physically, the use of a selective filter, which implicitly assumes the instabilities are of numerical kind, is not reasonable [113]. In addition, it is not straightforward to ensure that the selective filters impact the instabilities and not the acoustic part.

Marx [29] examined the case of convective instability in the time-domain and assessed the impact of selective filtering and grid size. He considered that if the instability is physical, increasing the grid size or strengthening the selective filters does not necessary attenuate the instability. Instead, he proposed to consider the nonlinear terms in the equations and even to perform direct numerical simulations to resolve the physical instabilities as realistically as possible.

Brambley & Gabard [120] studied the instabilities involved in the acoustic propagation with the use of the modified Myers boundary condition and a "plug flow". They indicated that both the genuine instabilities of the unstable and artificial instabilities introduced by the numerical discretization schemes existed in their temporally unstable system. Several spatial selective filters were designed and applied only on the impedance boundary rather than the whole computational domain. Finally, the encouraging performance of the seven point 4th order filter to remove the artificial kind of instabilities was demonstrated.

### 5.1.2 Viscous effect

With the assumption of small perturbations, LEE is utilized to study the acoustic propagation. However, because the viscous effect and nonlinear terms are neglected, the instabilities can grow infinitely due to the complex interaction between the acoustic waves, the mean flow and the liner. Researchers have attempted to evaluate the impact of the viscous effect on the instabilities.

The account for thermoviscous effects [124] or turbulent dissipation through an eddy viscosity profile [10, 98, 125] is capable of attenuating the instability. It can even lead the nature of instability to change from absolute to convective [10, 124]. Including turbulent dissipation shows that the properties of the instability appear to be close to the experimental results. More recently, numerical simulations of a channel flow with an acoustic liner using implicit large eddy

simulations [126] were performed. Surface waves with characteristics similar to the instability predicted by linear stability analysis were exhibited. However, very fine grids, and even tremendous computational resources for direct numerical simulations, are needed in those studies to properly capture the instability, which is a strong disadvantage if the goal of the simulations is the computation of the acoustic field.

### 5.1.3 Substitution of LEE

The third approach is the substitution of the underlying LEE by a new set of equations which are inherently stable. When LEE is employed to predict acoustic or vortical waves propagate through a strongly sheared mean flow, the Kelvin-Helmoltz (KH) instabilities usually complicate the results. Because of neglecting the nonlinear terms and viscous effect, the KH instabilities develop into boundlessly infinitely growing instabilities and they finally lead to divergent and inaccurate predictions. These instabilities exist in various shear flows, including fan exhaust noise [127, 128, 129, 130], two-dimensional shear layers [131, 128, 132] and ducted flows [131, 128, 132, 130]. Therefore, numerous studies have attempted to eliminate the KH instabilities. The KH instabilities which occur in the acoustic propagation are caused by the difference of velocity in the shear flows, for example free stream and jet stream at a nacelle exhaust. The mechanism of instabilities in a lined duct is however different from that of KH instabilities. Specifically, the instabilities in a lined flow duct will only be generated with the use of acoustic liners. In other words, instabilities are not present only because there is a shear flow. Even though it is worthwhile to attempt to apply these techniques to suppress the hydrodynamic instabilities of a lined flow duct.

Among them, we can mention the gradient term suppression method (GTS) [133, 128, 129, 134, 135], the acoustic perturbation equations (APE) [136, 130, 131], the linearized perturbed compressible equations [137, 138], or the gradient term filtering method(GTF) [132, 131].

Bogey *et al.* [133] presented an acoustic analogy based on LEE to study the acoustic far-field. The sound field generated by vortex pairings in mixing layers was studied. To avoid the growing instabilities introduced through the mean flow gradient term, a simplified LEE, which later was named as GTS method, was first proposed. Comparison between the original LEE and the simplified one was made to analyse the acoustic pressure generated by a harmonic source in a shear flow. They showed that the LEE with GTS gave a good approximation of acoustic propagation.

Later the uses of GTS method were widely applied to obtain acoustic propagation free of KH instabilities. Tester *et al.* [127] assessed the effect of the mean flow gradient term on fan exhaust propagation noise at a landing and take-off stage. Both the analytical and numerical methods were conducted to compare the difference of SPL between LEE and LEE with GTS (the mean flow gradient term is totally removed). They showed the effect of GTS is small and not significant. The author thought the GTS method could lead to an underestimation of acoustic radiation. It was because of the interaction between Kelvin-Helmholtz instabilities with sharp

lips and liner impedance instabilities [139].

Iob *et al.* [134] presented a numerical model for solving the exhaust noise radiation problem. The near-field acoustic propagation was investigated with LEE and the GTS method to remove Kelvin–Helmholtz instabilities. Coupled with the Ffowcs Williams and Hawkings method, the acoustic propagation in far-field was obtained.

Özyörük and Tester [129] studied the acoustic propagation of fan noise through the bypass exhaust jet and the radiation in the far-field based on a frequency-domain LEE solver. They compared the results of their approach with experimental data. Convective instabilities appeared in some of their results. In accordance with Michalke's instability criterion, they found that the convective instabilities referred to KH instabilities. They applied the GTS method to obtain a pressure field free from instabilities. A good agreement between their approach with GTS method and experimental data was reported, even if 2-3 dB deviation caused by suppressing the gradient term was noticed.

Richter *et al.* [128] proposed a new method to suppress shear layer instabilities and compared it with the method of Bogey [133], Ewert [136] and Li [140]. This method stabilizes the instabilities through including filtering of the base flow and its derivatives. The flow field then is modified with a less distinct inflection point and an increase of the shear layer thickness. The comparison showed that the new method can both suppress instabilities and allow an accurate prediction of acoustic field. However, the choice of the filtering and its filtering cycle needs to be specified according to each specific case. In practice, when the analytical solution is not available, these parameters are difficult to be set.

Zhang *et al.* [132] employed the Gradient Term Filtering (GTF) method on time-domain LEE to study the sound propagation in a shear flow. A divergence operator and a curl operator used as filters to maintain acoustic and vortical components. The results of the GTS method were compared on several benchmark cases. It was concluded that the GTF method has a rather small effect on the prediction of sound propagation and was capable of studying vortical waves. Regarding computational cost, the GTF method was relatively expensive but easy to implement.

The APE [136] model which is developed from LEE, constructs an acoustic filtering matrix to isolate the non-acoustic modes. Consequently, acoustic propagation free from instabilities is available. Several variants, for example, from APE1 to APE4, have been developed. It can be noted that the homogeneous APE without any source terms corresponds to the perturbation equations of Pierce [141].

Huang *et al.* [130] presented two numerical models in cylindrical coordinates, the revised 2.5D LEE model and the acoustic perturbations equation model(APE), to predict spinning modal sound propagation in a flow duct. The revised 2.5D LEE model [142, 143], which omits the mean flow gradient term to obtain a stable simulation, has a similar effect to the GTS method. They showed that both methods can effectively remove instabilities generated in the shear layers. The agreements between both methods for predicting acoustic propagation in the near-field and far-field were quite well. They suggested the APE approach to consider arbitrary background

flows.

Based on the existing techniques (GTS, GTF and APE methods), Sun *et al.* [131] proposed several new methods, namely GTS-2, GTS-3, GTF-2 and an artificial damping terms (ADT) method to remove KH instabilities. All the methods mentioned were tested on four benchmark cases. The comparisons of errors for all the methods for the different test cases were given. Even if depending on the certain benchmark case, the performance, the error and the computational costs of each method varied, they demonstrated the effectiveness of their proposed methods to limit the exponential growing waves in the sheared mean flow.

It has been shown that most of them are similarly effective for these particular flows [131]. The GTS method is opted in this study as a first approach to the case of acoustic liners. However, other methods might perform similarly or even better in certain cases. A future comparative study would certainly be useful.

## 5.2 Gradient term suppressing techniques

A natural generalization of the original GTS method is used here to suppress the instability, consisting of a partial suppression of the gradient term instead of a complete suppression. Eq. (3.1b) is modified by adding a coefficient $\epsilon$ in front of the term of $\mathrm{d}u_0/\mathrm{d}z$. Consequently, Eq. (3.1b) turns to

$$\frac{\partial u}{\partial t} + u_0 \frac{\partial u}{\partial x} + \epsilon \frac{\mathrm{d}u_0}{\mathrm{d}z} v + \frac{\partial p}{\partial x} = 0 \tag{5.1}$$

where $\epsilon$ adjusts the strength of the mean flow gradient term and ranges from 1 to 0.

Combining Eqs. (3.1a), (5.1) and (3.1c) leads to the wave equation:

$$\frac{\mathrm{D}}{\mathrm{D}t}\left(\frac{\mathrm{D}^2 p}{\mathrm{D}t^2} - \nabla^2 p\right) + (\epsilon + 1)\frac{\mathrm{d}u_0}{\mathrm{d}z}\frac{\partial^2 p}{\partial x \partial z} = \frac{\mathrm{D}^2 Q}{\mathrm{D}t^2} \tag{5.2}$$

where $\mathrm{D}/\mathrm{D}t = \partial/\partial t + u_0\,\partial/\partial x$ is the material derivative. In particular, the Lilley's equation is recovered for $\epsilon = 1$. The decrease of $\epsilon$ from 1 to 0 is thus equivalent to transform the original Lilley's equation, which sustains unstable modes, to a simplified form of Lilley's equation which appears to be inherently stable [133]. In addition, decreasing $\epsilon$ from 1 to 0 diminishes the refraction term proportional to $\mathrm{d}u_0/\mathrm{d}z$ in the original Lilley's equation by a factor of two. A gradual suppression of the instability is then expected when diminishing the value of $\epsilon$. It should be noted that the effect of the partial GTS method on acoustic propagation is mostly observed at low frequencies. It is because that with the decrease of $\epsilon$, the coefficient in front of the refraction term $\dfrac{\mathrm{d}u_0}{\mathrm{d}z}\dfrac{\partial^2 p}{\partial x \partial z}$ in Eq. (5.2) turns to $1+\epsilon$ while the coefficient is 2 in the original Lilly's equation. With frequency increasing, the high derivative term $\dfrac{\partial^2 p}{\partial x \partial z}$ in Eq. (5.2) becomes predominant [144, 145, 133]. As a result, the influence of $\epsilon$ on acoustic propagation is comparatively weak in the high frequency range.

It is also can be explained by conducting an order of magnitude analysis. The order of the

magnitude of each term in Eq.(5.1) is as follows:

$$\frac{\partial u}{\partial t} \sim \omega u,\ u_0\frac{\partial u}{\partial x} \sim Mku,\ \epsilon\frac{\mathrm{d}u_0}{\mathrm{d}z}v \sim \epsilon\frac{M}{\delta^*}v,\ \frac{\partial p}{\partial x} \sim kp, \tag{5.3}$$

where $\omega = k$ and $v \sim p$. Therefore, the effect of mean flow gradient term can be neglected if

$$\frac{\left|\dfrac{\epsilon v \mathrm{d}u_0}{\mathrm{d}z}\right|}{\left|\dfrac{\partial p}{\partial x}\right|} \ll 1. \tag{5.4}$$

Combining Eq.(5.4) with Eq.(5.3), leads to the conclusion

$$\left|\frac{\epsilon M}{\delta^*\omega}\right| \ll 1 \tag{5.5}$$

can thus be obtained. For $\omega \gg \dfrac{\epsilon M}{\delta^*}$, the impact of the mean flow gradient term can be neglected. It also explains why the high frequency components are less impacted.

## 5.3 Acoustic propagation with partial GTS method

Numerical simulations are performed to evaluate the viability of the partial GTS method to suppress instabilities and its effects on predicting acoustic propagation. The frequency-domain and time-domain analysis are carried out considering three cases, namely a rigid duct, a duct lined with the MSD liner and a duct with the CT57 liner. In the rigid duct case, no instabilities are expected. This case is designed to show the impacts of the partial GTS on the acoustic propagation. Then, the effect of the partial GTS on convective instabilities and absolute instabilities are demonstrated by using the MSD liner and the CT57 liner. Since the absolute instabilities are reported to be more severe than the convective one, we also want to check that how the partial GTS method acts on the two instabilities. The MSD liner and CT57 liner are the same as used in section 4.1.2 and 4.1.1, if there is no indication.

### 5.3.1 Frequency-domain study

The effect of the strength of mean flow gradient $\epsilon$ on the mode wavenumbers and mode shapes is analysed through the modal analysis approach. The default value of the number of grid points along the $z$-direction is 150. The frequency of the source is $\omega = 0.9271$ for all three cases.

#### Rigid duct

The wavenumbers of acoustic propagation along a rigid duct with a sheared mean flow are given in figure 5.1. The mean flow profile with an average Mach number $M = 0.3$ and a boundary layer thickness 5 % is shown in the right of figure 4.6. It can be clearly seen in figure 5.1 that the "plane

wave" modes propagating along the $+x$- and $-x$-direction are weakly affected by the strength of mean flow gradient $\epsilon$. The evanescent modes with order between 2 and 5 are influenced more greatly than the other modes. Even if the mean flow gradient term modifies the acoustic modes, its effect seems to be weak.

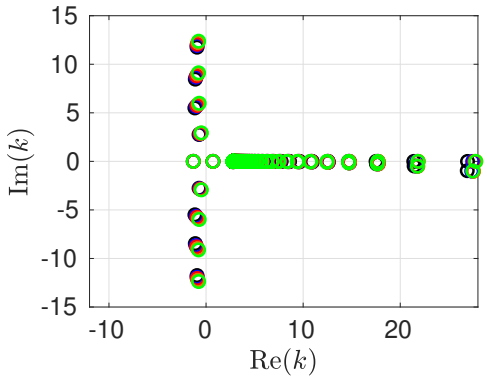


Figure 5.1: Wavenumbers in the $k$-plane at $\omega = 0.9271$ for a rigid duct and for different values of $\epsilon$: $\circ$ $\epsilon = 1$, $\circ$ $\epsilon = 0.7$, $\circ$ $\epsilon = 0.5$, $\circ$ $\epsilon = 0.2$ and $\circ$ $\epsilon = 0$.

The effect of $\epsilon$ on $|U|$, $|V|$ and $|P|$ are shown in figure 5.2. The shapes of 4 modes, namely the downstream and upstream "plane wave" mode and the first downstream and upstream evanescent mode, are illustrated. The modulus of all three variables is normalized by the maximum of $|P|$. Compared with $|U|$, the variations of $|V|$ and $|P|$ are more noticeable. The shapes of the downstream modes are impacted more seriously by the mean flow gradient term compared with the upstream modes regardless that the modes are propagative or evanescent. For example, there is a 12.3 % difference for the maximum of $|V|$ between $\epsilon = 0$ and $\epsilon = 1$ for downstream modes and a 4.4 % difference for upstream modes. The decrease of the strength of the mean flow gradient leads to an increase in the maximum of the $|V|$ except for the downstream evanescent mode.

The effect of $\epsilon$ on the cut-off frequency $\omega_n$ of the $n$-th mode is given in Table 5.1. The study has been conducted for three different values of the boundary layer thickness of the mean flow: $\delta^* =$ 0.5 %, 2 %, and 8 %. The average Mach number of the mean flow is $M = 0.3$. The corresponding cut-off frequencies for the uniform flow are attached as reference. The ratios of cut-off frequency between the sheared mean flow and the uniform flow are also given.

If we restrict ourselves to a specific mode, it is seen that the decrease of $\epsilon$ leads to the increase of the cut-off frequency. For the sheared mean flow with a thin boundary layer, the variation of $\omega_n$ is relatively small. For example, the ratio difference of $\omega_n$ is less than 0.1 % for the shear flow $\delta^* =$ 0.5 %, while it is up to 1.5 % for $\delta^* =$ 8 %.

As already mentioned in Table 3.2, the cut-off frequencies with a shear flow are usually lower than the ones with a uniform flow. However, the cut-off frequencies $\omega_n$ for a shear mean flow exceed the ones for a uniform flow when the mean flow gradient term is totally suppressed. For example, the cut-off frequency $\omega_n$ for $\delta^* = 2$ % and for $\epsilon = 0$ is 100.03 % compared with the uniform flow case.

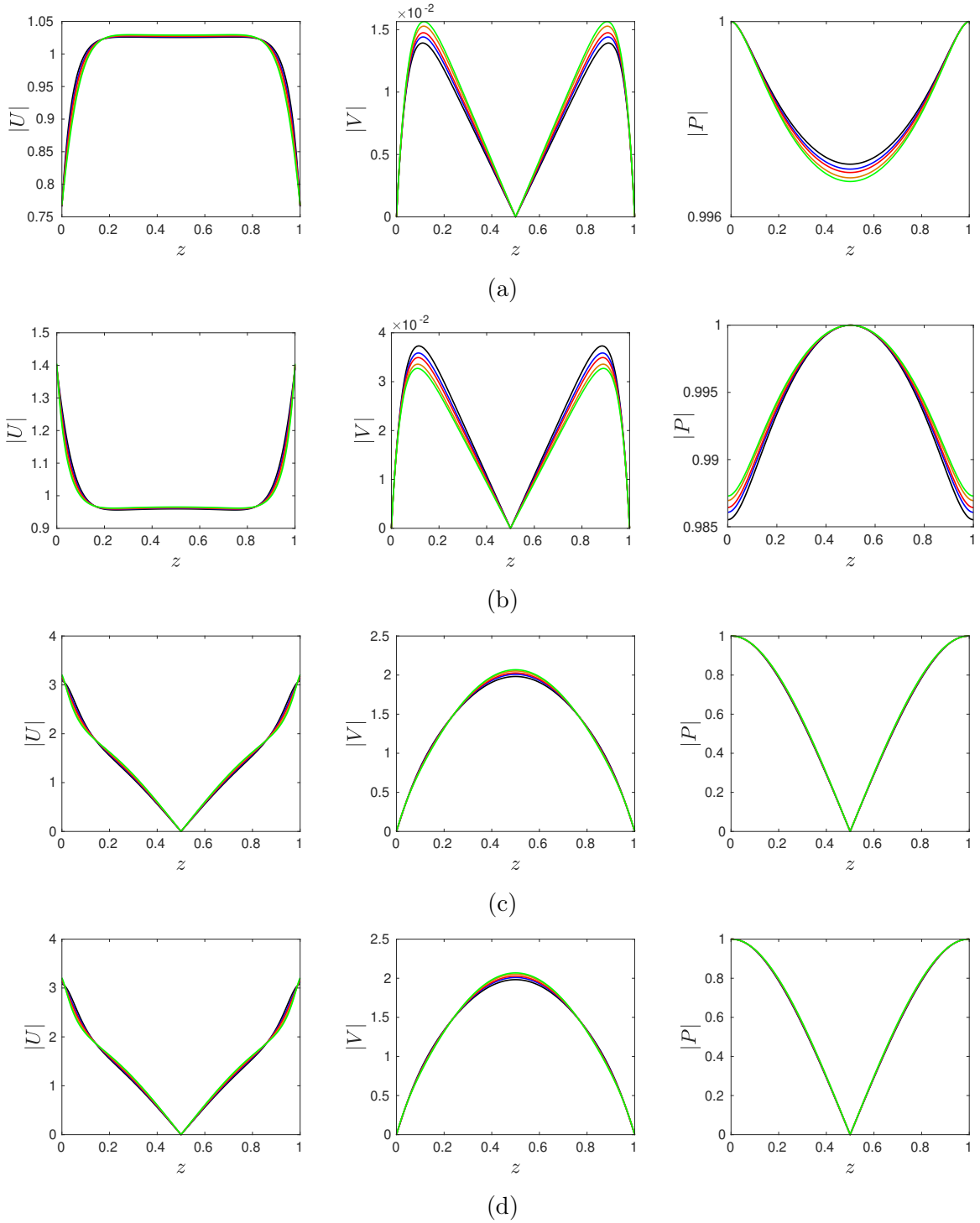


Figure 5.2: Mode shapes for the rigid duct at $\omega = 0.9271$ and for several values of $\epsilon$: $\epsilon = 1$, $\epsilon = 0.7$, $\epsilon = 0.5$, $\epsilon = 0.2$ and $\epsilon = 0$. (a) "Plane wave" mode (downstream); (b) "plane wave" mode (upstream); (c) the first downstream and (d) upstream evanescent modes for, from left to right, velocity components along $x$- and $z$-direction and pressure.

When we pay attention to a row in Table 5.1, we find that the ratio gets larger as the mode order increases. However, the row for $\delta^* = 8$ % and $\epsilon = 0$ is one exception: the monotonically increasing trend is not satisfied in this case.

Table 5.1: Cut-off frequency $\omega_n$ for the $n$-th mode on the $x$-direction for several values of $\delta^*$ and $\epsilon$.

The percentage in blue shows the ratios of cut-off frequency between the shear flow and the uniform flow.

| | $\epsilon$ | $n=2$ | $n=3$ | $n=4$ |
|---|---|---|---|---|
| uniform flow | | 2.9992 | 5.9946 | 8.9910 |
| $\delta^* = 0.5\ \%$ | $\epsilon = 1.0$ | 2.9945 (99.85 %) | 5.9891 (99.91 %) | 8.9836 (99.92 %) |
| | $\epsilon = 0.7$ | 2.9955 (99.88 %) | 5.9909 (99.94 %) | 8.9864 (99.95 %) |
| | $\epsilon = 0.5$ | 2.9964 (99.91 %) | 5.9919 (99.95 %) | 8.9883 (99.97 %) |
| | $\epsilon = 0.2$ | 2.9973 (99.94 %) | 5.9937 (99.98 %) | 8.9901 (99.99 %) |
| | $\epsilon = 0$ | 2.9973 (99.94 %) | 5.9946 (100 %) | 8.9920 (100.01 %) |
| $\delta^* = 2\ \%$ | $\epsilon = 1.0$ | 2.9871 (99.60 %) | 5.9752 (99.68 %) | 8.9642 (99.70 %) |
| | $\epsilon = 0.7$ | 2.9908 (99.72 %) | 5.9807 (99.78 %) | 8.9743 (99.80 %) |
| | $\epsilon = 0.5$ | 2.9927 (99.78 %) | 5.9863 (99.86 %) | 8.9799 (99.88 %) |
| | $\epsilon = 0.2$ | 2.9964 (99.91 %) | 5.9919 (99.95 %) | 8.9883 (99.97 %) |
| | $\epsilon = 0$ | 2.9982 (99.97 %) | 5.9965 (100.03 %) | 8.9938 (100.03 %) |
| $\delta^* = 8\ \%$ | $\epsilon = 1.0$ | 2.9556 (98.55 %) | 5.9427 (99.13 %) | 8.9456 (99.51 %) |
| | $\epsilon = 0.7$ | 2.9714 (99.07 %) | 5.9603 (99.43 %) | 8.9614 (99.67 %) |
| | $\epsilon = 0.5$ | 2.9806 (99.38 %) | 5.9724 (99.63 %) | 8.9716 (99.78 %) |
| | $\epsilon = 0.2$ | 2.9936 (99.81 %) | 5.9891 (99.91 %) | 8.9864 (99.95 %) |
| | $\epsilon = 0$ | 3.0020 (100.09 %) | 6.0002 (100.09 %) | 8.9966 (100.06 %) |

**MSD liner**

Acoustic propagation along the duct lined with the MSD liner is investigated when $\epsilon$ varies from 1 to 0. The mean flow is the same as the rigid duct case. Figure 5.3 depicts the wavenumbers for different values of $\epsilon$. It is first noticed that modifying $\epsilon$ tends to move all the modes in the complex $k$-plane. The instability for the lined duct, observed for $\epsilon = 1$, is not seen for the smaller values of $\epsilon$, which shows that a slight decrease of $\epsilon$ is sufficient to suppress the instability.

To analyse more finely the effect of $\epsilon$ on the instability, the variations of the instability wavenumber are plotted as a function of $\epsilon$ with a smaller step in figure 5.4. The results are shown for three different grid sizes ($N$ = 100, 200 and 300). The growth rate of the unstable mode decreases gradually with $\epsilon$ which proves the stabilizing effect of decreasing $\epsilon$. It is interesting to note that for $\epsilon \leq 0.94$, the wavenumber of the unstable mode starts depending on the grid size. There, the unstable mode merges into the continuous spectrum of vorticity modes near the real $k$-axis. The vorticity modes heavily depend on the discretization and they are not converging as the mesh size decreases.

This approach can bring us insights into the transition of unstable modes to another mode type *i.e* vorticity mode or evanescent mode, when the partial GTS method is applied. Specifically, the

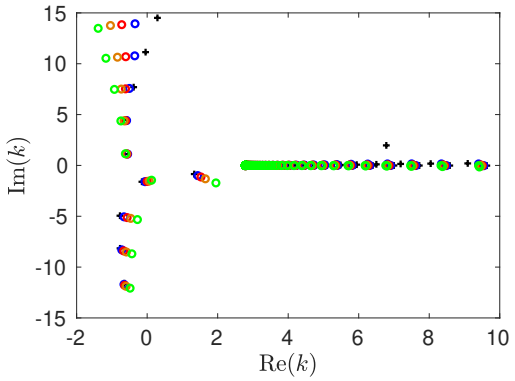


Figure 5.3: Wavenumbers in the $k$-plane at $\omega = 0.9271$ for a duct lined with the MSD liner and for different values of $\epsilon$: ○ $\epsilon = 1$, ○ $\epsilon = 0.7$, ○ $\epsilon = 0.5$, ○ $\epsilon = 0.2$ and ○ $\epsilon = 0$.

acoustic modes and unstable modes are converged with the mesh size, while the vorticity modes do not converge with the mesh size. This approach will be applied again in the study of CT57 liner to follow the transition of the unstable modes.

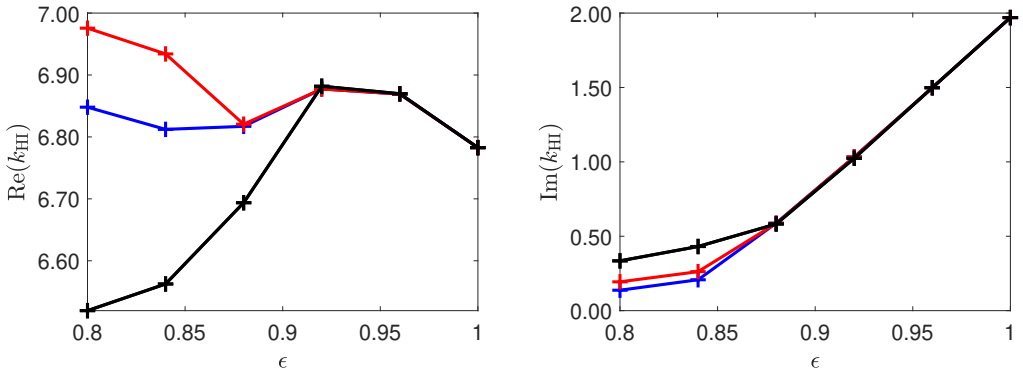


Figure 5.4: Variations of the (left) real and (right) imaginary parts of the instability wavenumber $k_{\mathrm{HI}}$ as a function of $\epsilon$ for different numbers of grid points: $N = 100$, $N = 200$ and $N = 300$.

Acoustic modes are also affected by reducing the parameter $\epsilon$. As an illustration, figure 5.5 depicts the mode shapes of the acoustic velocity components and pressure for the "plane waves" mode and for the leading upstream and downstream evanescent modes for different values of $\epsilon$. The modulus of all three variables are normalized by the maximum of $|P|$. Modifying $\epsilon$ has an evident impact on $|U|$ and $|V|$, noticeably near the lined wall. This effect is particularly dramatic for $|U|$, whose peak on the lined wall decreases by a factor of 10 from $\epsilon = 1$ to $\epsilon = 0$. Also, a noticeable increase of $|V|$ near the lined wall is observed as $\epsilon$ decreases. Concerning the pressure, the mode shape does not vary too much with $\epsilon$. For the "plane wave" mode, a decrease of the amplitude is noticed near the rigid wall, while for the evanescent modes, the amplitude grows gradually near the lined wall as $\epsilon$ decreases.

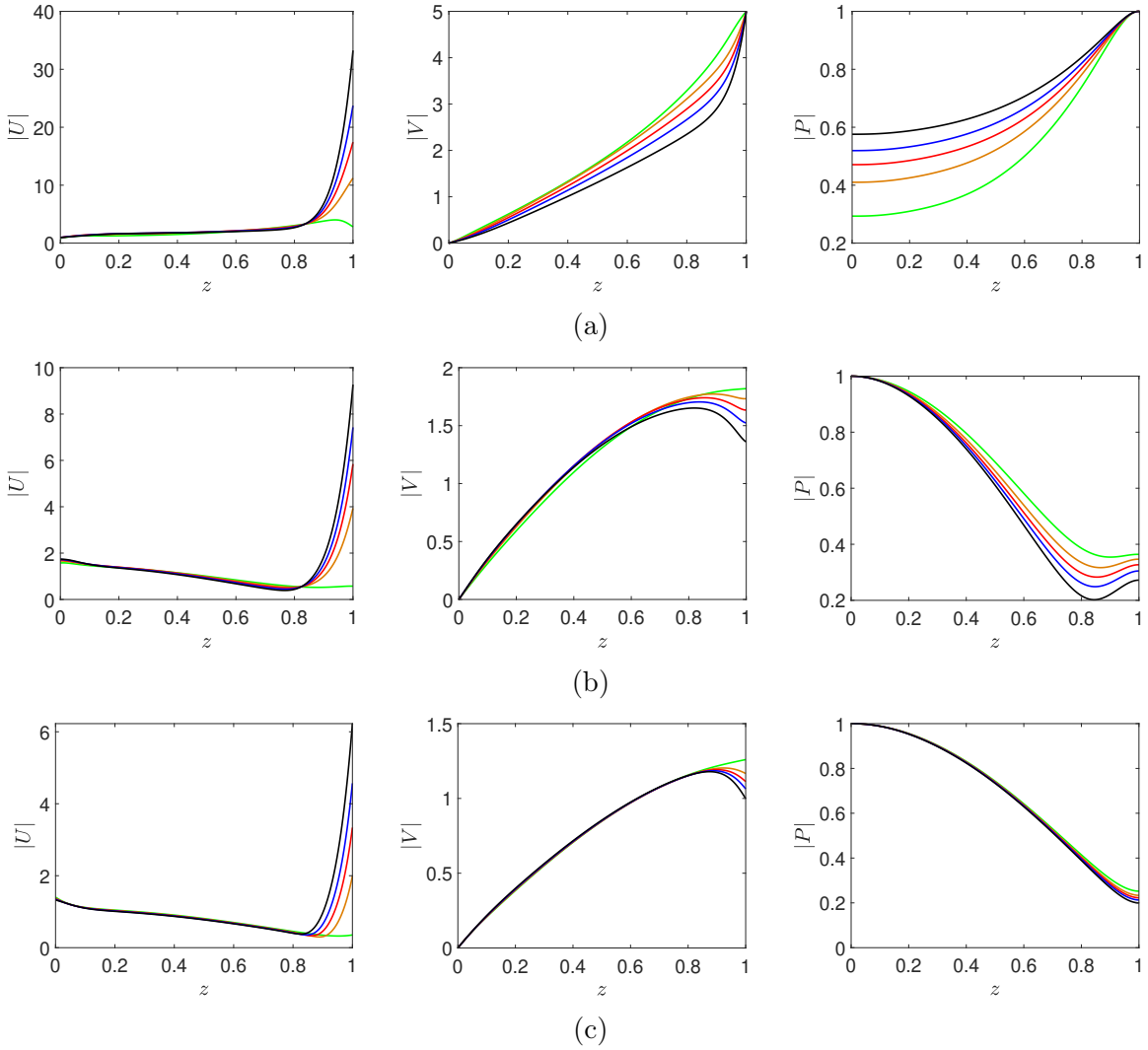


Figure 5.5: Mode shapes for the duct lined with MSD liner at $\omega = 0.9271$ and for several values of $\epsilon$: $\epsilon = 1$, $\epsilon = 0.7$, $\epsilon = 0.5$, $\epsilon = 0.2$ and $\epsilon = 0$. (a) "Plane wave" mode and leading (b) downstream and (c) upstream evanescent modes for, from left to right, velocity components along $x$- and $z$-direction and pressure.

### CT57 liner

The acoustic propagation along the duct lined with the CT57 liner with the mean flow for several values of $\epsilon$ is studied. The parameters of the mean flow are the same as given in section 4.1.4. Figure 5.6 shows the effect of variation of $\epsilon$ on mode wavenumbers. The unstable modes a and b are obtained for $\epsilon = 1$. Similar to the previous case, the unstable modes are modified significantly as $\epsilon$ is varying. For example, when $\epsilon$ decreases from 1 to 0.7, the unstable modes a and b both leave the upper right complex $k$-plane. The downstream and upstream "plane wave" mode are not affected obviously compared with other modes. As for the higher-order evanescent downstream and upstream modes, they move towards the right and left respectively with the decrease of $\epsilon$.

To better observe the evolution of the two unstable modes with $\epsilon$, figure 5.7 shows the wavenumbers varying with $\epsilon$ from 1 to 0.6 with a step of 0.04. Three different grid sizes $N = 100$,

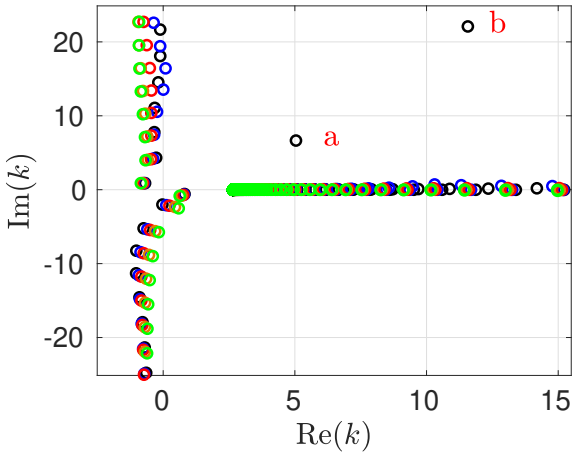


Figure 5.6: Wavenumbers in the $k$-plane at $\omega = 0.9271$ for a duct lined with the CT57 liner and for different values of $\epsilon$: ○ $\epsilon = 1$, ○ $\epsilon = 0.7$, ○ $\epsilon = 0.5$, ○ $\epsilon = 0.2$ and ○ $\epsilon = 0$.

$N = 200$ and $N = 300$ are applied in the study.

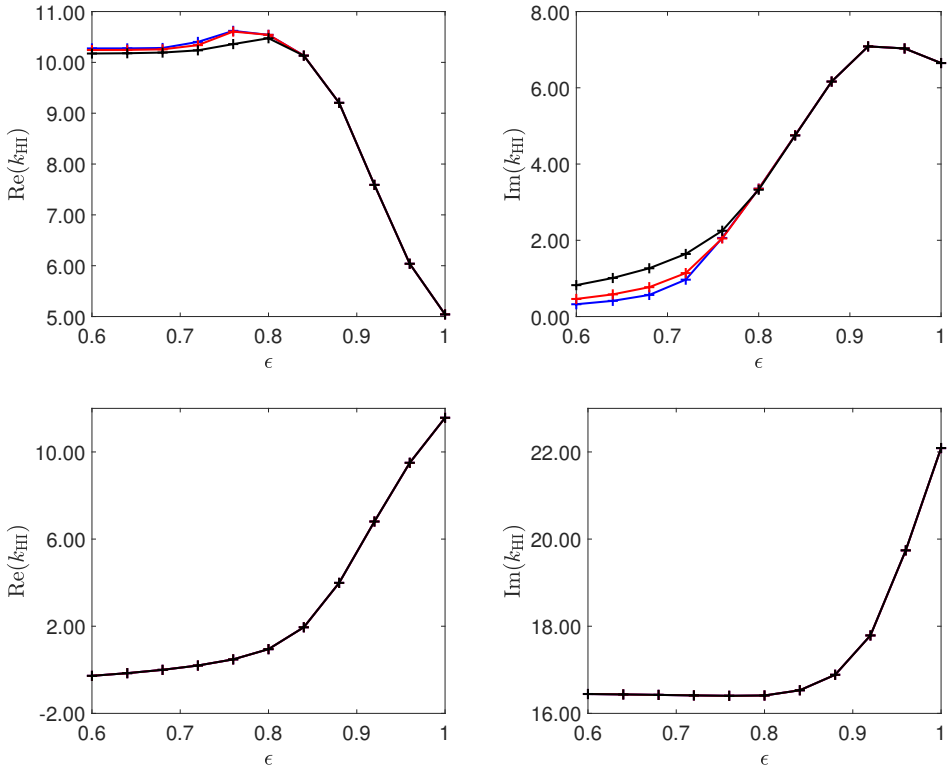


Figure 5.7: Variations of the real and imaginary parts of the wavenumbers of mode a and b as a function of $\epsilon$ for different numbers of grid points: $N = 100$, $N = 200$ and $N = 300$. Upper, mode a and lower mode b.

It is interesting to note that the spatial growth rate of mode a has a growing trend when $\epsilon$ decreases from 1 to 0.94. It indicates that the partial GTS method may not always inhibit the spatial growth rate of the instabilities. Then, when $\epsilon$ decreases from 0.94 to 0.6, $\mathrm{Im}(k_{\mathrm{HI}})$ of

the mode a gradually reduces to a relatively small number. The wavenumber is not converged anymore for the three different grid sizes when $\epsilon \leq 0.8$. It can be deduced that this unstable mode develops into a vorticity mode when $\epsilon$ gradually decreases from 1 to 0.6. For mode b, the wavelength of this mode increases and $\mathrm{Im}(k_{\mathrm{HI}})$ decreases with the reduction of $\epsilon$. It finally turns into an upstream evanescent mode.

The determination of the propagation direction of mode a and b for $\epsilon = 1$ and 0.5 is illustrated in figure 5.8. It is simple for the cases $\epsilon = 1$. For the cases $\epsilon = 0.5$, the wavenumber of two modes are firstly obtained when $\epsilon$ decrease from 1 to 0.5 for a real frequency $\omega = 0.9271$. Then these wavenumbers are used as entries to obtain the variation of $k$ when $\mathrm{Im}(\omega)$ varies from -2 to 0. These results validate our inference, which are during diminishing $\epsilon$, mode a turns to a vorticity mode. While, mode b develops in to a upstream evanescent mode. It can also be noted that the unstable mode b is transformed from a downstream amplified mode to a upstream evanescent mode during the reduction of $\epsilon$.

In summary, the decrease of $\epsilon$ makes the wavenumbers of the two unstable modes leave the upper right complex $k$-plane. However, the paths of the two modes have essential differences. The unstable mode can either become an upstream evanescent mode or a vorticity mode. In addition, suppressing the mean flow gradient term does not always restrain $\mathrm{Im}(k_{\mathrm{HI}})$.

Since the unstable modes already develop into other types of mode when the value of $\epsilon$ decreases from 1 to 0.6, figure 5.9 only shows shapes of the two unstable modes for $\epsilon = 1$. The modulus of all three variables is normalized by the maximum of $|P|$. For both modes, the peak of $|U|$, $|V|$ and $|P|$ is located on the lined wall or close to the lined wall. The peak value of $|U|$ is the largest compared with $|V|$ and $|P|$. For mode a, the maximum of $|U|$ is 15 times larger than the one of $|P|$, while for mode b, this ratio increases to 30. We also notice that the increasing trend of mode shapes for mode b from the rigid wall $z = 0$ to the lined wall $z = 1$ is relatively modest compared with mode a.

Shapes of acoustic modes for different values of $\epsilon$ are also presented in figure 5.10. The peak value of $|U|$, which is on the lined wall $z = 1$, decreases with $\epsilon$ for the three modes. The decrease of $\epsilon$ will lead to an amplification of $|V|$ for the downstream modes, even if $\epsilon = 0$ is an exception. The greatest variations occur for $|P|$ of the "plane wave" mode when $\epsilon$ decreases from 1 to 0. When $\epsilon \geq 0.5$, the maximum of $|P|$ is located on the lined wall. While for $\epsilon = 0.2$ and 0, the position of the maximum of $|P|$ is changed to the rigid wall. For the leading downstream evanescent mode, the position of the peak of $|P|$ also moves from the rigid wall to the lined wall when $\epsilon$ decreases. Compared with the two downstream modes, the upstream evanescent mode is not affected greatly. For this case, modifying $\epsilon$ will evidently alter the acoustic solution. Totally removing the mean flow gradient term is too brutal, as it is not desirable to have such dramatic modification of the acoustic field. The optimal value of $\epsilon$ should remove instabilities without too much modification of the acoustic field, Specifically, $\epsilon = 0.7$ seems to be a optimal value for the case of MSD liner, while the optimal value for the CT57 liner can be set between 0.5 and 0.7. These optimal value can be finally determined combining with the time-domain study.

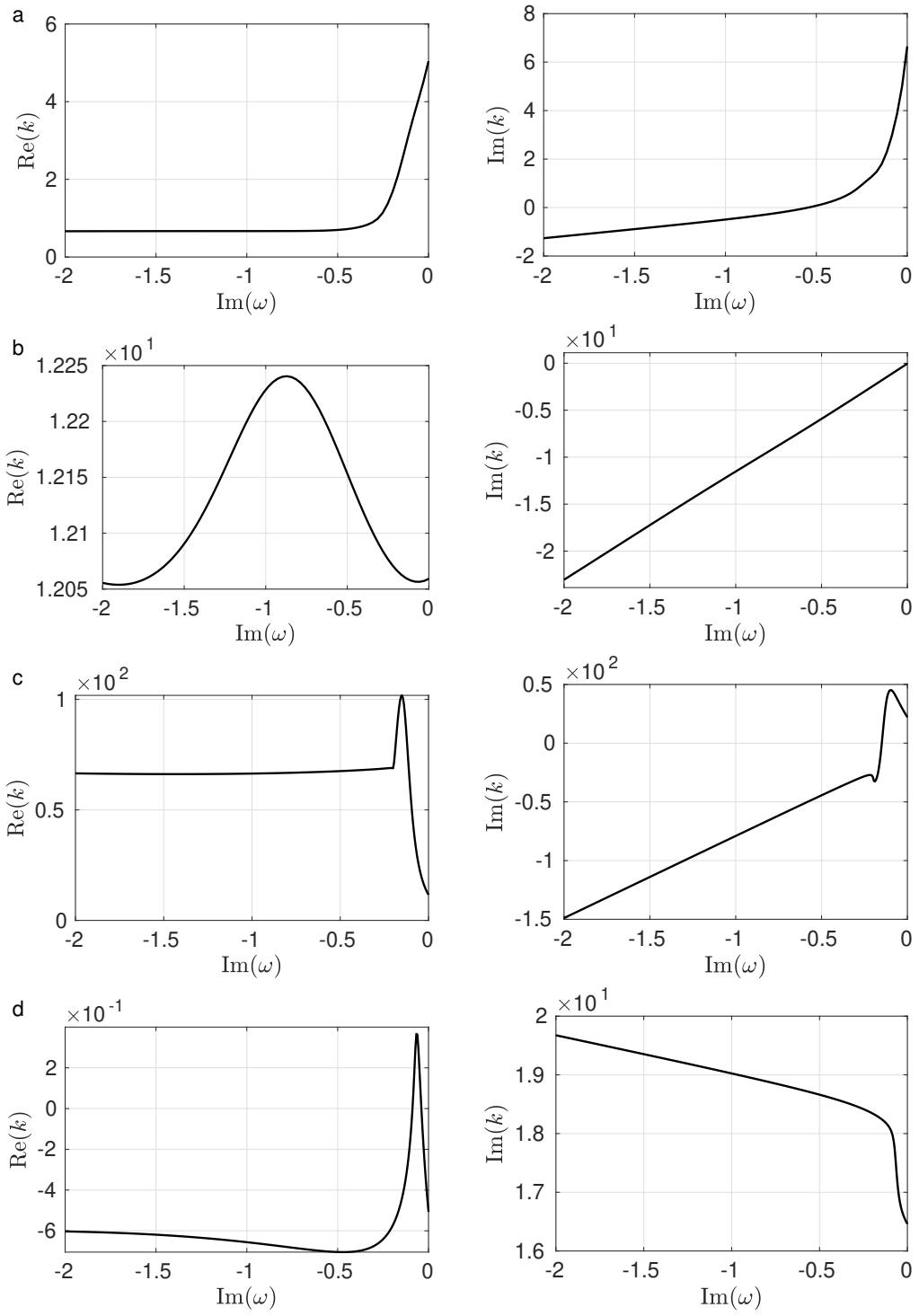


Figure 5.8: Propagation direction of mode a and b when Im($\omega$) varies from -2 to 0 for Re($\omega$) = 0.9271 and for different values of $\epsilon$. a, mode a, $\epsilon = 1$; b, mode a, $\epsilon = 0.5$; c, mode b, $\epsilon = 1$ and d, mode b, $\epsilon = 0.5$.

Considering that instability is the result of the complex interaction of many factors, the choice of $\epsilon$ are case dependent.

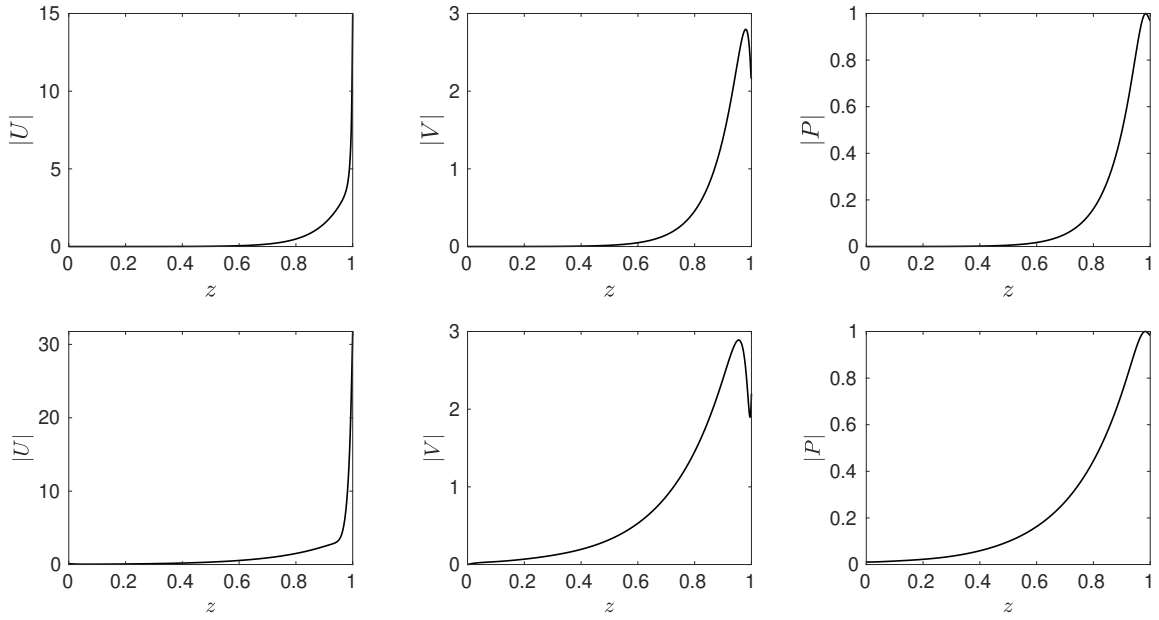


Figure 5.9: Shapes of the unstable mode a and b for the duct lined with the CT57 liner at $\omega = 0.9271$ for $\epsilon = 1$: upper, mode a and lower, mode b, from left to right, velocity components along $x$- and $z$-direction and pressure.

### 5.3.2 Time-domain study

The effect of suppressing the mean flow gradient on the acoustic propagation is assessed in the time domain approach. For the rigid duct and the duct lined with the MSD liner, the configuration is shown in figure 4.2. For the CT57 liner, the NASA GIT experiment set-up is considered.

The shear flow used in this section is the same as in the frequency-domain study. The impulsive source and the numerical parameters are kept as in section 4.1. Attention should be paid that the non-dimensional LEE is solved for the rigid duct case and the MSD liner case. For the CT57 liner case, the time-domain results are with dimensions. The same source and numerical parameters are applied for three cases, even if the two previous cases are without dimension and the last one with dimensions.

#### Rigid duct

Firstly, the partial GTS method is assessed for a rigid duct. The pressure responses on the wall $z = 0$ to an impulsive source varying with time for several values of $\epsilon$ are shown in figure 5.11. After the generation of the acoustic pulse, two branches related with the propagation of the "plane waves" along the downstream and upstream directions are observed. However, except for these two branches, a pattern similar to instabilities is observed for several values of $\epsilon$. Obviously, the amplitudes of the resembling instabilities are also impacted by $\epsilon$. However, there should be no instabilities for a rigid duct as shown in the frequency study, since no mode exists in the upper right complex $k$-plane except the vorticity modes with small positive $\mathrm{Im}(k)$. We infer that these patterns resembling instabilities are attributed to the vorticity modes.

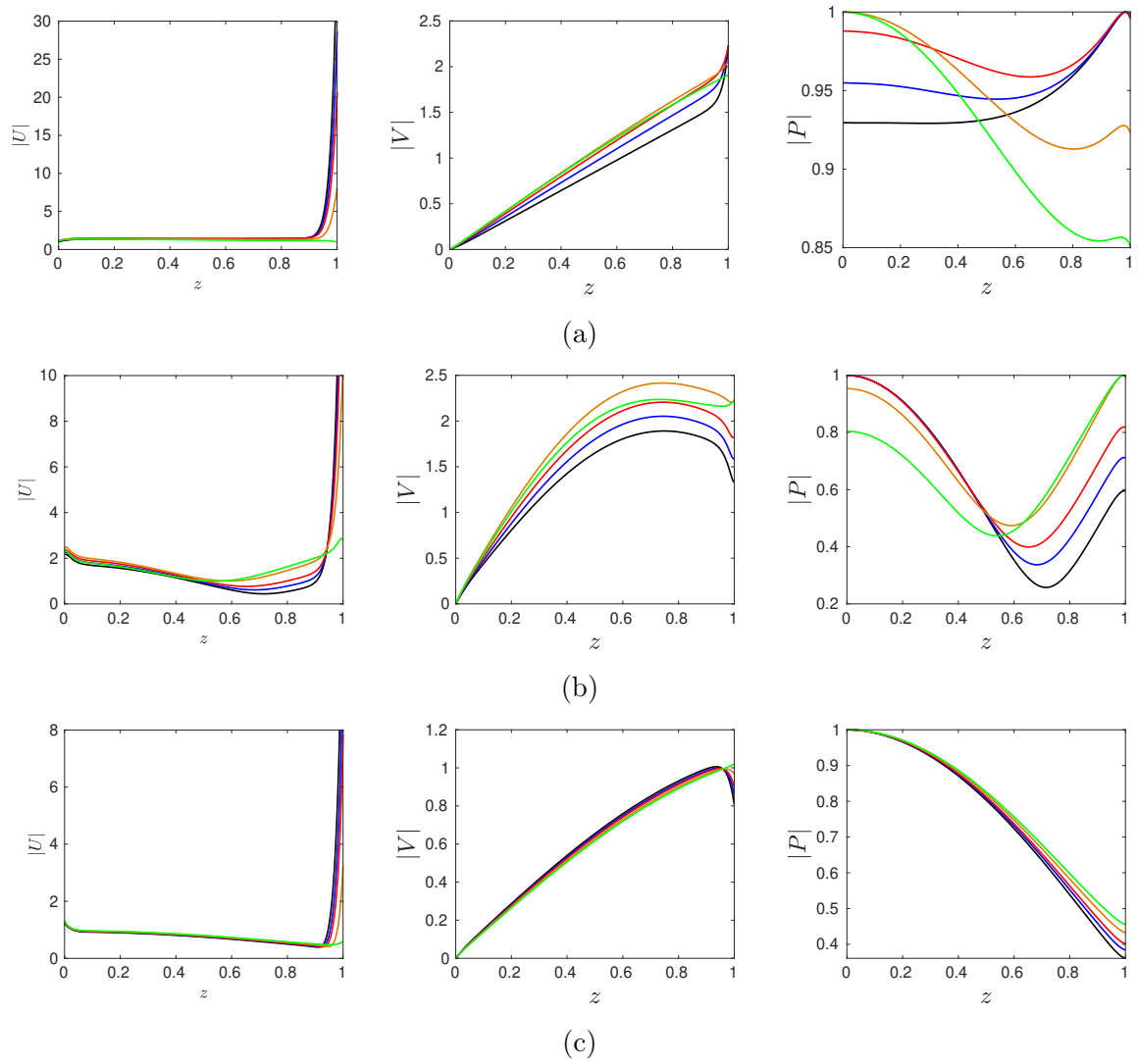


Figure 5.10: Mode shapes for the duct lined with the CT57 liner at $\omega = 0.9271$ and for several values of $\epsilon$: $\epsilon = 1$, $\epsilon = 0.7$, $\epsilon = 0.5$, $\epsilon = 0.2$ and $\epsilon = 0$. (a) "plane wave" mode and leading (b) downstream and (c) upstream evanescent modes for, from left to right, velocity components along $x$- and $z$-direction and pressure.

The snapshots of $\ln(|p|)$ in sequential order for the rigid duct case and for $\epsilon = 0$ are presented in figure 5.12. The acoustic waves propagate along both directions as the response to the impulsive source. At $t = 9.7$, the "plane waves" already leave the duct along the downstream direction. For $t \geq 13.7$, the waves patterns referring to the vorticity waves with relatively small amplitudes are observed near the rigid walls. These waves only appear in the downstream direction. Their velocities are much smaller when compared with the "plane waves". When $t = 30.6$, the vorticity waves leave the duct as well.

The pressure signals perceived with microphones located at $x = 1.9685$, $x = 3.9370$ and $x = 5.9055$ on the lower wall $z = 0$ for $\epsilon = 0$ are shown in figure 5.13. Acoustic propagation in the rigid duct is similar to "plane wave" propagation. The amplitude and the shape of the three pressure signals are quite similar. A zoom of these signals is shown in the right figure. As marked

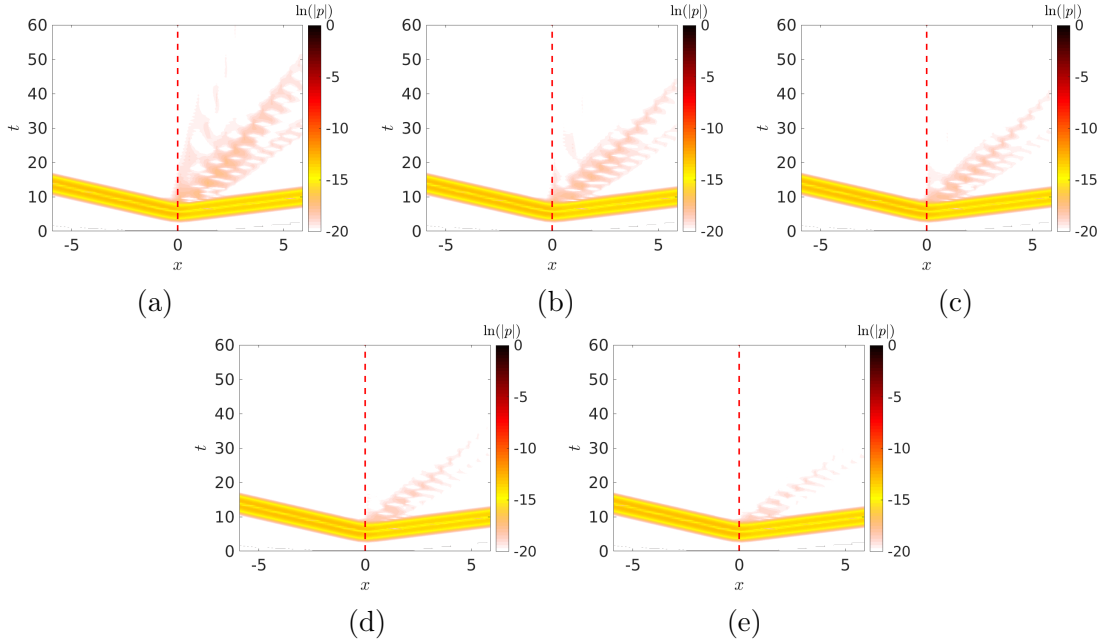


Figure 5.11: Pressure response $\ln|p(x, z = 0, t)|$ to an impulsive source for the rigid duct and for different values of $\epsilon$. The source position is indicated by the vertical dashed line. (a), $\epsilon = 1$; (b), $\epsilon = 0.7$; (c), $\epsilon = 0.5$; (d), $\epsilon = 0.2$; (e), $\epsilon = 0$.

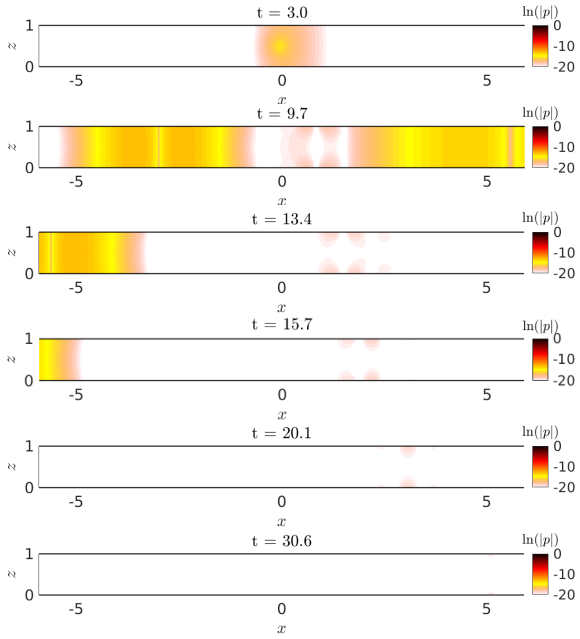


Figure 5.12: Snapshots of $\ln(|p|)$ for the rigid duct case and for $\epsilon = 0$.

inside the box, other wave packets, referring to vorticity waves, follow "plane waves" closely. The maximum of the amplitude of the vorticity waves is 3 % of the acoustic waves.

SPL and phase of the acoustic pressure on the wall $z = 0$ for the rigid duct varying with $\epsilon$ are given in figure 5.14. The reference is set to 130 dB and 0 °. No window is applied for the computation of SPL and phase. The acoustic pressures along the upstream direction are higher than the ones along the downstream direction. This phenomenon can simply be explained by the

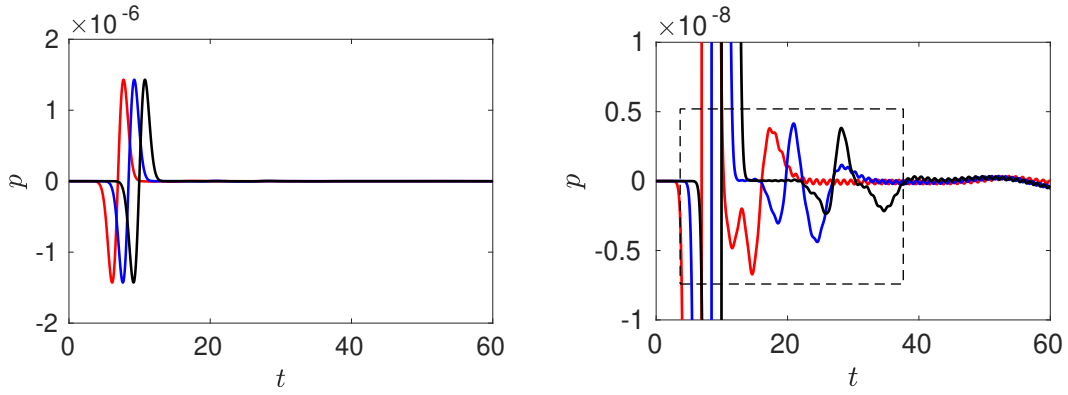


Figure 5.13: Pressure perceived with microphones on the rigid wall $z = 0$ for the rigid duct: $x = 1.9685$, $x = 3.9370$, $x = 5.9055$ and for $\epsilon = 0$. Left, pressure signals for whole time iterations, right, zoom of the pressure signals.

conservation of energy. Since the acoustic velocity in the upstream direction is smaller than the downstream direction, the acoustic pressure in the upstream direction is supposed to be higher than the one in the downstream direction.

As shown in the figure, suppressing the strength of the mean flow gradient term will lead to an increase of SPL in the upstream direction and a decrease in the downstream direction. However, the phase of the acoustic pressure is not impacted obviously by $\epsilon$. Another issue needs to be addressed is that fluctuations of SPL are observed along the downstream direction for $\omega \leq 1.8542$. As mentioned before, it may be caused by vorticity waves.

Figures 5.15 shows the acoustic powers at the plane $x = 0.9843$, at the plane $x = 5.9055$ and their ratio $\Delta W$ for several values of $\epsilon$. Similar to the study of SPL and phase, no window is applied. The power at the plane $x = 0.9843$ and $x = 5.9055$ are both impacted by the partial GTS method. Suppressing the mean flow gradient term leads to a decrease of acoustic power at both cross sections. Its influence is quite evident in the frequency range $1 \leq \omega \leq 1.5$. We also notice that acoustic power in this frequency range is much larger.

Similarly, the power difference deviates from zero for frequencies $\omega \leq 2$. When $\omega \geq 2$, the power difference $\Delta W$ proceeds towards zero for all five values of $\epsilon$. The effect of the partial GTS method on acoustic propagation is mostly observed in the low frequency range. It can also be noted that the power difference around $\omega = 1.3907$ for $\epsilon = 0.2$ and 0 is negative, indicating an increase of the acoustic power. It is maybe due to the vorticity modes which behave as instabilities. It is inferred that the fluctuations of the power difference are due to the modification of acoustic and vorticity waves by change of $\epsilon$.

### MSD liner

The effect of the partial GTS method on the instabilities in the duct lined with the MSD liner is investigated. Two sets of simulations are performed and they are presented in figure 5.16 and 5.17. Both figures depict the pressure response $\ln|p(x, z = 0, t)|$ for several value of $\epsilon$. The differences

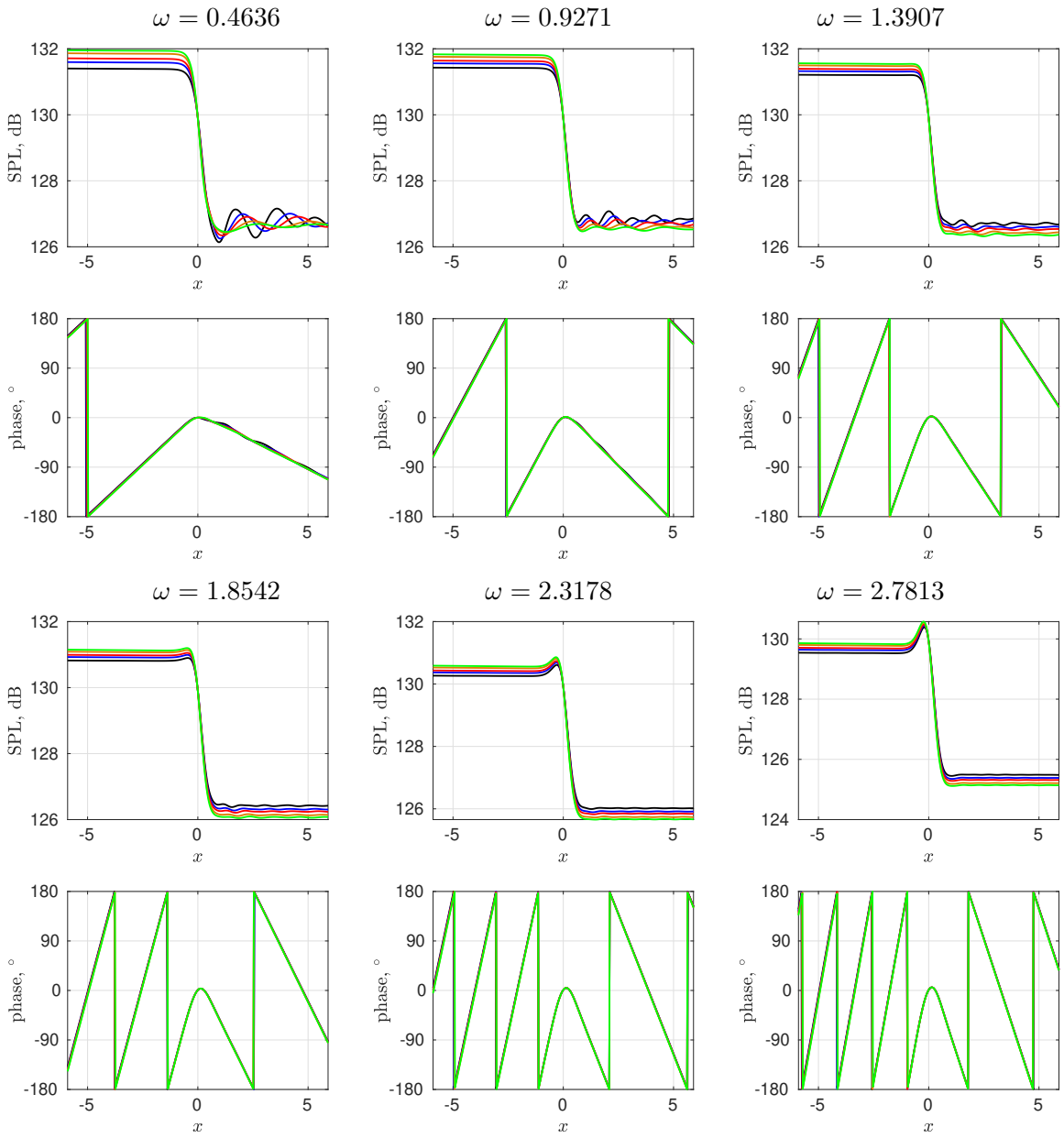


Figure 5.14: SPL and phase of the acoustic waves on the rigid wall $z = 0$ propagate along the rigid duct for six frequencies and for different values of $\epsilon$: $\epsilon = 1$, $\epsilon = 0.7$, $\epsilon = 0.5$, $\epsilon = 0.2$, $\epsilon = 0$.

between them lie in the time step and the resolution along the $z$-direction. For the case shown in figure 5.16, the time step is $\Delta t = 0.0014$ and there are 175 points along the $z$-direction. The time step is $\Delta t = 0.014$ and there are 55 points along the $z$-direction for the study shown in figure 5.17. The two sets of experiments show different phenomena when $\epsilon$ varying from 1 to 0.

In figure 5.16, the instabilities are obviously inhibited when $\epsilon$ decreases from 1 to 0.7. However, the instabilities are not continuously suppressed when $\epsilon$ gradually decreases from 0.7 to 0. The instabilities even amplify when $\epsilon$ decreases from 0.5 to 0. Combining with frequency-domain studies in section 5.3.1, the unstable mode already converts into vorticity mode for $\epsilon \leq 0.7$. Except for the vorticity modes whose wavenumbers have small positive imaginary parts, it is

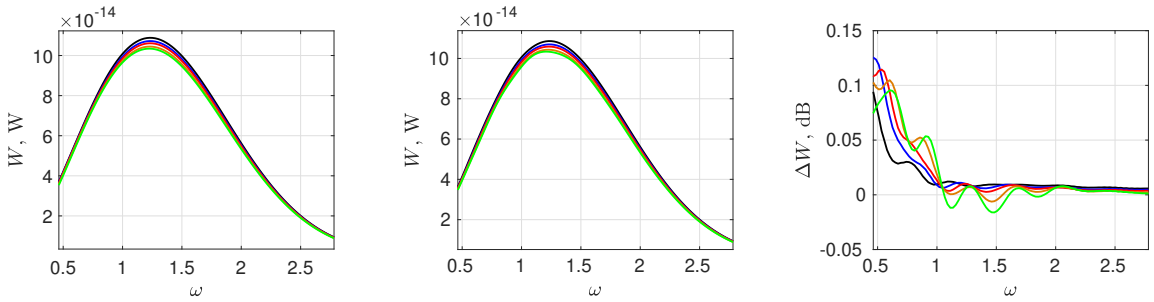


Figure 5.15: Acoustic power at the plane $x = 0.9843$ (left), at the plane $x = 5.9055$ (middle) and the power difference between the two planes (right) for the rigid duct and for different values of $\epsilon$: $\epsilon = 1$, $\epsilon = 0.7$, $\epsilon = 0.5$, $\epsilon = 0.2$, $\epsilon = 0$.

not expected that not any other modes contribute to the instabilities. We hence infer that the instabilities patterns for $\epsilon \leq 0.5$ may be due to vorticity waves. They are obvious for a very fine mesh.

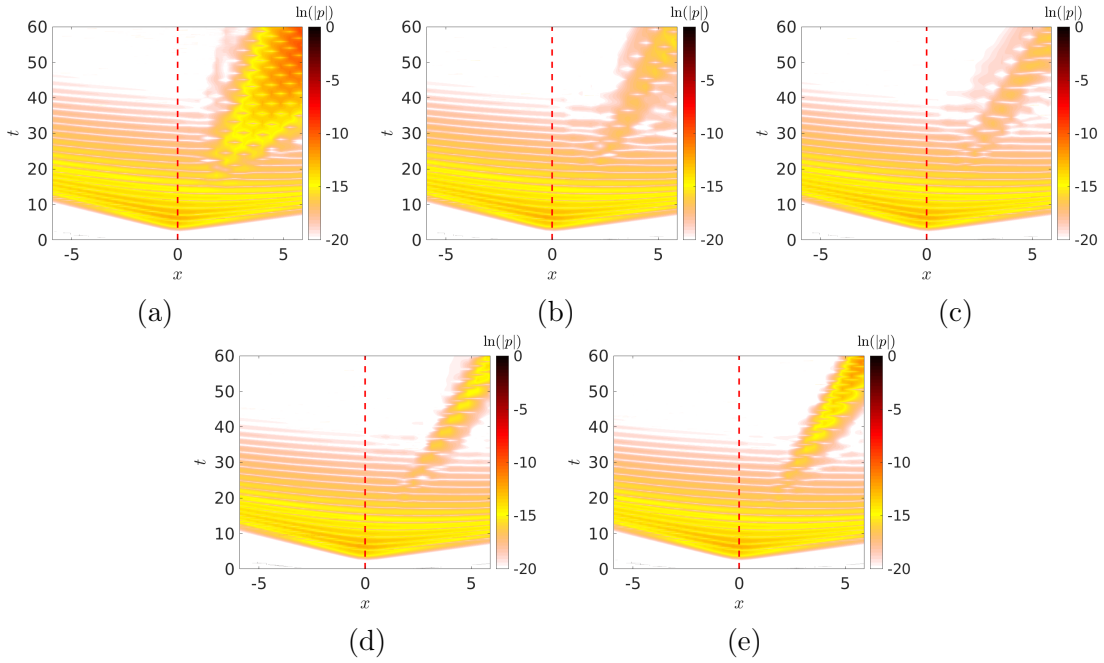


Figure 5.16: Pressure responses $\ln|p(x, z = 0, t)|$ to an impulsive source for the duct lined with the MSD liner with a refined mesh. The source position is indicated by the vertical dashed line. (a), $\epsilon = 1$; (b), $\epsilon = 0.7$; (c), $\epsilon = 0.5$; (d), $\epsilon = 0.2$ and (e), $\epsilon = 0$.

Figure 5.17 shows the instabilities are gradually suppressed as the value of $\epsilon$ is diminished. For $\epsilon \leq 0.5$, no instabilities are observed in this case. Compared with figure 5.16 and 5.17, the vorticity waves are significant for a refined mesh. We need to address that the main priority in practice is to predict acoustic propagation along the duct rather than to characterize the instabilities. Acoustic waves are already sufficiently described for a coarse mesh with far more than 8 points per wavelength.

Figure 5.18 shows the successive snapshots of acoustic propagation with the refined mesh

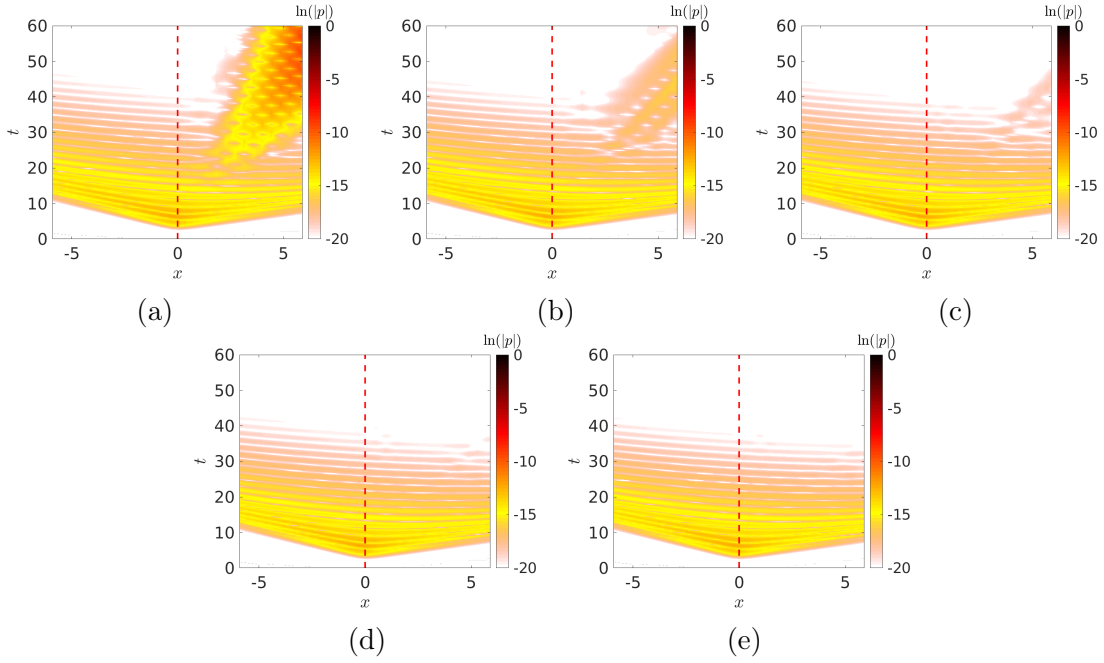


Figure 5.17: Pressure responses $\ln|p(x, z = 0, t)|$ to an impulsive source for the duct lined with the MSD liner with a coarse mesh. The source position is indicated by the vertical dashed line. (a), $\epsilon = 1$; (b), $\epsilon = 0.7$; (c), $\epsilon = 0.5$; (d), $\epsilon = 0.2$ and (e), $\epsilon = 0$.

case for $\epsilon = 1$ and 0.5. The left figure presents the generation of instabilities on the lined wall during the acoustic propagation for $\epsilon = 1$. The right figure shows that the acoustic field is free from hydrodynamic instabilities with $\epsilon = 0.5$. However, it involves vorticity waves. In the early stage of simulation $t \leq 9.8$, the acoustic waves are excited by an impulsive source. The acoustic propagation between $\epsilon = 1$ and 0.5 is quite similar. For $t \geq 15.7$, differences between the two figures become apparent. The hydrodynamic instabilities are suppressed for $\epsilon = 0.5$, however, the acoustic pressure in the downstream direction is not null.

Although, for $\epsilon = 0.5$, the vorticity waves are not negligible compared with the acoustic waves. They are however still several orders of magnitude less than the one of hydrodynamic instabilities. It indicates that once a lined duct system suffers from hydrodynamic instabilities, the effect of vorticity waves can be neglected. In other words, the effect of vorticity waves has a negligible impact on the process of characterising instabilities which demands a refined mesh. However compared with acoustic waves, the vorticity waves are not negligible. In practice, with consideration of viscosity and nonlinear terms, we infer that the vorticity waves may not be observed. For example, in the study of Marx [29], the vorticity waves can be stabilized with a dissipation term. The importance of viscosity is also addressed here. It needs to be pointed out that the use of extremely refined mesh is kind of a waste if the objective is a precise prediction of acoustic waves. Since it may lead to relatively strong vorticity waves interfering the acoustic field.

The studies presented below are conducted with a coarse mesh. Figure 5.19 shows acoustic pressure at $x = 1.9685$, $x = 3.9370$ and $x = 5.9055$ on the wall $z = 0$ for several values of $\epsilon$.

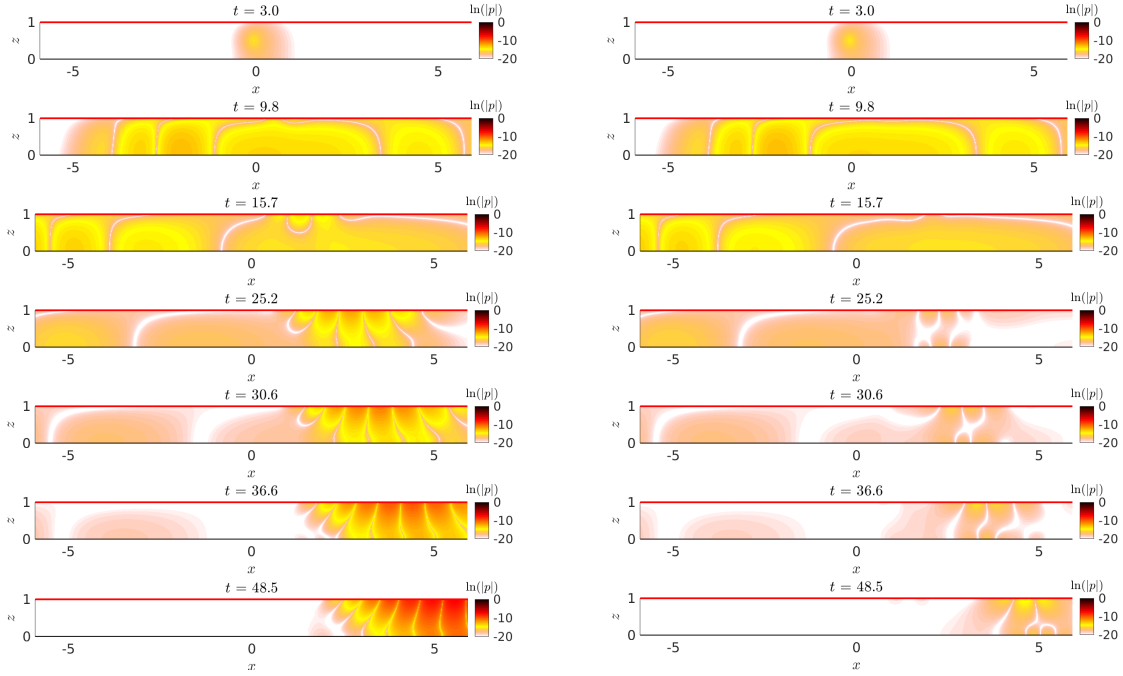


Figure 5.18: Snapshots of acoustic propagation in the duct lined with the MSD liner for $\epsilon = 1$ (left) $\epsilon = 0.5$ (right) with a refined mesh.

The instabilities are triggered by the acoustic propagation along the lined duct. They gradually amplify with the propagation of the acoustic wave packet, and finally lead to strong oscillations and then contaminate the acoustic signal. Most of the instabilities are suppressed for $\epsilon = 0.7$, even if some weak instabilities are still observed. For $\epsilon \leq 0.5$, such instabilities are nearly suppressed. The lower figures show the pressure in the early stages of the simulation. The pressures of the acoustic wave packet are also slightly modified with the decrease of $\epsilon$. However, these changes are not as significant as the impact on the instabilities. The wave packet related to vorticity modes can not be recognized because of their relatively small amplitudes.

The SPL and phase for different values of $\epsilon$ are shown in figure 5.20. The results without mean flow are also attached as reference values. A tapered cosine window is adopted when calculating the Fourier transform as shown in figure 5.21. Note that for the cases for which the partial GTS method induces a delay in the appearance of the instability, the window could have be chosen longer; moreover, for the cases for which the partial GTS allows a suppression of the instability, the window is not necessary. However, for coherency, the same window is applied on all the pressure signals and for all the cases considered. Even if the window is applied, the instabilities for $\epsilon = 1$ are still included inevitably.

Figure 5.20 shows that the pressures are greatly influenced by the mean flow gradient term in the frequency range $0.4636 \leq \omega \leq 1.3907$. It is especially noticeable for $\omega = 0.9271$, because the peak of the amplification rate for the unstable mode is close to this frequency. Generally speaking, when applying GTS, SPL is underestimated along the upstream direction. The effect on the SPL along the downstream direction is weak for the frequency range where the instabilities

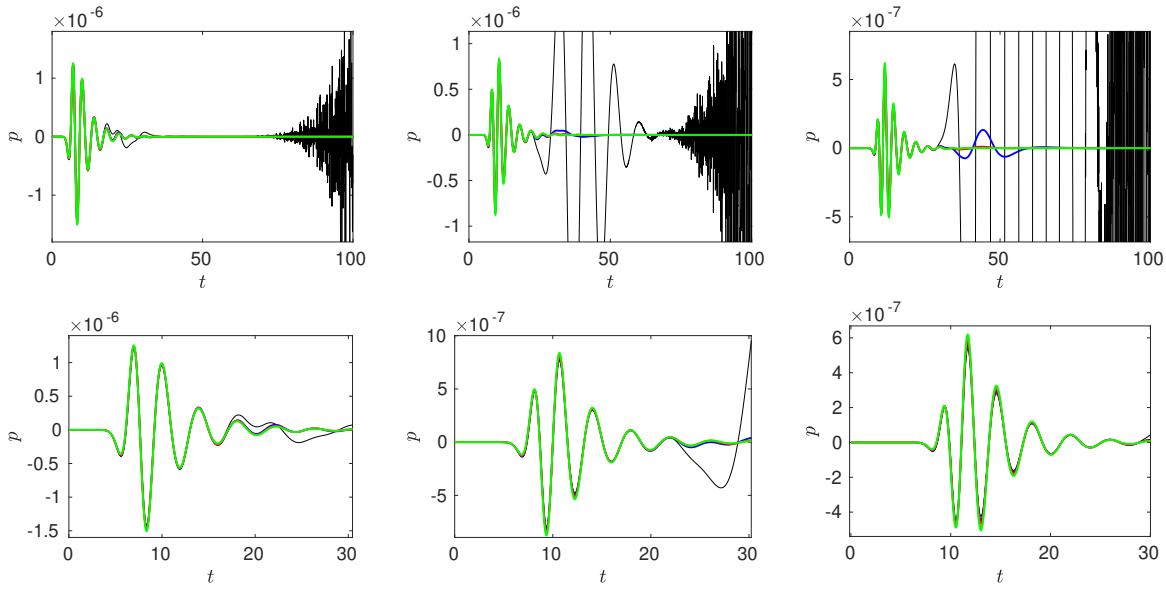


Figure 5.19: The pressure at $x = 1.9685$, $x = 3.9370$ and $x = 5.9055$ on the wall $z = 0$ during the acoustic propagation in the duct lined with the MSD liner for different values of $\epsilon$: $\epsilon = 1$, $\epsilon = 0.7$, $\epsilon = 0.5$, $\epsilon = 0.2$, $\epsilon = 0$. Upper, $0 \leq t \leq 100$ and lower, $0 \leq t \leq 30$.

are not expected. The modifications on phase are weaker compared with SPL, especially for high frequencies.

Figure 5.22 shows the power at the planes $x = 0.9843$ and $x = 5.9055$ and their ratio. Because of instability waves for $\epsilon = 1$, the acoustic power at both plane and the power difference are not reliable, particularly for the low-frequency range. For the MSD liner, a peak of the power difference is attained for $\omega \approx 1.4$. Except for $\epsilon = 1$, we find that the acoustic power is reduced at the plane $x = 0.9843$ and is amplified at the plane $x = 5.9055$ with the reduction of mean flow gradient term. As a consequence, the power difference may be underestimated with the use of the partial GTS method. This error becomes relatively large for frequencies $\omega \leq 2$.

### NASA GIT experiment

Section 2.4.3 reports the existence of instabilities in numeical simulation of the NASA GIT experiment [20]. Investigation of the partial GTS method on this realistic case is finally conducted. The numerical parameters are equivalent to those mentioned in section 2.4.3.

Figure 5.23 shows a series of successive pressure maps. The left and right columns correspond to the results without GTS ($\epsilon = 1$) and full GTS ($\epsilon = 0$), respectively. We focus first on the case without GTS. Once the incoming pulse encounters the liner leading edge, it splits into two wave fronts, a first one that is transmitted downstream and is progressively attenuated by the liner, and a second one that is reflected upstream. At the same time, the instability is generated at the leading edge of the liner. Briefly afterwards, when most of the transmitted and reflected acoustic pulses have left the computational domain, the instability takes over in the entire lined section, leading to a divergent pressure field. In the case of full GTS, the same overall behaviour

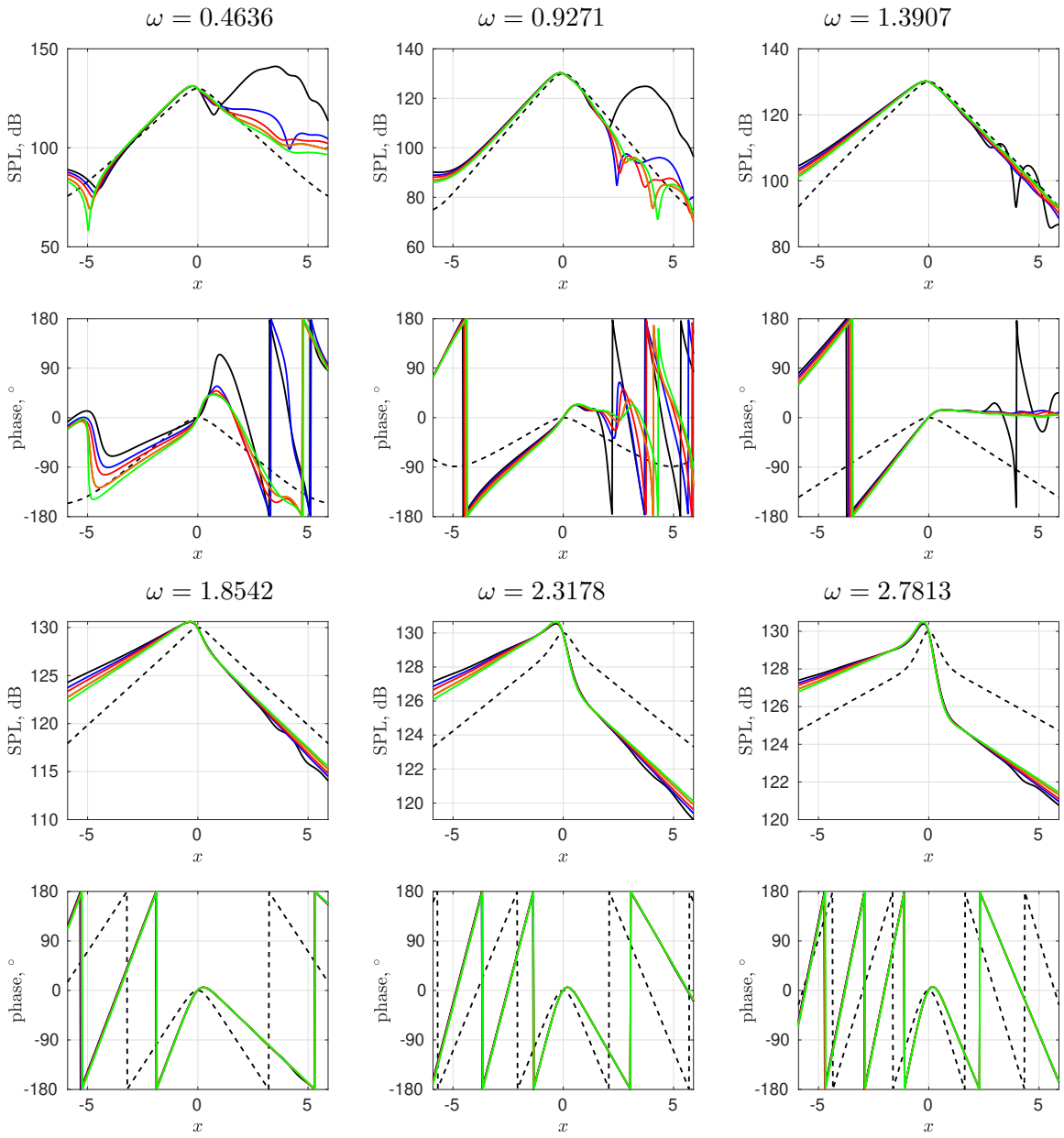


Figure 5.20: SPL and phase of acoustic pressures along the duct lined with the MSD liner for six frequencies and for different values of $\epsilon$: $\epsilon = 1$, $\epsilon = 0.7$, $\epsilon = 0.5$, $\epsilon = 0.2$, $\epsilon = 0$, $M = 0$.

is observed for the acoustic component. However, no instability is generated and the acoustic energy falls to zero at increasing times.

The time series of the pressure at three virtual microphones located on the rigid wall, at different axial locations, are shown in figure 5.24 for several values of $\epsilon$. The successive appearance of the initial acoustic pulse and the instability is observed at all three locations. The impact of $\epsilon$ is mainly on the instability component: decreasing values of $\epsilon$ induces a delay in the emergence of the instability. This is the expected behaviour, as decreasing $\epsilon$ causes a decrease of the amplification of the unstable mode, and thus it takes more time for the instability to leverage the acoustic pressure levels. For $\epsilon = 0.3$ and 0, no instability appears within the simulation time.

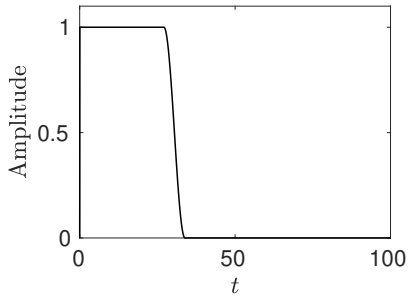


Figure 5.21: The window function used for performing Fourrier transform.

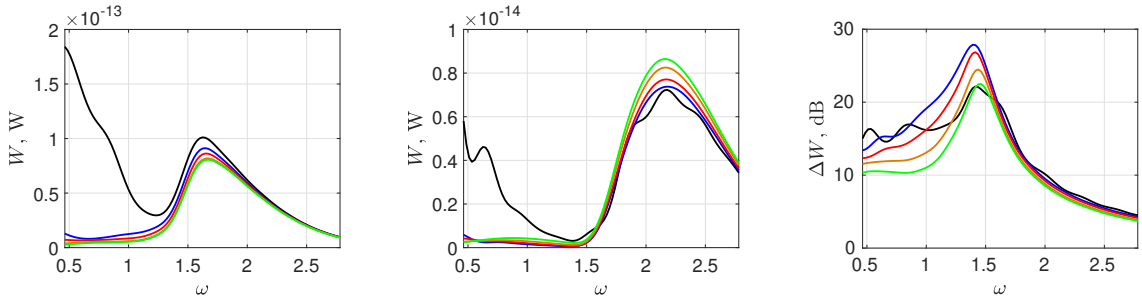


Figure 5.22: Acoustic power at the plane $x = 0.9843$ (left), at the plane $x = 5.9055$ (middle) and the power difference between the two planes (right) for the duct lined with MSD liner and for several values of $\epsilon$: $\epsilon = 1$, $\epsilon = 0.7$, $\epsilon = 0.5$, $\epsilon = 0.2$, $\epsilon = 0$.

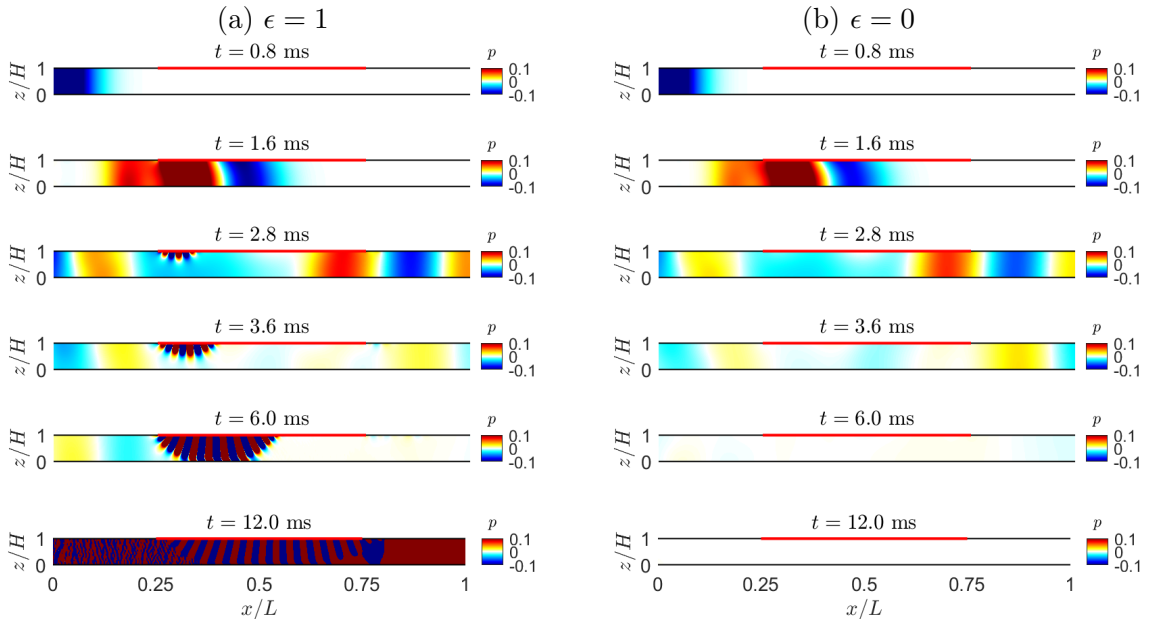


Figure 5.23: Pressure map (Pa) along the duct at different times for (a) $\epsilon = 1$ and (b) $\epsilon = 0$.

In the early stage of the simulation, we notice that the modification of acoustic pressure is especially evident for the unlined section $x = 0.12\,L$ and $x = 0.86\,L$. At $x = 0.12\,L$, the peak value of pressure for $\epsilon = 0$ is 81.50 % of the value of $\epsilon = 1$. This ratio is 83.99 % at $x = 0.86\,L$.

In order to obtain the frequency spectrum of the pressure field, a tapered cosine window is applied to the pressure signals to discard the instability component, as shown in figure 2.18. The

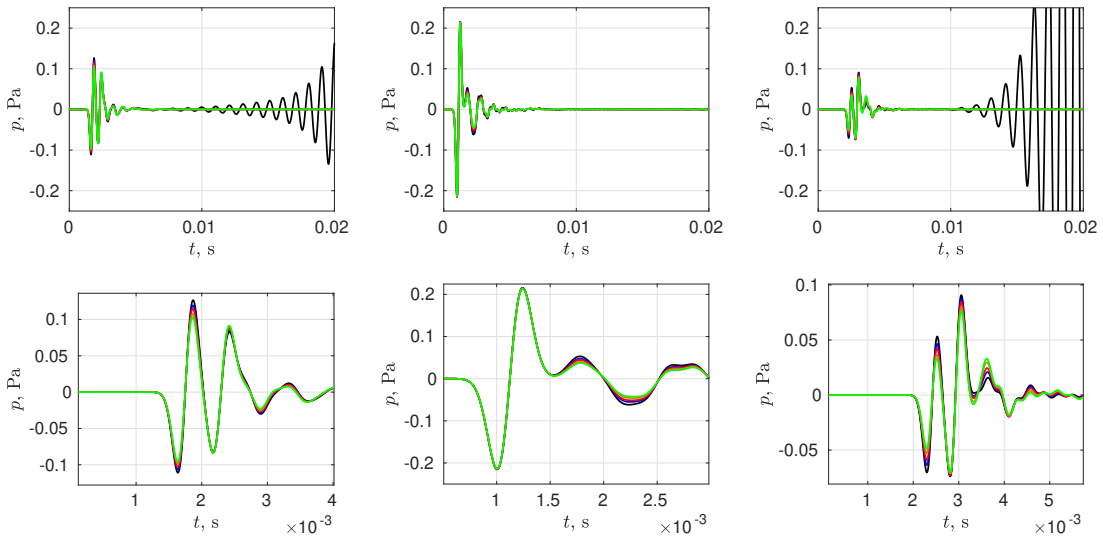


Figure 5.24: Time series of pressure on the rigid wall at (a) $x = 0.12\,L$, (b) $x = 0.5\,L$ and (c) $x = 0.86\,L$ for: $\epsilon = 1$, $\epsilon = 0.7$, $\epsilon = 0.5$, $\epsilon = 0.2$ and $\epsilon = 0$. Upper, whole time iterations, lower, zoom of the whole time iterations.

resulting SPL and phase of the acoustic pressure along the duct wall opposite to the liner are shown in figure 5.25, at different frequencies and for different values of $\epsilon$. For comparison with the NASA measurements, the curves are adjusted so that the SPL and the phase are 130 dB and 0, respectively, at $x = 0$. Without GTS ($\epsilon = 1$), some oscillations on the SPL and on the phase are observed at 500, 1000 and 1500 Hz in the lined section. These are due to the difficulty in isolating the acoustic contribution by simple windowing. Indeed, there is an overlap near $t = 0.005$ s between the acoustic pulse and the instability. An obvious deviation between the simulations and the experimental results is noticed at 3 kHz. One of the reasons is that the window function applied for calculating the Fourier transform does not account for the full acoustic signal. It can also be partly explained by the proximity of the cut-off frequency of the rigid duct, which induced a significant error in the impedance eduction of the liner in the GIT experiment. Overall, the SPL and the phase are modified with the variation of $\epsilon$. Decreasing $\epsilon$ tends how to underestimate the pressure levels, especially downstream of the liner. The largest discrepancies are observed at $f = 1000$ and 3000 Hz. For the other frequencies, the SPL predictions are within a few dBs from the measured values.

The effects of $\epsilon$ on the acoustic power at the sections $x = 0$ and $x = L$ are also studied. Two sets of the CT57 liner model are selected. The one used through the thesis is denoted as broadband. It is obtained from the fit of the analytical model. The other set of impedance model named as narrow is obtained from fitting NASA experiments educed values ranging from 500 Hz to 3 kHz. Their impedance and admittance graphs are shown in figure 5.26 and are compared with the "educed values" of NASA experiments. Even if both models approximate the CT57 liners used in the NASA experiment, deviations can still be noticed.

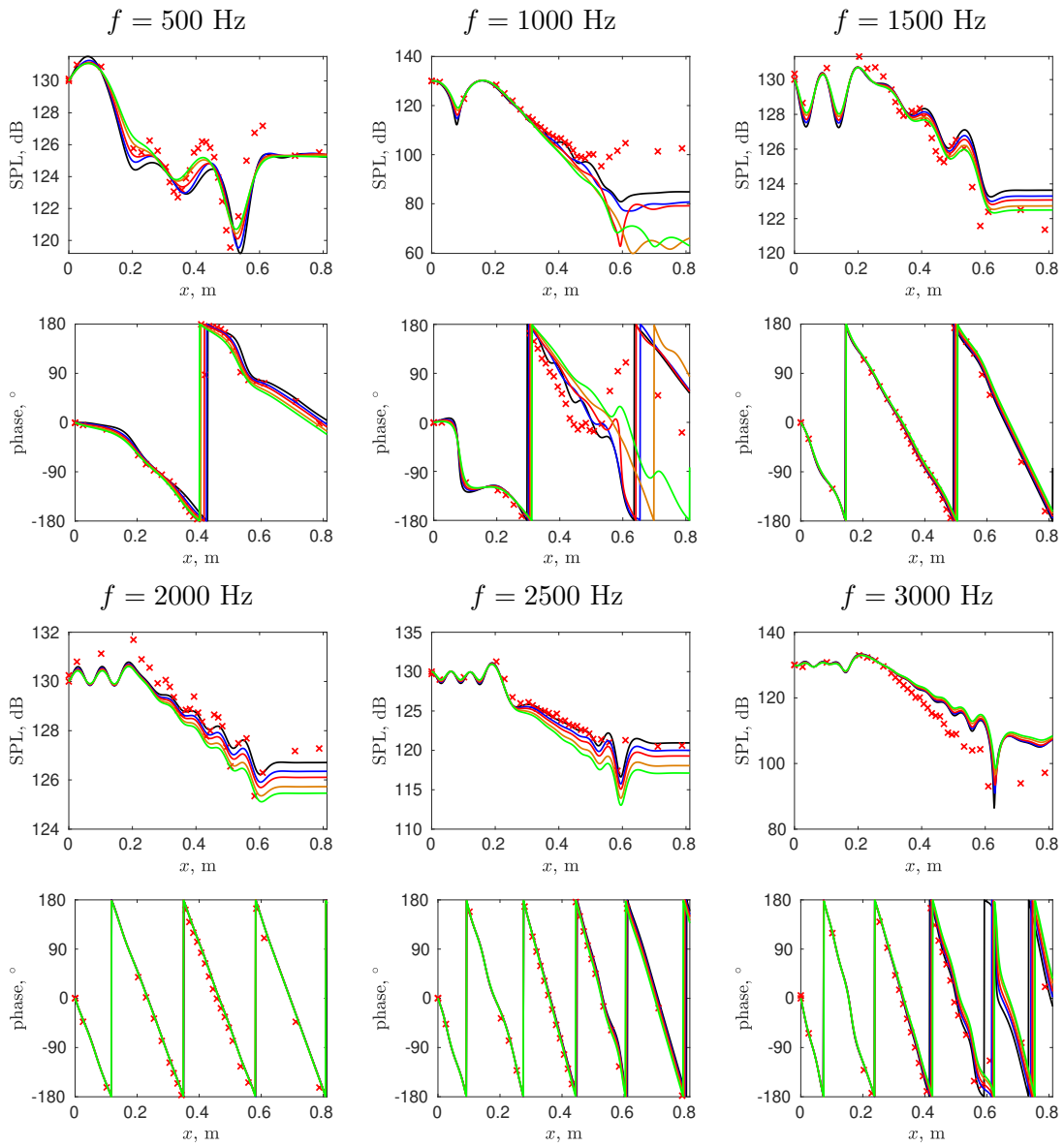


Figure 5.25: SPL and phase of the acoustic pressure along the duct for six frequencies and for different values of $\epsilon$: $\epsilon = 1$, $\epsilon = 0.7$, $\epsilon = 0.5$, $\epsilon = 0.2$, $\epsilon = 0$, $\times$ NASA experiments.

Finally, figure 5.27 shows the frequency variations of power difference calculated for different values of $\epsilon$ for both CT57 liner models as well as estimated from the NASA measurements. The window shown in figure 2.18 is applied for both cases. For the power difference of both CT57 liner model, a peak is observed close to the liner resonance (1.1 kHz) for $\epsilon = 1$ and 0.7, in good agreement with the experimental values. The impact of $\epsilon$ on the power difference is weak except in the immediate vicinity of the resonance and also for $f > 2.5$ kHz. Note that even if a significant increase of power difference is observed for $f > 2.5$ kHz when decreasing $\epsilon$, a good match is achieved for $\epsilon = 0.5$. Figure. 5.24 and 5.25 show that, for this particular case, $\epsilon = 0.5$ seems to be the optimal value ensuring a good compromise between stable simulation and accurate prediction. However, this is not a general conclusion, as the optimal value of $\epsilon$ may depend on

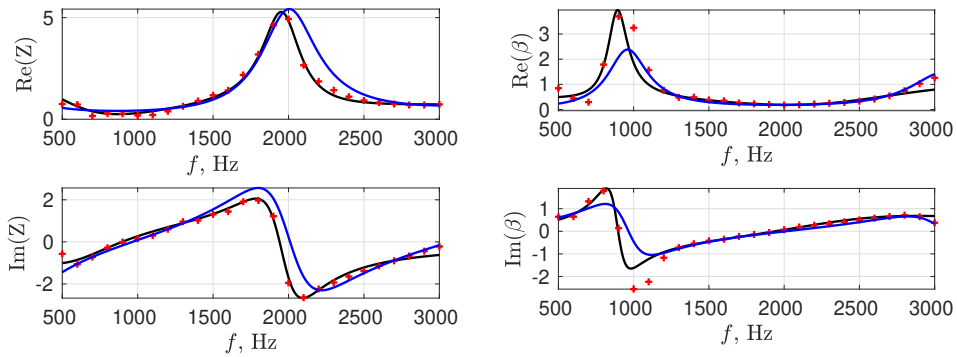


Figure 5.26: Impedance and admittance of two sets of CT57 liner model. broadband, narrow.

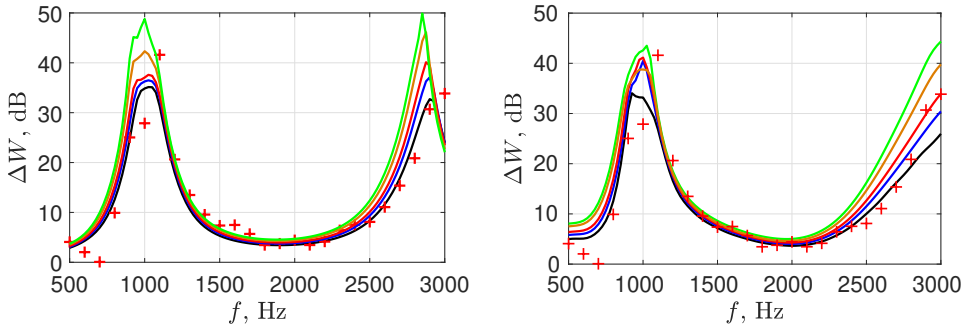


Figure 5.27: Power difference for $M = 0.335$ and for two CT57 liner models: left, impedance model and right, narrow impedance model. $\epsilon = 1$, $\epsilon = 0.7$, $\epsilon = 0.5$, $\epsilon = 0.2$, $\epsilon = 0$, + NASA experiments.

the flow profile, the Mach number and the liner, among others, and may thus be different from case to case.

Another important issue is that even if the two sets of CT57 impedance models do not manifest big differences between each other,these small deviations however lead to obvious differences of the power difference. This study confirms the importance of the precise description of liner impedance.

### COMSOL simulation

As shown in figure 3.4, the results of SPL and phase through COMSOL also indicate the instabilities at $f = 1000$ Hz for $M = 0.335$. Therefore, the partial GTS method is tested on this case. It can be set in the "Gradient Term Suppression Stabilization" in the "Linearized Euler Model". "Suppression of mean flow gradients" is selected, which stands for $\epsilon = 0$ in our case. Figure 5.28 shows the SPL and phase before and after suppressing the mean flow gradient term. Encouraging results of the suppressing mean flow gradient are observed to suppress instabilities. It is observed that the SPL is no more increasing in the lined section, which shows that the instabilities has been suppressed. The predictions of SPL and phase through COMSOL after suppressing mean flow gradient are more closer to the results of the NASA experiment.

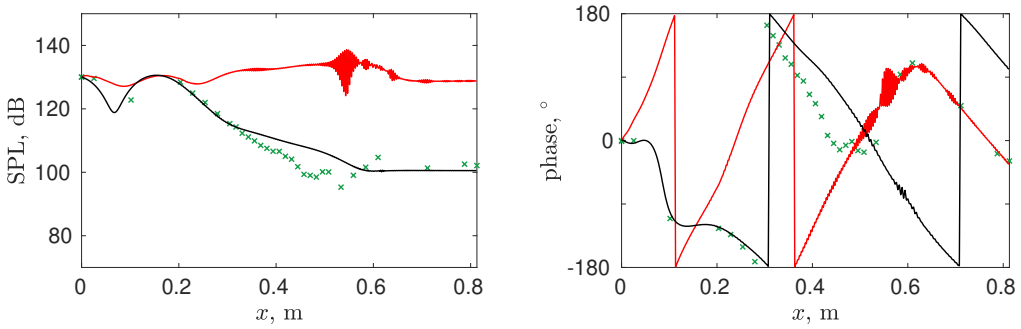


Figure 5.28: SPL and phase of the acoustic pressure at $f = 1000$ Hz obtained through COMSOL. $\epsilon = 1$; $\epsilon = 0$; $\times$ NASA experiments.

## 5.4 Conclusion

An analysis of the partial GTS method for suppressing physical instabilities in a lined flow duct was presented. Acoustic propagation in three cases, a rigid duct, a duct lined with the MSD liner and a duct lined with the CT57 lined, was investigated in the frequency domain and time domain to assess the impact of diminishing the mean flow gradient.

Compared with the acoustic modes, the unstable modes turn to be more sensitive to the mean flow gradient term. When diminishing the strength of the mean flow gradient term, unstable modes would gradually leave the upper right complex plane and might turn into a vorticity mode or an upstream evanescent mode. The system thus becomes relatively stable. In the meantime, acoustic modes are also affected by the partial GTS methods, and in particular for the downstream propagating modes.

In the time-domain study, the effectiveness of the partial GTS method has been shown. The cost is that the acoustic pressure will be slightly modified and the SPL is overestimated or underestimated by a few dBs for certain frequencies. The acoustic propagation in the low frequency range was observed to be especially impacted.

Totally removing the mean flow gradient term seems to be too brutal. From a practical point of view, the partial GTS method ensures a stable computation in the time domain, while providing a relatively accurate prediction of acoustic propagation. However, one limitation of the method is that the optimal $\epsilon$ is case dependent. The analysis of the partial GTS method informs us that the methods used for dealing with shear instabilities may be also applied to the instabilities in lined flow ducts.

# 6 Conclusion and perspectives

The main objective of this study was to investigate how the sound waves propagate in a lined duct with the presence of a mean flow. The time-domain LEE solver was used not only to give an accurate estimate of the sound field but also to predict the presence of other waves, such as, instability waves and vorticity waves. These waves have been characterized, and methods have been presented aimed at avoiding their generation. The partial GTS method has been studied in detail and particularly its impact on the acoustic fields.

Firstly, three approaches, the mode-matching method, solving LEE in the frequency domain and solving LEE in the time domain, were respectively presented. The comparison of the three methods was provided based on the NASA GIT benchmark experiment [20]. Two test cases, "plane wave" and higher-order modes propagation, were considered with and without a mean flow. Below the cut-off frequency ($f \approx 3$ kHz), these three methods were consistent with each other overall. The results provided by the three methods matched the experimental results well. When the frequency was above 3 kHz, the NASA experiment data were not available. The consistency of the results given by these three methods was also satisfactory. Therefore the test case on the NASA GIT benchmark made us confident in the LEE time-domain solver. Another important issue to be addressed is that instabilities existed in the solution of LEE. The instabilities at 1 kHz, related to a sheared mean flow and a acoustic liner, have been reported in many studies [93, 94, 33, 95].

Although the two other methods provide similar good predictions, they have several limitations in some aspects. The mode matching method, a semi-analytical method, solves the convective wave equation in the frequency domain. Assuming a uniform flow profile, it is not feasible to consider a shear mean flow. The other method is to apply commercial software COMSOL to solve LEE in the frequency domain. The results of this method are more costly to acquire compared with the other two approaches, especially considering higher-order modes propagation in 3D coordinates. Another limitation for both frequency-domain techniques is that they are suitable for solving acoustic propagation at a harmonic frequency, and therefore they are repetitive and tedious when results over broadband frequency ranges are required. On the contrary, the LEE time-domain solver is able to provide the results of a large number of frequencies in a single run; thus, it is ideal to solve broadband problems. Another advantage of the time-domain

method is that a complex flow profile can be imposed, and therefore the effect of a mean flow shear layer can be taken into account. Thus the LEE time-domain solver is utilised as the main tool to explore the lined flow duct problem.

As mentioned previously, the mode-matching method, which is based on the mode expansion, is computationally efficient; however, it is restricted to the use of uniform flow with its simple assumption. Then this study continued to find another way to interpret the sound field with its modal behaviour, namely the modal analysis approach. The LEE was rewritten in a suited form to obtain a modal solution. Then an eigenvalue problem was derived and solved with the Chebyshev spectral method. Validations were conducted with an analytical/semi-analytical method. The results suggested that characteristics of instabilities, namely mode wavenumbers and mode shapes, were predicted accurately through the modal analysis approach.

With the use of the modal approach, the acoustic propagation in a rigid and a lined duct was studied with and without a sheared mean flow. The effect of boundary layer thickness on the mode wavenumbers and mode shapes was also investigated. More importantly, the modal analysis approach threw lights upon the instabilities generated in a lined flow duct, and then details such as the wavelength, the spatial growth rate and mode shapes, etc., became available. With the use of the Briggs-Bers criterion, the unstable downstream propagating mode was detected from upstream decaying modes. The type of instabilities, convective or absolute, was determined. Four cases, which contained no instability, convective instabilities and absolute instabilities, were displayed by using the time-domain method and the modal analysis approach.

The characteristics of convective instabilities were analysed. The methods to obtain its wavelength and the spatial growth rate through time-domain simulations were presented. These characteristics obtained by using the LEE time-domain solver perfectly matched with those predicted by the modal analysis approach. These encouraging results demonstrated the capability of the LEE time-domain solver to predict not only acoustic waves and but also hydrodynamic waves. Since the use of selective filters and a coarse mesh could help to inhibit the numerical oscillation in the time domain, the impacts of these two parameters on the characterization of hydrodynamic instabilities were investigated. The results showed that although the characteristics of instabilities changed with the value of these two parameters, they nonetheless converged to the predicted values when the strength of a selective filter and a mesh size was relatively small. Notably, when decreasing the grid size to a certain value, the effect of continuously reducing the grid size on the instability characteristics is minimal. Indeed, for characterizing the instabilities, a sufficient fine mesh is necessary.

Hydrodynamic instabilities are due to the complex interaction between a mean flow, acoustic liners and acoustic waves. With the interaction of these factors, hydrodynamic instabilities may not exist or exist in a very strong form. Thus, a parametric study by using the modal analysis approach was performed to analyse the effect of the source frequency, the mean flow profile and the impedance of acoustic liners on hydrodynamic instabilities. The results revealed that hydrodynamic instabilities existed in a specific frequency range. A peak of the spatial growth rate

could be obtained in this frequency range. The mean flow profile, including the Mach number and the boundary layer thickness, has complex effects on the instabilities. A duct whose mean flow has a thin boundary layer was more likely to suffer from instabilities. When the boundary layer thickness remained at a certain value, the growth of the Mach number inhibited the spatial growth rate of instabilities. The instabilities were not likely to be generated for a acoustic liner with a large resistance. With the increase of reactance, instabilities became more severe, for example, transforming from convective instabilities to absolute instabilities.

Finally, the partial GTS method was investigated to suppress the instabilities related to acoustic liners. The GTS method proposed by Bogey *et al.* [133] was designed to suppress the KH instabilities generated in the acoustic propagation through a shear flow. The mean flow gradient was identified as the cause of KH instabilities, and the authors presented that the time-domain simulations were stabilized after removing the mean flow gradient. Inspired by its effectiveness to suppress the KH instabilities, the mean flow gradient term in Eq. (5.1) was weighted with $\epsilon$, ranging from 1 (original LEE equation) to 0 (mean flow gradient totally removed) to suppress the instabilities related to acoustic liners. Then studies on the acoustic waves and instability waves were performed on three cases, without instabilities, with convective instabilities and with absolute instabilities, for several values of $\epsilon$.

Firstly, when decreasing the value of $\epsilon$, the unstable modes left the upper right of the complex $k$-plane and developed into vorticity modes or upstream evanescent modes. It should be noted that diminishing $\epsilon$ does not always reduce the spatial growth rate of an unstable mode. As for the effect on acoustic modes, downstream modes were more vulnerable compared with the upstream modes. Secondly, the time-domain analysis evaluated the effectiveness of the partial GTS method. Instabilities were gradually suppressed and a stable acoustic propagation in the time domain was finally obtained. However, the effect of suppressing the mean flow gradient term was not limited to instability waves, and it also impacted acoustic waves, especially for the acoustic propagation in the low frequency range. The partial GTS method could cause a few dBs difference of SPL for certain frequencies. With an appropriate value of $\epsilon$, the partial GTS method not only prevented the system from unstable interferences but also gave a relatively accurate estimate of the sound field. Therefore, special attentions should be paid in choosing the value of $\epsilon$. One limitation of the partial GTS method is that there is no universal value of $\epsilon$ which can always be the optimal one. The choice of this parameter depends on the mean flow field, acoustic liners and acoustic propagation. Nonetheless, this analysis provided new ideas to suppress the instabilities related to a lined flow duct.

## Perspectives

Characterizing hydrodynamic instabilities is limited in this study to convective instabilities. This work can be extended to absolute instabilities, for instance, quantifying their convective velocity, the growth rate and checking if there are modes with a zero group velocity as seen in refer-

ence [120].

In section 5.3, it is noticed that the effect of vorticity waves becomes evident with the suppression of hydrodynamic instabilities. Vorticity waves could also be investigated in a following study [146]. Besides that, Marx [29] showed that vorticity modes with a relatively small positive $\mathrm{Im}(k_{\mathrm{HI}})$, which tended to contribute to instabilities, could be stabilized by using an additional dissipation similar to the effect of viscosity. So it is interesting to investigate the response of vorticity waves as well as the convective and absolute instabilities when considering the influence of viscosity by implementing an eddy viscosity profile [10, 98, 125].

The analysis of the partial GTS method shows the viability of the techniques, which were proposed to deal with KH instabilities in a sheared mean flow, to remove instabilities related to a lined flow duct. Therefore, other methods proposed in the literature, for example, GTF [132], APE [136], source filtering method [147], etc., can also be attempted to remove instabilities. Moreover, an evaluation of these methods could be performed to compare the effectiveness in inhibiting instabilities, the impact on the acoustic waves, the implementation complexity as well as the computation cost.

Future work could also be carried out to study the instability/acoustic waves interaction. As shown in [18], the instabilities scattered into acoustic waves and then propagated along the upstream direction. These upstream acoustic waves can trigger another instabilities. These feedback between the acoustic and instabilities could be investigated in the future.

# A Coefficients in Eq. (2.22)

For the modal base to be orthogonal, the following relation must be fulfilled:

$$\int_0^{L_y}\int_0^{L_y}\psi\psi \mathrm{d}y\mathrm{d}z = 1. \tag{A.1}$$

depending on the the indices $(m\,n)$ of the mode, the integral can be determined, yielding

$$\int_0^{L_y}\int_0^{L_y}\cos(\theta_m)\cos(\sigma_n)\mathrm{d}y\mathrm{d}z = \begin{cases} \dfrac{L_yL_z}{4},\ m\neq 0,\wedge\ n\neq 0 \\ \dfrac{L_yL_z}{2},\ m=0,\wedge\ n\neq 0 \\ \dfrac{L_yL_z}{2},\ m\neq 0,\wedge\ n=0 \\ L_yL_z,\ m=0,\wedge\ n=0 \end{cases} \tag{A.2}$$

Since the modal base is an orthonormal base, the factor $\Lambda_{m,\,n}$ is given as

$$\Lambda_{m,\,n} = \begin{cases} \dfrac{1}{\sqrt{L_yL_z}},\ m=n=0 \\ \sqrt{\dfrac{2}{L_yL_z}},\ m=0\oplus n=0 \\ \dfrac{2}{\sqrt{L_yL_z}},\ m\neq 0\wedge n\neq 0 \end{cases} \tag{A.3}$$

# B Matrices of the discretized eigenvalue problem

This appendix gives details the matrices $\mathbf{A}$, $\mathbf{B}$ and vectors $\mathbf{X}$ of the EVP. As mentioned before, the $\mathbf{X}$ is the column vector of unknowns at the grid points:

$$\mathbf{X} = \left[U(z_1)\cdots U(z_{N+1})\ (P-V)(z_1)\cdots(P-V)(z_{N+1})\ (P+V)(z_1)\cdots(P+V)(z_{N+1})\right]^T, \tag{B.1}$$

where $[\,]^T$ denotes the non-conjugate transpose. This vector contains the value of $U$, $P-V$ and $P+V$ at the discrete points. For example, $(P+V)(z_n)$ is the value of $P+V$ at the Chebyshev grid point $z_nE$. One should note that depending on the rigid and lined duct case, $\mathbf{A}$ has different expressions. The original information in the line $2N+2$ and $2N+3$ of matrix $\mathbf{A}$ and $\mathbf{B}$ are discarded and replaced by the boundary conditions.

For both the rigid and the lined duct case,

$$\mathbf{A} = \left[\begin{array}{c|c|c} \mathbf{I}_{(1:N+1),(1:N+1)} & -\frac{\epsilon}{2\mathrm{i}\omega}(\mathbf{DU_0})_{(1:N+1),(1:N+1)} & \frac{\epsilon}{2\mathrm{i}\omega}(\mathbf{DU_0})_{(1:N+1),(1:N+1)} \\ \hline \mathbf{0}_{N+1,N+1} & \begin{array}{c}\left(\mathbf{I}-\frac{1}{\mathrm{i}\omega}\mathbf{D}\right)_{(1:N),(1:N+1)} \\ \hdashline 0\ \ldots\ 0\quad -1-\beta\end{array} & \begin{array}{c}\mathbf{0}_{N,N+1} \\ \hdashline 0\ \ldots\ 0\quad 1-\beta\end{array} \\ \hline \mathbf{0}_{N+1,N+1} & \begin{array}{c}1\ 0\ \ldots\ 0 \\ \hdashline \mathbf{0}_{N,N+1}\end{array} & \begin{array}{c}-1\ 0\ \ldots\ 0 \\ \hdashline \left(\mathbf{I}+\frac{1}{\mathrm{i}\omega}\mathbf{D}\right)_{(2:N+1),(1:N+1)}\end{array} \end{array}\right]. \tag{B.2}$$

$$\mathbf{B} = \left[\begin{array}{c|c|c} \mathbf{U_0}_{(1:N+1),(1:N+1)} & \frac{1}{2}\mathbf{I}_{(1:N+1),(1:N+1)} & \frac{1}{2}\mathbf{I}_{(1:N+1),(1:N+1)} \\ \hline \mathbf{I}_{1:N,N+1} & \mathbf{U_0}_{(1:N),(1:N+1)} & \mathbf{0}_{N,N+1} \\ \hdashline \mathbf{0}_{1,N+1} & 0 \quad \dots \quad 0 \quad -u_{0(N+1)}\beta & 0 \quad \dots \quad 0 \quad -u_{0(N+1)}\beta \\ \hline \mathbf{0}_{1,1:N+1} & \mathbf{0}_{N+1,N+1} & \mathbf{0}_{1,N+1} \\ \hdashline \mathbf{I}_{(2:N+1,N+1)} & & \mathbf{U_0}_{(2:N+1),(1:N+1)} \end{array}\right], \tag{B.3}$$

where $\mathbf{0}_{I,J}$ is the zero matrix with $I$ rows and $J$ columns and $\mathbf{D}$ and $\mathbf{I}$ are the differentiation and identity matrix, respectively, both square matrices of size $N+1$. The matrix $\mathbf{U_0}$ is a diagonal matrix of size $N+1$ with diagonal elements $\mathbf{U_0}_{\,i,i} = u_0(z_i)$. In addition, the notation $\mathbf{M}_{(I:J),(K:L)}$ indicates the submatrix of $\mathbf{M}$ formed by rows $I$ to $J$ and columns $K$ to $L$. Finally, the parameter $\epsilon$ in matrix $\mathbf{A}$ controls the mean flow gradient term and is equal to $\epsilon = 1$ for the LEE equations and to $\epsilon = 0$ for the full GTS method.

# C Introduction of the Briggs-Bers criterion

This appendix introduces the Briggs-Bers criterion for analysing the hydrodynamic instabilities appearing in acoustic propagation in a lined flow duct. This stability analysis considers the response of the system to a perturbation in a long time limit. By performing a Fourier-Laplace transform, the response of the system

$$G(x,t) = \frac{1}{4\pi^2}\int_{\ell_\omega}\int_{\ell_k} \frac{-\mathrm{i}e^{\mathrm{i}(\omega t - kx)}}{(\omega-\omega_f)\,D(k,\omega)}\mathrm{d}k\mathrm{d}\omega \tag{C.1}$$

is studied, where $\omega_f$ is the forcing frequency, $\ell_\omega$ and $\ell_k$ are the integral paths. $\ell_\omega$ and $\ell_k$ are constrained by the requirement of causality ($G \equiv 0$ for $t \leq 0$) and the requirement of the integrals. $\ell_k$ is along the real axis of $k$, and $\ell_\omega$ is deformed to ensure the path is below all the poles of the integrand. As talked about Brambley[31], the long-time limit can be obtained by deforming the contour around any poles of the integrand. The lowest poles in the $\omega$-plane has the exponentially dominating long-time contribution, and the remaining other poles have relatively less contributions. In order to avoid poles crossing the $k$-plane during the process, the $\ell_k$ contour may also need to be deformed. Three possibilities are respectively:

• The poles in the $k$ plane do not across the real $k$-axis. $\ell_\omega$ contour is deformed around the poles at forcing frequency $\omega_f$ around the real axis, and no deformation is necessary for the $\ell_k$ contour as shown in figure C.1.(a).

• The poles in the $k$-plane cross the real $k$-axis. Figure C.1.(b) shows that $\ell_\omega$ contour is deformed around the poles at forcing frequency $\omega_f$ around the real axis, and $\ell_k$ contour also needs to be deformed. During the variation of $\omega$, the mode crosses the real $k$-axis will have an exponential spatial growth rate if the mode is a downstream propagating one.

• The poles in the $k$-plane cross the real $k$-axis, and two modes are located at opposite sides of $\ell_k$ contour as shown in figure C.1.(c). Thus a branch cut should be taken at the frequency $\omega_s$, at which the pinch appears. $\ell_\omega$ contour needs to be deformed along the singularity near the branch cut. The long-time contribution is in the form of $e^{\mathrm{i}\omega t - \mathrm{i}k_s x}/\sqrt{t}$. With $\mathrm{Im}(\omega_s) < 0$, the solution grows exponentially with $t$, and the type of the instability is absolute one.

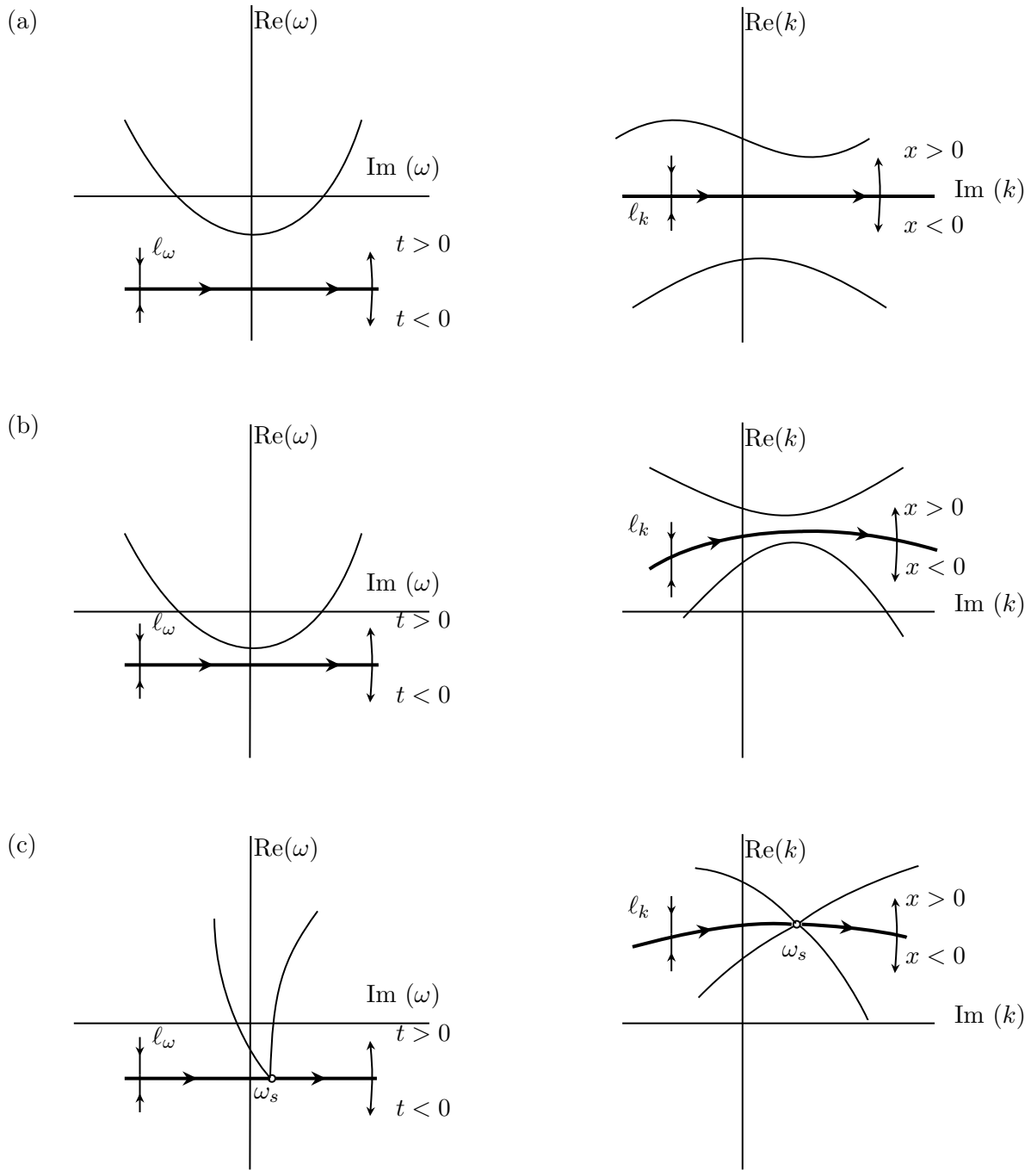


Figure C.1: Intergrand path for several cases.

# Bibliography


[1] Advisory Council for Aviation Research and Innovation in Europe, "The goals of Flightpath 2050," website, `https://www.acare4europe.org/sria/flightpath-2050-goals/protecting-environment-and-energy-supply-0/`, (last viewed: 10 October 2020).

[2] Hultgren, L. S. and Arechiga, R. O., "Full-Scale Turbofan Engine Noise-Source Separation Using a Four-Signal Method," Tech. Rep. NASA/TM-2016-219419, University of Zurich, Department of Informatics, 2016.

[3] Casalino, D., Diozzi, F., Sannino, R., and Paonessa, A., "Aircraft noise reduction technologies: a bibliographic review," *Aerospace Science and Technology*, Vol. 12, No. 1, 2008, pp. 1–17.

[4] Astley, R. J., "Numerical methods for noise propagation in moving flows, with application to turbofan engines," *Acoustical science and technology*, Vol. 30, No. 4, 2009, pp. 227–239.

[5] Marburg, S. and Nolte, B., *Computational acoustics of noise propagation in fluids: finite and boundary element methods*, Vol. 578, Springer, 2008.

[6] Meyer, E., Mechel, F., and Kurtze, G., "Experiments on the influence of flow on sound attenuation in absorbing ducts," *Journal of the Acoustical Society of America*, Vol. 30, No. 3, 1958, pp. 165–174.

[7] Brandes, M. and Ronneberger, D., "Sound amplification in flow ducts lined with a periodic sequence of resonators," *1st AIAA/CEAS Aeroacoustics Conference*, AIAA Paper 95-126, Munich, Germany, 1995, pp. 893–901.

[8] Aurégan, Y. and Leroux, M., "Experimental evidence of an instability over an impedance wall in a duct with flow," *Journal of Sound and Vibration*, Vol. 317, No. 3-5, 2008, pp. 432–439.

[9] Aurégan, Y. and Kumar Singh, D., "Experimental observation of a hydrodynamic mode in a flow duct with a porous material," *Journal of the Acoustical Society of America*, Vol. 136, No. 2, 2014, pp. 567–572.

[10] Marx, D. and Aurégan, Y., "Effect of turbulent eddy viscosity on the unstable surface mode above an acoustic liner," *Journal of Sound and Vibration*, Vol. 332, No. 15, 2013, pp. 3803–3820.

[11] Troian, R., Dragna, D., Bailly, C., and Galland, M.-A., "Broadband eduction of liner impedance under multimodal acoustic propagation," *22nd AIAA/CEAS Aeroacoustics Conference*, AIAA Paper 2016-2725, Lyon, France, 2016.

[12] Richter, C., Hay, J. A., Schönwald, N., Busse, S., Thiele, F., et al., "A review of time-domain impedance modelling and applications," *Journal of Sound and Vibration*, Vol. 330, No. 16, 2011, pp. 3859–3873.

[13] Monteghetti, F., Matignon, D., Piot, E., and Pascal, L., "Design of broadband time-domain impedance boundary conditions using the oscillatory-diffusive representation of acoustical models," *Journal of the Acoustical Society of America*, Vol. 140, No. 3, 2016, pp. 1663–1674.

[14] Aurégan, Y. and Leroux, M., "Failures in the discrete models for flow duct with perforations: an experimental investigation," *Journal of Sound and Vibration*, Vol. 265, No. 1, 2003, pp. 109–121.

[15] Kirby, R. and Denia, F. D., "Analytic mode matching for a circular dissipative silencer containing mean flow and a perforated pipe," *Journal of the Acoustical Society of America*, Vol. 122, No. 6, 2007, pp. 3471–3482.

[16] Gabard, G., "A comparison of impedance boundary conditions for flow acoustics," *Journal of Sound and Vibration*, Vol. 332, No. 4, 2013, pp. 714–724.

[17] Vilenski, G. G. and Rienstra, S. W., "On hydrodynamic and acoustic modes in a ducted shear flow with wall lining," *Journal of Fluid Mechanics*, Vol. 583, 2007, pp. 45–70.

[18] Alomar, A. and Aurégan, Y., "Particle image velocimetry measurement of an instability wave over a porous wall in a duct with flow," *Journal of Sound and Vibration*, Vol. 386, 2017, pp. 208–224.

[19] Troian, R., Dragna, D., Bailly, C., and Galland, M.-A., "Broadband liner impedance eduction for multimodal acoustic propagation in the presence of a mean flow," *Journal of Sound and Vibration*, Vol. 392, 2017, pp. 200–216.

[20] Jones, M., Watson, W., and Parrott, T., "Benchmark data for evaluation of aeroacoustic propagation codes with grazing flow," *11th AIAA/CEAS Aeroacoustics Conference*, AIAA Paper 2005-2853, CA, USA, 2005.

[21] Olson, H. F. and May, E. G., "Electronic sound absorber," *Journal of the Acoustical Society of America*, Vol. 25, No. 6, 1953, pp. 1130–1136.

[22] Fuller, C. R., "Active control of sound transmission/radiation from elastic plates by vibration inputs: I. Analysis," *Journal of Sound and Vibration*, Vol. 136, No. 1, 1990, pp. 1–15.

[23] Thenail, D., Lacour, O., Galland, M., and Furstoss, M., "The active control of wall impedance," *Acta Acustica united with Acustica*, Vol. 83, No. 6, 1997, pp. 1039–1044.

[24] Galland, M.-A., Mazeaud, B., and Sellen, N., "Hybrid passive/active absorbers for flow ducts," *Applied Acoustics*, Vol. 66, No. 6, 2005, pp. 691–708, Innovative Applications of Materials for Acoustic Purposes.

[25] Kostek, T. M. and Franchek, M. A., "Hybrid noise control in ducts," *Journal of Sound and Vibration*, Vol. 237, No. 1, 2000, pp. 81–100.

[26] Furstoss, M., Thenail, D., and Galland, M.-A., "Surface impedance control for sound absorption: direct and hybrid passive/active strategies," *Journal of Sound and Vibration*, Vol. 203, No. 2, 1997, pp. 219–236.

[27] Tam, C. K. and Auriault, L., "Time-domain impedance boundary conditions for computational aeroacoustics," *AIAA journal*, Vol. 34, No. 5, 1996, pp. 917–923.

[28] Rienstra, S., "Impedance models in time domain, including the extended Helmholtz resonator model," *12th AIAA/CEAS Aeroacoustics Conference*, AIAA Paper 2006-2686, Cambridge, MA, USA, 2006.

[29] Marx, D., "Numerical computation of a lined duct instability using the linearized Euler equations," *AIAA Journal*, Vol. 53, No. 8, 2015, pp. 2379–2388.

[30] Rienstra, S. and Darau, M., "Mean flow boundary layer effects of hydrodynamic instability of impedance wall," *Procedia Engineering*, Vol. 6, 2010, pp. 124–132.

[31] Brambley, E. J., "Fundamental problems with the model of uniform flow over acoustic linings," *Journal of Sound and Vibration*, Vol. 322, No. 4-5, 2009, pp. 1026–1037.

[32] Parrott, T. L. and Jones, M. G., "Parallel-element liner impedances for improved absorption of broadband sound in ducts," *Noise Control Engineering Journal*, Vol. 43, No. 6, 1995, pp. 183–195.

[33] Burak, M. O., Billson, M., Eriksson, L.-E., and Baralon, S., "Validation of a time- and frequency domain grazing flow acoustic liner model," *AIAA Journal*, Vol. 47, No. 8, 2009, pp. 1841–1848.

[34] Özyörük, Y., Long, L. N., and Jones, M. G., "Time-domain numerical simulation of a flow impedance tube," *Journal of Computational Physics*, Vol. 146, No. 1, 1998, pp. 29–57.

[35] Primus, J., Piot, E., and Simon, F., "An adjoint-based method for liner impedance eduction: Validation and numerical investigation," *Journal of Sound and Vibration*, Vol. 332, No. 1, 2013, pp. 58–75.

[36] Reymen, Y., Baelmans, M., and Desmet, W., "Efficient Implementation of Tam and Auriault's Time-Domain Impedance Boundary Condition," *AIAA Journal*, Vol. 46, No. 9, 2008, pp. 2368–2376.

[37] Jones, M., Watson, W., and Nark, D., "Effects of flow profile on educed acoustic liner impedance," *16th AIAA/CEAS Aeroacoustics Conference*, AIAA paper 2010-3763, Stockholm, Sweden, 2010, p. 3763.

[38] Bruneau, M., *Fundamentals of acoustics*, ISTE Ltd, London, UK, 2006.

[39] Boulandet, R., Lissek, H., Karkar, S., Collet, M., Matten, G., Ouisse, M., and Versaevel, M., "Duct modes damping through an adjustable electroacoustic liner under grazing incidence," *Journal of Sound and Vibration*, Vol. 426, 2018, pp. 19–33.

[40] Guess, A. W., "Calculation of perforated plate liner parameters from specified acoustic resistance and reactance," *Journal of Sound and Vibration*, Vol. 40, No. 1, 1975, pp. 119–137.

[41] Kooi, J. and Sarin, S., "An experimental study of the acoustic impedance of Helmholtz resonator arrays under a turbulent boundary layer," *7th Aeroacoustics Conference*, 1981, p. 1998.

[42] Motsinger, R. and Kraft, R., "Design and performance of duct acoustic treatment," 1991.

[43] Elnady, T. and Boden, H., "On semi-empirical liner impedance modeling with grazing flow," *9th AIAA/CEAS Aeroacoustics Conference*, AIAA Paper 2003-3304, SC,USA, 2003.

[44] Ingard, U., "Absorption characteristics of nonlinear acoustic resonators," *Journal of the Acoustical Society of America*, Vol. 44, No. 4, 1968, pp. 1155–1156.

[45] Busse-Gerstengarbe, S., Richter, C., Thiele, F. H., Lahiri, C., Enghardt, L., Roehle, I., Ferrante, P., and Scofano, A., "Impedance eduction based on microphone measurements of liners under grazing flow conditions," *AIAA Journal*, Vol. 50, No. 4, 2012, pp. 867–879.

[46] Peat, K., "A transfer matrix for an absorption silencer element," *Journal of Sound Vibration*, Vol. 146, 1991, pp. 353–360.

[47] Kirby, R., "Simplified techniques for predicting the transmission loss of a circular dissipative silencer," *Journal of Sound and Vibration*, Vol. 243, No. 3, 2001, pp. 403–426.

[48] Cummings, A. and Chang, I.-J., "Sound attenuation of a finite length dissipative flow duct silencer with internal mean flow in the absorbent," *Journal of Sound and Vibration*, Vol. 127, No. 1, 1988, pp. 1–17.

[49] Panigrahi, S. and Munjal, M., "Comparison of various methods for analyzing lined circular ducts," *Journal of Sound and Vibration*, Vol. 285, No. 4-5, 2005, pp. 905–923.

[50] Xu, M., Selamet, A., Lee, I.-J., and Huff, N., "Sound attenuation in dissipative expansion chambers," *Journal of Sound and Vibration*, Vol. 272, No. 3-5, 2004, pp. 1125–1133.

[51] Selamet, A., Xu, M., Lee, I.-J., and Huff, N., "Analytical approach for sound attenuation in perforated dissipative silencers," *Journal of the Acoustical Society of America*, Vol. 115, No. 5, 2004, pp. 2091–2099.

[52] Gabard, G., "Mode-matching techniques for sound propagation in lined ducts with flow," *16th AIAA/CEAS Aeroacoustics Conference*, AIAA Paper 2010-3940, American Institute of Aeronautics and Astronautics, Stockholm, Sweden, 2010.

[53] Astley, R., Cummings, A., and Sormaz, N., "A finite element scheme for acoustic propagation in flexible-walled ducts with bulk-reacting liners, and comparison with experiment," *Journal of Sound and Vibration*, Vol. 150, No. 1, 1991, pp. 119–138.

[54] Félix, S. and Pagneux, V., "Sound propagation in rigid bends: A multimodal approach," *The Journal of the Acoustical Society of America*, Vol. 110, No. 3, 2001, pp. 1329–1337.

[55] Félix, S. and Pagneux, V., "Multimodal analysis of acoustic propagation in three-dimensional bends," *Wave Motion*, Vol. 36, No. 2, 2002, pp. 157–168.

[56] Bi, W., Pagneux, V., Lafarge, D., and Aurégan, Y., "An improved multimodal method for sound propagation in nonuniform lined ducts," *The Journal of the Acoustical Society of America*, Vol. 122, No. 1, 2007, pp. 280–290.

[57] Glav, R., "The point-matching method on dissipative silencers of arbitrary cross-section," *Journal of sound and Vibration*, Vol. 189, No. 1, 1996, pp. 123–135.

[58] Glav, R., "The transfer matrix for a dissipative silencer of arbitrary cross-section," *Journal of Sound and Vibration*, Vol. 236, No. 4, 2000, pp. 575–594.

[59] Kirby, R., "A comparison between analytic and numerical methods for modelling automotive dissipative silencers with mean flow," *Journal of Sound and Vibration*, Vol. 325, No. 3, 2009, pp. 565–582.

[60] Kirby, R., "Transmission loss predictions for dissipative silencers of arbitrary cross section in the presence of mean flow," *Journal of the Acoustical Society of America*, Vol. 114, No. 1, 2003, pp. 200–209.

[61] Peat, K. and Rathi, K., "A finite element analysis of the convected acoustic wave motion in dissipative silencers," *Journal of Sound and Vibration*, Vol. 184, No. 3, 1995, pp. 529–545.

[62] Betgen, B., *Comportement d'un absorbant actif en écoulement : étude théorique et expérimentale*, PhD Thesis, No. 2010-19, École Centrale de Lyon, 2010.

[63] Rienstra, S. W., "A classification of duct modes based on surface waves," *Wave Motion*, Vol. 37, No. 2, 2003, pp. 119–135.

[64] Özyörük, Y., Long, L. N., and Jones, M. G., "Time-domain numerical simulation of a flow-impedance tube," *Journal of Computational Physics*, Vol. 146, No. 1, 1998, pp. 29–57.

[65] Richter, C., Thiele, F. H., Li, X. D., and Zhuang, M., "Comparison of time-domain impedance boundary conditions for lined duct flows," *AIAA Journal*, Vol. 45, No. 6, 2007, pp. 1333–1345.

[66] Busse-Gerstengarbe, S., Richter, C., Thiele, F. H., Lahiri, C., Enghardt, L., Roehle, I., Ferrante, P., and Scofano, A., "Impedance eduction based on microphone measurements of liners under grazing flow conditions," *AIAA Journal*, Vol. 50, No. 4, 2012, pp. 867–879.

[67] Spillere, A. M., Medeiros, A. A., and Cordioli, J. A., "An improved impedance eduction technique based on impedance models and the mode matching method," *Applied Acoustics*, Vol. 129, 2018, pp. 322–334.

[68] Tam, C. K., Webb, J. C., et al., "Dispersion-relation-preserving finite difference schemes for computational acoustics," *Journal of computational physics*, Vol. 107, No. 2, 1993, pp. 262–281.

[69] Bogey, C. and Bailly, C., "A family of low dispersive and low dissipative explicit schemes for flow and noise computations," *Journal of Computational Physics*, Vol. 194, No. 1, 2004, pp. 194–214.

[70] Berland, J., Bogey, C., Marsden, O., and Bailly, C., "High-order, low dispersive and low dissipative explicit schemes for multiple-scale and boundary problems," *Journal of Computational Physics*, Vol. 224, No. 2, 2007, pp. 637–662.

[71] Hu, F., Hussaini, M., and Manthey, J., "Low-Dissipation and Low-Dispersion Runge–Kutta Schemes for Computational Acoustics," *Journal of Computational Physics*, Vol. 124, No. 1, 1996, pp. 177–191.

[72] Jameson, A., "Time dependent calculations using multigrid, with applications to unsteady flows past airfoils and wings," *10th Computational Fluid Dynamics Conference*, 1991, p. 1596.

[73] Allampalli, V., Hixon, R., Nallasamy, M., and Sawyer, S. D., "High-accuracy large-step explicit Runge–Kutta (HALE-RK) schemes for computational aeroacoustics," *Journal of Computational Physics*, Vol. 228, No. 10, 2009, pp. 3837–3850.

[74] Berland, J., Bogey, C., and Bailly, C., "Low-dissipation and low-dispersion fourth-order Runge–Kutta algorithm," *Computers & Fluids*, Vol. 35, No. 10, 2006, pp. 1459–1463.

[75] Tam, C. K., Webb, J. C., and Dong, Z., "A study of the short wave components in computational acoustics," *Journal of Computational Acoustics*, Vol. 1, No. 01, 1993, pp. 1–30.

[76] Bogey, C., de Cacqueray, N., and Bailly, C., "A shock-capturing methodology based on adaptative spatial filtering for high-order non-linear computations," *Journal of Computational Physics*, Vol. 228, No. 5, 2009, pp. 1447–1465.

[77] Özyörük, Y. and Long, L. N., "A time-domain implementation of surface acoustic impedance condition with and without flow," *Journal of Computational Acoustics*, Vol. 5, No. 03, 1997, pp. 277–296.

[78] Fung, K.-Y., Ju, H., and Tallapragada, B., "Impedance and its time-domain extensions," *AIAA journal*, Vol. 38, No. 1, 2000, pp. 30–38.

[79] Li, X. D., Richter, C., and Thiele, F., "Time-domain impedance boundary conditions for surfaces with subsonic mean flows," *Journal of the Acoustical Society of America*, Vol. 119, No. 5, 2006, pp. 2665–2676.

[80] Chevaugeon, N., Remacle, J.-F., and Gallez, X., "Discontinuous Galerkin implementation of the extended Helmholtz resonator model in time domain," *12th AIAA/CEAS Aeroacoustics Conference*, AIAA paper 2006-2569, Cambridge, MA, USA, 2006.

[81] Pascal, L., Piot, E., and Casalis, G., "A new implementation of the extended Helmholtz resonator acoustic liner impedance model in time domain CAA," *Journal of Computational Acoustics*, Vol. 24, No. 01, 2016, pp. 1550015.

[82] Li, X., Li, X., and Tam, C. K., "Improved multipole broadband time-domain impedance boundary condition," *AIAA journal*, Vol. 50, No. 4, 2012, pp. 980–984.

[83] Dragna, D., Pineau, P., and Blanc-Benon, P., "A generalized recursive convolution method for time-domain propagation in porous media," *Journal of the Acoustical Society of America*, Vol. 138, No. 2, 2015, pp. 1030–1042.

[84] Bin, J., Yousuff Hussaini, M., and Lee, S., "Broadband impedance boundary conditions for the simulation of sound propagation in the time domain," *Journal of the Acoustical Society of America*, Vol. 125, No. 2, 2009, pp. 664–675.

[85] Zhong, S., Zhang, X., and Huang, X., "A controllable canonical form implementation of time domain impedance boundary conditions for broadband aeroacoustic computation," *Journal of Computational Physics*, Vol. 313, 2016, pp. 713–725.

[86] Gustavsen, B. and Semlyen, A., "Rational approximation of frequency domain responses by vector fitting," *IEEE Transactions on Power Delivery*, Vol. 14, No. 3, 1999, pp. 1052–1061.

[87] Joseph, R. M., Hagness, S. C., and Taflove, A., "Direct time integration of Maxwell's equations in linear dispersive media with absorption for scattering and propagation of femtosecond electromagnetic pulses," *Optics Letters*, Vol. 16, No. 18, 1991, pp. 1412–1414.

[88] Bayliss, A. and Turkel, E., "Far field boundary conditions for compressible flows," *Journal of Computational Physics*, Vol. 48, No. 2, 1982, pp. 182–199.

[89] Tam, C. K. and Dong, Z., "Radiation and outflow boundary conditions for direct computation of acoustic and flow disturbances in a nonuniform mean flow," *Journal of computational acoustics*, Vol. 4, No. 02, 1996, pp. 175–201.

[90] Bogey, C. and Bailly, C., "Three-dimensional non-reflective boundary conditions for acoustic simulations: far field formulation and validation test cases," *Acta Acustica united with Acustica*, Vol. 88, No. 4, 2002, pp. 463–471.

[91] Hu, F. Q., "On absorbing boundary conditions for linearized Euler equations by a perfectly matched layer," *Journal of Computational Physics*, Vol. 129, No. 1, 1996, pp. 201–219.

[92] Berenger, J.-P. et al., "A perfectly matched layer for the absorption of electromagnetic waves," *Journal of computational physics*, Vol. 114, No. 2, 1994, pp. 185–200.

[93] Aurégan, Y. and Leroux, M., "Experimental evidence of an instability over an impedance wall in a duct with flow," *Journal of Sound and Vibration*, Vol. 317, No. 3-5, 2008, pp. 432–439.

[94] Marx, D., Aurégan, Y., Bailliet, H., and Valière, J.-C., "Evidence of hydrodynamic instability over a liner in a duct with flow," *15th AIAA/CEAS Aeroacoustics Conference*, AIAA Paper 2009-3170, American Institute of Aeronautics and Astronautics, Miami, FL, USA.

[95] Dai, X. and Aurégan, Y., "A cavity-by-cavity description of the aeroacoustic instability over a liner with a grazing flow," *Journal of Fluid Mechanics*, Vol. 852, 2018, pp. 126–145.

[96] Myers, M. K., "Transport of energy by disturbances in arbitrary steady flows," *Journal of Fluid Mechanics*, Vol. 226, 1991, pp. 383–400.

[97] Boyer, G., Piot, E., and Brazier, J.-P., "Theoretical investigation of hydrodynamic surface mode in a lined duct with sheared flow and comparison with experiment," *Journal of Sound and Vibration*, Vol. 330, No. 8, 2011, pp. 1793–1809.

[98] Rodríguez Sánchez, J., *Étude théorique et numérique des modes propres acoustiques dans un conduit avec écoulement et parois absorbantes*, thesis, Toulouse, ISAE, 2016.

[99] Fung, K.-Y., Ju, H., and Tallapragada, B., "Impedance and its time-domain extensions," *AIAA Journal*, Vol. 38, No. 1, 2000, pp. 30–38.

[100] Trefethen, L. N., *Spectral methods in MATLAB*, Vol. 10, Siam, 2000.

[101] Marx, D., Aurégan, Y., Bailliet, H., and Valière, J.-C., "PIV and LDV evidence of hydrodynamic instability over a liner in a duct with flow," *Journal of Sound and Vibration*, Vol. 329, No. 18, 2010, pp. 3798–3812.

[102] Ingard, U., "Influence of fluid motion past a plane boundary on sound reflection , absorption, and transmission," *Journal of the Acoustical Society of America*, Vol. 31, No. 7, 1959, pp. 1035–1036.

[103] Myers, M., "On the acoustic boundary condition in the presence of flow," *Journal of Sound and Vibration*, Vol. 71, No. 3, 1980, pp. 429–434.

[104] Tester, B. J., "The propagation and attenuation of sound in lined ducts containing uniform or "plug" flow," *Journal of Sound and Vibration*, Vol. 28, No. 2, 1973, pp. 151–203.

[105] Rienstra, S. W. and Tester, B. J., "An analytic Green's function for a lined circular duct containing uniform mean flow," *Journal of Sound and Vibration*, Vol. 317, 2008, pp. 994–1016.

[106] Briggs, R., *Electron–Stream Interaction with Plasmas*, MIT Press, Cambridge, 1964.

[107] Bers, A., "Space-time evolution of plasma instabilities-absolute and convective," *Basic plasma physics. 1*, 1983.

[108] Aurégan, Y., Leroux, M., and Pagneux, V., "Measurement of liner impedance with flow by an inverse Method," *10th AIAA/CEAS Aeroacoustics Conference*, AIAA Paper 2004-2838, American Institute of Aeronautics and Astronautics, Manchester, UK, 2004.

[109] Brambley, E. J., "Well posed boundary condition for acoustic liners in straight ducts with flow," *AIAA Journal*, Vol. 49, No. 6, 2011, pp. 1272–1282.

[110] Rienstra, S. W. and Darau, M., "Boundary-layer thickness effects of the hydrodynamic instability along an impedance wall," *Journal of Fluid Mechanics*, Vol. 671, 2011, pp. 559–573.

[111] Marx, D., "A piecewise linear mean flow model for studying stability in a lined channel," *Journal of Sound and Vibration*, Vol. 331, No. 16, 2012, pp. 3809–3823.

[112] Pascal, L., Piot, E., and Casalis, G., "Global linear stability analysis of flow in a lined duct," *Journal of Sound and Vibration*, Vol. 410, 2017, pp. 19–34.

[113] Gabard, G. and Brambley, E., "A full discrete dispersion analysis of time-domain simulations of acoustic liners with flow," *Journal of Computational Physics*, Vol. 273, 2014, pp. 310–326.

[114] Deng, Y., Dragna, D., Galland, M.-A., and Alomar, A., "Comparison of three numerical methods for acoustic propagation in a lined duct with flow," *25th AIAA/CEAS Aeroacoustics Conference*, AIAA Paper 2019-2658, Delft, The Netherlands, 2019.

[115] Vilenski, G. G. and Rienstra, S. W., "Numerical study of acoustic modes in ducted shear flow," *Journal of Sound and Vibration*, Vol. 307, No. 3-5, 2007, pp. 610–626.

[116] Huerre, P. and Monkewitz, P. A., "Absolute and convective instabilities in free shear layers," *Journal of Fluid Mechanics*, Vol. 159, No. -1, 1985, pp. 151.

[117] Huerre, P. and Monkewitz, P. A., "Local and global instabilities in spatially developing flows," *Annual review of fluid mechanics*, Vol. 22, No. 1, 1990, pp. 473–537.

[118] Peake, N., "On the behaviour of a fluid-loaded cylindrical shell with mean flow," *Journal of Fluid Mechanics*, Vol. 338, 1997, pp. 387–410.

[119] Brambley, E. and Peake, N., "Stability and acoustic scattering in a cylindrical thin shell containing compressible mean flow," *Journal of Fluid Mechanics*, Vol. 602, 2008, pp. 403–426.

[120] Brambley, E. and Gabard, G., "Time-domain implementation of an impedance boundary condition with boundary layer correction," *Journal of Computational Physics*, Vol. 321, 2016, pp. 755–775.

[121] Richter, C., Thiele, F. H., Li, X. D., and Zhuang, M., "Comparison of Time-Domain Impedance Boundary Conditions for Lined Duct Flows," *AIAA Journal*, Vol. 45, No. 6, 2007, pp. 1333–1345.

[122] Ju, H. and Fung, K.-Y., "Time-domain impedance boundary conditions with mean flow effects," *AIAA Journal*, Vol. 39, No. 9, 2001, pp. 1683–1690.

[123] Richter, C. and Thiele, F., "Stability of time Explicit impedance models," *13th AIAA/CEAS Aeroacoustics Conference*, AIAA Paper 2007-3538, American Institute of Aeronautics and Astronautics, Rome, Italy, 2007.

[124] Khamis, D. and Brambley, E. J., "Viscous effects on the acoustics and stability of a shear layer over an impedance wall," *J. Fluid Mech.*, Vol. 810, 2017, pp. 489–534.

[125] Xin, B., Sun, D., Jing, X., and Sun, X., "Numerical study of acoustic instability in a partly lined flow duct using the full linearized Navier–Stokes equations," *Journal of Sound and Vibration*, Vol. 373, 2016, pp. 132–146.

[126] Sebastian, R., Marx, D., and Fortuné, V., "Numerical simulation of a turbulent channel flow with an acoustic liner," *J. Sound Vib.*, Vol. 456, 2019, pp. 306–330.

[127] Tester, B., Gabard, G., and Özyörük, Y., "Influence of mean flow gradients on fan exhaust noise predictions," *14th AIAA/CEAS Aeroacoustics Conference*, AIAA Paper 2008-2825, Vancouver, British Columbia, Canada, 2008.

[128] Richter, C., Lueck, H., PANEK, Ł., and Thiele, F., "Methods for suppressing shear layer instabilities for CAA," *Journal of Computational Acoustics*, Vol. 19, No. 02, 2011, pp. 181–203.

[129] Özyörük, Y. and Tester, B. J., "Application of frequency-domain linearized Euler solutions to the prediction of aft fan tones and comparison with experimental measurements on model scale turbofan exhaust nozzles," *Journal of Sound and Vibration*, Vol. 330, No. 16, 2011, pp. 3846–3858.

[130] Huang, X., Chen, X., Ma, Z., and Zhang, X., "Efficient computation of spinning modal radiation through an engine bypass duct," *AIAA journal*, Vol. 46, No. 6, 2008, pp. 1413–1423.

[131] Sun, Y., Fattah, R., Zhong, S., and Zhang, X., "Stable time-domain CAA simulations with linearised governing equations," *Computers and Fluids*, Vol. 167, 2018, pp. 187–195.

[132] Zhang, X., Chen, X., and Gill, J., "Gradient Term Filtering for Stable Sound Propagation with Linearized Euler Equations," *20th AIAA/CEAS Aeroacoustics Conference*, AIAA Paper 2014-3306, Atlanta, GA, 2014.

[133] Bogey, C., Bailly, C., and Juvé, D., "Computation of flow noise using source terms in linearized Euler's equations," *AIAA journal*, Vol. 40, No. 2, 2002, pp. 235–243.

[134] Iob, A., Arina, R., and Schipani, C., "Frequency-domain linearized Euler model for turbomachinery noise radiation through engine exhaust," *AIAA journal*, Vol. 48, No. 4, 2010, pp. 848–858.

[135] Li, X., Schemel, C., Michel, U., and Thiele, F., "Azimuthal sound mode propagation in axisymmetric flow ducts," *AIAA journal*, Vol. 42, No. 10, 2004, pp. 2019–2027.

[136] Ewert, R. and Schröder, W., "Acoustic perturbation equations based on flow decomposition via source filtering," *Journal of Computational Physics*, Vol. 188, No. 2, 2003, pp. 365–398.

[137] Seo, J.-H. and Moon, Y. J., "Perturbed compressible equations for aeroacoustic noise prediction at low mach numbers," *AIAA journal*, Vol. 43, No. 8, 2005, pp. 1716–1724.

[138] Seo, J. H. and Moon, Y. J., "Linearized perturbed compressible equations for low Mach number aeroacoustics," *Journal of Computational Physics*, Vol. 218, No. 2, 2006, pp. 702–719.

[139] Manera, J., Schiltz, B., Leneveu, R., Caro, S., Jacqmot, J., and Rienstra, S., "Kelvin-Helmholtz instabilities occurring at a nacelle exhaust," *14th AIAA/CEAS Aeroacoustics Conference*, AIAA Paper 2008-2883, Vancouver, British Columbia, Canada, 2008.

[140] Li, X., Gao, J., Eschricht, D., and Thiele, F., "Numerical computation of the radiation and refraction of sound waves through a two-dimensional shear layer," *NASA CP Paper*, 2004-212954, 2004.

[141] Pierce, A. D., "Wave equation for sound in fluids with unsteady inhomogeneous flow," *The Journal of the Acoustical Society of America*, Vol. 87, No. 6, 1990, pp. 2292–2299.

[142] Zhang, X., Chen, X., Morfey, C., and Nelson, P., "Computation of spinning modal radiation from an unflanged duct," *AIAA journal*, Vol. 42, No. 9, 2004, pp. 1795–1801.

[143] Zhang, X., Chen, X., and Morfey, C., "Acoustic radiation from a semi-infinite duct with a subsonic jet," *International Journal of Aeroacoustics*, Vol. 4, No. 1-2, 2005, pp. 169–184.

[144] Goldstein, M. E., *Aeroacoustics*, McGraw-Hill Book Company, New York, 1976.

[145] Candel, S. M., "Numerical solution of conservation equations arising in linear wave theory: application to aeroacoustics," *Journal of Fluid Mechanics*, Vol. 83, No. 3, 1977, pp. 465–493.

[146] Rienstra, S. W., Darau, M., and Brambley, E. J., "The trailing vorticity field behind a line source in two-dimensional incompressible linear shear flow," *Journal of Fluid Mechanics*, Vol. 720, 2013, pp. 618–636.

[147] Hu, F. Q., Li, X., Li, X., and Jiang, M., "Time domain wave packet method and suppression of instability waves in aeroacoustic computations," *Journal of Fluids Engineering*, Vol. 136, No. 6, 2014.

*dernière page de la thèse*

# AUTORISATION DE SOUTENANCE

Vu les dispositions de l'arrêté du 25 mai 2016,

Vu la demande du directeur de thèse

Madame M-A. GALLAND

et les rapports de

M. G. GABARD
Senior Researcher - Université du Mans - LAUM - Avenue Olivier Messiaen
72085 LE MANS cedex 9

et de

Mme E. PIOT
Ingénieure de Recherche - ONERA / DMPE - Université de Toulouse - 31055 TOULOUSE

**Madame DENG Yuanyuan**

est autorisée à soutenir une thèse pour l'obtention du grade de **DOCTEUR**

**Ecole doctorale** MECANIQUE, ENERGETIQUE, GENIE CIVIL ET ACOUSTIQUE

Fait à Ecully, le 20 novembre 2020

P/Le directeur de l'E.C.L.
Le directeur des Etudes

Grégory VIAL